



UNIL | Université de Lausanne

Unicentre

CH-1015 Lausanne

<http://serval.unil.ch>

Year : 2022

Hydrologic processes analysis in a high Alpine catchment: the case of the Vallon de Nant

Michelon Anthony

Michelon Anthony, 2022, Hydrologic processes analysis in a high Alpine catchment: the case of the Vallon de Nant

Originally published at : Thesis, University of Lausanne

Posted at the University of Lausanne Open Archive <http://serval.unil.ch>

Document URN : urn:nbn:ch:serval-BIB_0C61AF7447303

Droits d'auteur

L'Université de Lausanne attire expressément l'attention des utilisateurs sur le fait que tous les documents publiés dans l'Archive SERVAL sont protégés par le droit d'auteur, conformément à la loi fédérale sur le droit d'auteur et les droits voisins (LDA). A ce titre, il est indispensable d'obtenir le consentement préalable de l'auteur et/ou de l'éditeur avant toute utilisation d'une oeuvre ou d'une partie d'une oeuvre ne relevant pas d'une utilisation à des fins personnelles au sens de la LDA (art. 19, al. 1 lettre a). A défaut, tout contrevenant s'expose aux sanctions prévues par cette loi. Nous déclinons toute responsabilité en la matière.

Copyright

The University of Lausanne expressly draws the attention of users to the fact that all documents published in the SERVAL Archive are protected by copyright in accordance with federal law on copyright and similar rights (LDA). Accordingly it is indispensable to obtain prior consent from the author and/or publisher before any use of a work or part of a work for purposes other than personal use within the meaning of LDA (art. 19, para. 1 letter a). Failure to do so will expose offenders to the sanctions laid down by this law. We accept no liability in this respect.



UNIL | Université de Lausanne

Unicentre

CH-1015 Lausanne

<http://serval.unil.ch>

Year : 2022

Hydrologic processes analysis in a high Alpine catchment: the case of the Vallon de Nant

Anthony Michelon

Michelon Anthony, 2022, Hydrologic processes analysis in a high Alpine catchment: the case of the Vallon de Nant

Originally published at : Thesis, University of Lausanne

Posted at the University of Lausanne Open Archive <http://serval.unil.ch>

Document URN :

Droits d'auteur

L'Université de Lausanne attire expressément l'attention des utilisateurs sur le fait que tous les documents publiés dans l'Archive SERVAL sont protégés par le droit d'auteur, conformément à la loi fédérale sur le droit d'auteur et les droits voisins (LDA). A ce titre, il est indispensable d'obtenir le consentement préalable de l'auteur et/ou de l'éditeur avant toute utilisation d'une oeuvre ou d'une partie d'une oeuvre ne relevant pas d'une utilisation à des fins personnelles au sens de la LDA (art. 19, al. 1 lettre a). A défaut, tout contrevenant s'expose aux sanctions prévues par cette loi. Nous déclinons toute responsabilité en la matière.

Copyright

The University of Lausanne expressly draws the attention of users to the fact that all documents published in the SERVAL Archive are protected by copyright in accordance with federal law on copyright and similar rights (LDA). Accordingly it is indispensable to obtain prior consent from the author and/or publisher before any use of a work or part of a work for purposes other than personal use within the meaning of LDA (art. 19, para. 1 letter a). Failure to do so will expose offenders to the sanctions laid down by this law. We accept no liability in this respect.



UNIL | Université de Lausanne

Faculté des Géosciences et de l'Environnement (FGSE)
Institut des dynamiques de la surface terrestre (IDYST)

Hydrologic processes analysis in a high Alpine catchment: the case of the Vallon de Nant

Thèse de doctorat

Présentée à la

Faculté des géosciences et de l'environnement
de l'Université de Lausanne

par

Anthony Michelon

Pour l'obtention du grade de
Docteur en Géographie

JURY

Prof. Bettina Schaefli	Directeur de thèse
Prof. Torsten Vennemann	Co-directeur de thèse
Prof. Grégoire Mariéthoz	Expert interne
Dr. Ilja Van Meerveld	Expert externe
Prof. Marie-Elodie Perga	Présidente du Jury

Lausanne, 2021



UNIL | Université de Lausanne
Faculté des géosciences et de l'environnement
bâtiment Géopolis bureau 4631

IMPRIMATUR

Vu le rapport présenté par le jury d'examen, composé de

Présidente de la séance publique :	Mme la Professeure Marie-Elodie Perga
Présidente du colloque :	Mme la Professeure Marie-Elodie Perga
Co-directrice de thèse :	Mme la Professeure Bettina Schaepli
Co-directeur de thèse :	M. le Professeur Torsten Vennemann
Expert interne :	M. le Professeur Grégoire Mariéthoz
Experte externe :	Mme la Professeure Ilja Van Meerveld

Le Doyen de la Faculté des géosciences et de l'environnement autorise l'impression de la thèse de

Monsieur Anthony MICHELON

*Titulaire d'un
Master en Sciences de la Terre
de l'Université de Grenoble Alpes*

intitulée

**HYDROLOGIC PROCESSES ANALYSIS IN A HIGH ALPINE CATCHMENT:
THE CASE OF THE VALLON DE NANT**

Lausanne, le 26 janvier 2022

Pour le Doyen de la Faculté des géosciences et de
l'environnement

Professeure Marie-Elodie Perga

Table of Contents

Table of Contents.....	vii
List of Figures.....	i
List of Tables.....	xiv
Acknowledgement.....	xvii
Abstract.....	xix
Résumé	xxi
1 General introduction	1
<i>Background</i>	<i>1</i>
<i>Flow path tracing with the help of the stable isotopes of water</i>	<i>2</i>
<i>Hydrological research in the Vallon de Nant catchment</i>	<i>4</i>
<i>Research objectives.....</i>	<i>4</i>
<i>Structure of this thesis</i>	<i>5</i>
2 Study area	6
2.1 Definition and interest of the study area	7
2.2 Climate and moisture sources	8
2.3 Geology.....	8
2.4 Surface water catchment vs. groundwater catchment.....	8
2.5 Hydrological units and land use	10
<i>Hydrological units</i>	<i>10</i>
<i>Vegetation.....</i>	<i>12</i>
<i>Land use and activities.....</i>	<i>12</i>
2.6 Previous research in this catchment	13
2.7 Summary.....	13
3 Hydrological data.....	16
3.1 Streamflow along the stream network	17
3.2 Observed streamflow at the outlet.....	20
3.3 Streamflow uncertainties related to river bed dynamic	24
<i>Observation via time lapse imagery</i>	<i>24</i>
<i>Quantification of river stage measurement bias related to river bed dynamics.....</i>	<i>27</i>
3.4 Other sources of streamflow uncertainty	28
<i>Streamflow blocking by ice / snow jam</i>	<i>28</i>
<i>Modifications of stream channel path after a storm.....</i>	<i>30</i>
<i>Subsurface flow.....</i>	<i>31</i>
<i>Groundwater export.....</i>	<i>31</i>
3.5 Summary.....	32
Appendix 3 – 1: Theoretical streamflow calculation for the gauging station using the Poleni formula applied to a trapezoidal cross-section.....	33

4	 Meteorological data	36
4.1	Weather stations in Vallon de Nant	37
4.1.1	On the challenges of a weather station network in the Vallon de Nant	37
4.1.2	Location and communication of the weather stations	37
4.1.3	Accessibility and environmental constraints	40
4.1.4	Design of the remote weather stations	40
4.1.5	Power supply	41
4.1.6	Weather station network details	45
4.1.7	Meteorological data	48
	<i>Air temperature and lapse rate</i>	48
	<i>Precipitation</i>	50
	<i>Local and high altitude winds</i>	50
	<i>Solar radiation</i>	52
4.1.8	Pluvimates raingauges	52
4.1.9	Comparison of precipitation measurements	53
4.2	Snowcover characterization	56
4.2.1	Lysimeters	56
4.2.2	Satellite images and snow-covered areas	58
4.3	Summary	60
	Appendix 4 – 1: Weather stations network in the Vallon de Nant before 2016	62
	Appendix 4 – 2: Drop-counting rain gauge calibration and data correction	63
5	 Benefits from high density rain gauge observations for hydrological response analysis in a small alpine catchment	64
5.1	Introduction	66
5.2	Instruments and methods	69
5.2.1	Instruments	69
5.2.2	Rainfall event characterization	70
	<i>Event identification</i>	70
	<i>Spatial rainfall pattern metrics</i>	70
5.2.3	Streamflow response	73
	<i>Identification of streamflow events and fast runoff</i>	73
	<i>Streamflow metrics</i>	74
5.2.4	Rainfall-streamflow response characterization	75
	<i>Pseudo-dynamic stream network extent</i>	75
	<i>Regression analysis</i>	76
5.2.5	Raingauge network configuration analysis	77
5.2.6	Rainfall-runoff model	78
5.3	Results	78
5.3.1	Rainfall events	78
	<i>Areal rainfall and asymmetry</i>	78
	<i>Geomorphological and topographical distance metrics</i>	81
	<i>Temporal evolution of rainfall metrics</i>	82

5.3.2	Hydrologic response.....	83
	<i>Observed streamflow events</i>	83
	<i>Streamflow generation processes, RC and lag</i>	85
	<i>Dynamic stream network state</i>	86
5.3.3	Identification of dominant hydrologic drivers via regression analysis	88
5.3.4	Measurement network analysis.....	90
	<i>Raingauge density analysis</i>	90
	<i>Optimum network identification</i>	91
	<i>Optimum network evaluation</i>	93
5.4	Discussion	95
5.4.1	Spatial heterogeneity of rainfall.....	95
5.4.2	Raingauge network density.....	97
5.5	Conclusion	98
6	 Studying the dynamic of a high alpine catchment through the scope of multiple natural tracers	100
6.1	Introduction.....	102
6.2	Case study area.....	103
6.3	Methods.....	105
6.3.1	Stable isotopes of water.....	105
	<i>Water sampling</i>	105
6.3.2	Analysis of the isotopic composition of water	107
6.3.3	Water temperature and conductivity measures.....	108
6.3.4	Additional data sources.....	109
6.4	Results.....	109
6.4.1	Identification of streamflow periods	109
6.4.2	Soil temperature	110
	<i>Temporal patterns</i>	110
	<i>Link to streamflow</i>	111
6.4.3	Water temperature	112
	<i>Influence of air temperature on stream temperature</i>	112
	<i>Spring temperature</i>	113
	<i>Flowpath depth estimation</i>	114
6.4.4	Electrical conductivity	115
6.4.5	Stable isotopes of water.....	117
	<i>Ranges of $\delta^2\text{H}$, $\delta^{17}\text{O}$ and $\delta^{18}\text{O}$</i>	117
	<i>Dynamics of $\delta^2\text{H}$, $\delta^{17}\text{O}$ and $\delta^{18}\text{O}$ in springs</i>	121
	<i>Dynamics of $\delta^2\text{H}$, $\delta^{17}\text{O}$ and $\delta^{18}\text{O}$ in streamflow</i>	122
	<i>d-excess</i>	122
	<i>LC-excess</i>	123
	<i>^{17}O-excess</i>	123
6.5	Discussion	124
6.5.1	Origin of winter streamflow	124

6.5.2	Dominant runoff processes driving streamflow generation during early spring snow melt.....	125
6.5.3	Dominant runoff processes during melt periods.....	125
6.5.4	Dominant runoff processes during the seasonal recession.....	126
6.5.5	Interplay of shallow groundwater in the hillslopes and of alluvial or talus groundwater systems.....	126
6.5.6	Transferable insights into the value of the observed variables for hydrologic process investigations in comparable catchments.....	127
	<i>Water sources temperature and shallow soil temperature.....</i>	<i>127</i>
	<i>Isotopic composition of springs and stream water.....</i>	<i>128</i>
	<i>The added value of EC.....</i>	<i>129</i>
6.6	Conclusion	129
	Appendix 6 - 1: Influence of air on the isotopic composition of a water sample ($\delta^2\text{H}$, $\delta^{17}\text{O}$ and $\delta^{18}\text{O}$) within a sealed container	131
	Appendix 6 - 2: Estimate of water flow depth based on a soil temperature model	134
	Appendix 6 - 3: Lapse rate estimation.....	136
7	 Discussion	138
7.1	Preliminary remarks	139
7.2	Part 1: Hydro-meteorological measurements.....	139
7.2.1	Measuring streamflow and other variables at the outlet.....	139
7.2.2	Identification of stream network extent and along stream gauging.....	141
7.2.3	Weather station network.....	141
7.2.4	Precipitation measures	142
7.2.5	Snow cover and snowmelt observations	143
7.2.6	Flow depth and flow path deduced from water sources temperature	144
7.3	Part 2: What did we learn about the hydrology of the Vallon de Nant	144
7.4	Part 3: Outlook for hydrological research in the Vallon de Nant	146
7.4.1	Avenues for future research in the Vallon de Nant	146
7.4.2	Recommendations for future hydrological processes studies in ungauged Alpine headwater catchments	147
8	 General conclusion	150
	References.....	154
	Supplementary Material	168
	Supplementary material - Chapter 2.....	169
	Supplementary material - Chapter 4.....	170
	Supplementary material - Chapter 5.....	171
	Supplementary material - Chapter 6.....	212

List of Figures

Figure 1. Map of hydrological units and dense forest areas in the Vallon de Nant. The delineation of forested areas is made by hand, based on satellite images..... 7

Figure 2. Localization (on the left) of the geological cross-sections of the Vallon de Nant (on the right) adapted from Badoux (1991). The A-B cross-section is going through the Pointe des Savolaires and the Petit Muveran (north-west/south-east); the C-D cross-section follows the same orientation, going through the Grand Muveran 1.5 km further north. The dashed line represents the limit between the Morcles nappe (above) and the flysches (below). 9

Figure 3. Pictures of the Vallon de Nant focusing on A) the riparian wetland and forested area at the lower part of the valley, B) the large slopes on the west side, C) the moraines and glacier (covered with snow on the picture) on the upper part, and D) the steep slopes on the east side. 11

Figure 4. Altitude distribution and hypsometric curve of the Vallon de Nant catchment, separated by landscape units. Note that the forest area is superposed to the other landscape units. Calculations are based on a 2x2 m DEM (swissAlti3D, 2012b). 11

Figure 5. Map of the stream network extent in the Vallon de Nant. C1 and C2 are the two main avalanche couloirs that follow the stream path. The letters a and b identify the different streams options for the along stream gaugings reported in Figure 7. The dashed purple line shows the main stream path after 1 August 2017 storm (until 20 August 2017), based on a satellite images on 2 August 2017 from Planet satellites (Planet, 2017). The Glacier des Martinets extent is based on the Swiss Glacier Inventory 2010 (Fischer et al., 2014)..... 18

Figure 6. Result of the two dye tracer injections on 30 March 2017 (UTC). The plain lines correspond to the measures of rhodamine B and fluorescein concentrations at the outlet, and the dashed lines to their respective injection time at 2.75 and 1.85 km upstream. In blue is the streamflow measured at the outlet (mean value of 2.3 mm.d⁻¹) with its 95% confidence interval. 19

Figure 7. Discharge (top) and specific discharge (bottom) along the main stream measured by the Stream Biofilm and Ecosystem Research Laboratory group (EPFL) and the Catchment hydrology group (UNIL). The mean specific discharge measured at the outlet during the measures was 2.2 mm d⁻¹ (1.7

to 2.8 mm d⁻¹) on 13 Sept. 2016, 2.0 mm d⁻¹ (1.5 to 2.5 mm d⁻¹) on 3 Nov. 2016, and 3.6 mm d⁻¹ (2.9 to 4.4 mm d⁻¹) on 9 Aug. 2017. The vertical line at 4.15 km shows the stream network node beyond which the followed path diverges between the main stream (3 Nov. 2016) and an affluent (13 Sept. 2016 and 9 Aug. 2017), noted a and b on the map of the Figure 5..... 20

Figure 8. Trapezoidal shaped weir at the outlet of the Vallon de Nant. The metallic arm holds the optical height gauge device above the middle point of the weir. Temperature, conductivity, and turbidity probes are located downstream within the 2 metal tubes visible on the left. Sediment transport is measured using geophones located under each metal plate across the weir section..... 21

Figure 9. Rating curve for the Avançon de Nant river at the outlet of the Vallon de Nant, based on 55 salt streamflow measurements. The theoretical rating curve based on the Poleni formula is shown in red..... 22

Figure 10. Five years of streamflow and stream temperature measured at the outlet of the Vallon de Nant catchment HyS1 (1 January 2016 to 1 January 2021). For a streamflow measured at HyS1, the conversion between m³ s⁻¹ and mm d⁻¹ can be done by dividing values by a coefficient of 6.448. 23

Figure 11. Adaptation of a cheap sport camera to an automatic time lapse camera for field observations. The camera control buttons are turned into electronic controls by soldering a wire (A); A clock wakes up an Arduino nano board every hour and i) opens a relay that power the camera and ii) commands the switch on/off and triggering of the camera using logic levels (B); the cameras are enclosed in a waterproof box and attached to a mast, shown here for the Glacier weather station (C) and at the gauging station at the outlet (D). 24

Figure 12. Pictures of the Avançon de Nant at the outlet taken automatically by a camera, showing (A) a normal streamflow, (B) a flood event, (C) the stream channelized in the middle of the weir, (D) the streamflow being split into two parts flowing mainly along the sides of the weir, (E) the stream flowing mainly on the left bank of the weir, (F) an exceptional configuration with a rock being deposited right upstream the middle point of the section after a flood event and affecting dramatically the river stage measurement, (G) the stream almost completely frozen and (H) some maintenance on the weir. 25

Figure 13. Quality check of the streamflow data using pictures. September 7th, 2017 to June 11th, 2019 27

Figure 14. Measure (on the left) of 3 stream profiles and (on the right) comparison of streamflow based on i) a point measurement in the middle point of the weir

or ii) considering the mean height of the stream profile. The three measurements are realized (profile #1) on 20/09/2018 at 7:15, (profile #2) on 20/09/2018 at 7:50 and (profile #3) on 10/10/2018 at 14:55 (UTC). Error bars on the streamflow estimation account for the 95% confidence interval from the rating curve, and for the profile integration an additional error due to the manual measure of the stream profile.....	28
Figure 15. Pictures of a large wet avalanche in the Vallon de Nant on January 31 st , 2018 in the avalanche corridor C1 (see map Figure 5), taken (A) from the left bank of the main stream and (B) from the avalanche itself, looking downward in the direction of the main stream.	29
Figure 16. Streamflow disturbance on January 22 nd , 2018 attributed to a river jam caused by an avalanche. The dark blue curve and light blue envelop correspond to the streamflow and its 95% confidence interval, estimated from the rating curve of Figure 9.	30
Figure 17. Pictures showing stream bed modifications after the storm of 1 August 2017, with A) a major deviation of the main stream (see details on map Figure 5) that deviate water from the dry bed visible on the left (with bridge) toward a new channel on the right, and minor deviations of the stream bed forced by a large accumulation of sediments carried by a temporary stream and deviates the main stream over grassy soils.	31
Figure 18. Conservation of the total head H over a weir (Böll, 1997).....	33
Figure 19. A Sensorscope datalogger at the Glacier weather station. Each datalogger is energetically self-sufficient, with a solar panel and batteries to supply low consumption sensors up to 5 days without sun. Each box can receive 3 modules, each connected to a sensor. An additional card can transform a datalogger into a master station and transmit the data to a server using the mobile 4G LTE network.	38
Figure 20. Map showing the location of the previous six stations and the four new stations (Table 5) weather stations (WS) in the Vallon de Nant. The relay of the new weather stations network is used only as a repeater to transmit the data from the Auberge to the other stations despite the curvature of the valley. The Glacier is the master station that transmits the data to a server through the wireless 4G LTE network.	39
Figure 21. Trajectory of the sun along the year and shadow of the terrain at the Chalet and Glacier sites.	41

Figure 22. Theoretical duration of diffuse and direct radiation received daily at the Glacier weather station (46.20873° N, 7.08972° E) during the year. The diffuse radiation only accounts for the latitude of the point (46.2°N), while the direct radiation also accounts for the topography based on a 2x2 m DEM (swissAlti3D, 2012b). For 69 days there is no direction radiation, from November 14 th to January 22 nd	42
Figure 23. Example of simulation result to evaluate the energy necessary to power a Lufft WS400 as if it was exposed to the weather conditions (temperature and precipitation amount) recorded for 10 years at the Pilatus weather station (2106 masl), with the theoretical direct and diffuse radiation conditions at the Glacier site. The top plot shows the periods in red when heating is required. The middle plot shows the periods in red when the station is not accessible. The bottom plot shows the energy consumption at the station, when the batteries should be switched (purple dots), and periods of data loss in red when the batteries are empty and the station not accessible.....	44
Figure 24. Pictures of the weather stations at (A) the Auberge, (B) the Chalet, (C) La Chaux and (D) the Glacier. The Madd raingauge at the Auberge is located 2.5 meters above the ground, and the Lufft WS400 sensors at the Auberge, Chalet and Glacier are at least 3.5 meters above the ground.	45
Figure 25. Availability (when color bars) of meteorological parameters for the four weather stations in Vallon de Nant.....	47
Figure 26. Daily air temperature at the Auberge, Chalet and Glacier weather stations in 2017; the mean air temperature over the year is respectively 6.1 °C, 6.3 °C and 2.8 °C (time series include 16.4 %, 30.1 % and 0.8 % of data gap, respectively).	48
Figure 27. Altitudinal gradient of temperature during the day between Auberge and Glacier, Chalet and Glacier, for all year, February, and September. Based on common times series: between 67.6 % and 81.5 % of the period for all year, and between 97.1 % and 100 % for the individual months. The blue line is 0 °C/100 m and the red line -0.65 °C/100 m.....	49
Figure 28. Cumulated precipitation (rainfall and snowfall) measured at three weather stations in 2017. Note that the time series for this year have 17.2 % , 30.0 % and 1.2 % of missing data.....	50
Figure 29. Wind direction at the Auberge, Chalet and Glacier weather stations, relatively to their working periods.....	51

Figure 30. Frequency of wind direction above the Vallon de Nant at 500 hPa (ECMWF ERA5) on a 6-hour time scale. The grey histogram represents the wind occurrence during the working period of the precipitation sensors, and the blue histogram the wind when precipitation was recorded.....	51
Figure 31. Drop-counting rain gauge used. The Pluvimate is set-up vertically between 0.8 and 1.2 meters above the ground (a). A tip at the end of the funnel (b) creates a calibrated drop of water that falls on the sensor, (c) which counts and records the number of drops during a given amount of time.	53
Figure 32. Comparison (left) of rainfall amounts ($r^2 = 0.73$) and (right) maximum intensity over 2 minutes ($r^2 = 0.49$) measured at the Auberge by the Lufft sensor vs. Pluvimate raingauge, at event scale.	54
Figure 33. Comparison of rainfall amounts ($r^2 = 0.95$) and maximum intensity over 2 minutes ($r^2 = 0.72$) measured at the Auberge by the Lufft WS400 sensor vs. the Madd raingauge, at event scale. The maximum rainfall data from the Madd sensor have been aggregated from 1-minute to 2-minute time step resolution for comparison.....	54
Figure 34. Comparison of measurements between an OTT Pluvio ² sheltered by a double fence intercomparison reference (DFIR) and a Lufft WS600 (using the same 24 GHz sensor as the Lufft WS400), recorded between 14 Dec. 2013 and 17 Jun. 2014 at the Moléson weather station, Switzerland, by MeteoSwiss (Nitu et al., 2018). Data received from Yves-Alain Roulet (MeteoSwiss), reproduced here with the permission of the original author.....	55
Figure 35. (A) Picture of the co-located lysimeters next to the Chalet weather station. (B) A trench allows a tube to collect independently the melted water from each raingauge in two bags in an insulated plastic box at lower altitude.....	56
Figure 36. Snow water equivalent (SWE) measure at the lysimeters at the four weather stations for the 2017/2018 winter. The Chaux and Glacier time series are complete (up to the complete snowpack melt), but the Auberge and Chalet time series are cut prematurely before the period when it was estimated the raingauge measuring snow melt was flood/clogged.	57
Figure 37. Snow covered area in Vallon de Nant between 1 January 2015 and 1 January 2018 using 53 satellite images from Landsat 8 (L8) and 36 satellite images from Sentinel-2 (S2).	59
Figure 38. Monthly maps of probability of presence of snow for the Vallon de Nant, based on 2 years of snow cover maps between 1 March 2015 and 1 March	

2017. Each map and part of the catchment is based on a different number of snow cover maps, presented in Supplementary Material.....	60
Figure 39. Calibration curve (on top) of the Pluvimate rain gauges based on experimental measures with controlled rainfall input, and (at the bottom) the data frequency measured in situ.	63
Figure 40. Map of the Vallon de Nant and location of the 12 rain gauges. The streamflow is measured on the main river at the outlet (46.25301 N / 7.10954 E in WGS84 coordinates). The red dashed line splits the catchment area into two parts of equal area. The small numbers next to the streams indicate the Strahler stream order (Strahler, 1957).....	69
Figure 41. Summary of the recorded rainfall and streamflow for the rainfall event of July 24 th 2018 at 6:32 PM (UTC).	73
Figure 42. Summary of the recorded rainfall and streamflow for the rainfall events of August 24 th 2018 at 2:46 AM (top) and August 29 th 2018 at 11:52 AM (bottom).	74
Figure 43. Scatterplot of the rainfall amounts over the northern and the southern parts of the catchment for all 48 rainfall events. The dotted lines show the 1/2 and 2/1 lines which correspond to twice more rainfall in one part of the catchment than in the other or to $ I_{ASYM} > 0.33$. The highest event is an outlier (event of 6-Aug with 43.5 mm of rainfall in total) and is flagged without streamflow response because the river stage measure was disturbed during this period.....	80
Figure 44. Scatterplots of the distance metrics for the dry network state versus the wet state, for all 48 rainfall events. The bars indicate the standard deviation obtained from the 20 rainfall field realisations. r^2 indicates the linear correlation.	82
Figure 45. Scatterplots of A) total rainfall amounts versus fast streamflow (highlighting the threshold for streamflow response) and B) of rainfall amounts in the northern and the southern part against fast streamflow (for separation line, see Figure 40a). The bars show the standard deviation of estimated rainfall (Section 5.2.2) and of streamflow. The events of July 24 th ($P_{ALL}=8.0$ mm, $Q_{FAST} = 30.4$ mm) and of Aug 6 th ($P_{ALL}=43.5$ mm, Q not recorded) are out of the axes in A and in B.....	84
Figure 46. Runoff coefficient against D_{HILLS} , highlighting events with high rainfall amounts in the southern part, i.e. events with $P_{SOUTH}>4.5$ mm; the July 24 th	

event with $3.02 < RC < 4.85$ and $D_{HILLS} = 740 \pm 140$ m has been discarded (see Section 5.3.1).....	87
Figure 47. A) Number of rainfall events for which the total amount of rainfall is overestimated or underestimated by a factor 2, according to the rain gauge density, going from 0.07 to 0.82 rain gauges per km ² (respectively 1 to 11 rain gauges within the catchment). B) Error on the maximum rainfall over 10 minutes $P_{MAX}(10 \text{ min})$ according to the raingauge density. For each rain gauge density, all possible combinations of rain gauge networks are tested. The reference value is estimated from the full 12-rain gauge network. The bottom and top of each box are the 25th and 75th percentiles of the sample, the middle line the sample median. The whiskers go up to 1.5 times the interquartile range; values beyond the whiskers (outliers) are marked with circles.....	91
Figure 48. Best (green) and second best (purple) networks and associated RMSE values for 1 to 5 stations resulting from the minimization of the RMSE over 23 events for the P_{ALL} , P_{MAX} , I_{ASYM} and D_{STREAM} . The red dashed line splits the catchments into two parts of equal area.....	92
Figure 49. Sensitivity test over the best network from 1 to 3 stations, evaluated by removing from 1 to 3 events over the 23 events (2047 combinations) for the P_{ALL} and I_{ASYM} . The result is presented graphically: larger dots and wider links represent configurations that are found more frequently than others over the different simulations. The red dashed line splits the catchments into two parts of equal area.	93
Figure 50. Comparison of streamflow response metrics ratios between a partial network (best 3-station, best 1-station and worst 3-station networks) and the full rain gauge network, using the RC (left) and lag time $\Delta_{P/Q}$ (right). The dataset is subset#4 of Table 2. Larger dots highlight events where events where only 2 of 3 stations were operational (see Section 4.1.1). The lines connect the events to improve readability.....	94
Figure 51. Analysis of 15 rainfall-runoff model events (subset #3, Table 2) with the correlation coefficient between simulated and observed streamflow for different rainfall fields inputs: the stochastic generation of rainfall fields based on all available rain gauge stations, the best 3-stations and the best 1-station network, and the worst 3-stations network. Larger dots highlight events for which only 2 of 3 stations were operational (see Section 4.1.1). The lines connect the events to improve readability.....	95

Figure 52. The map A) shows the location of the sampling sites in the Vallon de Nant (outlet at 46.25301°N, 7.10954°E in WGS84). Note that the AUBG spring location shows where the spring is taken, whereas the water from this spring is sampled at the Auberge weather station point, 800 m further north. The topographic map is based on a 2-m digital elevation model (swissAlti3D, 2012a). The stream network shows its full extend during snowmelt periods. ‘Soil temperature’ shows locations of the sensor network of Vittoz (2021). The map B) identifies the dominant hydrological units of the Vallon de Nant and the hatched area corresponds to forested areas. 104

Figure 53. Comparison of the streamflow evolution (on top) and cumulative (bottom) over a year (April 10th to April 9th next year) for 3 years. Note that there are gaps in the data, and 6.4%, 3.2% and 4.6% of the timeseries are missing (respectively in 2016-2017, 2017-2018 and 2018-2019)..... 105

Figure 54. Evolution of soil temperature (top) at 3 locations within the Vallon de Nant catchment and (bottom) of the stream at the outlet, 4 springs and groundwater at 2 locations between January 2016 and October 2018. A summary of dates is available in the Supplementary Material, 112

Figure 55. Range of $\delta^2\text{H}$, $\delta^{17}\text{O}$, $\delta^{18}\text{O}$, conductivity, d-excess, lc-excess and ^{17}O -excess for stream, springs, groundwater, rainfall, snowpack, glacier and vegetation water samples. The left and right end of each box show the 25th and 75th percentiles, and the middle point is the median. The whiskers go up to 1.5 times the interquartile range; values beyond the whiskers (outliers) are marked with circles. The values on the right y-axis of the figures are the number of samples in each category. Note that there are no conductivity measurements for snowpack and vegetation water samples. For ^{17}O -excess the values of vegetations samples are out of the box (median 572 ‰, 25th and 75th percentiles are 374 ‰ and 742‰, resp., and whiskers are from 31 ‰ to 8329 ‰). 116

Figure 56. Time series of $\delta^2\text{H}$, $\delta^{17}\text{O}$, $\delta^{18}\text{O}$, conductivity, d-excess, lc-excess and ^{17}O -excess for 5 springs (location on map Figure 52 A)..... 118

Figure 57. Time series of $\delta^2\text{H}$, $\delta^{17}\text{O}$, $\delta^{18}\text{O}$, conductivity, d-excess, lc-excess and ^{17}O -excess at the Vallon de Nant outlet HyS1 and at the upper subcatchment HyS2 (location on map Figure 52 A)..... 119

Figure 58. Time series of $\delta^2\text{H}$, $\delta^{17}\text{O}$, $\delta^{18}\text{O}$, conductivity, d-excess, lc-excess and ^{17}O -excess for rainfall (from Auberge and Chalet weather stations, location on map Figure 52 A) and snowpack. Note that the conductivity of snowpack has not been measured. 120

Figure 59. Changes in $\delta^2\text{H}$, $\delta^{17}\text{O}$ and $\delta^{18}\text{O}$ of a water sample depending on the initial isotopic composition of the water vapor of the air locked up with the sample. The results are completed for saturated air (continuous line) and dry air (dashed line), for ratios of sample volume over container volume from 1/2 to 1/1000. The red dashed line represents the detection limit of the measuring device.	133
Figure 60. Measured and modelized air and soil temperature for 2 piezometers (PZ1 and PZ2) and 4 springs (GRAS, ROCK, BRDG and ICEC).	135
Figure 61. State of the Glacier weather station in spring 2017 (A), spring 2018 (B) and spring 2019 (C).	142
Figure S62. Comparison of vegetation cover between a historical picture (1912 or before, on top) and an actual picture (2017, on bottom). Credit for the top picture: Robert di Salvo.	169
Figure S63. Maps showing the number of images used to compute the snowcover maps. The square shapes are due to the removal of a part of an image with clouds.	170
Figure S64. River discharge measured at the Vallon de Nant outlet (in $\text{m}^3\cdot\text{s}^{-1}$ and $\text{mm}\cdot\text{day}^{-1}$) over 2018. The study period (from July 1 st 2018 to September 23 th 2018) is marked out by the two red dashed lines.	171
Figure S65. Initial streamflow for the 15 rainfall events causing a river reaction as function of the day of the year. The grey area corresponds to the period when the streamflow gauge readings were perturbed and thus discarded from the present analysis.	172
Figure S66. River quickflow for 15 rainfall events (P event) causing a noticeable river reaction (Q event). The length of events is normalized.	173
Figure S67. Distribution of the distance metrics D_{HILLS} , D_{STREAM} and H_{HAND} for all 48 rainfall events.	174
Figure S68. Distribution of D_{HILLS} for the northern part (left column) and the southern part (right column) of the catch men, with respect to the wet network (top row) and the dry network (bottom row). The median of the wet distances are 329 m shorter than the dry distances in the northern part (top), in the southern part (bottom) they are 634 m shorter.	175
Figure S69. Map of the Vallon de Nant (Map data from www.map.geo.admin.ch , © CNES, Spot Image, swisstopo, NPOC) showing the 25 subcatchments and the stream network geometry used for the modelization.	176

Figure S70. Results of simulation. For each of the 15 events having a streamflow reaction is plotted the observed streamflow (black curve), the simulated streamflow based on stochastic rainfall fields (blue curve and band), the simulated streamflow based on the best 3-station and 1-station network (respectively with plain and dashed green curves), and the simulated streamflow based on the worst 3-station network (dotted red curve)..... 177

Figure S71. Cumulated results of simulation. For each of the 15 events having a streamflow reaction is plotted the cumulated observed streamflow (black curve), the cumulated simulated streamflow based on stochastic rainfall fields (blue curve and band), the cumulated simulated streamflow based on the best 3-station and 1-station network (respectively with plain and dashed green curves), and the cumulated simulated streamflow based on the worst 3-station network (dotted red curve). The amounts of streamflow are normalized by the cumulated amount of observed streamflow. 178

Figure S72: Deviation between the two spatial rainfall interpolation methods used in this paper, in terms of cumulated rainfall (left) and per event (right). 179

Figure S73. Evolution of rainfall intensity and I_{ASYM} for the 15 rainfall events (P event) associated with a river reaction (Q event). 180

Figure S74. Evolution of D_{HILLS} for the 15 rainfall events (P event) associated with a river reaction (Q event). 181

Figure S75. Evolution of D_{STREAM} for the 15 rainfall events (P event) associated with a river reaction (Q event). 182

Figure S76. Precipitation event No. 1 from July 2nd 04:42 PM to July 2nd 06:56 PM 188

Figure S77. Precipitation event No. 2 from July 2nd 09:58 PM to July 2nd 10:40 PM and discharge event No. 1 from July 2nd 10:43 PM to July 2nd 11:27 PM 188

Figure S78. Precipitation event No. 3 from July 3rd 04:50 AM to July 3rd 05:44 AM 189

Figure S79. Precipitation event No. 4 from July 3rd 05:00 PM to July 3rd 05:40 PM and discharge event No. 2 from July 3rd 05:21 PM to July 3rd 07:36 PM..... 189

Figure S80. Precipitation event No. 5 from July 5th 04:28 AM to July 5th 05:28 AM 190

Figure S81. Precipitation event No. 6 from July 5th 09:38 AM to July 5th 12:08 PM 190

Figure S82. Precipitation event No. 7 from July 5th 01:48 PM to July 5th 05:32 PM and discharge event No. 3 from July 5th 04:33 PM to July 5th 09:42 PM..... 191

Figure S83. Precipitation event No. 8 from July 6th 01:14 AM to July 6th 03:36 AM 191

Figure S84. Precipitation event No. 9 from July 6th 05:38 AM to July 6th 01:36 PM and discharge event No. 4 from July 6th 06:55 AM to July 6th 04:42 PM.....	192
Figure S85. Precipitation event No. 10 from July 14th 03:00 PM to July 14th 08:58 PM and discharge event No. 5 from July 14th 04:51 PM to July 14th 09:53 PM.....	192
Figure S86. Precipitation event No. 11 from July 15th 05:42 PM to July 15th 07:58 PM and discharge event No. 6 from July 15th 06:20 PM to July 15th 11:01 PM.....	193
Figure S87. Precipitation event No. 12 from July 19th 01:26 AM to July 19th 03:10 AM	193
Figure S88. Precipitation event No. 13 from July 20th 05:40 PM to July 20th 10:28 PM and discharge event No. 7 from July 20th 07:01 PM to July 20th 10:49 PM.....	194
Figure S89. Precipitation event No. 14 from July 21st 10:46 AM to July 21st 12:00 PM	194
Figure S90. Precipitation event No. 15 from July 21st 04:06 PM to July 21st 05:42 PM.....	195
Figure S91. Precipitation event No. 16 from July 24th 06:32 PM to July 24th 10:12 PM and discharge event No. 8 from July 24th 08:07 PM to July 24th 11:56 PM.....	195
Figure S92. Precipitation event No. 17 from July 28th 05:18 AM to July 28th 06:16 AM	196
Figure S93. Precipitation event No. 18 from July 28th 10:02 AM to July 28th 02:06 PM	196
Figure S94. Precipitation event No. 19 from August 1st 03:34 PM to August 1st 07:50 PM	197
Figure S95. Precipitation event No. 20 from August 3rd 03:18 PM to August 3rd 04:26 PM	197
Figure S96. Precipitation event No. 21 from August 5th 02:56 PM to August 5th 03:28 PM	198
Figure S97. Precipitation event No. 22 from August 6th 04:36 PM to August 6th 07:44 PM	198
Figure S98. Precipitation event No. 23 from August 8th 02:32 PM to August 8th 03:04 PM	199
Figure S99. Precipitation event No. 24 from August 9th 11:40 AM to August 9th 01:54 PM	199
Figure S100. Precipitation event No. 25 from August 9th 10:12 PM to August 9th 11:24 PM	200
Figure S101. Precipitation event No. 26 from August 10th 02:30 AM to August 10th 06:36 AM	200

Figure S102. Precipitation event No. 27 from August 13th 07:52 AM to August 13th 09:38 AM	201
Figure S103. Precipitation event No. 28 from August 13th 02:08 PM to August 13th 03:06 PM	201
Figure S104. Precipitation event No. 29 from August 14th 02:16 AM to August 14th 05:40 AM and discharge event No. 9 from August 14th 03:46 AM to August 14th 06:18 AM.....	202
Figure S105. Precipitation event No. 30 from August 14th 12:54 PM to August 14th 02:28 PM	202
Figure S106. Precipitation event No. 31 from August 17th 12:04 PM to August 17th 02:36 PM and discharge event No. 10 from August 17th 01:53 PM to August 17th 03:42 PM	203
Figure S107. Precipitation event No. 32 from August 19th 03:22 PM to August 19th 04:00 PM	203
Figure S108. Precipitation event No. 33 from August 22nd 07:10 PM to August 22nd 08:42 PM	204
Figure S109. Precipitation event No. 34 from August 23rd 04:26 PM to August 23rd 10:54 PM and discharge event No. 11 from August 23rd 06:32 PM to August 23rd 10:29 PM.....	204
Figure S110. Precipitation event No. 35 from August 24th 02:46 AM to August 24th 05:24 AM and discharge event No. 12 from August 24th 04:10 AM to August 24th 05:57 AM.....	205
Figure S111. Precipitation event No. 36 from August 25th 10:22 AM to August 25th 11:24 AM	205
Figure S112. Precipitation event No. 37 from August 25th 01:26 PM to August 25th 04:20 PM	206
Figure S113. Precipitation event No. 38 from August 25th 06:58 PM to August 25th 09:16 PM	206
Figure S114. Precipitation event No. 39 from August 26th 08:02 AM to August 26th 10:06 AM	207
Figure S115. Precipitation event No. 40 from August 29th 11:52 AM to August 29th 01:06 PM	207

Figure S116. Precipitation event No. 41 from August 29th 05:32 PM to August 29th 06:44 PM and discharge event No. 13 from August 29th 06:38 PM to August 29th 08:34 PM	208
Figure S117. Precipitation event No. 42 from August 31th 03:46 PM to August 31st 07:16 PM	208
Figure S118. Precipitation event No. 43 from September 1st 05:36 AM to September 1st 04:04 PM and discharge event No. 14 from September 1st 11:49 AM to September 1st 05:30 PM.....	209
Figure S119. Precipitation event No. 44 from September 6th 10:58 PM to September 7th 02:54 AM.....	209
Figure S120. Precipitation event No. 45 from September 13th 02:54 PM to September 13th 09:04 PM and discharge event No. 15 from September 13th 08:39 PM to September 13th 09:38 PM.....	210
Figure S121. Precipitation event No. 46 from September 14th 12:42 AM to September 14th 02:00 AM.....	210
Figure S122. Precipitation event No. 47 from September 18th 06:04 PM to September 18th 08:18 PM	211
Figure S123. Precipitation event No. 48 from September 21st 02:24 PM to September 21st 11:20 PM	211
Figure S124. Comparison of 38 samples conductivity measured on the field using a WTW Multi 3510 IDS with a WTW TetraCon 925 probe (Xylem Analytics Germany Sales GmbH & Co, Weilheim, Germany) or later in the laboratory directly within the 12 mL amber silicate vials using a JENWAY 4510 Conductivity Meter with a 6 mm glass probe (Stone, UK).....	212
Figure S125. Water table depth (top) and temperature (bottom) at PZ1 and PZ2 from 1 July 2017 to 1 October 2018. Water table depth and temperature data are from Thornton et al. (2021a).....	213

List of Tables

Table 1. Topographic characteristics of the main landscape units in the Vallon de Nant. Here the glacier unit includes the glacier area (0.58 km ²) and the upstream area. Note that the forest area is superposed to the other landscape units. Calculations are based on a 2x2 m DEM (swissAlti3D, 2012b).	12
Table 2. General statistics of streamflow from 2016 to 2020. For each parameter are displayed in parenthesis the inferior and superior values given by the 95% confidence interval on the rating curve. Original data have a 1-minute resolution, so the instant maximum concerns a maximum specific discharge over 1 minute.	23
Table 3. Classification of the 5745 pictures taken between September 7 th , 2017 and June 11 th , 2019 (642 days, 193 days without data) into seven categories. Periods with more than 24 hours between two consecutive data are considered as periods without data and are not accounted into the total duration.....	26
Table 4. Results of simulation based on 10-year records of temperature and precipitations data from 6 weather stations in Switzerland, and the theoretical direct and diffuse radiation conditions at the Chalet and Glacier sites. The simulations are summarized here through statistics of mean and maximum number of battery switches per year, and the number and maximum duration of data gaps.	43
Table 5. Location and altitude of the four weather stations of the Vallon de Nant.....	45
Table 6. List and properties of sensors used for the weather stations in the Vallon de Nant.....	46
Table 7. Statistics of daily net radiations (in W/m ²) at the Chalet, La Chaux and Glacier weather stations. The mean value is computed over 217 days between 1 January 2017 and 31 December 2017.....	52
Table 8. Melt rate statistics at the Chaux and Glacier lysimeters for a 3-month cold period from 15 December 2017 to 15 March 2018 and during their respective melt period.	57
Table 9. Details about the previous weather stations network setup in the Vallon de Nant (locations on Figure 20).....	62
Table 10. List of used metrics, with corresponding parameter name or abbreviation.	76

Table 11. Summary of the different subsets of rainfall events used within this study. The streamflow response outlier event discarded in subset #4 corresponds to July 24 th 2018.	79
Table 12. Correlations between rainfall metrics and hydrologic response metrics for event series #4 of Table 2. Absolute values equal or higher than 0.60 are in bold.....	81
Table 13. List of recorded precipitation events with streamflow response (event series #3 of Table 2). Full details are available in Michelin et al. (2021a).	83
Table 14. Correlations between distance metrics for rainfall events with streamflow response (series #4 of Table 2). Absolute values equal or higher than 0.60 are in bold. Correlations for all rainfall events are available in the Table S20 in Supplementary Material.	87
Table 15. List of the tested predictors for the RC with a pure quadratic regression, and corresponding statistics: root mean square error (RMSE), coefficient of determination (R^2), variance of residuals (var. residuals), p-value, corrected Akaike criterion (AICc) and AICc ranking. The acceptable p-values (≤ 0.05) and first 3 ranks are highlighted. The analysis is over the 14 events of series #4 of Table 2.	88
Table 16. As Table 15 but for the lag $\Delta_{P/Q}$	89
Table 17. Statistics on temperature time series recorded in the stream, piezometers, and springs. The dampening depth estimated for the BRDG spring (*) is biased because of a positive anomaly of temperature due to snowmelt input (see text).....	115
Table 18. Characteristics of the sinusoidal air and water temperatures used for the soil temperature model, and characteristics of the soil temperature at the estimate depth corresponding to the water temperature.	135
Table S19. Distance metrics for each streamflow event with respect to the extended (wet) and the retracted (dry) network and the combined distance if a threshold of antecedent precipitation of 20 mm is applied.	183
Table S20. Correlations between distance metrics for all the rainfall events (subset #1, Table 4 in the main text). Absolute values equal or over 0.60 are in bold.	184
Table S21. For the 23 events measured by the full network setup: number of stations wrong by a factor 2 compared to the average of all the stations.....	185

Table S22. For the 23 events measured by the full network setup: number of events for which the station is wrong by a factor 2 compared to the average of all the stations.	186
Table S23. Start and end dates of each hydrological period.	214
Table S24. Start and end dates of each snowcover period at the soil temperature points	215

Acknowledgement

My primary gratitude is obviously addressed to Bettina, my thesis supervisor, for the trust that she has placed in me since our first interview, for the freedom she allowed me to undertake my research, for all the sage advice and passionate discussions we had over the years.

I also thank Torsten, my co-supervisor. Torsten has a wealth of knowledge that commands respect, and with whom a discussion necessarily leads to gleaning seemingly tons of new knowledge and exploring new fields of possibilities. Thank you for all your advice.

I gratefully acknowledge the jury members, Prof. Grégoire Mariéthoz and Prof. Ilja Van Meerveld who accepted to read and evaluate my thesis.

I had the chance to share these years with wonderful colleagues: Natalie, Harsh, Tom, Moctar, and Josh. I am proud to have met them during their scientist youth, as I am certain their names will resonate for a very long time on renowned articles and announcements of prestigious conferences.

The success of my experience at IDYST has been made possible grace to many doors, always open, to colleagues and professors ready to give advice, answer a question, share ideas, and start collaborations.

It is impossible to talk about life at IDYST without mentioning the cafeteria, which is a meeting place for the coffee- and chocolate-addicted people, where productivity gives way to the craziest digressions. The most assiduous who I name here: Gustavo, Fabio, Andrea, Manuel, Elisa, Sassi, Philip, Leanne, Charlotte, Francesco, Gabriel, Gelare, Iignes, Joanne, Lilly... I reserve to Inigo the status of slackline mate, as we shared many lunch times in equilibrium.

A special thanks to Mathieu, with his free and challenging mind always ready to (create and) solve the most twisted problems. And I don't forget my two sunshines: Clémence and Marie-Noëlle.

Thank you to Laetitia, Micaela and Aurélien for their efficient work in the lab and the field. Thank you to Carole and Sabrina for their precious work at IDYST. Thank you to François from the botanical garden *La Thomasia* for its support.

And I have to say a huge thank you for all people that helped with field work: the hours of carrying heavy loads, up and down, often in harsh conditions. By foot, by ski, and while pulling a pulka. I particularly thank Natalie, who shared so many difficult days in the field, under cold rain, storms and in the snow. Thank you, Lionel, for following me up the steepest terrain. I have no doubt that your departure for tropical lands is not unrelated. I will not be able to cite all people who helped in the field, but I wanted to cite at least those who also join for the most serious conditions, namely François, James, and Pascal.

But the list is not complete, I could probably add 50 more names of people who helped me to go through all these years...

Final line: I carry in my heart each of your passions for science, mountains, unsolvable problems, games of perplexion and debate.

Thank you.

Anthony

Abstract

High elevation headwater catchments play a key role in the Alpine water cycle. However, the ongoing increase of mean temperatures induces a shift in the precipitation phase, with more precipitation falling as rainfall, and less snowpack accumulation. The overall consequences on the hydrologic dynamic are a shift of the timing of annual maximum streamflow to earlier periods, impacting the water resources later in the year when they are the most required. This tendency is well known and already observed. Detailed hydrological studies on snowmelt flow paths are, however, still rare. Accordingly, the approaches developed to include snow in hydrological models suffer from a lack of knowledge about the flowpath processes at work at the catchment scale.

In this thesis, we proposed to address the question of the flowpath dynamic in Alpine environments by studying a small (13.4 km²) snow-dominated headwater catchment in the Western Swiss Alps, the Vallon de Nant. This catchment is one of the few relatively undisturbed catchments (by human water use) in Switzerland and the focus of a wide range of geosciences research. Hydrological research was initiated here with the work on this thesis, i.e. almost everything remained to be done. Accordingly, a starting point was the detailed observation of meteorological processes relevant for hydrology. Although the study area is small, a first question to answer was the impact of the spatial heterogeneity of rainfall on the hydrological response of the catchment. A 12-station (temporary) raingauge network was deployed and measured 48 summer rainfall events. Thanks to the development of new streamflow response metrics, we found that spatial rainfall patterns might play a key role to explain the hydrologic response in small Alpine catchments because of the interplay of variable drainage density, the distance along the stream network to the outlet, and of spatially variable subsurface storage potential. Our conclusion is that a 3-station network (1 station per 0.22 km²) is necessary to capture most of the spatial heterogeneity of precipitation in this catchment.

In a second step, the water flowpaths were studied for different hydrological units defined within the studied catchment based on prior knowledge of geomorphology. This study was based on environmental tracers of water, by monitoring the temperature of various subsurface water sources in the catchment (in springs and piezometers) and by analyzing electroconductivity (EC) and the triple stable isotopes of water ($\delta^2\text{H}$, $\delta^{17}\text{O}$ and $\delta^{18}\text{O}$) for 2861

samples (mainly springs, stream, rainfall, snowpack). The combination of these tracers showed the dominance of subsurface flow contributions to streamflow throughout the year. Even during the peak of the melt season, when high inputs lead to a complete flushing of the system with recent snowmelt, the snowmelt reaches the stream essentially via subsurface flowpaths. We also detected some continuous inflow to the stream even during winter baseflow and could identify the activation of shallow flowpaths during rainfall events that occur during the melt season.

Beyond site-specific conclusions, our detailed analysis of the different tracers shows how they jointly convey information on the dominant processes. Spring water temperature contains information on local flowpath depth and connectivity. EC data from springs and the main stream can be interpreted in terms of water age and thereby provide information about subsurface flow path length. In addition to these two tracers that are impacted by local subsurface properties, stable water isotopes reflect the history of the air mass generating the precipitations. They inform about the presence of recent snowmelt in streamflow and are thus complementary to temperature and EC measurements. In addition, the variation in the isotopic composition observed in subsurface water can give additional insights into reservoir size or flow rates. It is noteworthy that for this study, we used the δ -values directly; neither d-excess nor ^{17}O -excess could be interpreted in terms of local-scale hydrological processes. Our hope is that the presented data might, in future research, contribute to understand their value for local-scale process analysis.

To conclude this thesis and based on the knowledge gained during the field work, we propose a wide range of recommendations on the instrumentation and sampling of comparable catchments for future work.

Résumé

Les bassins versant supérieurs de haute altitude jouent un rôle primordial dans le cycle de l'eau en milieu Alpin. L'augmentation actuelle des températures moyennes provoque toutefois un changement du type de précipitations, avec d'avantage de pluie et moins d'accumulation de neige. La dynamique hydrologique s'en retrouve modifiée par un décalage du pic annuel de débit plus tôt dans la saison, ce qui impact la disponibilité en eau plus tard dans l'année, lorsqu'elle devient primordiale. Bien que cette tendance soit déjà observée et bien documentée, les études hydrologiques sur les chemins d'écoulement de l'eau de fonte sont rares, et les modèles souffrent du manque de connaissance sur ces processus à l'échelle du bassin versant.

Dans cette thèse, nous proposons de répondre à la question de la dynamique des chemins d'écoulements de l'eau dans un tel environnement Alpin en étudiant le Vallon de Nant, un petit (13.4 km²) bassin versant supérieur situé dans la partie ouest des Alpes Suisses. Ce bassin, très largement influencé par la neige, est l'un des rares bassins non perturbé (en termes d'utilisation humaine des ressources en eau) en Suisse, et intéresse de très divers domaines de recherches en géosciences. Les recherches hydrologiques dans ce bassin ont toutefois commencé en même temps que cette thèse, avec donc aucune connaissances préalables. Un point de départ pour cette étude fut l'observation détaillée des processus météorologiques intéressants pour l'hydrologie. Bien que le terrain d'étude soit petit, l'une des premières interrogations concernait l'impact de l'hétérogénéité spatiale de la pluie sur la réponse hydrologique du bassin versant. Un réseau temporaire de 12 pluviomètres a été déployé et 48 évènements de pluie ont été enregistrés. Grâce au développement de nouvelles métriques caractérisant la réponse hydrologique, nous avons trouvé que l'hétérogénéité spatiale des précipitations pouvait expliquer la réponse hydrologique de tels bassin du fait de la variation de la densité de drainage du réseau de rivières, de la distance d'un point à l'exutoire, ainsi que par la variation spatiale de la capacité potentielle de stockage de l'eau dans le sol. Notre conclusion est qu'un réseau de 3 pluviomètres (1 station pour 0.22 km²) est nécessaire pour saisir l'essentiel de l'hétérogénéité des précipitations dans ce bassin versant.

Dans un second temps, différentes unités hydrologiques ont été identifiées au sein de ce bassin versant sur la base de données géomorphologiques, et les chemins d'écoulement de l'eau ont été étudiés pour chacune de ces unités. L'étude s'est appuyée sur des traceurs

environnementaux, en suivant la température de plusieurs sources d'eau provenant d'un écoulement de subsurface (sources et piézomètres), et grâce aux mesures d'électroconductivité (EC) et de la composition en isotopes stables de l'eau ($\delta^2\text{H}$, $\delta^{17}\text{O}$ et $\delta^{18}\text{O}$) de 2861 échantillons d'eau (provenant principalement de sources, de rivières, de l'eau de pluie, et du manteau neigeux). L'étude conjointe de ces traceurs a montré l'importance de l'écoulement de subsurface dans le débit de la rivière au cours de l'année. Même au cours du pic annuel de débit, lorsque les apports en eau de fonte sont si importants que l'eau de toutes les sources montrent des caractéristiques similaires, l'eau de fonte s'écoule jusqu'à la rivière par un chemin de subsurface. Nous avons également mesuré un apport continu d'eau à la rivière lors de la période de débit de base en hiver, et nous avons identifié l'activation d'écoulements de faible profondeur au cours d'évènements de pluie qui surviennent pendant la période de fonte de neige.

Au-delà des conclusions spécifiques à ce terrain d'étude, notre analyse détaillée des différents traceurs a montré comment, ensemble, ils contenaient des informations. La température de l'eau des sources renseigne sur la profondeur des chemins d'écoulement locaux, ainsi que sur la connectivité. Les valeurs d'EC des sources et du cours d'eau principal peuvent être interprétés en termes d'âge de l'eau, et donc informer sur la longueur du chemin d'écoulement de subsurface. Contrairement à la température et à l'EC, qui eux sont impactés par les propriétés locales du sol qui est traversé, les isotopes stables de l'eau fournissent des informations sur l'origine des précipitations avant qu'elles ne pénètrent le sol. Par exemple, les isotopes stables de l'eau informent sur la présence d'eau de fonte récente dans la rivière, et donc sont complémentaires à la température et à l'EC. De plus, le rythme de variation observé en subsurface peut fournir des indices supplémentaires sur la taille des réservoirs, ou sur la vitesse d'écoulement de l'eau dans le sol. Les valeurs de $\delta^2\text{H}$, $\delta^{17}\text{O}$ et $\delta^{18}\text{O}$ ont été utilisées indépendamment comme traceur ; toutefois, ni le d-excess, ni le ^{17}O -excess n'ont pu être interprétés en termes de processus hydrologique à l'échelle locale. Nous espérons que le jeu de données acquis pourra contribuer à comprendre l'utilité de ces valeurs dans l'analyse de phénomènes à l'échelle locale pour de futures recherches.

Grâce au travail de terrain extrêmement riche qui a été réalisé au cours de cette thèse, nous proposons à la fin de cette thèse diverses recommandations sur l'instrumentation et l'échantillonnage au sein de bassins versants ayant des propriétés similaires au Vallon de Nant.

1 | General introduction



Photograph: stream flowing under a melting snowpack

Background

Mountains under mid-latitudes play a key role in providing freshwater supply and deserve the name of “water towers for humanity” (Viviroli et al., 2007) for their capacity to store water on a seasonal time scale as snowpack, and over a longer time in the form of glaciers. In most mountain ranges, the snow and ice accumulated during the cold seasons is later released during the periods of higher energy input, driven by the yearly cycle of incoming radiation and air temperature (Kaser et al., 2010). Switzerland is a good example of a country dependent on mountain water resources, as 70 % of its territory is occupied by mountains (Alps and Jura) and has headwater catchments that contribute to the four main rivers feeding western Europe (in particular the Rhine and the Rhone rivers), with snowmelt contributing up to 40 % of the mean annual streamflow (OFEV, 2012). In addition to agricultural, industrial and household needs, Switzerland is especially interested and dependent on water for its power production. In 2020, hydropower plants provided 58.1 % of the annual energy requirements (SFOE, 2021). However, rising temperatures observed during the 20th century reduced snow accumulation (Hammond et al., 2018; Bormann et al., 2018; Laternser and Schneebeli, 2003) and caused mass loss in most of glaciers (Zemp et al., 2020). The temperature increase is even more alarming as models predict the warming rate in mountains areas to double or triple during the coming century (Nogues-Bravo et al., 2007).

The increase of mean temperatures in mountains leads to a precipitation phase shift with more precipitation falling as rainfall, less snow accumulation, and an earlier snowmelt season (Barnhart et al., 2016; Bard et al., 2015). This has a strong impact on the hydrologic dynamics, shifting the annual river peak flow to earlier seasons, causing at many places a lack of water resources later in the year when it is the most required (Barnett et al., 2005; Zampieri et al., 2015), and with an increased risk of late summer droughts.

There is no doubt that warming leads to declining snowfall and reduced snow water resources (Musselman et al., 2021) and the general effect of rising temperatures on snow-influenced hydrologic regimes is well understood (Beniston et al., 2018; Brunner et al., 2019; Huss et al., 2017). There are, however, some key questions that have been opened by the analysis of a large ensemble of catchments, mostly in the US. This includes the question why a general reduction of the share of precipitation falling as snow leads to a reduction of total annual flow (Berghuijs et al., 2014). To date it is unclear what drives this tendency and whether it holds everywhere. Next, some authors postulated a general trend of slower snow melt in a warmer

world, but again based on climates observed in the US (Musselman et al., 2017). Similarly, shifts of rain-on-snow flood events have largely been studied in the US (Musselman et al., 2018).

The above calls into question the widespread view that we already have a relatively good understanding of how snow melt interacts with hydrological processes at the catchment scale. There is also a widespread paradigm that the difficulty of observing solid precipitation is one of the most important sources of uncertainty in water balance estimates for snow-dominated environments. This well-known difficulty is due to poor measurements of winter precipitation and unreliable estimates of spatial snow water equivalent of snowpack (Jonas et al., 2009). The focus on this paradigm lead to important efforts in developing and comparing snow (Brauchli et al., 2017; Wever et al., 2017; Gunther et al., 2019; Sohrabi et al., 2018; Engel et al., 2017) in hydrological models at the cost of at least partly neglecting the role of subsurface hydrological processes in high elevation catchments.

A way forward to better understand how a reduction in snowfall might influence hydrological processes in currently snow-dominated environments is the detailed analysis of the interplay of all dominant hydrological processes during the entire year, i.e., not only during the melt season, which might yield an incomplete picture. Such an analysis is challenging because Alpine environments are typically difficult to access (especially in some periods of the year). The extreme weather conditions and the lack of power supply makes long term measurements difficult, while for regular surveys that are time consuming and exposed to dangers (Bocquet and Thomas, 1989; Jobard, 2009).

Flow path tracing with the help of the stable isotopes of water

A key focus of this thesis is thus to explore the dynamic of flowpaths during the year, using different tracers for water. The stable isotopes of water (^2H , ^{17}O and ^{18}O) have been used for many years as conservative tracers for hydrological processes at the catchment scale to study the contribution of snowmelt, glacier melt and rainfall to streamflow (for a review, see Beria et al., 2018). The isotopic composition of stable water isotopes is impacted by the physical processes of phase changes (i.e. evaporation, condensation, sublimation), which leads to fractionation, i.e. to a change of the ratio of heavy to light isotopes. In contrast, the isotopic composition is preserved in closed systems, such as subsurface flow, groundwater reservoirs, or streamflow (when phase exchange with air is negligible)

Two kind of isotopic fractionation processes occur during water phase change. The first is equilibrium fractionation, determined by the ratio of the saturating vapor pressure of the isotopically heavier to the isotopically lighter molecule of water. This process is a function of the temperature (Mook, 2000) and occurs for example during condensation, which is considered in equilibrium.

The second process is kinetic fractionation, which is due to the lower diffusivity of light isotopologues compared to heavy isotopologues, and the processes are incomplete during evaporation, solid condensation and supersaturation compared to ice crystals.

H-isotope fractionations ($^2\text{H}/^1\text{H}$) under equilibrium conditions are about a factor of eight times higher than those for the $^{18}\text{O}/^{16}\text{O}$ fractionations between the different water isotopologues. During kinetic processes, the relative mass differences of the different water isotopologues need to be considered. As such, during evaporation under low humidity conditions, the lighter water molecules will preferentially enter the vapour phase compared to the isotopically heavier molecules. Hence, the $^1\text{H}_2^{16}\text{O}$ molecule (18 atomic mass units, AMU) will be the kinetically favored molecule of the vapour phase, followed by $^1\text{H}^2\text{H}^{16}\text{O}$ (AMU 19) and finally $^1\text{H}_2^{18}\text{O}$ (AMU 20). The latter remaining preferentially in the liquid phase. Accordingly, d-excess (d-excess = $\delta^2\text{H} - 8 \times \delta^{18}\text{O}$, see Section 6.3.2) has been introduced as a metric to measure kinetic fractionation processes (Dansgaard, 1964).

^{17}O is the least abundant of the stable isotopes of water, but recent technological advances make it possible to routinely measure it jointly with ^2H and ^{18}O in CRDS (Cavity Ring Down Spectrometer) devices (i.e. Picarro L2140-i). The similar effects of temperature on kinetic fractionation processes for ^{17}O and ^{18}O led to the introduction of the ^{17}O excess (^{17}O -excess = $\ln(\delta^{17}\text{O} + 1) - 0.528 \times \ln(\delta^{18}\text{O} + 1)$, see Section 6.3.2) Unlike d-excess, ^{17}O -excess is not influenced by the temperature of moisture sources and therefore has the potential to provide additional information on the physical processes undergone by water during its course from source to sink (Barkan and Luz, 2005; Landais et al., 2006).

To date, few hydrological studies at mid-latitudes include ^{17}O measurements and most of them are in North-America (Li et al., 2015; Bershaw et al., 2020; Passey and Ji, 2019). This thesis proposes to use the three isotopes of water to investigate the flow paths in a high Alpine catchment, in addition to electric conductivity (a geochemical tracer, noted later EC), and water temperature.

Such tracers are often used in studies to characterize end-members of water to determine the final composition of water at the outlet (Munoz-Villers and McDonnell, 2012; Schmieder et al., 2018; Penna et al., 2014; Penna et al., 2017). Few studies, however, explore the question of flowpaths in high elevation catchments. Examples of detailed hydrological process investigations in high elevation alpine catchments include the work of Engel et al. (2019), Penna and van Meerveld (2019) and Zuecco et al. (2019). Their investigations are namely the basis for our further investigations on the use of stable isotopes of water and electricity conductivity (Chapter 6).

Hydrological research in the Vallon de Nant catchment

This thesis intends to investigate the contribution of stable water isotopes composition to the analysis of water flowpaths in snow-fed catchments with a complex terrain such as in the Swiss Alps. We study the hydrological processes in the Vallon de Nant catchment, a snow-dominated headwater catchment of 13.4 km² in area located in the western Swiss Alps (Chapter 2). The special focus is hereby on the analysis and characterization of hydrological flow paths with the help of temperature, EC, and the stable isotopes of water.

It is important to point out here that hydrological investigations in this catchment started with the start of this research project. Previously, research focused there on vegetation dynamics, geomorphology, and some aspects of summer climate (for an overview, see Chapter 2). Accordingly, from a hydrological view point almost everything remained to be done in this area, starting with the development of an all year-round meteorological network, the characterization of precipitation input but also a better understanding of actual streamflow measurements or the dynamics of the streamflow network itself. This task was overwhelming at times. At the same time, several research groups started new projects, which led to initially unplanned synergies that namely resulted in a detailed analysis of summer rainfall and its impact on streamflow generation, which was initially not planned during this thesis (Chapter 5).

Research objectives

In the context to better understand the hydrological processes in the Vallon de Nant catchment, our research questions were the following:

- What are the spatial and temporal rainfall variability in the study area and what is the necessary raingauge network density and configuration to capture its variability in order to explain the hydrological response to rainfall input?
- What are the dominant hydrological processes and flowpaths of the different hydrological units in the catchment? And which ones are dominant for the hydrological response at the catchment scale at different periods of the year?
- Do stable isotopes of water, and particularly ^{17}O , give additional insights on flow paths and flow rates, that could not be obtained from electrical conductivity or temperature tracers?

Structure of this thesis

The thesis is structured as follows. Next to this general introduction, the Chapter 2 describes the Vallon de Nant catchment in which all the work of this thesis was conducted. Chapter 3 presents a hydrological description of the study area, and the experiments carried out there. Chapter 4 details the technical work of deployment and maintenance of the weather station network, as well as snow cover assessment work. Chapter 5 is an adapted version of a published paper (Michelon et al., 2021a) concerning the summer rainfall characterization using a high density raingauge network. Chapter 6 is an adapted version of a manuscript under revision that deals with flow paths and water reservoirs, studied based on multiple natural tracers of water (temperature, EC and stable isotopes of water). Chapter 7 presents the general discussion of the work, of its findings and future perspectives, and the overall conclusion is given in Chapter 8. A Supplementary Material for each chapter is added at the end of this manuscript.

2 | Study area



Photograph: view in the Vallon de Nant from the Chalet weather station in direction to the floodplain area and the large slopes to the west. The two peaks are the Dent Favre (2,916 masl) on the left and the Pointe des Savolaires (2,294 masl) on the right.

2.1 Definition and interest of the study area

The Vallon de Nant is a narrow and steep headwater catchment located in the western Swiss Alps (Figure 1). The extent of the Vallon de Nant was delimited based on the position of the streamflow gauging station (46.25301° N / 7.10954° E in WGS84 coordinates, 574622 E / 122451 N in CH1903 coordinates) on its main river, the Avançon de Nant. The chosen outlet has a catchment area of 13.4 km² ranging from 1,200 to 3,051 m above sea level (masl) and bordered by the peaks of the Grand Muveran and Petit Muveran, the Dent Favre, the Dent de Morcles, the Pointe des Martinets and Pointe des Savolaires. The mean elevation of the catchment is 2,012 masl.

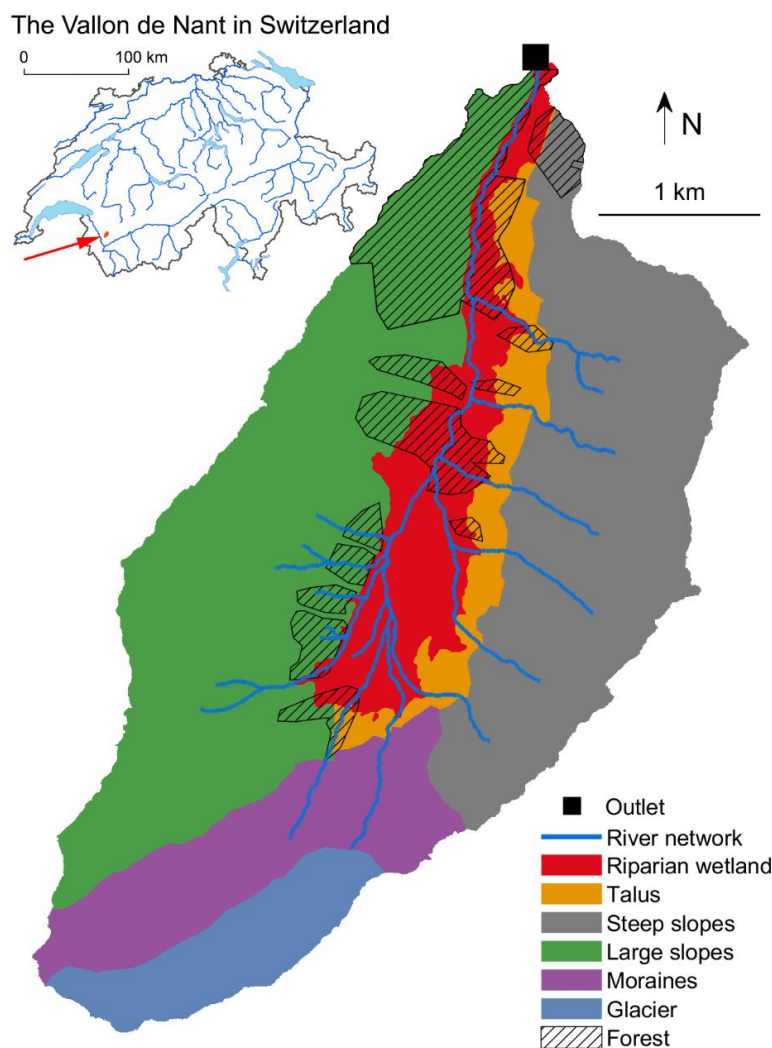


Figure 1. Map of hydrological units and dense forest areas in the Vallon de Nant. The delineation of forested areas is made by hand, based on satellite images.

The Vallon de Nant has a protected status (Natural Reserve of the Muveran) since 1969 and is of national importance for Switzerland in terms of biodiversity (Cherix and Vittoz, 2009).

2.2 Climate and moisture sources

According to Sodemann and Zubler (2010), precipitation reaching the Alps originates mostly from the North Atlantic Ocean (39.6 %), then the Mediterranean Sea (23.3 %), followed by contributions from the Arctic, North and Baltic sea, and finally land sources from Central Europe. In terms of seasonality, winter precipitation is mainly from the North Atlantic Ocean, while the first contributor to summer rainfall is Central Europe.

In 2017, in the Vallon de Nant, the weather station of the Glacier (2,136 masl, see Chapter 4) measured 1,723 mm of precipitation (rainfall and snowfall). The mean air temperature at the mean catchment elevation (2,012 masl) was around 3.1°C, and the mean water temperature of the stream at the outlet was 5.0°C. Further details on the meteorologic conditions of the Vallon de Nant will be given in Chapter 4.

2.3 Geology

The Vallon de Nant belongs to the backside of the Morcles nappe (Huggenberger, 1985). The Cretaceous and Tertiary lithologies are a succession of thick, blocky layers of limestones that are exposed throughout the surrounding valley (Figure 2). They lie on a substratum of flysch, i.e. softer rocks (schistose marls and sandstone benches), which explains the deepening and widening of the valley at its southern part (Badoux, 1991). The detailed geological structure of the area is summarized in the work of Thornton et al. (2018).

2.4 Surface water catchment vs. groundwater catchment

The limestone dominating the rock walls and slopes surrounding the valley bottom do not show visible signs of karstic features, which does however not imply that they are absent in the subsurface (Thornton et al., 2018). Most notably, tracer tests showed some water export from the area of the Pointe des Savoires, exfiltrating downstream of the Vallon de Nant outlet at the Plans-sur-Bex (ibid.).

Thornton et al. (2018) closed the catchment at a lower location for their hydrogeological simulations to avoid any water balance errors arising from water export on the northern crest or from water flowing under the gauging station, but it is not entirely clear to date whether the geology leads to substantial groundwater export, i.e. precipitation falling on the catchment area but not showing up at the gauging station.

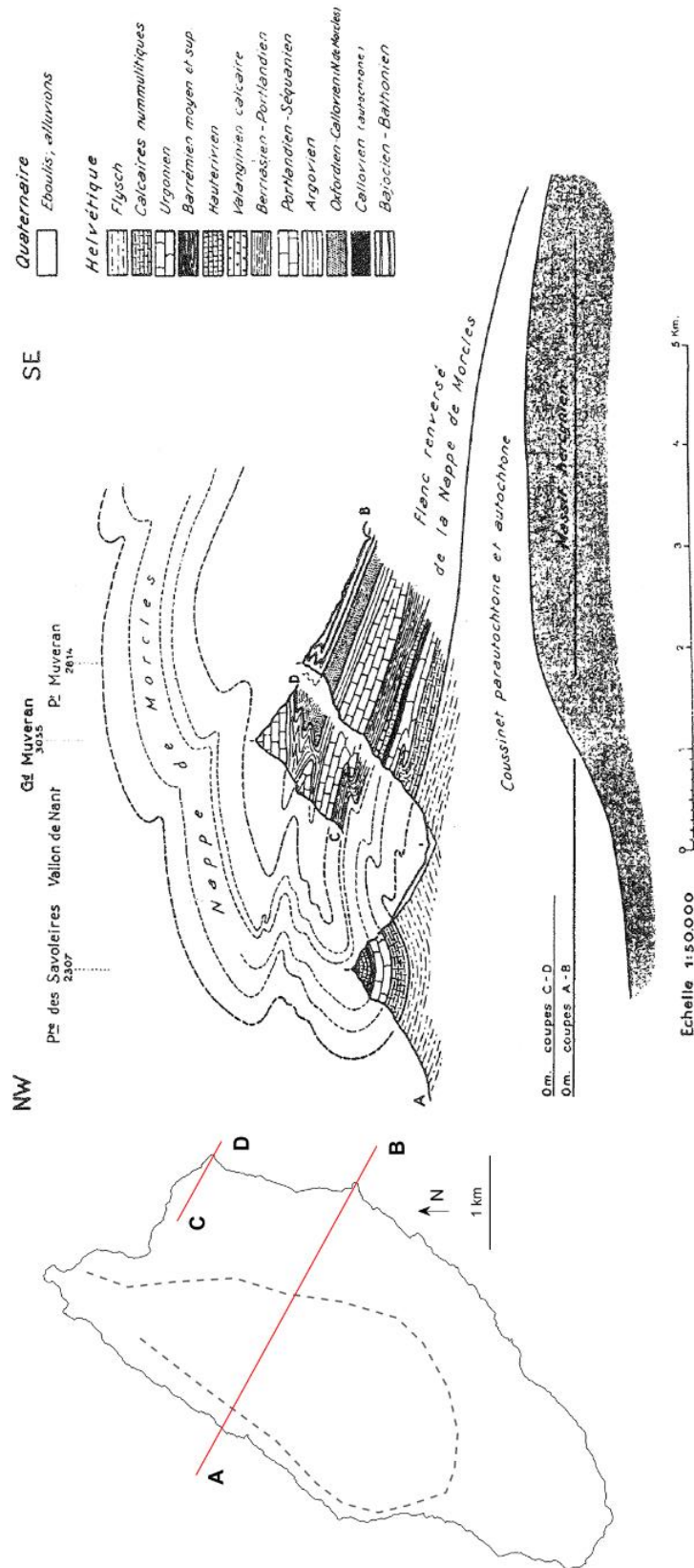


Figure 2. Localization (on the left) of the geological cross-sections of the Vallon de Nant (on the right) adapted from Badoux (1991). The A-B cross-section is going through the Pointe des Savoires and the Petit Mueran (north-west/south-east); the C-D cross-section follows the same orientation, going through the Grand Mueran 1.5 km further north. The dashed line represents the limit between the Morcles nappe (above) and the flysches (below).

2.5 Hydrological units and land use

Hydrological units

Since the catchment extends over an elevation range of 1,851 m, the variation in geomorphology and vegetation cover is large. Figure 1 summarizes the dominant hydrological units that we have delineated based on the dominant landscape features prior to the deployment of our field campaigns.

In the southern part of the valley, the Glacier des Martinets, with an area of 0.58 km² in 2016 (Linsbauer et al., 2021) survives at relatively low elevation (2,126 to 2,685 masl), as it lies on the northern, shady side of the Dent de Morcles. Due to its small size, its high debris cover and low radiation exposure, the glacier is likely to have a small contribution to the catchment-scale streamflow (Mächler et al., 2021). The water flow paths through and below the debris-covered glacier are unknown to date and are not specifically investigated as part of the present research.

The eastern side of the catchment is marked by steep and rocky slopes (Figure 3 D) associated with shallow soils and debris cones at the foot of the rock walls in the north-eastern part. Along the rock walls, all lateral tributaries are ephemeral, flowing principally during the snowmelt season or shortly after the rainfall events; their extent fluctuates and is not known precisely.

The western side of the valley is associated with grassy slopes (Figure 3 B), relatively well-developed soils and hence relatively high water storage capacities; these high storage capacities are also confirmed by salt gaugings along the main stream during the late summer and autumn streamflow recession period in 2016 and 2017 (see Chapter 3).

At the foot of the cliffs, large alluvial cones and scree extend up to the river. The bottom of the valley is mainly composed of fine alluvial deposits with a large water storage capacity. The riparian wetland (Figure 3 A), at least in its southern part, is made of coarse and permeable alluvial sediments associated with a high hydraulic conductivity; it could potentially contain dynamic water storage to its full depth, which can exceed 80 m (Thornton, 2021).

These delineated hydrological units show very different elevation distributions (Figure 4 and Table 1). Elevation-related meteorological variables like air temperature and precipitation phase can be expected to be relatively uniform over areas with a relatively narrow range of elevations (i.e. riparian wetland, glacier), whereas for areas that extent over almost the whole

range of elevation of the catchment (i.e. steep slopes, large slopes), the weather conditions will affect the top and bottom areas of the units in a very different way.



Figure 3. Pictures of the Vallon de Nant focusing on A) the riparian wetland and forested area at the lower part of the valley, B) the large slopes on the west side, C) the moraines and glacier (covered with snow on the picture) on the upper part, and D) the steep slopes on the east side.

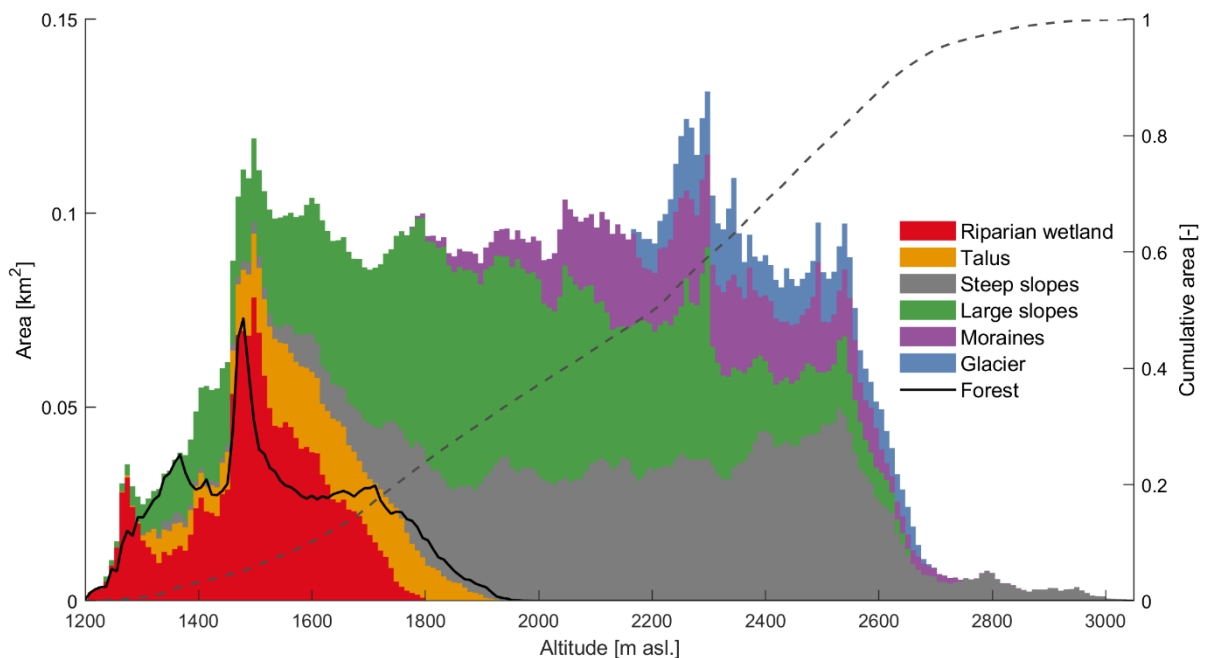


Figure 4. Altitude distribution and hypsometric curve of the Vallon de Nant catchment, separated by landscape units. Note that the forest area is superposed to the other landscape units. Calculations are based on a 2x2 m DEM (swissAlti3D, 2012b).

Table 1. Topographic characteristics of the main landscape units in the Vallon de Nant. Here the glacier unit includes the glacier area (0.58 km²) and the upstream area. Note that the forest area is superposed to the other landscape units. Calculations are based on a 2x2 m DEM (swissAlti3D, 2012b).

Landscape units	Area		Elevation [m asl.]				Mean slope [°]	Mean aspect [°]
	[km ²]	[%]	mean	min	max	range		
Riparian wetland	1.65	12.3	1506	1200	1799	599	17.7	350
Talus	0.80	6.0	1605	1261	1932	671	37.8	298
Steep slopes	3.73	27.8	2199	1281	3051	1770	47.5	296
Large slopes	4.80	35.8	1937	1200	2653	1453	34.4	91
Moraines	1.55	11.6	2288	1763	2917	1154	31.8	14
Glacier	0.87	6.5	2472	2167	2969	802	34.6	9
All catchment	13.4	100	2012	1200	3051	1851	35.9	36
Forest	1.87	14.0	1535	1200	1982	782	32.7	74

The location of springs seems correlated with low slopes and this topographic particularity might be enough to explain the location of springs along the right bank of the main stream and within the grassy slopes in the west area of the catchment, where the slopes are low. In the same way, the absence of tributaries over the north-western parts of the catchment can be related to steep slopes but can also be explained by a large hydraulic conductivity and locally well-developed soils.

Vegetation

Comparison of historical and recent photographs (see Supplementary Material) shows a relatively stable vegetation cover, composed of grassland, stands, and spruce (Dutoit, 1983), which are intermixed with corridors of scrub vegetation and controlled by regular avalanches. About 14 % of the catchment area is covered with dense forest (Figure 4 and Table 1), dominated by *Picea abies* (Norway spruce) at the lower elevation, and *Larix decidua* (Larch) in the middle part of the catchment (Ba, 2019). Alpine meadow covers a large part of the forest-free area below approximately 2,000 masl. The vegetation between 1,950 and 2,550 masl is described in detail in the work of Giaccone (2020).

Land use and activities

The Vallon de Nant is little disturbed by human presence. In summer, the activity is centered on hiking trails that cross the valley. There is a road access to a parking lot at 1,250 masl next to a small restaurant and guest house and a botanical garden. The main hiking trail provides access to a barn at 1,500 masl and is used by the only shepherd who lets his cows graze between 1,250 and about 1,900 masl. A bridge allows hikers to cross the Avançon de Nant at

1,480 masl A second bridge was built at 1,450 masl in July 2017, but a storm on 1 August 2017 deviated the main stream from the bridge (see Section 3.4 in Chapter 3) and the Commune de Bex decided to modify the main stream flow into its initial bed, under the bridge. This bridge got swept away 50 meters downstream by an avalanche in winter 2020/2021.

In winter, the access road is covered by snow and the Vallon de Nant is no longer accessible by car. The only activity is ski touring and snow shoeing. The main hiking trail would remain blocked even into early summer because of regular wet snow avalanches in spring; however, heavy machinery is used every spring after the melt season to make the track up to the barn passable. The same machinery is used occasionally to re-open access after storm events that cover the main trail with large debris falling and flowing down the rock wall on the right-hand river side.

2.6 Previous research in this catchment

This catchment has been the focus of a number of recent research projects, in disciplines such as hydrology (Michelon et al., 2021a; Beria et al., 2020), hydrogeology (Thornton et al., 2021a), sediment transport (Antoniazza et al., 2021), pedology (Rowley et al., 2018) biogeochemical cycling (Grand et al., 2016), geomorphology (Lane et al., 2016) and vegetation ecology (Vittoz, 2012; Giaccone et al., 2019), as well as interaction between biology and hydrology (Mächler et al., 2021) and stream ecology (Horgby et al., 2019a; Horgby et al., 2019b). The respective work is reviewed and cited in the different Chapters of this thesis.

2.7 Summary

The Vallon de Nant is a small Alpine headwater catchment with a large variety of landscape features that are typical for Alpine environments, but also with specific particularities, e.g. its north aspect and large shadowed areas. The cold temperatures resulting from its relatively high elevation and the northern aspect make the valley largely influenced by snow, and even enables the presence of a small glacier.

Many research teams have become interested in the Vallon de Nant as it is one of the few high elevation head water catchments in Switzerland that are relatively undisturbed by human presence and do not suffer major terrain modifications. Its relatively good accessibility allows a continuous monitoring and a good maintenance of the deployed equipment. However, the snow and extreme weather conditions in winter are challenging with regard to access and equipment maintenance.

Hydrological process studies in the Vallon de Nant just started at the beginning of this thesis and are detailed in the next Chapter.

3 | Hydrological data



Photograph: the gauging station at the outlet of the Vallon de Nant in winter, with a partially frozen stream.

The overall work of this thesis relies on streamflow and meteorological characterization that will be respectively presented in this chapter and the following one. The study period started in 2016 at the same time as the commissioning of the gauging station at the outlet of the Vallon de Nant and benefited from its measures, but in there are no historical records. The first part of this chapter presents the stream network (Section 3.1) and discusses in detail the streamflow measurements at the outlet (Section 3.2) and their quality (Sections 3.3 and 3.4).

Some additional data sets acquired for this thesis work are excluded from this chapter and will be analyzed and discussed extensively in the Chapter 6 which presents the core of the hydrological process analysis; these data include soil temperature, water temperature, water conductivity and stable water isotopes.

3.1 Streamflow along the stream network

The Avançon de Nant is the main river that drains the Vallon de Nant up to its outlet at 1,200 m. asl. The length of the Avançon de Nant is 6 km in early summer (up to the Glacier des Martinets outlet), but during autumn and winter low flow, the main stream may start to flow as low as 1480 masl, reducing the in-stream flow distance to the outlet to 2.95 km. The extent of the stream network (Figure 5) is based on observations during summer 2017 (dry and wet periods), and its exact path is calculated using MatLab based on the Swiss digital elevation model with a resolution of 2 m (swissAlti3D, 2012b) and the topo toolbox (Schwanghart and Scherler, 2014).

The river velocity in the main stream has been evaluated once using dye tracing (Figure 6). A fluorometer Albillia GGUN-FL30 (Albillia Sàrl, Neuchâtel, Switzerland) was set at the outlet while 5 g of rhodamine B and 5 g of fluorescein were injected in the main stream 2.75 and 1.85 km upstream. Using the peak concentration as reference, the mean velocity of the stream between the two injection points was 0.28 m.s^{-1} , accelerating to 0.59 m.s^{-1} over the last 1.85 km (0.29 m.s^{-1} and 0.48 m.s^{-1} based on rising times).

Three along stream discharge estimates along the stream have been realized by the Stream Biofilm and Ecosystem Research Laboratory group (EPFL) and the Catchment hydrology group (UNIL) from early August to early September in 2016 and 2017, by using salt streamflow measurement (see Figure 7). Here are few remarks about these measures:

- Beyond 4.15 km upstream the outlet, the path taken for measurements diverges (streams *a* and *b* on the map Figure 5).

- On 9 August 2017, the streamflow measured by the gauging station (2.9 to 4.4 mm d⁻¹) is two times lower than the salt streamflow measurement near the outlet (7.5 mm d⁻¹). This difference may be due to a measure bias induced by low flows at the gauging station (see Section 3.3).
- For the series of measurements carried out in September (EPFL), the specific discharge value calculated for the furthest point is abnormally high. It might be due to an underestimation of the upstream area based on the DEM, while in reality this area (not necessarily fitting the surface topography) is larger.

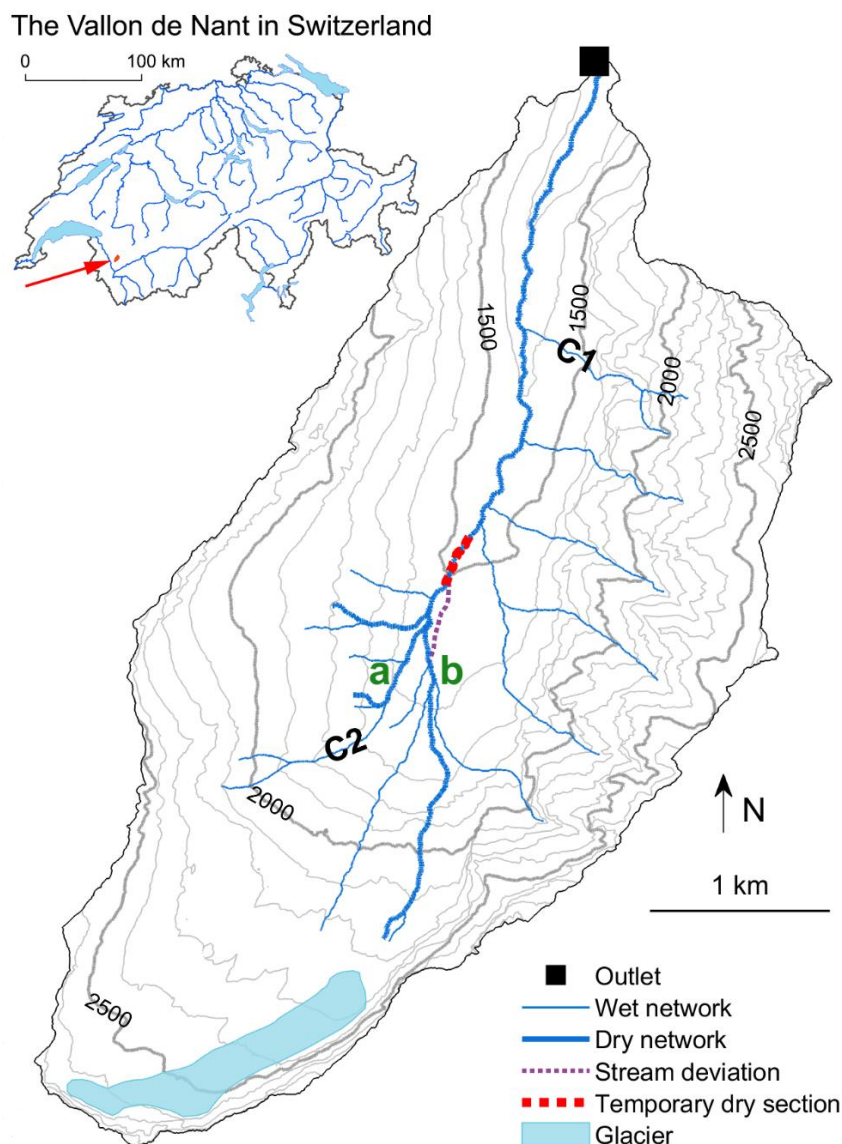


Figure 5. Map of the stream network extent in the Vallon de Nant. C1 and C2 are the two main avalanche couloirs that follow the stream path. The letters a and b identify the different streams options for the along stream gaugings reported in Figure 7. The dashed purple line shows the main stream path after 1 August 2017 storm (until 20 August 2017), based on a satellite images on 2 August 2017 from Planet satellites (Planet, 2017). The Glacier des Martinets extent is based on the Swiss Glacier Inventory 2010 (Fischer et al., 2014).

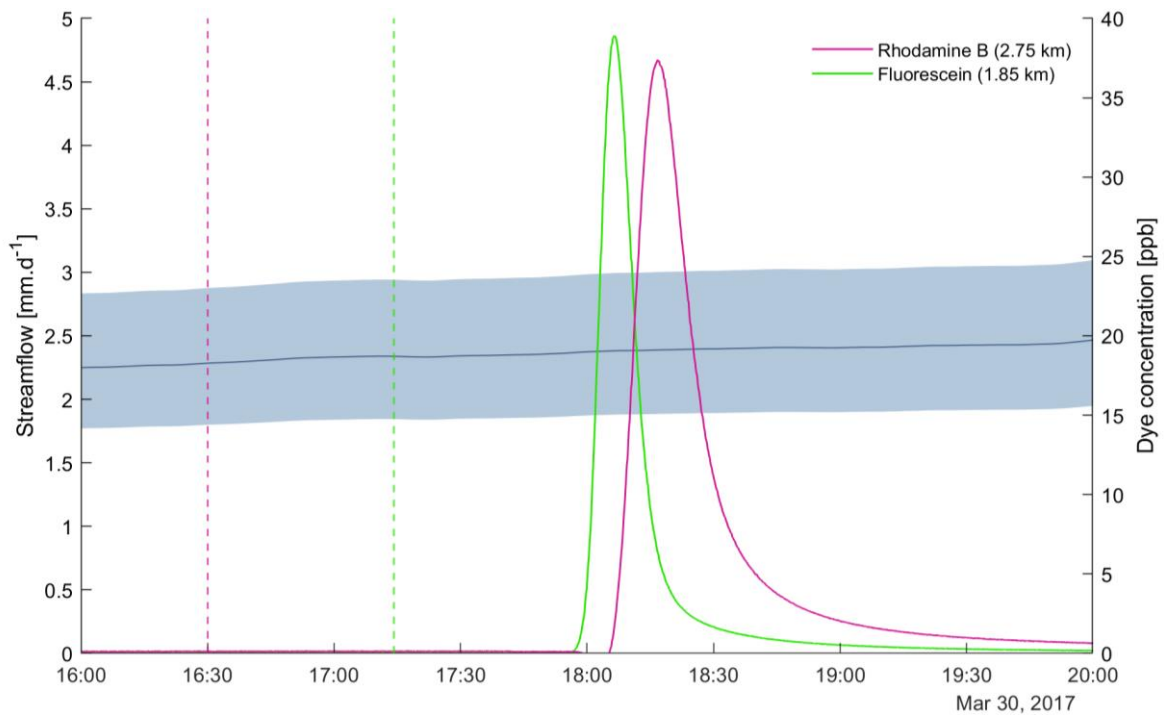


Figure 6. Result of the two dye tracer injections on 30 March 2017 (UTC). The plain lines correspond to the measures of rhodamine B and fluorescein concentrations at the outlet, and the dashed lines to their respective injection time at 2.75 and 1.85 km upstream. In blue is the streamflow measured at the outlet (mean value of 2.3 mm.d^{-1}) with its 95% confidence interval.

Over the first 3.5 km, the slight streamflow decrease measured in September and November indicates that the main stream is mainly fed by the southern part of the catchment, while in August the more strongly decreasing streamflow shows, in addition to water supplied by the southern part, a contribution from the northern slopes of the catchment.

The three series of measurements have a drop in specific discharge around 4 km upstream of the outlet, probably due to river bed infiltration, as observed later in September 2018 (see Section 3.4). Similarly, the streamflow measurements along stream b also show a loss of streamflow (see blue line in Figure 3 top plot), indicating that the water coming from the glacier infiltrates from the stream to the floodplain area.

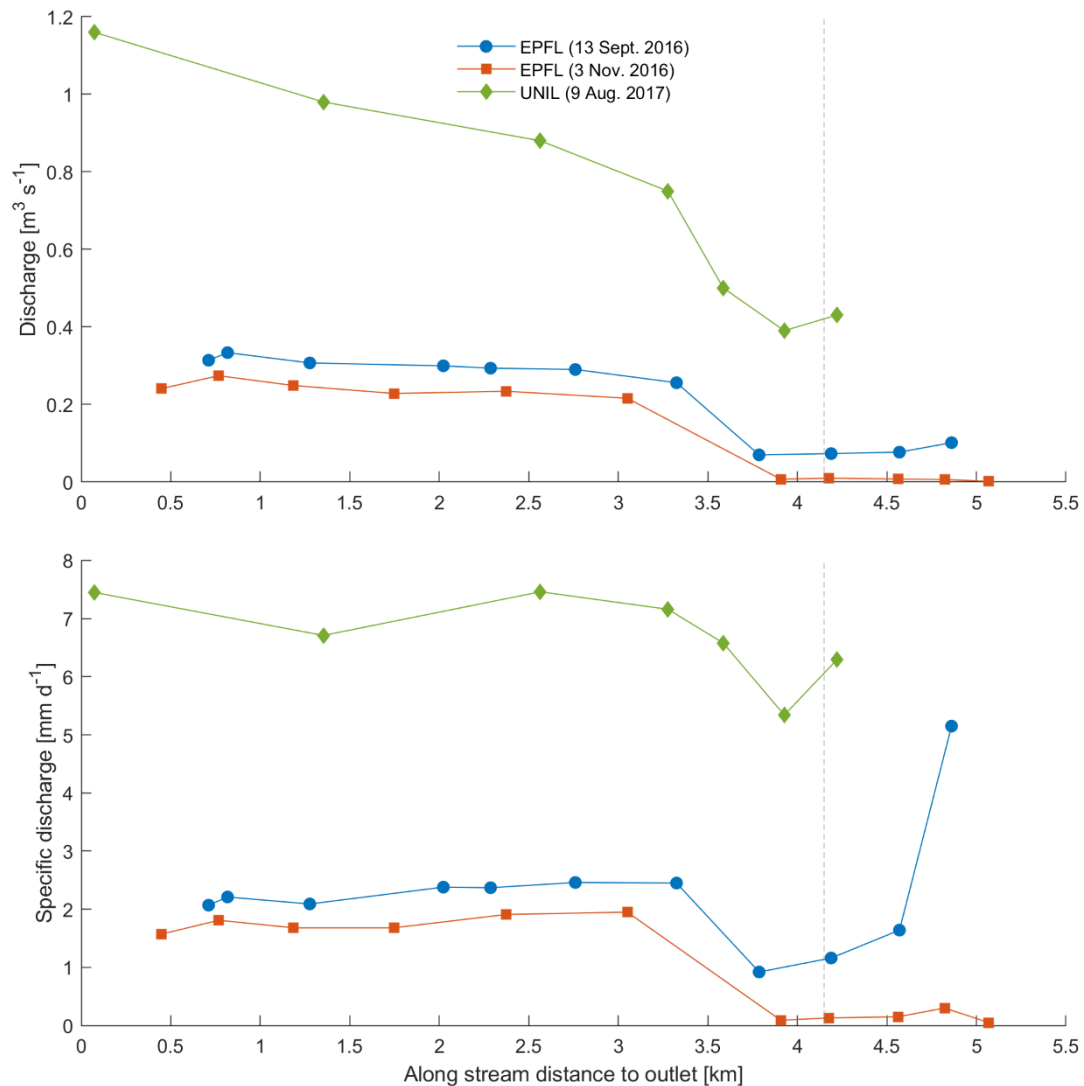


Figure 7. Discharge (top) and specific discharge (bottom) along the main stream measured by the Stream Biofilm and Ecosystem Research Laboratory group (EPFL) and the Catchment hydrology group (UNIL). The mean specific discharge measured at the outlet during the measures was 2.2 mm d^{-1} (1.7 to 2.8 mm d^{-1}) on 13 Sept. 2016, 2.0 mm d^{-1} (1.5 to 2.5 mm d^{-1}) on 3 Nov. 2016, and 3.6 mm d^{-1} (2.9 to 4.4 mm d^{-1}) on 9 Aug. 2017. The vertical line at 4.15 km shows the stream network node beyond which the followed path diverges between the main stream (3 Nov. 2016) and an affluent (13 Sept. 2016 and 9 Aug. 2017), noted a and b on the map of the Figure 5.

3.2 Observed streamflow at the outlet

Since September 2016 the gauging station funded jointly by UNIL (IDYST) and the WSL (Forschungsanstalt für Wald, Schnee und Landschaft) measures and sends data of river stage, temperature, conductivity, turbidity, and sediment transport (Figure 8).



Figure 8. Trapezoidal shaped weir at the outlet of the Vallon de Nant. The metallic arm holds the optical height gauge device above the middle point of the weir. Temperature, conductivity, and turbidity probes are located downstream within the 2 metal tubes visible on the left. Sediment transport is measured using geophones located under each metal plate across the weir section.

The water stage is averaged over a minute using an optical height gauge (VEGAPULS WL-61, VEGA, Schiltach, Germany) located above the middle point of a trapezoidal shaped weir. Every minute the temperature and conductivity are measured by a WTW LF 296 probe and a TetraCon 325 probe (Xylem Analytics Germany Sales GmbH & Co, Weilheim, Germany), and the turbidity is measured by a Campbell Scientific OBS300 probe (Campbell Scientific Ltd, Montrouge, France). The conductivity and turbidity data are however unusable as the tubes sheltering the sensors are too frequently clogged by sediments. Sediment transport is measured via a set of geophones, described in detail in the work of Mayoraz (2018), which also describes the gauging station in more detail.

A rating curve (Figure 9) has been established from 55 salt dilution measurements (Ceperley et al., 2018). The standard method was hereby the following: 1 to 5 kg of salt was dissolved in a bucket with stream water, injected from a bridge 120 meters upstream and salinity is measured at the weir using two salinometers (MADD Easyflow, Madd Technologies Sàrl, Yverdon-les-Bains, Switzerland). A power-relationship was fitted using the nonlinear least squares fitting algorithm of MatLab's "fit" function (MathWorks MatLab 2017a) with the trust region algorithm and least absolute residual method to obtain a 95% confidence interval. The theoretical rating curve for a trapezoidal shaped weir was calculated using the Poleni formula (see Appendix 3 - 1).

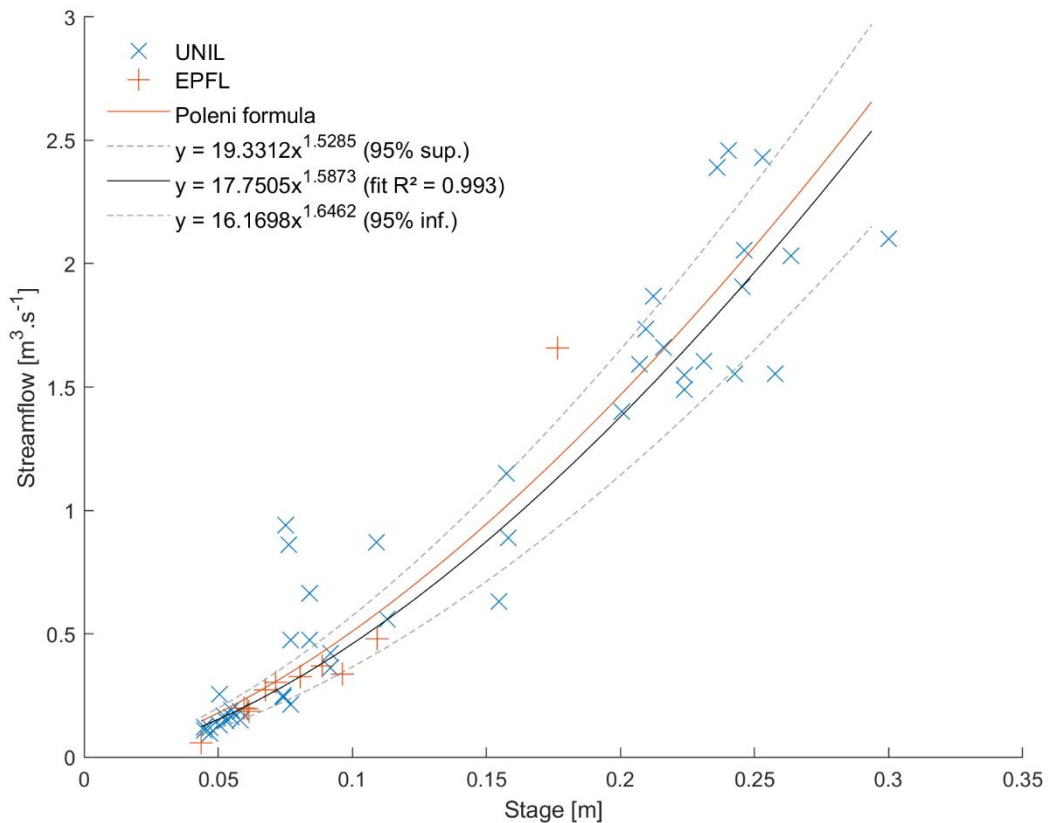


Figure 9. Rating curve for the Avançon de Nant river at the outlet of the Vallon de Nant, based on 55 salt streamflow measurements. The theoretical rating curve based on the Poleni formula is shown in red.

Figure 10 shows five years of streamflow data estimated based on the rating curve. The hydrograph shows a typical snow dominated streamflow regime, with low flow during winter and a high flow period during spring and early summer when the snowpack melts. Significant interannual variations can nevertheless be observed, like the drier year in 2017 (see Table 2) or the occurrence of mid-winter melt in 2018, 2019 and 2020. The peaks (flood events) in summer is due to intense rainfall events, usually associated with summer storms during the afternoon or the evening.

The mean annual water temperature measured at the outlet is 5.0 °C, ranging from a partially frozen river during some days in winter to a mean temperature of 8.5 °C during summer (from 1 July to 31 August 2017).

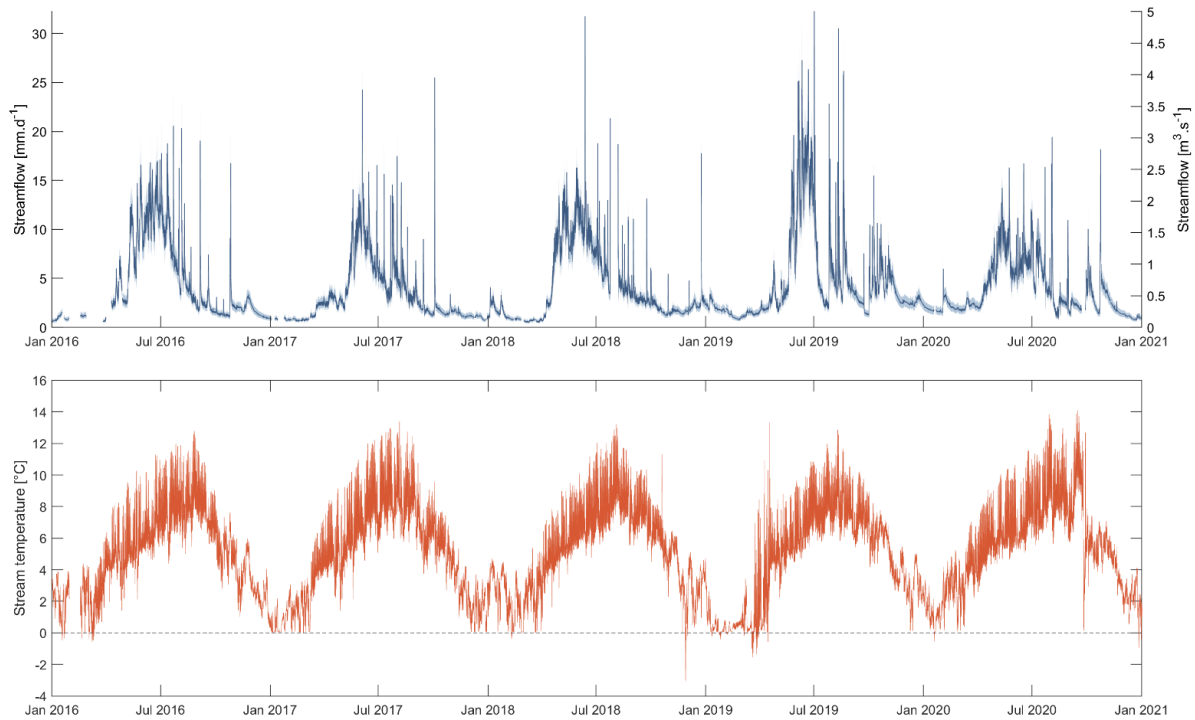


Figure 10. Five years of streamflow and stream temperature measured at the outlet of the Vallon de Nant catchment HyS1 (1 January 2016 to 1 January 2021). For a streamflow measured at HyS1, the conversion between $m^3 s^{-1}$ and $mm d^{-1}$ can be done by dividing values by a coefficient of 6.448.

Table 2. General statistics of streamflow from 2016 to 2020. For each parameter are displayed in parenthesis the inferior and superior values given by the 95% confidence interval on the rating curve. Original data have a 1-minute resolution, so the instant maximum concerns a maximum specific discharge over 1 minute.

Year	Data gaps [%]	Annual total [mm]	Annual mean [mm.d ⁻¹]	Daily min. [mm.d ⁻¹]	Daily max. [mm.d ⁻¹]	Instant max. [mm.d ⁻¹]
2016	11.5	1351 (1105 - 1641)	3.7 (3.0 - 4.5)	0.4 (0.3 - 0.6)	14.4 (12.2 - 16.9)	24.6 (21.2 - 28.4)
2017	6.8	1087 (877 - 1337)	3.0 (2.4 - 3.7)	0.7 (0.5 - 0.9)	15.7 (13.3 - 18.4)	31.5 (27.4 - 36.0)
2018	6.1	1372 (1118 - 1672)	3.8 (3.1 - 4.6)	0.5 (0.4 - 0.7)	14.4 (12.2 - 17.0)	40.8 (35.8 - 46.1)
2019	1.2	1590 (1299 - 1932)	4.4 (3.6 - 5.3)	0.8 (0.6 - 1.1)	19.0 (16.2 - 22.1)	61.3 (54.6 - 68.4)
2020	2.5	1271 (1026 - 1563)	3.5 (2.8 - 4.3)	0.8 (0.6 - 1.0)	11.5 (9.6 - 13.6)	27.6 (23.8 - 31.7)

A quality check of the hydrological data is realized by removing i) erroneous records that are flagged as such by the device recordings and ii) known streamflow disturbance periods due either to gauging station maintenance, frozen stream, or large sediment perturbations. The identification of these disturbance periods is based on water temperature (frozen river) and on pictures taken hourly at the gauging station (see Section 3.3).

3.3 Streamflow uncertainties related to river bed dynamic

Observation via time lapse imagery

A set of cheap sport cameras Xiaomi Yi 1080p (Xiaomi Inc., Beijing, China) were turned into automatic time lapse cameras using an electronic circuit based on an Arduino Nano board (Arduino, 2021) to take a picture every hour during daylight time (see Figure 11).

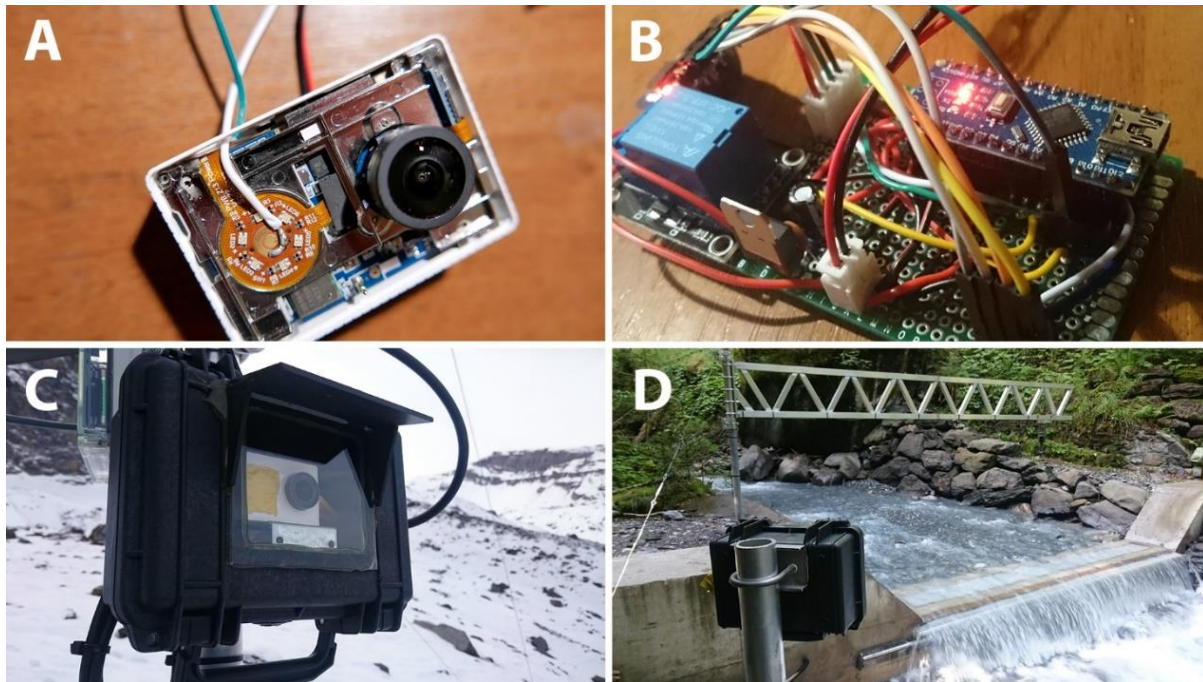


Figure 11. Adaptation of a cheap sport camera to an automatic time lapse camera for field observations. The camera control buttons are turned into electronic controls by soldering a wire (A); A clock wakes up an Arduino nano board every hour and i) opens a relay that power the camera and ii) commands the switch on/off and triggering of the camera using logic levels (B); the cameras are enclosed in a waterproof box and attached to a mast, shown here for the Glacier weather station (C) and at the gauging station at the outlet (D).

One camera system was set up at the Vallon de Nant outlet to look at the stream, and three others at the Auberge, Chalet and Glacier weather stations (see map Figure 20 in Chapter 4) to observe visible meteorological events. The cameras set up at the weather stations quickly faced power supply shortages and unidentified issues, so they did not work properly for more than three months. Their maintenance was abandoned after one year due to lack of time.

From September 7th, 2017 to June 11th, 2019, the camera setup at the outlet has taken 5745 images (Figure 12), used for data quality control. It allows one to identify or confirm exceptional situations like flood events, frozen stream, accidental streamflow perturbations or instruments maintenance (Figure 12 B, G, F and H).



Figure 12. Pictures of the Avançon de Nant at the outlet taken automatically by a camera, showing (A) a normal streamflow, (B) a flood event, (C) the stream channelized in the middle of the weir, (D) the streamflow being split into two parts flowing mainly along the sides of the weir, (E) the stream flowing mainly on the left bank of the weir, (F) an exceptional configuration with a rock being deposited right upstream the middle point of the section after a flood event and affecting dramatically the river stage measurement, (G) the stream almost completely frozen and (H) some maintenance on the weir.

Long term perturbations were also identified, during low flow ($< 5 \text{ mm.d}^{-1}$) when the stream is i) channelized into one small stream bed in the middle of the weir section, ii) split in two parts flowing on each side of the section, but also iii) during normal streamflow periods (10 to 20 mm.d^{-1} , Figure 13) when the stream was flowing mainly on one side of the weir section (Figure 12 C D and E). These 3 long-term perturbations are problematic as the river stage measurement is a point measurement in the middle of the weir, leading to overestimation or underestimation of the stream stage (and thus the streamflow).

The classification of the pictures (visual assessments) shows that, over 1.5 years of photographic surveys, the stream profile was evenly distributed below the stage level sensor during 30.1 % of the time (Table 3, Figure 13). Configurations with a channelized river in the middle of the weir (overestimation of the streamflow) or divided into two channels flowing on both sides of the weir (underestimation of the streamflow) happened 63.2 % of the time, but only during low flow (less than 6.0 mm.d^{-1}). A configuration with the stream channel flowing mainly on one side of the weir has been observed only 0.9 % of the time but with a streamflow between 9.8 and 21.0 mm.d^{-1} , showing that uneven water stage does not concern only low flows.

Table 3. Classification of the 5745 pictures taken between September 7th, 2017 and June 11th, 2019 (642 days, 193 days without data) into seven categories. Periods with more than 24 hours between two consecutive data are consider as periods without data and are not accounted into the total duration.

Stream classification	# of pictures	% of total duration
Normal flow	2034	30.1
Middle flow, 1 channel	1569	26.3
Side flow, 2 channels	1691	36.9
Side flow, 1 channel	62	0.9
Frozen stream	125	2.4
Rock disturbance	204	2.8
Maintenance/experiments	60	0.7

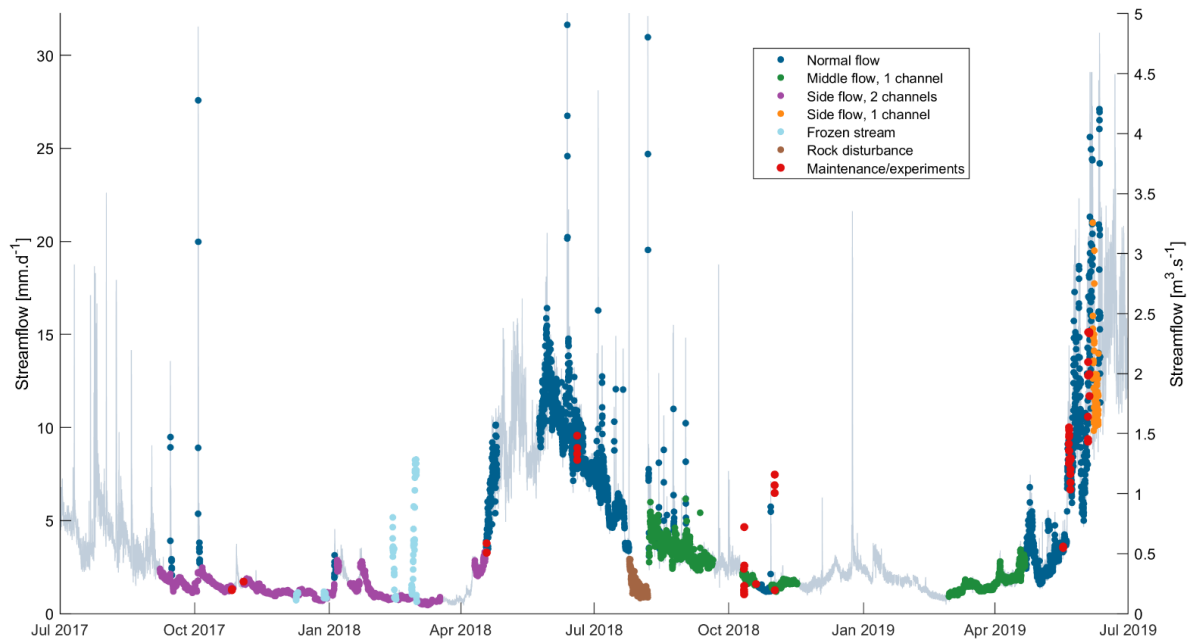


Figure 13. Quality check of the streamflow data using pictures. September 7th, 2017 to June 11th, 2019

It appears that a camera is a precious instrument to critically analyze the data. The simple camera used here can only take pictures during daylight and should be upgraded for nighttime imagery, as it misses all events that could happen during nighttime, such as most of flood events linked to strong summer rainfall events that usually happen during evenings.

Quantification of river stage measurement bias related to river bed dynamics

An experiment has been realized to evaluate the potential bias caused by a point stage measurement in a channelized river. Three river stage profiles were measured in the field, by hand, using a ruler to estimate the difference between a point measurement in the center point of the weir and an estimate of the average river stage across the whole stream profile (Figure 14). In a configuration with the stream being channelized in the middle of the weir, the streamflow could be overestimated by a factor between 1.6 and 1.9. This shows that for such a large weir, the lateral dynamic of the river bed is too important, and a point measurement is not enough to account for these fluctuations; a 2-point or 3-point measurement should be used permanently for a good estimation of the river stage.

Given that the degree of river channelization evolves continuously, the above estimated factors cannot be used directly to estimate an error estimate but give a first estimation of the possible overestimation in this configuration. In the following, streamflow data are mostly shown as uncorrected measurements without error estimations (for practical reason). Known periods of gauging station maintenance and other obvious erroneous measurements are

shown as missing data. Where appropriate, the order of magnitude of the measurement uncertainty is included in the discussion of results.

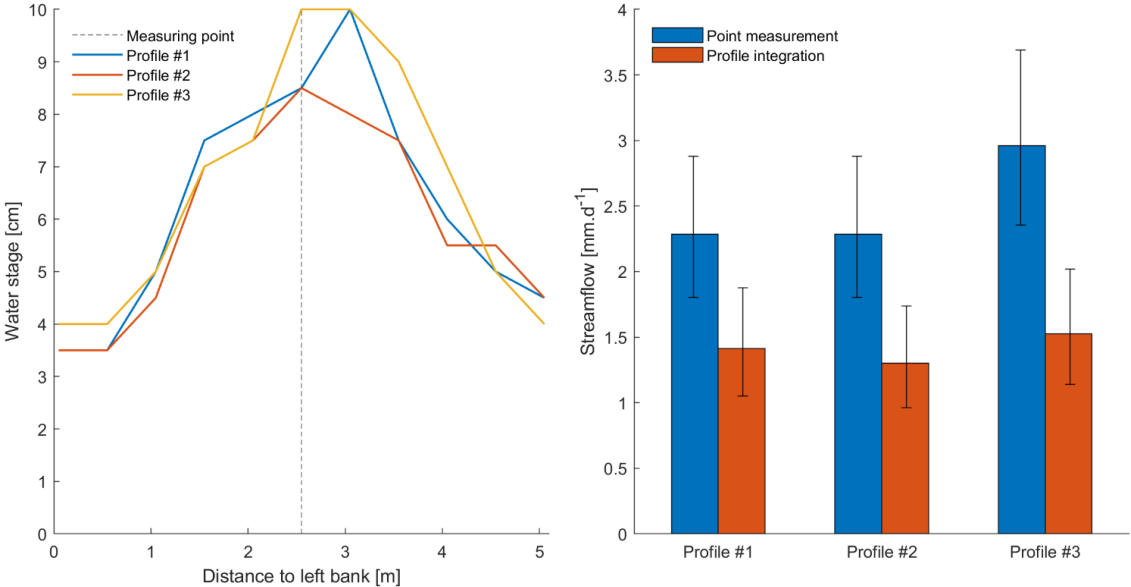


Figure 14. Measure (on the left) of 3 stream profiles and (on the right) comparison of streamflow based on i) a point measurement in the middle point of the weir or ii) considering the mean height of the stream profile. The three measurements are realized (profile #1) on 20/09/2018 at 7:15, (profile #2) on 20/09/2018 at 7:50 and (profile #3) on 10/10/2018 at 14:55 (UTC). Error bars on the streamflow estimation account for the 95% confidence interval from the rating curve, and for the profile integration an additional error due to the manual measure of the stream profile.

3.4 Other sources of streamflow uncertainty

Streamflow blocking by ice / snow jam

Avalanches occur regularly in the Vallon de Nant, especially during the melt season when wet snow avalanches form along the steep slopes along the main stream. It is possible then to count a dozen of avalanches per day, occurring mainly among the steep rocky slopes to the east, and across the steepest grassy slopes on the northwest part of the catchment. The snow packed at the bottom of these slopes creates patches of snow at low elevation that will melt weeks after the surrounding snowpack. This is particularly true for two corridors (C1 and C2 on map Figure 5) where, each year, wet avalanches pack snow up to 5 meters thick over distances of several hundred meters.

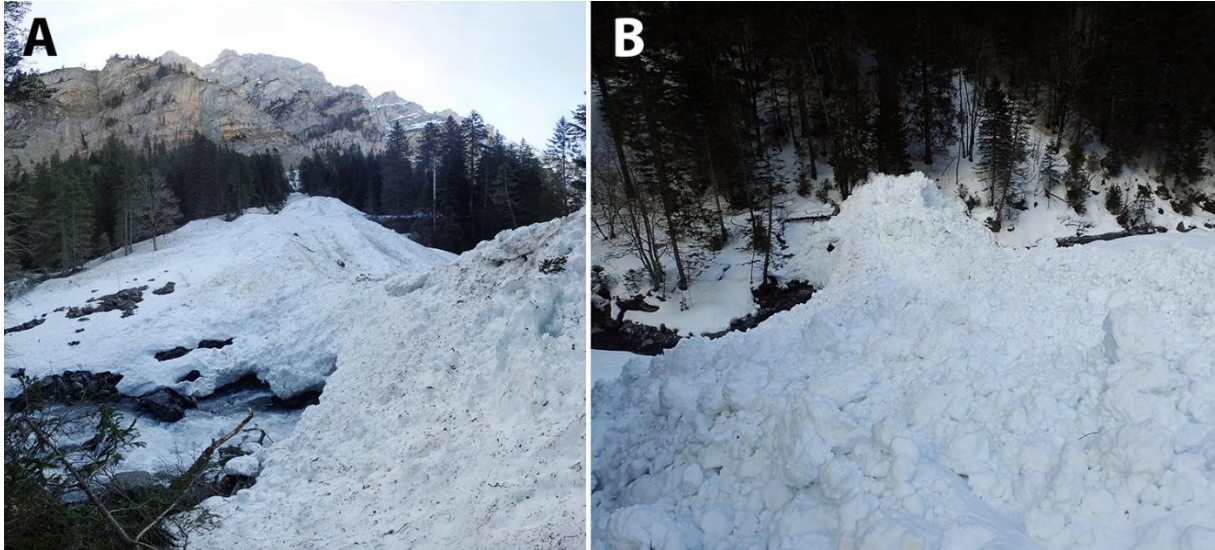


Figure 15. Pictures of a large wet avalanche in the Vallon de Nant on January 31st, 2018 in the avalanche corridor C1 (see map Figure 5), taken (A) from the left bank of the main stream and (B) from the avalanche itself, looking downward in the direction of the main stream.

In 2018, the avalanche in the corridor C1 reached and disturbed the streamflow of the main stream (Figure 15). From field observations, we know that this event occurred between January 11th and January 31st, 2018 probably due to a large snowfall event between January 15 and 17. No further evidence can be provided by the satellite imagery. This avalanche, located around 1.4 km upstream, most likely created a streamflow anomaly on January 22 at 1h25 UTC (Figure 16). Indeed, the streamflow drops for 30 minutes, shows a peak and is then back to normal. Taking the mean streamflow estimation for the 30 minutes before the discharge drop (0.20 and 0.33 m³/s), we estimate that 30 minutes of water accumulation represent 360 to 600 m³ of water. The snow accumulation over the river blocked the water until the pressure was too high and releasing suddenly the reservoir.

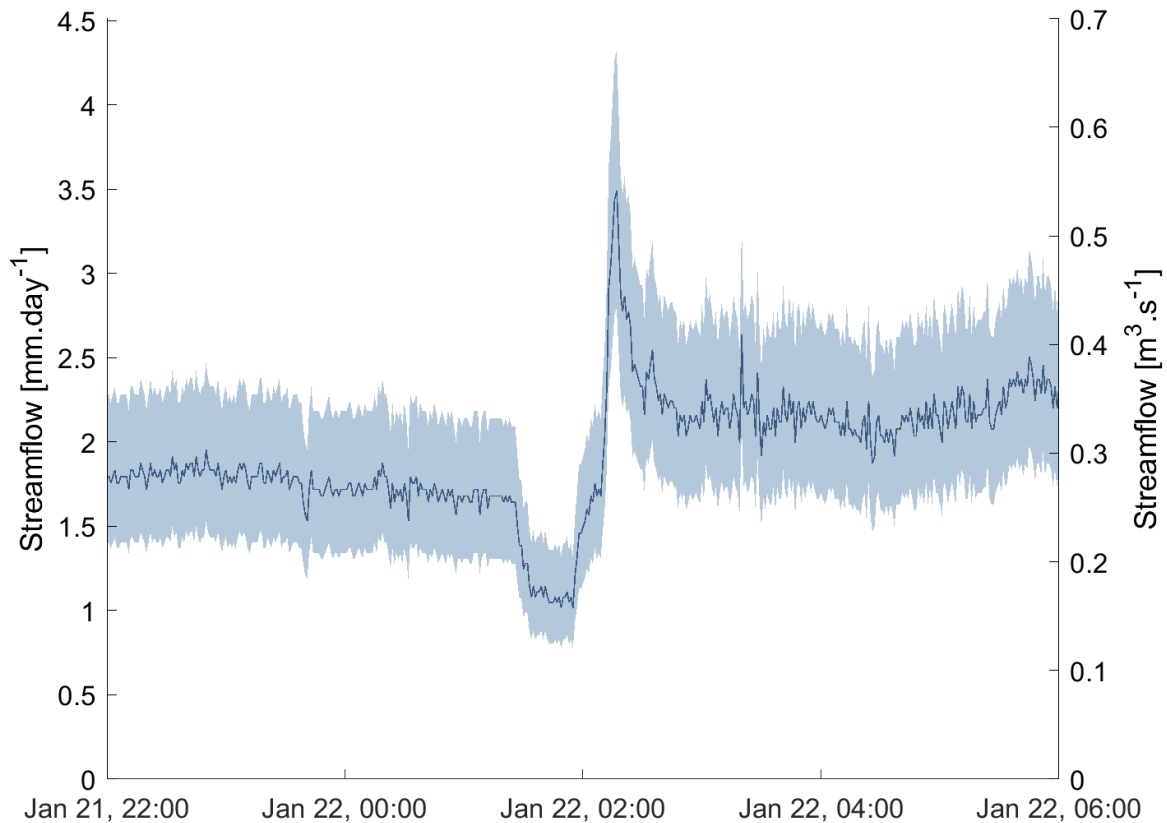


Figure 16. Streamflow disturbance on January 22nd, 2018 attributed to a river jam caused by an avalanche. The dark blue curve and light blue envelop correspond to the streamflow and its 95% confidence interval, estimated from the rating curve of Figure 9.

Modifications of stream channel path after a storm

A storm in the evening of the 1st of August 2017 changed the path of the main stream over more than 500 meters and led to a deviation of the stream bed 100 meters eastward (see Figure 17, Figure 5). After this event, fast erosion created a new stream channel. However, the river bed was reworked shortly thereafter by the Commune of Bex to put the main stream back in the previous channel and flow under the pedestrian bridge built three weeks before. To date, such stream network changes (and ensuing human intervention) are difficult to trace in this catchment. While these kinds of events do not directly influence the observed streamflow at the outlet, they might impact in an unquantifiable way our distributed stream water sampling, water temperature observations as well as piezometric recordings (see Section 3.3).



Figure 17. Pictures showing stream bed modifications after the storm of 1 August 2017, with A) a major deviation of the main stream (see details on map Figure 5) that deviate water from the dry bed visible on the left (with bridge) toward a new channel on the right, and minor deviations of the stream bed forced by a large accumulation of sediments carried by a temporary stream and deviates the main stream over grassy soils.

Subsurface flow

A second dye tracing experiment was completed during an exceptionally dry period, on 20 September 2018 (streamflow at the outlet of $2.8 \text{ mm}\cdot\text{d}^{-1}$ or $0.44 \text{ m}^3 \text{ s}^{-1}$). The amount of recorded rainfall during the preceding week was 2.4 mm, and during the preceding three weeks 19.3 mm. On 20 September 2018, the Avançon de Nant main stream was dry over 430 m at 4,030 m from the outlet (see map Figure 5). The discharge at the disappearing point was visually estimated to a few liters per minute. A fluorometer was set up 250 m downstream of the resurgence and 14 g of rhodamine was injected at the infiltration point. 24 hours later, no signal was measured.

This experiment suggests that either the travel time of infiltrated water through the subsurface ground is very slow or ii) the subsurface travel path during this low flow period led to water export beyond the point of measurement. Even if this experiment does not allow a definite conclusion, streamflow exfiltration to a deeper groundwater system might well be present along the main stream.

Groundwater export

Groundwater export below the gauging station is a common challenge for hydrological studies that rely on streamflow observations at a selected outlet. To date, it is unclear if a part of the streamflow generated within the catchment leaves the catchment as groundwater flow that is not measured at the gauging station. In the work of Thornton et al. (2021a), the decision was made to close the catchment at an outlet downstream for modelling purposes to minimize potential groundwater losses.

Our along stream gauging reveal infiltration in the floodplain area (see Section 3.1), up to potentially a complete disappearance of the stream (discussed above), but there is no evidence that the water infiltrated at this point leaves the catchment, and it is more likely that it will emerge at a short distance downstream.

3.5 Summary

The stream network in the Vallon de Nant is dynamic in extent, with a permanent stream network flowing all along the year, and tributaries appearing during the snowmelt period and intense rainfall events. Part of the water flowing from the glacier infiltrates in the floodplain area, which in exceptional situations can lead to a dry stream bed over a few hundred meters.

The exposition of the stream network to extreme events such as avalanches or intense rainfall events can lead to important modifications of its morphology, and a regular monitoring of the stream network is needed for a good understanding of hydrological processes.

We demonstrated the value of a time lapse camera to give a qualitative evaluation of the streamflow measurement at the outlet, demonstrating the need for a river stage measurement accounting for the river bed dynamic, either to have a more accurate measure of the streamflow, or at least to quantify its uncertainty.

A deeper understanding of subsurface flow processes is given through springs and piezometer water temperature monitoring, water conductivity measures and stable isotopes measurements that will be presented and discussed in Chapter 6.

Appendix 3 – 1: Theoretical streamflow calculation for the gauging station using the Poleni formula applied to a trapezoidal cross-section

The river discharge Q [$m^3 \cdot s^{-1}$] for a rectangular section (Poleni, 1717) can be written as:

$$Q = \frac{2}{3} \mu \bar{b} \sqrt{2g} H^{\frac{3}{2}}, \quad (1)$$

where μ is a factor that accounts for the overfall shape [-], where μ can be taken as 0,55 as a typical value recommended for check dams; \bar{b} the mean equivalent section width [m], g the acceleration due to the gravity ($g = 9.81 m \cdot s^{-2}$) and H the total head [m].

Due to the particular geometry of the weir, with border slopes of 45° , the mean width equals:

$$\bar{b} = b + y_c, \quad (2)$$

with b the weir width at the base, $b = 5,3 m$ in our case.

Like the water height is measured at the critical point (Figure 18), the dimensionless Froude number Fr expressing the ratio between kinetic and potential energy is equal to 1:

$$Fr = \frac{v_c}{\sqrt{gy_c}} = 1, \quad (3)$$

with v_c the critical velocity [$m \cdot s^{-1}$] and y_c the critical water height [m].

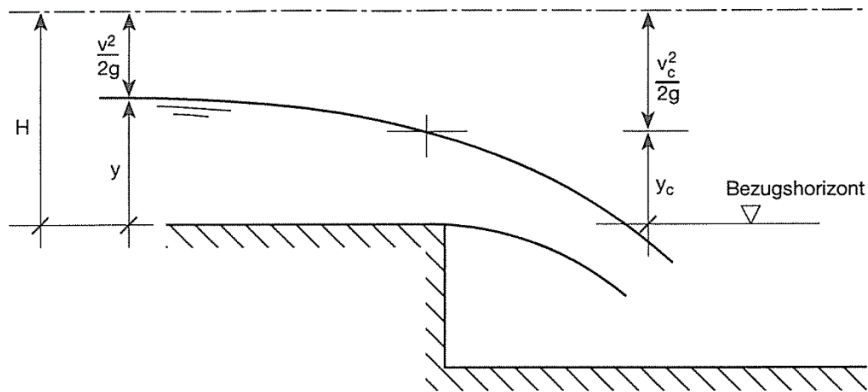


Figure 18. Conservation of the total head H over a weir (Böll, 1997).

So, we deduce from (3) the critical velocity:

$$v_c = \sqrt{gy_c} \quad (4)$$

The Bernoulli theorem of conservation of energy (total head) along a streamline of flowing fluid gives:

$$H = y_c + \frac{v_c^2}{2g} \quad (5)$$

Using (4) and (5):

$$H = y_c + \frac{gy_c}{2g} \quad (6)$$

$$\leftrightarrow H = \frac{3}{2}y_c \quad (7)$$

The total head expression (3) and the equivalent section width equation (2) can be express by the formula (1) as:

$$Q = \frac{2}{3}\mu(b + y_c)\sqrt{2g} \left(\frac{3}{2}y_c\right)^{\frac{3}{2}} \quad (8)$$

$$\leftrightarrow Q = \frac{2}{3} \left(\frac{3}{2}\right)^{\frac{3}{2}} \mu\sqrt{2g}(b + y_c)(y_c)^{\frac{3}{2}} \quad (9)$$

$$\leftrightarrow Q = \mu\sqrt{3gy_c}(b + y_c)y_c \quad (10)$$

4 | Meteorological data



Photograph: morning view from the Glacier weather station toward the bottom (north) part of the Vallon de Nant, covered by clouds.

Before 2016, the weather station network in the Vallon de Nant was insufficient and suffered from many issues (details in Appendix 2). In this chapter, we present the design and deployment of new weather stations, addressing the many technical and environmental constraints (Sections 4.1.1 to 4.1.5) to implement the new weather station network (Section 4.1.6); some relevant meteorological data are presented in Section 4.1.7. We briefly introduce, in Section 4.1.8, the temporary high-density rainfall network composed of Pluvimate raingauges, which are presented in more detail in Chapter 5. Section 4.1.9 shows a comparison between all the precipitation measuring devices used in the catchment. Finally, the last two sections are dedicated to snowcover characterization, using lysimeters (4.2.1) and satellite images (4.2.2), two data sets which were acquired during this PhD research but could not be fully exploited within the time frame of this work

4.1 Weather stations in Vallon de Nant

4.1.1 On the challenges of a weather station network in the Vallon de Nant

The recent interest of many research groups for the Vallon de Nant (see Chapter 2) has justified the need for a reliable weather stations network. In 2016, the weather station network in the Vallon de Nant did not fulfill the new requirements and suffered many issues (see details in Appendix 4 - 1). The author of this thesis dedicated large efforts to improve the existing weather stations network according to the different need. It was particularly required that i) precipitations would be recorded continuously throughout the year (including snowfall in winter), and included additional measurements such as snowpack height, soil surface temperature, soil temperature and soil moisture, ii) the network should represent the different areas and altitudes of the catchment, and iii) a remote access to the devices and to the operating status of the weather stations was necessary to ensure the maintenance of the stations and sharing data between the different users.

We do not use any further data from the Swiss meteorological network since there are no ground measurement stations nearby, and the Vallon de Nant catchment is largely in the shadow of the Swiss weather radar network (Foehn et al., 2018b), which might see here at best rainfall above 2800 masl (Marco Gabella personal communication, February 27th 2019).

4.1.2 Location and communication of the weather stations

Data transmission is a key challenge since the mobile network coverage is weak or inexistant in the most accessible parts of the Vallon de Nant. The choice was made to base the new weather stations network on the DS3 radio dataloggers (Figure 19) proposed by Sensorscope

(Sensorscope, Lausanne, Switzerland). Most of the existing sensors existing on the market can be plugged to these dataloggers (some of them requiring development from the company) and each datalogger can monitor 3 individual sensors. The dataloggers communicate with each other by radio (868/915 MHz), creating a multi-hop network to route the data up to a master station that has the capability to send the collected data to a server via the mobile 4G LTE (long term evolution) network. The radio communication between the stations is supposed to be limited to a 1 km range, but tests in the field showed that with straight lines without obstacles between the dataloggers, distances up to 2.5 km could be reached.



Figure 19. A Sensorscope datalogger at the Glacier weather station. Each datalogger is energetically self-sufficient, with a solar panel and batteries to supply low consumption sensors up to 5 days without sun. Each box can receive 3 modules, each connected to a sensor. An additional card can transform a datalogger into a master station and transmit the data to a server using the mobile 4G LTE network.

The new weather station network includes four locations (Figure 20, Figure 24, Table 5): 3 of them already existing (Auberge, Chalet and La Chaux), and a new one (Glacier) set up next to the terminal tongue of the Martinet Glacier at 2136 masl (Figure 20). The new weather station in the upper (south) part of the Vallon de Nant was expected to fulfill two main objectives: i) from a scientific point of view, the Glacier weather station ensures a better distribution of the measuring points and complete the north/south transect with the Auberge and Chalet weather stations, and ii) the Glacier weather station is also a key point for data transmission to a server as the 4G LTE network at this place is extremely good, and an unobstructed point of view allows a radio communication with La Chaux and the Chalet weather stations (2.2 km

and 2.5 km away, respectively). The curvature of the valley requires an extra datalogger to work as a hop (the relay station, see Figure 20) and link the isolated weather station of the Auberge to the rest of the dataloggers network.

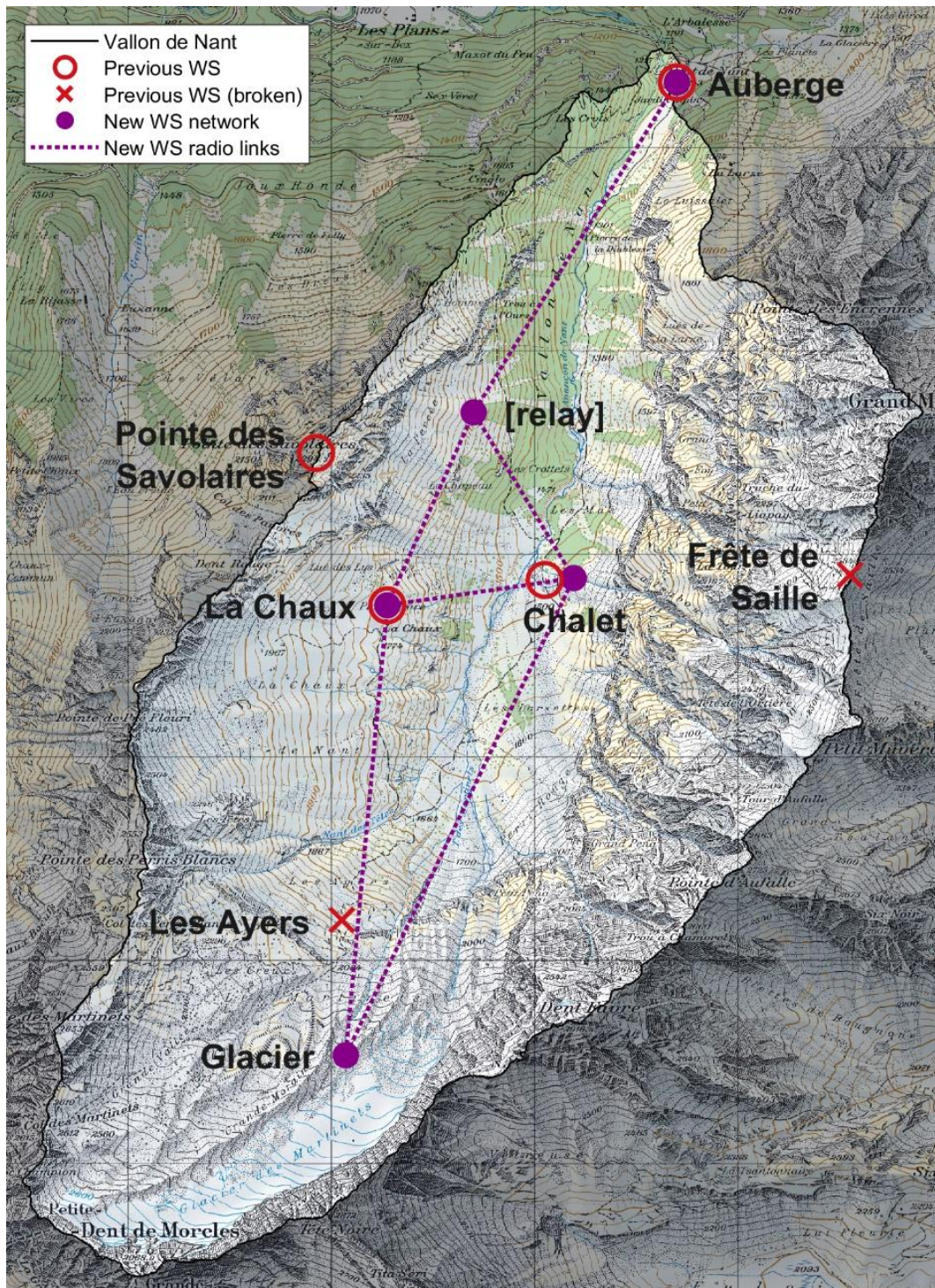


Figure 20. Map showing the location of the previous six stations and the four new stations (Table 5) weather stations (WS) in the Vallon de Nant. The relay of the new weather stations network is used only as a repeater to transmit the data from the Auberge to the other stations despite the curvature of the valley. The Glacier is the master station that transmits the data to a server through the wireless 4G LTE network.

4.1.3 Accessibility and environmental constraints

The Glacier weather station is crucial to remotely access the data from the whole network. In summer, the Glacier weather station is reached after a 6.3 km walk with 880 m of elevation gain from the Auberge weather station, without any particular risk. In winter the station is accessible by ski after 7.8 km and 1040 m of elevation gain from the village of Les Plans-sur-Bex but with serious risks of avalanches. The access intermittency to this station for its maintenance was considered in its design in terms of energy needs and as a possible source of data gap in time series (Section 4.1.5). The Chalet, La Chaux and relay stations are also sensitive to the risk of avalanche, and to a lesser extent the Auberge weather station.

The protection status of the area (Reserve of the Muveran, see Chapter 2) imposed constraints: i) the new Glacier weather station had to be at least 500 m away from the trail and be hardly visible from afar and ii) the existing Chalet weather station had to be moved to a less visible place.

The Glacier weather station is located nearby the Glacier des Martinets tongue. At this place the slope is around 20° which reduces locally the risk of avalanche for the installation. To compensate for the slow movement of the terrain during the year, cable tension must be adjusted regularly. For the Chalet weather station, the new site is located on a large rock below an alluvial cone and a couloir, not an ideal location but the only place inaccessible to cattle, visually discreet and allowing radio communications with the other dataloggers.

4.1.4 Design of the remote weather stations

Since the instruments measuring precipitation are by far the most energy-intensive devices, the energy needs of the other sensors (Table 5) will be neglected here. The most frequently used device to measure snowfall is a heated tipping bucket raingauge, but it requires a large amount of energy to heat the raingauge when the air temperature drops below 5 °C (18W for a 200 cm² catchment surface raingauge). Furthermore, the heating induces some sublimation that leads to a bias in the measurements. In addition, tipping buckets are extremely error prone for snowfall measurements due to undercatch related to wind, which can potentially be prevented with wind shields (Yang, 2014; Nitu et al., 2018) which are however expensive and have a potentially large visual impact.

For these reasons, the choice was made to use Lufft WS400 sensors (Lufft Mess- und Regeltechnik GmbH, Fellbach, Switzerland) that, in addition to air temperature, air pressure and relative humidity, measure liquid and solid precipitations via a 24 GHz Doppler radar.

When the air temperature is above 5 °C, the device only requires 0.17 W to run. Below 5 °C, the heating uses 20 W of energy to prevent ice formation or snow accumulation, but only when precipitation is detected, which significantly reduces energy requirements compared to a tipping bucket raingauge that is heated continuously.

Lufft WS400 sensors were installed at the Auberge, Chalet and Glacier weather stations. A power supply is available at the Auberge, so the energy requirements were not an issue and the Lufft WS400 is co-located with a heated tipping bucket raingauge (Table 6).

4.1.5 Power supply

At the Chalet and Glacier locations the use of a solar panel is the easiest solution, although it remains challenging: as the valley is deep and open to the north. In winter very few hours of sun are available at these places (Figure 21), and no direct radiation reaches the Glacier for around 67 days in a row (Figure 22).

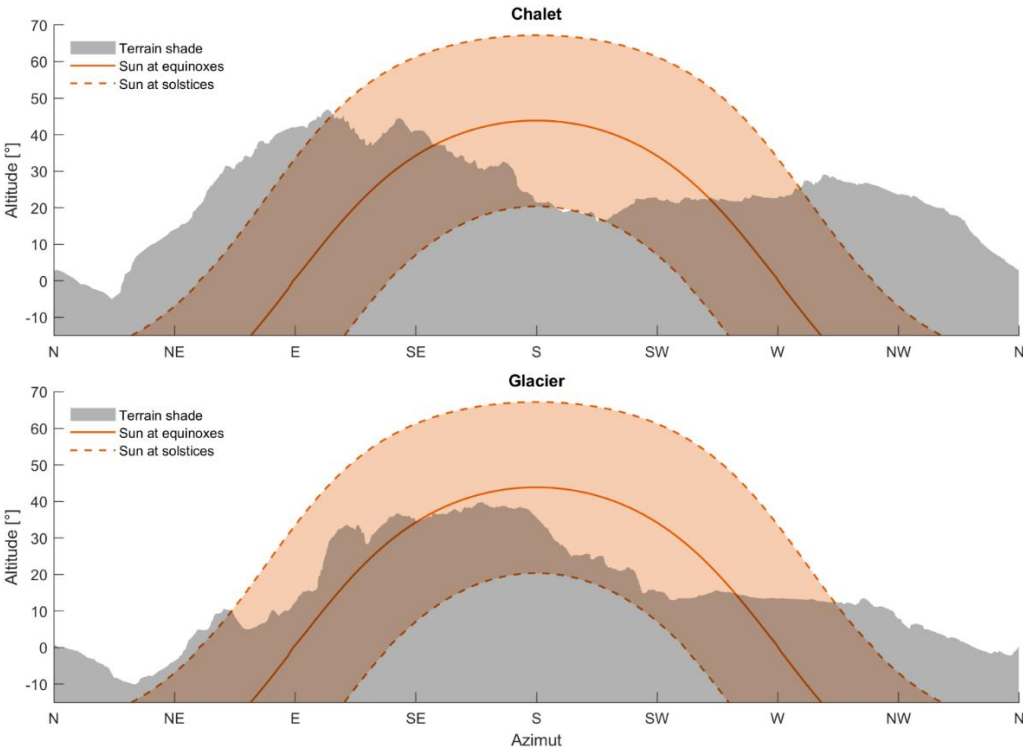


Figure 21. Trajectory of the sun along the year and shadow of the terrain at the Chalet and Glacier sites.

The maximum efficiency of a solar panel is reached with an orientation that follows the sun's course in the sky or with a fixed tilt optimizing the direct and diffuse radiations, but to limit the amount of structure required on the field, prevent the accumulation of airborne particles (dust, snow), and have a maintenance as low as possible, the solar panel was set up fixed and vertically. The choice was made for a 330 W monocrystalline solar panel.

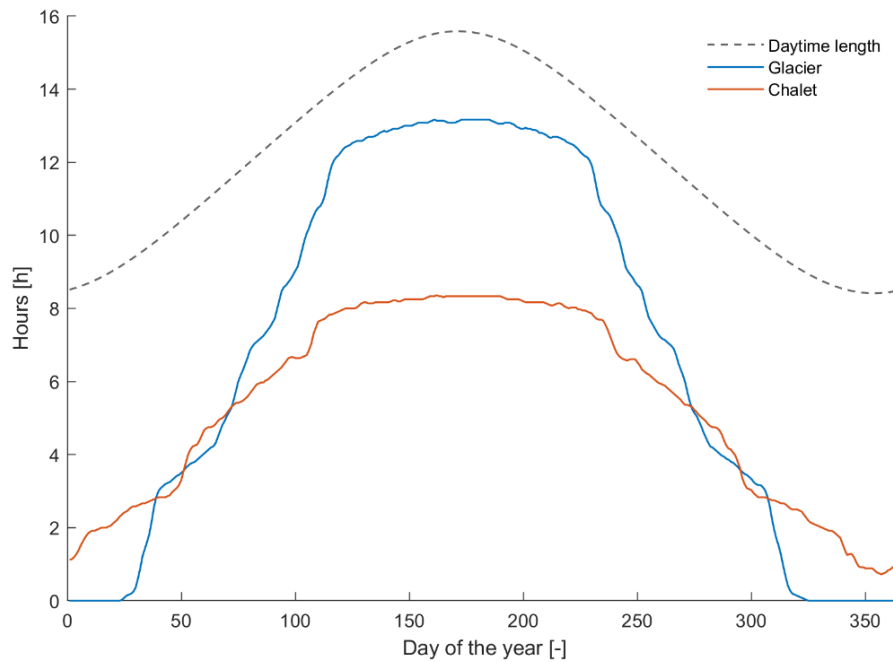


Figure 22. Theoretical duration of diffuse and direct radiation received daily at the Glacier weather station (46.20873° N, 7.08972° E) during the year. The diffuse radiation only accounts for the latitude of the point (46.2°N), while the direct radiation also accounts for the topography based on a 2x2 m DEM (swissAlti3D, 2012b). For 69 days there is no direction radiation, from November 14th to January 22nd.

A battery pack is used to store the energy produced by the solar panel during the day and compensate the sun intermittencies. However, the stored energy could never be enough to provide a continuous 20 W of power during an exceptionally long precipitation event occurring in winter. The strategy adopted is to have a pack of batteries that could be switched on occasionally during winter. The choice was made for 24 V lithium iron phosphate (LiFePO₄) batteries of 20 Ah capacity each. The LiFePO₄ technology offers a good efficiency at low temperatures and have a high energy density (5 kg per battery). On the field, one person can carry 2 of these batteries in a backpack or drag 8 of them in a pulka up to approximately 1650 masl

Simulations have been realized to forecast the frequency of battery switches in winter. These simulations account for i) the electricity production of the solar panels, ii) the sites accessibility (risk of avalanche after a recent snowfall) and iii) the energy requirements that depend on the duration of precipitation events. No detailed information was found at the time on the yield of a photovoltaic solar installation operating solely on diffuse radiation.

The configuration of the Vallon de Nant in winter also have advantages as i) the yield of monocrystalline solar cells (the solar cell technology having the best yield) increases with

lower temperatures, ii) the snow-covered surfaces of the valley act as a reflector for direct and diffuse radiation (up to 80-90% with fresh snow), and iii) the low clarity of the sky frequently encountered during winter increases the diffuse radiation.

In absence of reference values for simple simulations, the following rules were applied to the simulations :

- The maximum power of the solar panel (330 W) improves with lower temperature (- 0.004 %/°C under 20 °C).
- The solar panel produces energy only during periods without precipitations.
- During hours with direct radiation, a coefficient of 0.7 was applied to account for the fixed vertical position of the solar panel.
- A coefficient of 0.3 was applied for the diffuse radiation, with an additional coefficient of 0.5 as the diffuse radiation is used as a constant from sunrise to sunset.
- The Chalet is accessible after 2 days when a snowfall exceeds 40 cm of fresh snow or 40 mm of snow water equivalent (SWE).
- The Glacier is accessible after 4 days when a snowfall exceeds 20 mm of SWE.

For temperature and precipitation data, the 10-year records of six high altitude weather stations in Switzerland (belonging to the Swiss measurement network SwissMetNet, (Heimo et al., 2006)) between 2106 to 3302 masl under different climatic conditions (between 1165 and 2597 mm of precipitation per year) were used (Table 4). An example of simulation result is shown in Figure 23. The statistics kept for the design of the solar panel were the mean and maximum number of battery switches per winter, and the number of periods with lost data and its maximum duration (Table 4).

Table 4. Results of simulation based on 10-year records of temperature and precipitations data from 6 weather stations in Switzerland, and the theoretical direct and diffuse radiation conditions at the Chalet and Glacier sites. The simulations are summarized here through statistics of mean and maximum number of battery switches per year, and the number and maximum duration of data gaps.

Station name	Altitude [m asl.]	Mean annual precip. [mm]	Mean # of switches per year		Maximum # of switches per year		Mean # of data gaps per year		Data gap maximum duration [hours]	
			Chalet	Glacier	Chalet	Glacier	Chalet	Glacier	Chalet	Glacier
Pilatus	2106	1790	0.2	1.4	1	3	0	0.2	-	198
Gütsch ob Andermatt	2283	1354	1.2	2.9	3	5	0.1	0.9	14	166
Col du Grand St-Bernard	2472	2128	0.1	1.1	1	2	0	0.1	-	84
Säntis	2502	2597	0.9	2.6	3	4	0	0.4	-	189
Weissflujoch	2691	1314	1.7	2.9	4	5	0.3	1.1	9	158
Piz Corvatsch	3302	1165	0.2	1.3	1	3	0	0.2	-	25

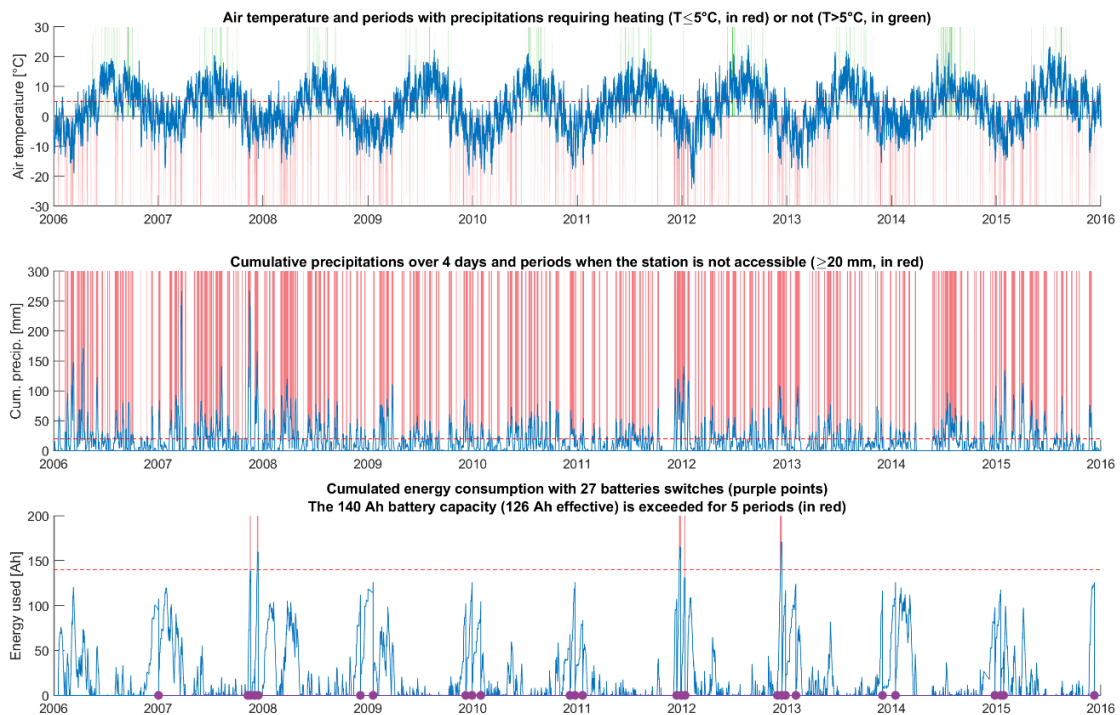


Figure 23. Example of simulation result to evaluate the energy necessary to power a Lufft WS400 as if it was exposed to the weather conditions (temperature and precipitation amount) recorded for 10 years at the Pilatus weather station (2106 masl), with the theoretical direct and diffuse radiation conditions at the Glacier site. The top plot shows the periods in red when heating is required. The middle plot shows the periods in red when the station is not accessible. The bottom plot shows the energy consumption at the station, when the batteries should be switched (purple dots), and periods of data loss in red when the batteries are empty and the station not accessible.

This simulation shows that the mean annual precipitation amount is not necessarily correlated with a bigger number of battery switches (2.6 switches a year with 2597 mm at Säntis; 2.9 switches a year with 1314 mm at Weissflujoch, Table 4). The reason is probably due to more intense events (at Säntis), for the same duration. The elevation (and temperatures) of the six stations is probably not making a big difference as a temperature below 5°C is easily reached throughout winter (Figure 23).

The conditions at the Pilatus weather station, with an elevation and mean annual precipitations close to the Vallon de Nant may not necessarily be representative, and the length of events is more critical.

However, based on these simulations, large efforts might be necessary (up to five switches a year) to keep the Glacier weather station working throughout winter. The probability to have data gaps remains low (from 0.1 to 1.1), but with a duration of up to 198 hours (8 days), corresponding to exceptional conditions. It was decided to go with this option anyway, despite of possible data gaps.

4.1.6 Weather station network details

Four stations based on the Sensorscope dataloggers were set up at the Auberge, Chalet, La Chaux and Glacier sites (details in Table 5, pictures of the station in Figure 24). The stations measure every 2 minutes air temperature, air pressure, relative humidity, incoming solar radiation, wind speed and direction, surface temperature, soil temperature and water content, snow height, and precipitation (details in Table 6); exception from this list of measurements are: the Auberge does not measure direct solar radiation (technical issue), La Chaux station does not record precipitation, and the Glacier station does not record soil temperature and water content (moraine soil). For the three weather stations recording precipitation (Auberge, Chalet and Glacier), the spatial density is one station for 4.5 km², and the greatest distance between a point of the catchment and a weather station is 2.1 km.

Table 5. Location and altitude of the four weather stations of the Vallon de Nant.

Station name	WGS84 coordinates		CH1903 coordinates [m]		Altitude [masl]
	Latitude	Longitude	Easting (X)	Northing (Y)	
Auberge	46.25108° N	7.11037° E	574684	122236	1253
Chalet	46.22990° N	7.10412° E	574192	119884	1530
La Chaux	46.22795° N	7.09190° E	573248	119671	1780
Glacier	46.20873° N	7.08972° E	573071	117535	2136

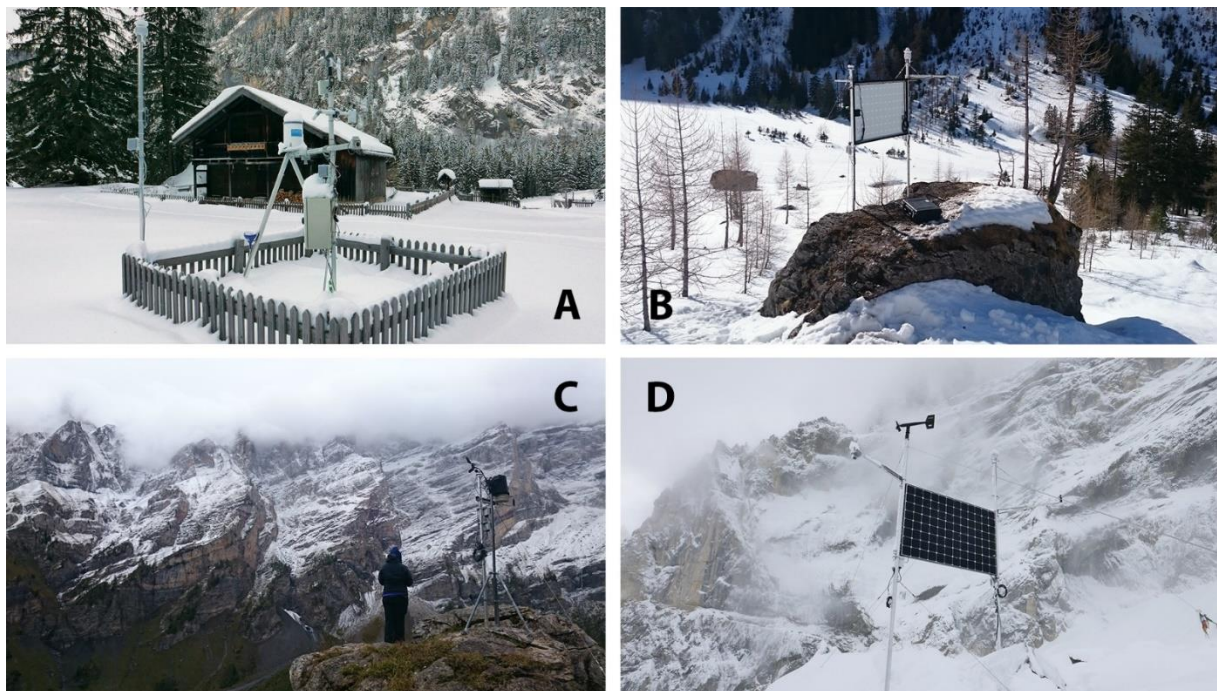


Figure 24. Pictures of the weather stations at (A) the Auberge, (B) the Chalet, (C) La Chaux and (D) the Glacier. The Madd raingauge at the Auberge is located 2.5 meters above the ground, and the Lufft WS400 sensors at the Auberge, Chalet and Glacier are at least 3.5 meters above the ground.

Table 6. List and properties of sensors used for the weather stations in the Vallon de Nant.

Company	Sensor	Variable	Basic characteristics	Auberge	Chalet	La Chaux	Glacier
Madd Technologies Sàrl, Yverdon-les-Bains, Switzerland	PluvioMADD	Precipitation amount (heated tipping bucket raingauge)	0.2 mm per tip	X			
G. Luftt Mess- und Regeltechnik GmbH, Fellbach, Switzerland	WS400-UMB	Air temperature	± 0.2°C from -20 to 50°C	X	X		X
		Air pressure	± 0.5 hPa from 300 to 1200 hPa	X	X		X
		Relative humidity	± 2 %RH from 0 to 100 %RH	X	X		X
		Precipitation intensity (24 GHz Doppler radar)	0.01 mm/h of detection sensitivity Particle size 0.3 to 5 mm (liquid) 5.1 to ~30mm (solid) Particle velocity 0.9 to 15.5 m/s 20% Accuracy & reproducibility >90%	X	X		X
		Precipitation type	Rain/snow	X	X		X
	WS300-UMB	Air temperature	± 0.2°C from -20°C to +50°C			X	
		Air pressure	± 0.5 hPa from 300 to 1200 hPa			X	
		Relative humidity	± 2 %RH from 0 to 100 %RH			X	
Apogee Instruments, Inc., Logan, Utah, USA	SP-230	Short wave solar radiation (360 to 1120 nm)	< 1% (repeatability)		X	X	X
Young Company, Traverse City, Michigan, USA	Wind Monitor HD-Alpine	Wind speed	± 0.3 m/s from 1.0 to 100 m/s				X
		Wind direction	± 3°				X
	Wind Monitor	Wind speed	± 0.3 m/s from 1.0 to 100 m/s	X			
		Wind direction	± 3°	X			
Decagon Devices, Inc., Pullman, Washington, USA	DS-2 Sonic	Wind speed	± 0.3 m/s from 0 to 30 m/s		X	X	
		Wind direction	± 3°		X	X	
	STM	Volumetric water content	± 0.03 m ³ /m ³ from 0.0 to 1.0 m ³ /m ³	X	X	X	
		Soil temperature	± 1°C from -40 to +60°C	X	X	X	
Sensorscope, Lausanne, Switzerland	IRT	Surface temperature	± 2 % from -33 to +220°C	X	X	X	X
	SONAR	Snow height	± 1 cm from 0.5 to 10 m	X	X		X

Figure 25 shows the period of data availability for each variable of each weather station. The data gaps are due to several reasons including cables cut by rodents, power supply shortage, water infiltration, data communication issues (snowpack blocking the radio signal), hardware or software malfunction of the dataloggers, and maybe lightning strikes.

The Glacier weather station worked well during the 2016/2017 winter, without any power supply shortage. A pole of the structure broke due to an excessive tension of support cables caused by the weight of the snowpack during winter. For 2017/2018 winter, the exceptional snowfall completely buried the weather station (more than 4.5 m of snow was measured when the station was accessible again). Damages affected mainly the solar panel that broke due to the cold flow of the snowpack. The structure and solar panel broke again during the 2018/2019 winter and the Glacier weather station was finally dismantled at the end of this data series.

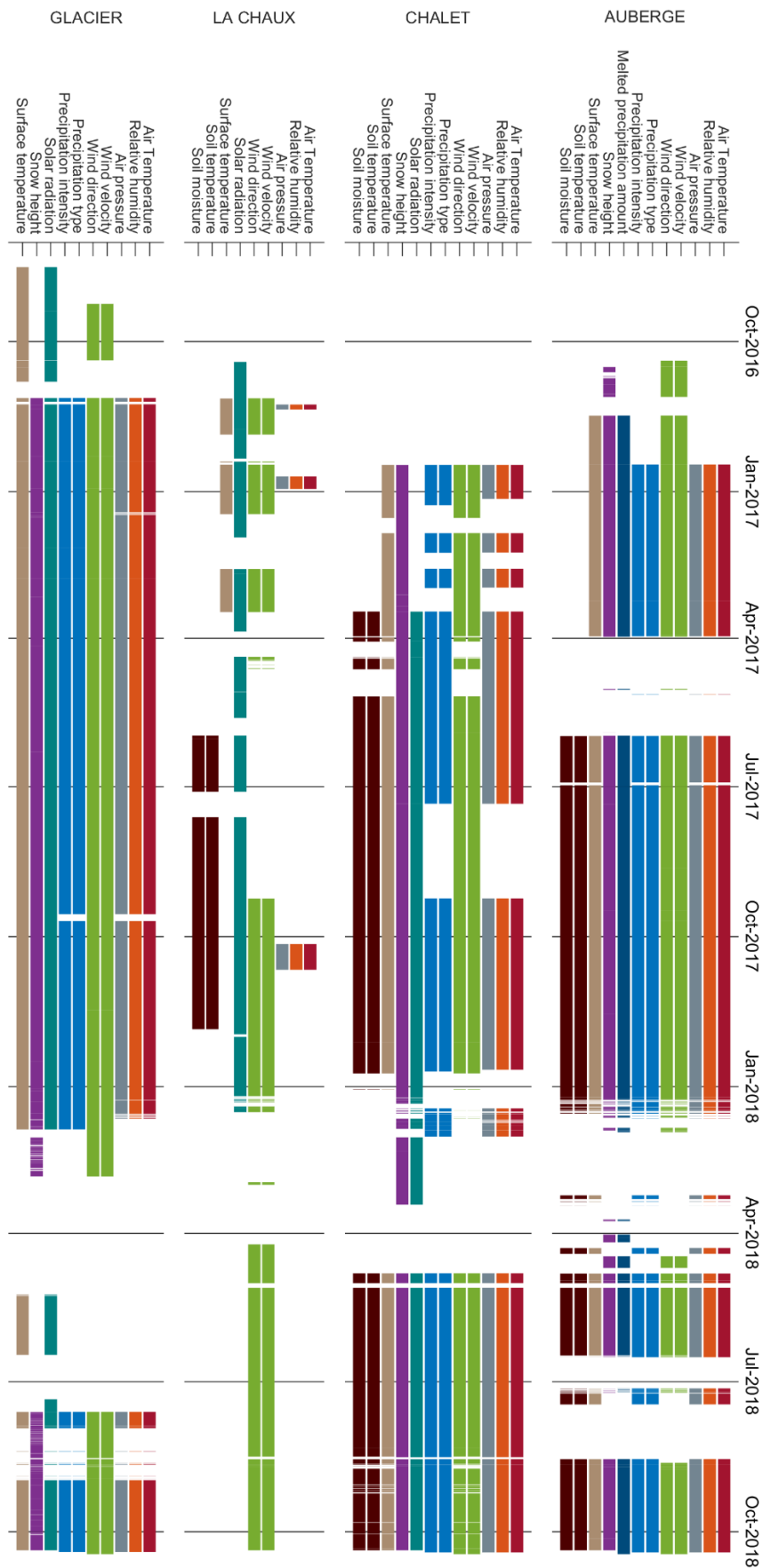


Figure 25. Availability (when color bars) of meteorological parameters for the four weather stations in Vallon de Nant.

The use of the DS3 dataloggers showed mixed results as several system failures led to important gaps in the data. The capacity of these devices to store data waiting for being transmitted is limited to a few days (variable with the amount of data collected by the sensors) and they get definitively lost if the communication issue lasts too long. Furthermore, the Sensorscope company stopped its activity in 2021, so no further development or support can be done with the DS3 dataloggers.

4.1.7 Meteorological data

All meteorological data collected by the weather stations from 16 August 2016 to 14 October 2018 are publicly available on Zenodo (Michelon et al., 2021b). We give in this section some results and statistics based on the Auberge, Chalet and Glacier weather stations between 1 January and 31 December 2017 (period and stations with the least data gaps).

Air temperature and lapse rate

The daily air temperature time series from 2017 (Figure 26) are well correlated: $R^2 = 0.95$ for Auberge/Chalet, $R^2 = 0.84$ for Auberge/Glacier and $R^2 = 0.93$ for Chalet/Glacier.

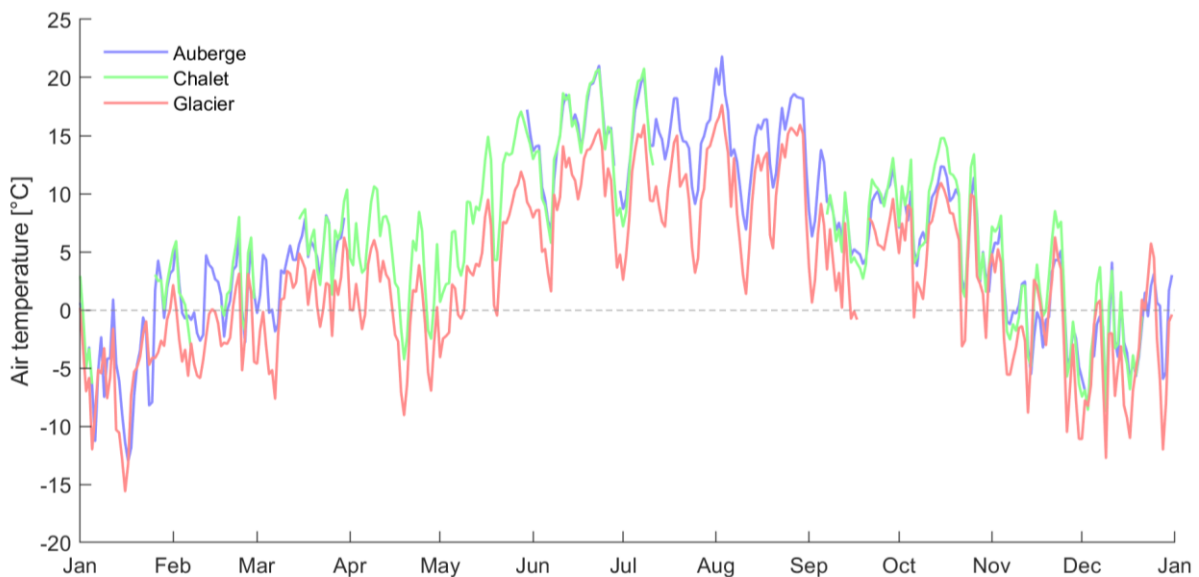


Figure 26. Daily air temperature at the Auberge, Chalet and Glacier weather stations in 2017; the mean air temperature over the year is respectively 6.1 °C, 6.3 °C and 2.8 °C (time series include 16.4 %, 30.1 % and 0.8 % of data gap, respectively).

For this study, the lapse rate is an important parameter to interpolate spatially the temperature and estimate the snowmelt areas. Based on the annual mean values, we compute a lapse rate of -0.36 °C/100 m for Auberge/Glacier and -0.63 °C/100 m for Chalet/Glacier. The Chalet/Glacier lapse rate is close to the -0.65 °C/100 m standard value

from the international standard atmosphere (ISO, 1975). We explain the difference by an accumulation of cold air at the bottom of the valley in the Auberge area.

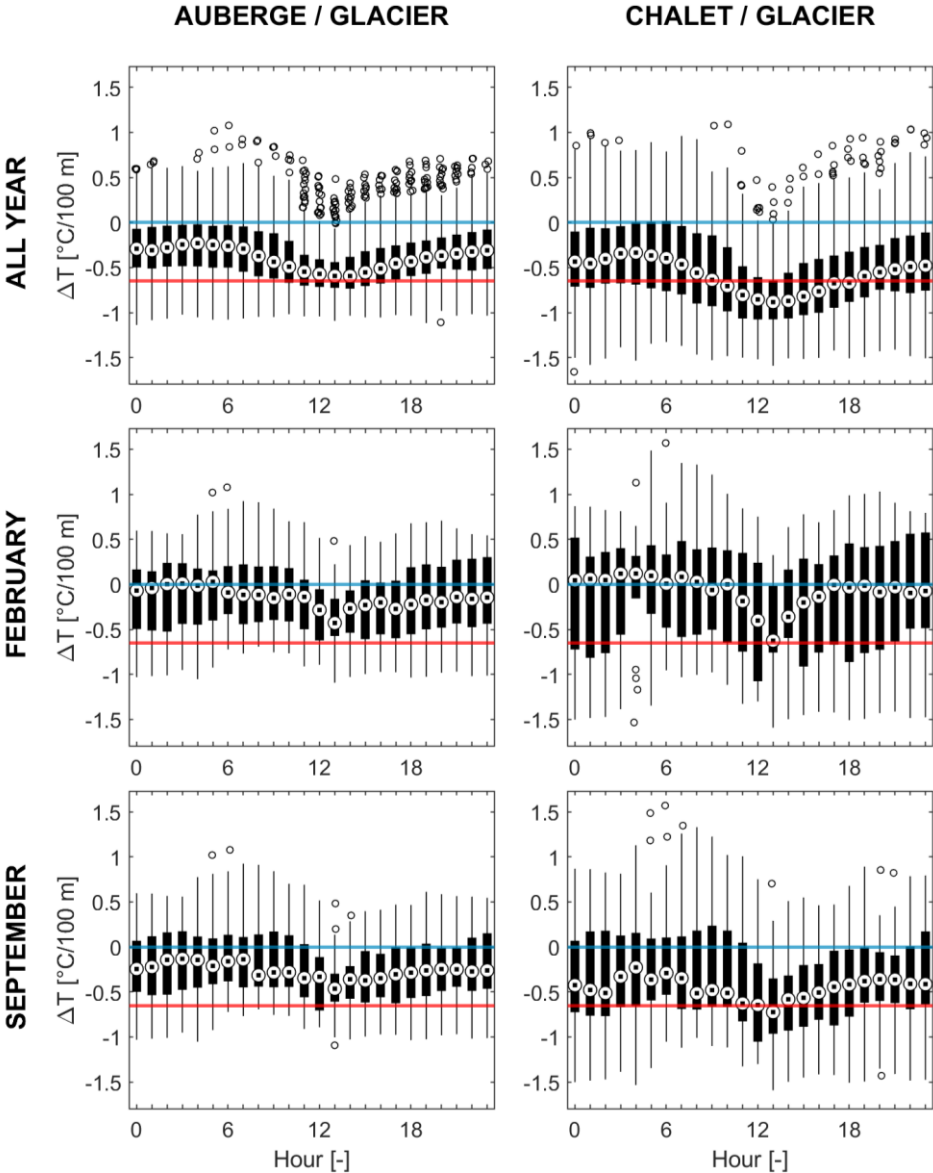


Figure 27. Altitudinal gradient of temperature during the day between Auberge and Glacier, Chalet and Glacier, for all year, February, and September. Based on common times series: between 67.6 % and 81.5 % of the period for all year, and between 97.1 % and 100 % for the individual months. The blue line is 0 °C/100 m and the red line -0.65 °C/100 m.

Figure 27 shows that the lapse rates of Auberge/Glacier and Chalet/Glacier follows diurnal and annual cycles. Daily, the lapse rate is marked by a minimum around 1 p.m. and is weaker during the nighttime. Over a year, comparing February to September, the lapse rate varies from -0.15 °C/100 m to -0.22 °C/100 m for Auberge/Glacier, and from -0.14 °C/100 m to -0.36 °C/100 m for Chalet/Glacier. The low lapse rate variation for Auberge/Glacier shows that cold air tends to accumulate in the Auberge area all the year, while the phenomenon is important

enough to be also recorded at the Chalet during winter. The existence of cold air accumulation in the valley bottom makes the spatial interpolation of temperature over the catchment difficult. The lower the temperature gradient and the slopes, the greater the uncertainty.

Precipitation

In 2017, the Glacier weather station (2,136 masl) measured 1,723 mm of precipitation (rainfall and snowfall). By comparing periods with common time series, the Chalet (1,530 masl) recorded -2.2 % of precipitation (over 252 days), and the Auberge (1,253 masl) +6.5 % (over 288 days). These data tend to show a precipitation lapse rate between the Chalet and Glacier, but a higher amount of precipitation falling at the Auberge, despite its lower elevation. This could be explained either i) by a spatial variability of precipitation amounts that is more important than the lapse rate, or ii) by topographic effects that increase the amount of precipitation over the Auberge area.

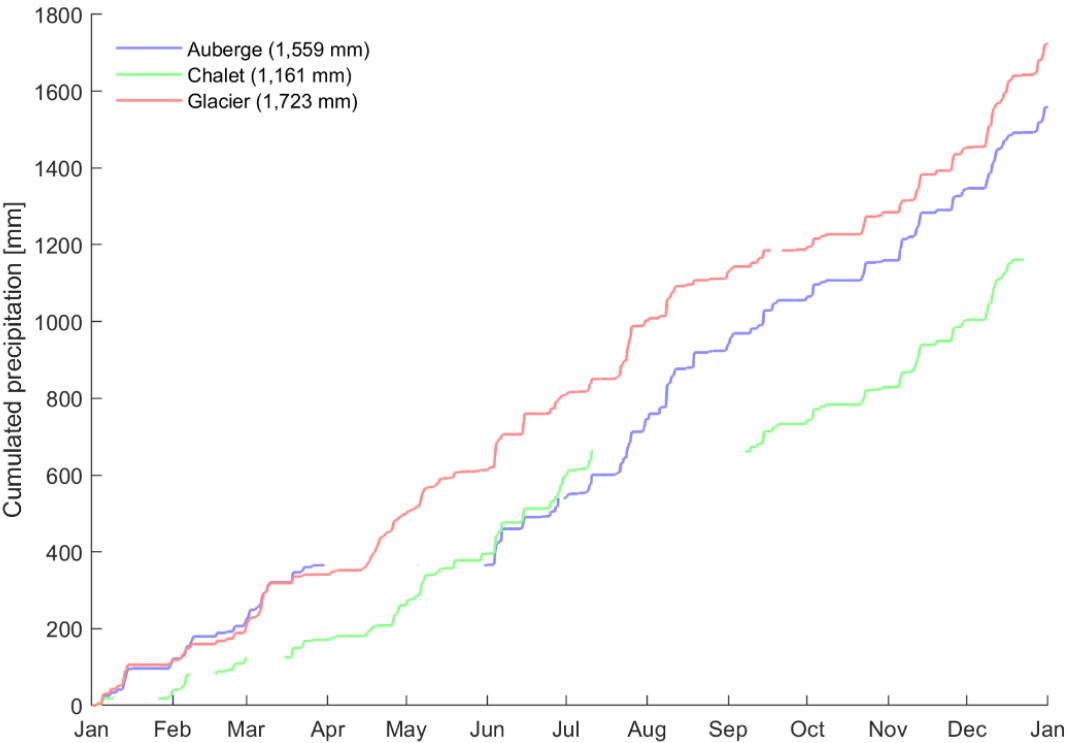


Figure 28. Cumulated precipitation (rainfall and snowfall) measured at three weather stations in 2017. Note that the time series for this year have 17.2 %, 30.0 % and 1.2 % of missing data.

Local and high altitude winds

The wind direction measured by the weather stations in the Vallon de Nant is largely influenced by the topography of the valley (Figure 29) and each station measures predominant

wind coming from the upstream area. It reflects frequent catabatic winds, in accordance with the phenomenon of cold air accumulation during the night mentioned above.

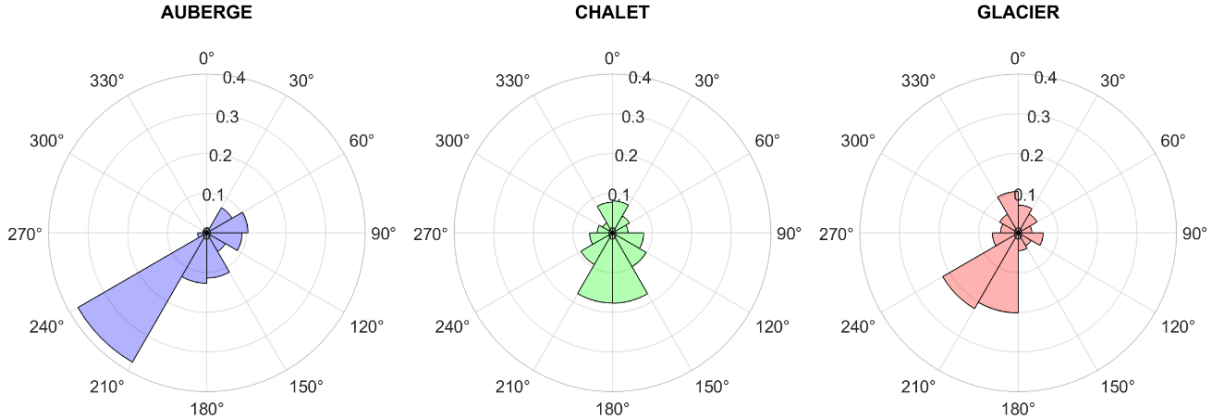


Figure 29. Wind direction at the Auberge, Chalet and Glacier weather stations, relatively to their working periods.

Thus, the local wind measures do not give information about the general atmospheric circulation. Figure 30 shows the occurrence of wind calculated at the 500 hPa geopotential height (approximately 5500 masl), in connection with precipitation events over the catchment. We see that air masses mainly originate from south-west to north, and air masses accompanied by precipitations originate from south-west to north-west. The higher probability to have precipitation events travelling from west to east highlights the higher importance, to capture most of the spatial heterogeneity of precipitation events in this area, to measure precipitations along a north-south transect than along a west-east transect.

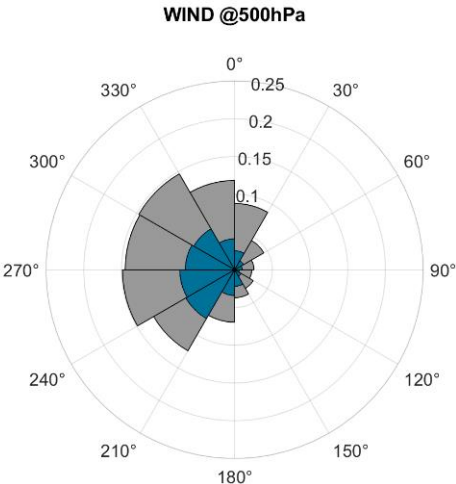


Figure 30. Frequency of wind direction above the Vallon de Nant at 500 hPa (ECMWF ERA5) on a 6-hour time scale. The grey histogram represents the wind occurrence during the working period of the precipitation sensors, and the blue histogram the wind when precipitation was recorded.

Solar radiation

The topography of the Vallon de Nant, characterized by a valley facing north and surrounded by high peaks shading large areas (see Chapter 2), is confirmed by the measured of solar radiation at the weather stations (Table 7) with i) low amounts during winter, ii) high amounts in summer, and iii) a large difference between the mean values.

Table 7. Statistics of daily net radiations (in W/m²) at the Chalet, La Chaux and Glacier weather stations. The mean value is computed over 217 days between 1 January 2017 and 31 December 2017.

Station	Minimum (24 Dec. 2017)	Maximum (8 Jun. 2017)	Mean (over 217 days)
Chalet	7.6	302.5	91.7
La Chaux	33.6	333.0	144.1
Glacier	6.7	322.0	90.0

4.1.8 Pluvimates raingauges

A network of 12 Pluvimate drop-counting rain gauges (www.driptych.com) was distributed across the Vallon de Nant catchment from 30th June to 4th October 2017 and from July 1st to September 23rd, 2018 to monitor rainfall (see Figure 40 in Chapter 5). Data for the 2018 season are available on Zenodo (Michelon et al., 2020). A similar deployment during the cold season would not be possible due to snowfall at all elevations throughout the winter.

The gauges are low-cost (around 600 USD each), consisting of a tube (11 cm of diameter, 40 cm of length) mounted to an aluminum funnel (Figure 31). The collected rainwater is concentrated to a nozzle that creates a drop of water of a calibrated size (0.125 mL), which then falls on the impact-sensitive surface of the sensor, 30 cm below. The datalogger counts and records the number of drops over a time up to 2 minutes. In the field, the devices were set up vertically, attached to a wooden stick. The funnel aperture was between 0.8 and 1.2 m above the ground.

The Pluvimates were set-up to count drops over an interval of 2 minutes, with an accuracy of 0.3 mm/h. Benoit et al. (2018) experimentally evaluated the device uncertainty to 5 % for rainfall intensities under 20 mm/h. Given that some of the rainfall intensities measured exceed this value (intensities up to 140 mm/h were recorded), we extended the calibration to intensities up to 150 mm/h, and few saturation effects were noticed (Appendix 4 - 2).

To prevent clogging, steel sponges were put in the funnel of each Pluvimate. This appeared to have caused i) a dampening effect on low rainfall intensities as it delayed slightly the beginning of very small events (lower than 1 mm/h) and ii) created drops remaining after the end of an event. The data are not corrected for these effects.



Figure 31. Drop-counting rain gauge used. The Pluvimate is set-up vertically between 0.8 and 1.2 meters above the ground (a). A tip at the end of the funnel (b) creates a calibrated drop of water that falls on the sensor, (c) which counts and records the number of drops during a given amount of time.

Additional artefacts were recorded, probably generated by strong winds creating resonance. Some stations in fact recorded very strong and highly variable rainfall over several hours during periods with high wind velocity but during days without any observed rainfall in the combined MeteoSwiss radar-rain gauge data (Sideris et al., 2014). Four periods (over 4 different days) have been manually removed from the data.

4.1.9 Comparison of precipitation measurements

Figure 32 compares summer rainfall events measured jointly by the Lufft WS400 sensors at the Auberge, Chalet and Glacier stations (see Section 4.1.4) and a Pluvimate (see Section

4.1.8). Although the linear regression does not show a bias ($y = 0.98x$) we note some dispersion. For the maximum rainfall over 2 minutes, there is however a certain bias, with an overestimation of the Lufft sensor relatively to the Pluvimate raingauges ($y = 0.85x$), mainly due to events measured at the Auberge.

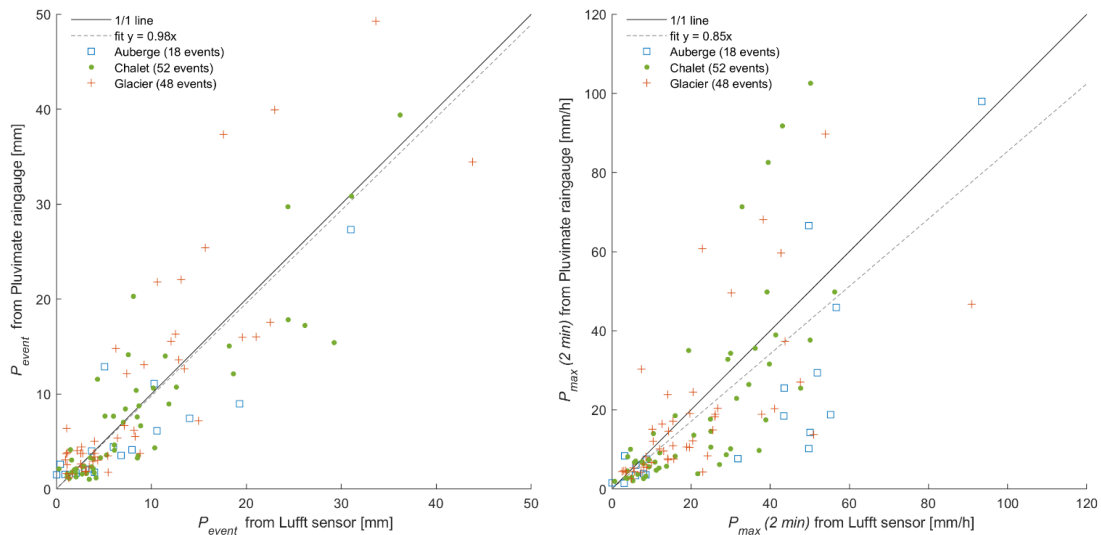


Figure 32. Comparison (left) of rainfall amounts ($r^2 = 0.73$) and (right) maximum intensity over 2 minutes ($r^2 = 0.49$) measured at the Auberge by the Lufft sensor vs. Pluvimate rain gauge, at event scale.

Compared to the Madd rain gauge (Figure 33), the Lufft WS400 overestimates the total amount of precipitation for events over 5 mm ($y = 0.82x$), and a similar overestimation trend is observed for the maximum rainfall intensity over 2 minutes ($y = 0.70x$).

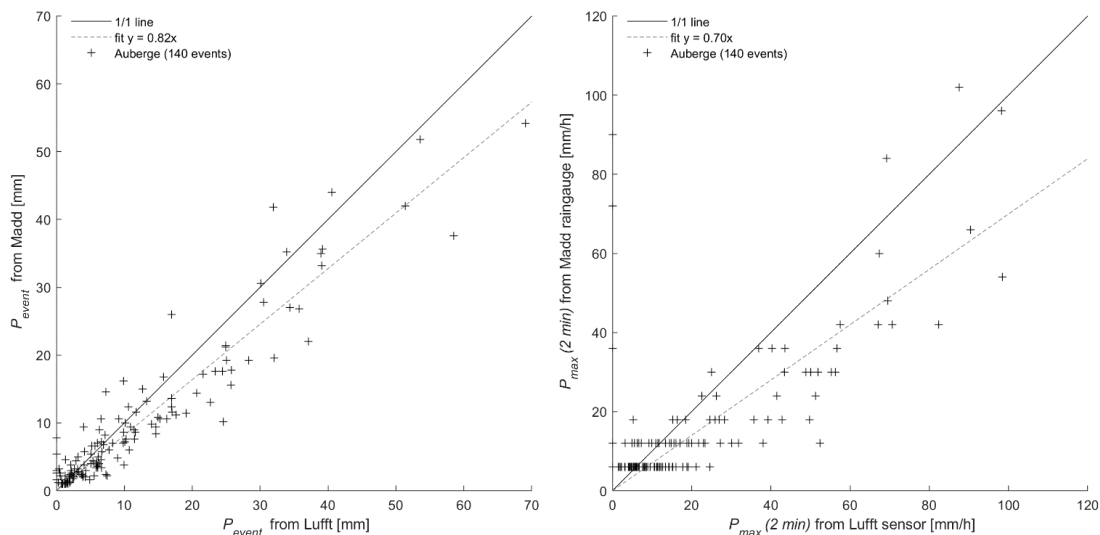


Figure 33. Comparison of rainfall amounts ($r^2 = 0.95$) and maximum intensity over 2 minutes ($r^2 = 0.72$) measured at the Auberge by the Lufft WS400 sensor vs. the Madd rain gauge, at event scale. The maximum rainfall data from the Madd sensor have been aggregated from 1-minute to 2-minute time step resolution for comparison.

Further insights into the performance of the used sensors can be obtained from a comparative measurement from MeteoSwiss between a reference measurement using a raingauge OTT Pluvio² (OTT HydroMet Sàrl, Aix-en-Provence, France) located inside a double fence intercomparison reference (DFIR), and a Lufft WS600 (similar to the Lufft WS400) located nearby outside the wind shelter (Figure 34). This comparison measurement was completed in the context of the large sensor intercomparison project SPICE (Nitu et al., 2018) but the Lufft sensor was not considered in the final project report.

Over one year and a half, the measurements sometimes differ but without a particular bias. We conclude from these data that the absence of wind protection (like for the setup in the Vallon de Nant) induces a larger dispersion of the measurements, but not a particular bias. The bias observed for the comparison in the Vallon de Nant can then be attributed to wind effect over the funnels of the Madd and Pluvimate raingauges that induce an underestimation of the rainfall. The height of the sensors could explain that the Madd raingauge (2.5 m above the ground, Figure 24) is more impacted than the Pluvimate raingauges (0.8 to 1.2 m above to the ground, see Section 4.1.8).

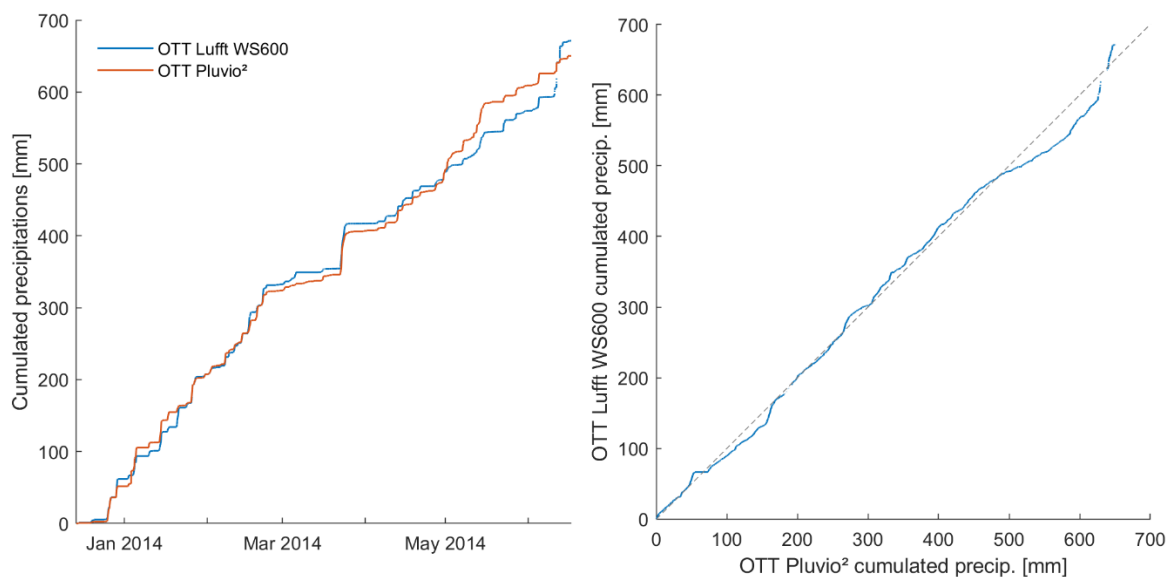


Figure 34. Comparison of measurements between an OTT Pluvio² sheltered by a double fence intercomparison reference (DFIR) and a Lufft WS600 (using the same 24 GHz sensor as the Lufft WS400), recorded between 14 Dec. 2013 and 17 Jun. 2014 at the Moléson weather station, Switzerland, by MeteoSwiss (Nitu et al., 2018). Data received from Yves-Alain Roulet (MeteoSwiss), reproduced here with the permission of the original author.

4.2 Snowcover characterization

4.2.1 Lysimeters

At the beginning of 2017 winter, six lysimeters have been set up within the catchment. Pairs of collocated lysimeters were set up nearby the Auberge and Chalet weather stations (2.5 m one from each other), and two others were set up near the La Chaux and the Glacier weather station (location on map Figure 20). These lysimeters have been used in a previous study (Würzer et al., 2017; Brauchli et al., 2017) and consist of a 0.45 m diameter plastic funnel covered with a metal grid (Figure 35) that collects snow melt. The snow melt rate is measured by a Decagon tipping bucket raingauge ECRN-100 (Decagon Devices, Inc., Pullman, Washington, USA) with a 0.2 mm resolution (0.025 mm resolution due to the large collector funnel). At the Auberge and Chalet sites it was also attempted to collect the melted snow, by putting a collector under the lysimeters and tubes on a low slope up to plastic bags at lower altitude.

This experiment failed due to different reasons (filled bags and flood of the raingauges, contamination of water by silicon, raingauges clogged due to airborne sediment trapped in the snow).



Figure 35. (A) Picture of the co-located lysimeters next to the Chalet weather station. (B) A trench allows a tube to collect independently the melted water from each raingauge in two bags in an insulated plastic box at lower altitude.

Figure 36 shows the snow melt measured by the lysimeters at the four locations. The Auberge and Chalet locations lysimeters suffered from rapid clogging due to a large amount of airborne particles, carried before the snowfall and within the snowpack. One of the two co-located lysimeters did not work properly for this reason, and the second worked for a few months only before it was clogged.

We see that the snowpack at the Auberge and Chalet locations, at lower altitude (1253 and 1530 masl, Table 5), were sensitive to positive temperatures (large steps on the plot), while at the Chaux and Glacier (1780 and 2136 masl), the snowpack started significantly to melt respectively on 7 April 2018 and 25 April 2018. At the Chaux, a maximum melt rate of 112.0 mm.d⁻¹ was recorded (Table 8).

We remark that the mean melt rate over 3 months during the cold period (0.02 and 0.30 mm.d⁻¹, Table 8) is way smaller than the standard value of 1 mm.d⁻¹ typically used in models (Schaeffli et al., 2014) to account for cold periods water supply and is not applicable for this catchment or it should at least not be an evenly distributed value.

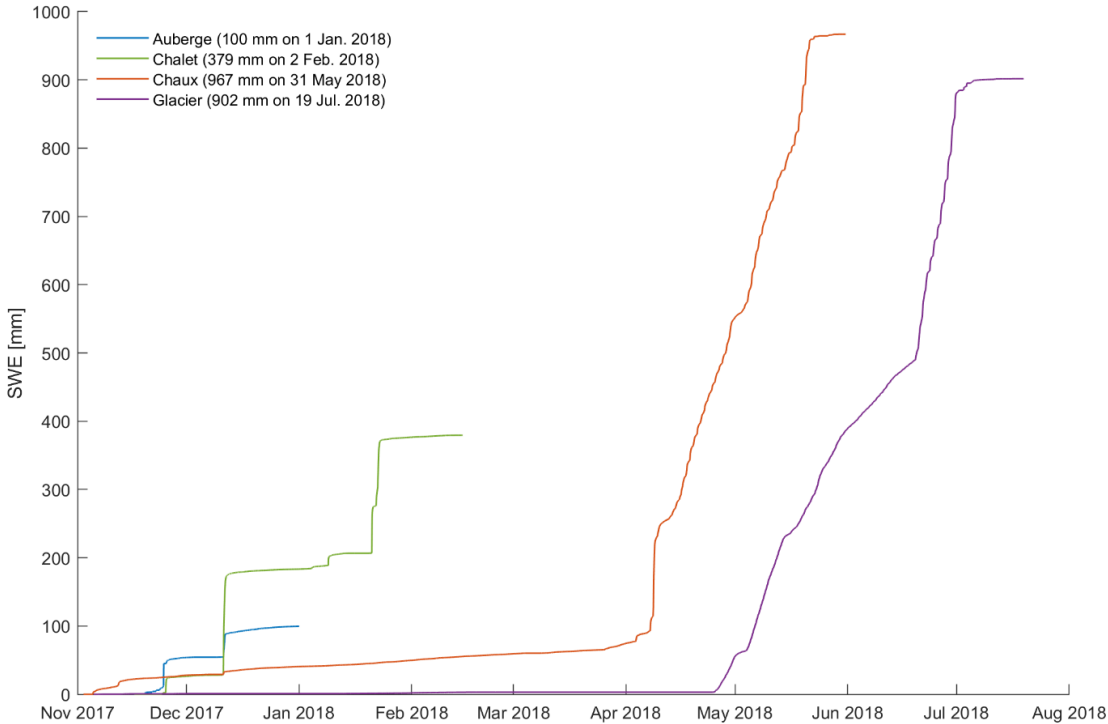


Figure 36. Snow water equivalent (SWE) measure at the lysimeters at the four weather stations for the 2017/2018 winter. The Chaux and Glacier time series are complete (up to the complete snowpack melt), but the Auberge and Chalet time series are cut prematurely before the period when it was estimated the raingauge measuring snow melt was flood/clogged.

Table 8. Melt rate statistics at the Chaux and Glacier lysimeters for a 3-month cold period from 15 December 2017 to 15 March 2018 and during their respective melt period.

Station	Altitude [m asl.]	3-month cold period (15 Dec. to 15 Mar.)			Melt period		
		Mean soil T [°C]		Melt rate [mm.d ⁻¹]	Duration [d]	Melt rate [mm.d ⁻¹]	
		@10 cm	@20 cm			mean	max
Chaux	1780	0.9	1.2	0.30	45	19.3	112.0
Glacier	2136	0.7	0.9	0.02	67	4.8	47.0

4.2.2 Satellite images and snow-covered areas

The evolution of the snow cover area (SCA) is analyzed using satellite images from Landsat 8 (30 m resolution) and from Sentinel-2 (10 m resolution upscaled to 30 m). The images with a cloud cover < 80 % (over the whole image) are processed manually by applying a mask over areas with eventual remaining clouds.

The SCA is estimated from the normalized difference snow index (NDSI, noted here I_{NDSI}), using the green (b_G) and SWIR-1 (b_{SWIR1} , shortwave infrared between 1,57 and 1,65 μm) bands:

$$I_{NDSI} = \frac{b_G - b_{SWIR1}}{b_G + b_{SWIR1}}. \quad (11)$$

The I_{NDSI} gives for each pixel a value between -1 and 1, and a common threshold (usually around 0.2) allows one to classify snow-free from snow-covered pixels. However, it has been found that a unique value cannot be used for some of these images, due to a significant shadow area caused by the steep slopes and cliffs in its southern part of the valley. The sunny and shadow areas are therefore considered separately.

The shadow was first identified by calculating the projected shadow based on the known position of the sun at the time of the picture and a 2 x 2 DEM of the catchment (swissAlti3D, 2012b), but i) important parallax issues appeared on the cliffs and steep slopes in the southern and eastern parts of the catchment, requiring an additional processing step, ii) the DEM is not accurate enough on the edges to give accurate results on the projected shadow, and iii) this method fails to consider additional snow layers on the edges (up to few meters in winter) and shadow caused by clouds over or near the catchment areas.

For all these reasons, the shadow areas are computed from the satellite images themselves. A shadow index S_{index} using the red (b_R), green (b_G), blue (b_B), near infrared (b_{NIR}) and SWIR1 (b_{SWIR1}) bands is defined as follow:

$$S_{index} = [(1 - b_R) \times (1 - b_G) \times (1 - b_B) \times (1 - b_{NIR}) \times (1 - b_{SWIR1})]^{\frac{1}{5}}, \quad (12)$$

and gives a value between 0 and 1. A threshold is then adjusted manually to define the shadow areas. Thus, the area is first separated between sunny and shadow area using S_{index} , and the I_{NDSI} adjusted manually for each area. The total SCA over the catchment is the sum of the SCA estimated for the shadow area and the sunny area.

The whole process relies strongly on visual evaluation, and this estimation may vary from one person to the other. In total, 53 images from Landsat 8 and 36 images from Sentinel-2 have

been processed over a period of 3 years between 1 January 2015 and 1 January 2018 (Figure 37). As the satellite images can detect only snow accumulated over the forest canopy but not in the undergrowth, it was been chosen to consider only the area of catchment without dense forested areas.

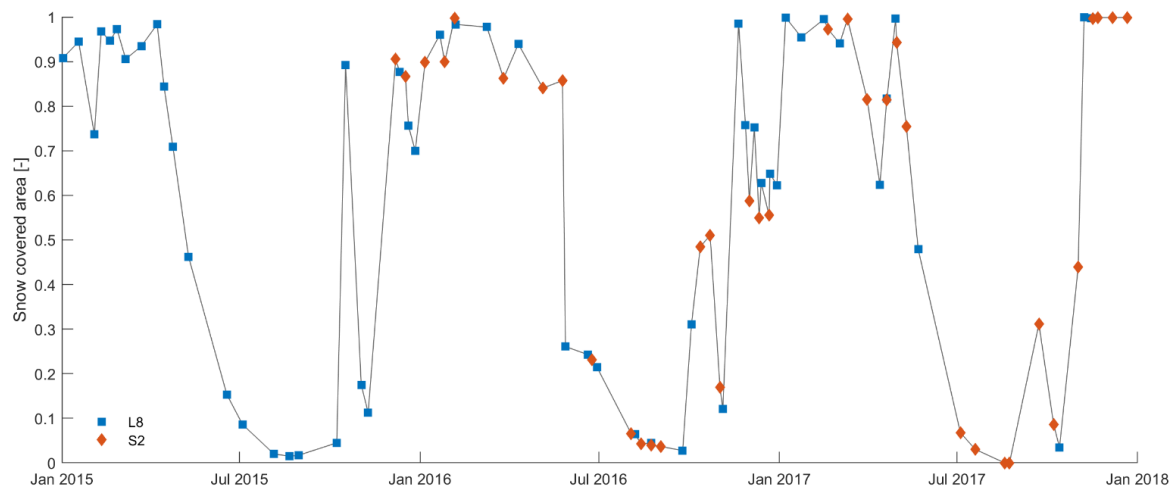


Figure 37. Snow covered area in Vallon de Nant between 1 January 2015 and 1 January 2018 using 53 satellite images from Landsat 8 (L8) and 36 satellite images from Sentinel-2 (S2).

Figure 38 shows maps of probability of presence of snow for each month of the year. These maps are however not a robust statistic as they are based on a 2-year time series of satellite images. Note that the presence of dense forested areas at low altitude led to a bias in the probability during the winter months, for the reasons mentioned above, and that the glacier area appears as a snow-covered area.

From the SCA evolution plot (Figure 37) and the maps of the probability of presence of snow (Figure 38) we see that in general the fluctuations of the snowcover occur over short periods of time (to the exception of the melt season in 2015). Due to the time interval between images, the need for high resolution images is questionable. During the first snowmelt, the snow-covered area is strongly correlated with the profile of temperature, and so to the altitude.

It would have to be verified if the area covered with snow follows a similar pattern from one year to the other. This assumes that temperature and sunshine conditions are roughly similar across the catchment during snowmelt, and that the snow layer thickness is not affected. To compensate for the lack of temporal resolution of satellite images, multiple years of images taken during snowmelt periods could be combined and associating images together when they have the snow cover extent at similar control points, check how sparse is the snow line

in the rest of the catchment. This would allow to infer a precise spatial distribution of the snowcover at a given time by using on-field devices like soil thermometers (see Chapter 5).

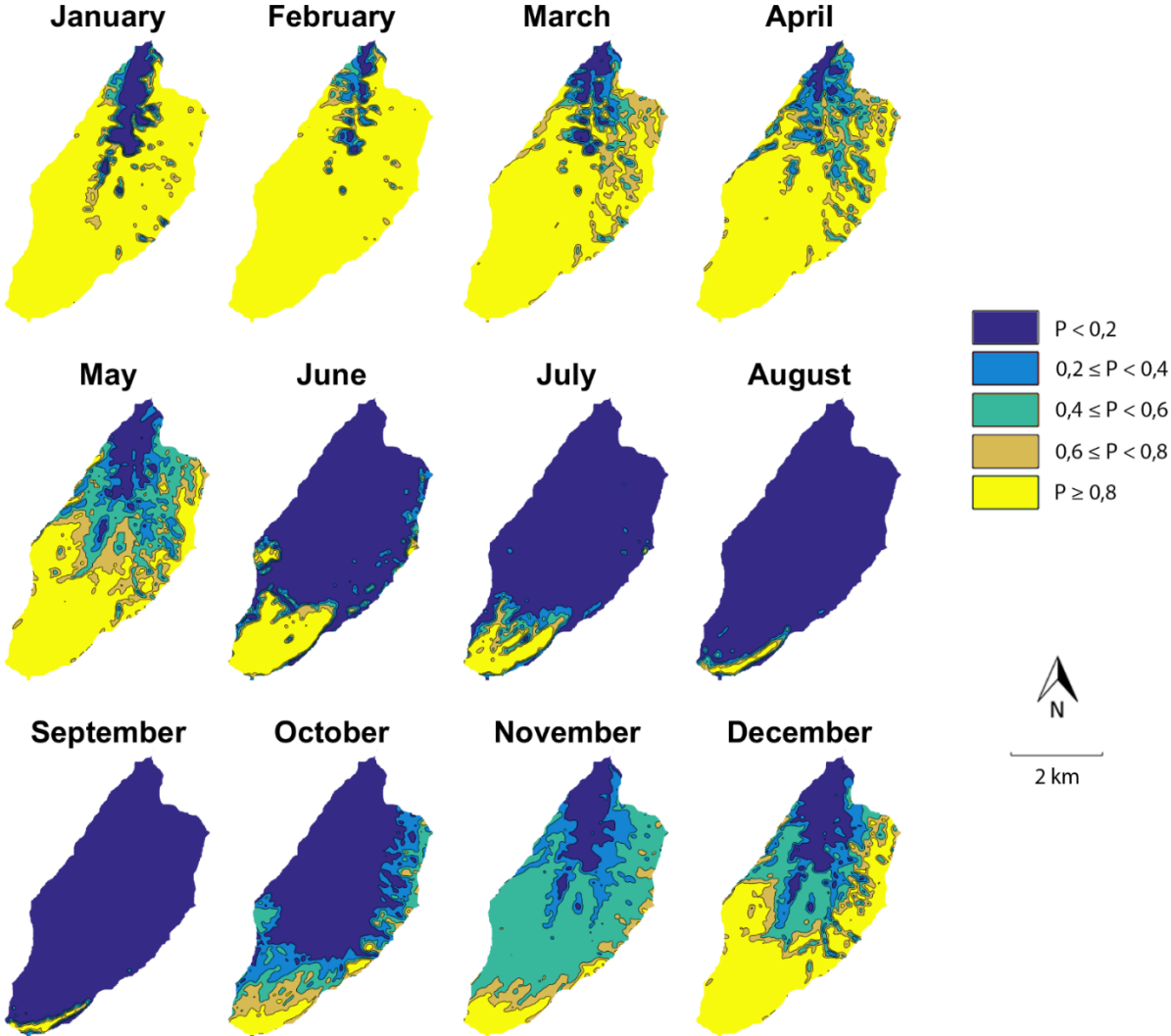


Figure 38. Monthly maps of probability of presence of snow for the Vallon de Nant, based on 2 years of snow cover maps between 1 March 2015 and 1 March 2017. Each map and part of the catchment is based on a different number of snow cover maps, presented in Supplementary Material.

4.3 Summary

The design and maintenance of a weather station network that operates throughout the year in the Vallon de Nant is challenging due to the constraints of extreme weather conditions, poor network connection, power supply difficulties relative to long lasting shadow in winter, and accessibility. The solutions developed here have shown their viability, but the multiple failures of the dataloggers, as well as the undersizing of the physical structure of the glacier weather station (to resist snowpack accumulation) led to important data gaps. The used precipitation and raingauges do not have the same accuracy as measurement devices used

e.g. by the Swiss Meteorological Office, but offer a continuous measure throughout the year for locations where daily maintenance is not possible and the power supply limited. The lessons learned, however, will help to equip this or other study areas with similar conditions.

For the work of this thesis, the most important meteorological parameters are the precipitation and temperature. The temperature recordings show the recurrent presence of cold air accumulation at the valley bottom, which implies that its amplitude and fluctuations should be studied in more detail to allow a good spatial interpolation of temperature over the catchment. Based on three measurement points, the precipitation recordings over a year showed a spatial heterogeneity that cannot be explained by a simple elevation-dependent relationship. A high density raingauge observation (0.22 raingauges per square km) is presented in Chapter 5.

Despite failures, the lysimeters network provides an estimation of the snowmelt rate for the cold season and the melt season. Satellite image analysis is difficult to automatize at such high resolution and in areas with such a predominant shadow area as in the Vallon de Nant. The snow cover area analysis can be complemented with data from soil temperature sensors, as presented in Chapter 6.

Appendix 4 – 1: Weather stations network in the Vallon de Nant before 2016

A first network of 6 weather stations was deployed in the Vallon de Nant starting in 2007 (details in Table 9, locations on the map Figure 20) along a transversal and longitudinal transect (Coquelin, 2008). Each station measured air temperature, relative humidity, air pressure, solar radiation, wind speed and direction, and precipitations. Two types of tipping buckets raingauges were installed: i) at the Auberge, a raingauge Madd PluvioMADD (Madd Technologies Sàrl, Yverdon-les-Bains, Switzerland) heated (when air temperature < 5 °C) to measure snowfall; ii) at la Chaux, a non-heated raingauge from Davis (Davis Instruments Corporation, Hayward, California, USA). In addition, four Vaïisala WXT 510 sensors (Vaïisala Corporation, Helsinki, Finland) were installed at the Chalet, Les Ayers, La Pointe des Savolaires and Frête de Saille; these sensors quantify precipitation based on the analysis of the impact of hydrometeors on a convex surface. The method is adapted to rainfall events but is unsuitable (without heating) for winter conditions as the formation of ice or accumulation of snow prevents precipitation detection (Roth, 2011).

Two of the weather stations (Les Ayers and Frête de Saille) were swept away in the following years (avalanche, storm). After 2011, different breakdowns affected the remaining stations due a lack of maintenance: communication issues, electronic failures and maybe a lightning impact caused several gaps in the data (Jean-Michel Fallot personal communication, 25 August 2021).

Table 9. Details about the previous weather stations network setup in the Vallon de Nant (locations on Figure 20).

Weather station	Auberge	Chalet	La Chaux	Les Ayers	Pointe des Savolaires	Frête de Saille
Altitude [m asl.]	1253	1500	1780	1980	2250	2580
Sensor company	Madd	Vaïisala	Davis	Vaïisala	Vaïisala	Vaïisala
Method for precip. measurements	Heated tipping bucket raingauge	Impact sensor	Tipping bucket raingauge	Impact sensor	Impact sensor	Impact sensor
Start date	19/12/2007	02/01/2008	01/03/2010	19/01/2010	02/01/2008	01/02/2008
End date	01/12/2016	2015	13/06/2019	20/08/2010	11/2015	26/10/2012
End reason	Migration to Sensorscope	Migration to Sensorscope	Migration to Sensorscope	Avalanche	Dismantling	Storm

Appendix 4 – 2: Drop-counting rain gauge calibration and data correction

Technical characteristics of the Pluvimate drop-counting rain gauges are detailed in the work of Benoit et al. (2018); for this study we extended the experimental tests to intensities up to 150 mm/h. It appears that for intensities up to 20 mm/h (99.88 % of the measured 2-min intensities during the 2018 observation period) the linear relationship between drop count and rain intensity gives a good estimate (uncertainty below 5 %); beyond 20 mm/h the linear relationship underestimates the rainfall intensities, to reach 10 % of error at 60 mm/h and 15 % at 150 mm/h (Figure 39). For this study, rainfall intensities over 20 mm/h are corrected using a polynomial law based on the experimental data.

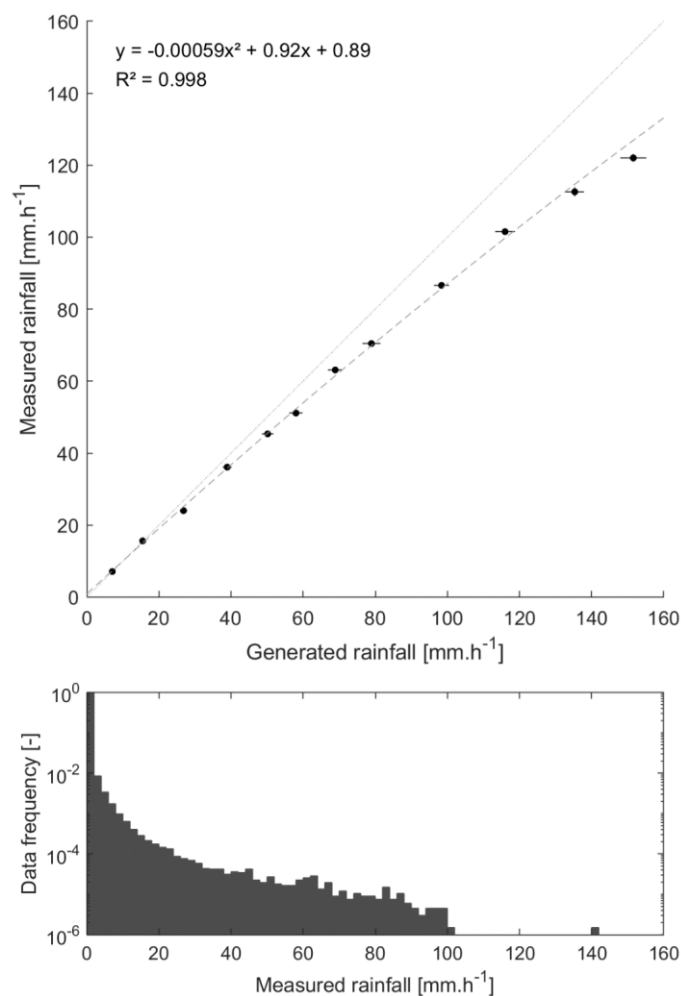


Figure 39. Calibration curve (on top) of the Pluvimate rain gauges based on experimental measures with controlled rainfall input, and (at the bottom) the data frequency measured in situ.

5 | Benefits from high density rain gauge observations for hydrological response analysis in a small alpine catchment



Photograph: Rainfall intensity measurement using a Pluvimate (on the right) next to the moraine area.

A version of this chapter has been published in Hydrology and Earth System Sciences journal:

Michelon, A., Benoit, L., Beria, H., Ceperley, N., and Schaefli, B.: Benefits from high-density rain gauge observations for hydrological response analysis in a small alpine catchment, *Hydrol. Earth Syst. Sci.*, 25, 2301-2325, 10.5194/hess-25-2301-2021, 2021.

Author contributions. AM and BS conceived the ideas and designed methodology. AM, LB and HB collected the rainfall data. AM and LB analyzed the data. AM and BS led the writing of the paper. All authors contributed critically to the drafts and gave final approval for publication.

Abstract

Spatial rainfall patterns exert a key control on the catchment scale hydrologic response. Despite recent advances in radar-based rainfall sensing, rainfall observation remains a challenge particularly in mountain environments. This paper analyzes the importance of high-density rainfall observations for a 13.4 km² catchment located in the Swiss Alps where rainfall events were monitored during three summer months using a network of 12 low-cost, drop-counting rain gauges. We developed a data-based analysis framework to assess the importance of high-density rainfall observations to help predict the hydrological response. The framework involves the definition of spatial rainfall distribution metrics based on hydrological and geomorphological considerations, and a regression analysis of how these metrics explain the hydrologic response in terms of runoff coefficient and lag time. The gained insights on dominant predictors are then used to investigate the optimal rain gauge network density for predicting the streamflow response metrics, including an extensive test of the effect of down-sampled rain gauge networks and an event-based rainfall-runoff model to evaluate the resulting optimal rain gauge network configuration. The analysis unravels that besides rainfall amount and intensity, the rainfall distance from the outlet along the stream network is a key spatial rainfall metric. This result calls for more detailed observations of stream network expansions, as well as the parameterization of along stream processes in rainfall-runoff models. In addition, despite the small spatial scale of this case study, the results show that an accurate representation of the rainfall field (with at least three rain gauges) is of prime importance to capture the key characteristics of the hydrologic response in terms of generated runoff volumes and delay for the studied catchment (0.22 raingauges/km²). The potential of the developed rainfall monitoring and analysis framework for rainfall-runoff analysis in small catchments remains to be fully unraveled in future studies, potentially including also urban catchments.

5.1 Introduction

Rainfall is known to be highly variable in space even at small scales, in particular in mountain areas (Henn et al., 2018; Tetzlaff and Uhlenbrook, 2005). Despite recent progress in the observation of spatial rainfall in mountainous areas with the help of radar (Berne and Krajewski, 2013; Germann et al., 2006; Germann et al., 2015), it remains crucially difficult to observe and spatially interpolate (Foehn et al., 2018a; Sideris et al., 2014).

Understanding the interrelation between spatial rainfall patterns and the hydrologic response has been of concern for many decades, ranging from a theoretical viewpoint (Shah et al., 1996; Singh, 1997; Woods and Sivapalan, 1999), to a rainfall-runoff model perspective (Obled et al., 1994; Nikolopoulos et al., 2011), and extending to a hydrological process understanding perspective (Guastini et al., 2019; Zillgens et al., 2007). Even earlier work in this field focused on the model-based investigation of optimal rain gauge density for reliable areal rainfall estimation (Bras and Rodriguez-Iturbe, 1976a) and runoff prediction (Bras and Rodriguez-Iturbe, 1976b; Tarboton et al., 1987). Chacon-Hurtado (2017) provides a recent review on rain gauge network optimisation.

A wide range of methods has been proposed to analyze the hydrologic response as a function of spatial rainfall patterns. We can broadly distinguish between empirical methods that identify systematic response patterns by scrutinizing individual observed events (Blume et al., 2007) and model-based methods that try to identify systematic or theoretical relationships between rainfall and the hydrologic response. In this latter category, we first of all find stochastic methods that describe the stochastic aspects of the hydrologic response as a function of the rainfall field properties. These approaches range from simplified stochastic models (Tarboton et al., 1987) to full space-time representations of rainfall forcing and streamflow generation (Mei et al., 2014; Pechlivanidis et al., 2017; Viglione et al., 2010; Woods and Sivapalan, 1999; Zocatelli et al., 2015). These stochastic tools are developed to understand the relative importance of the two key components of the hydrologic response, i) the runoff generation processes at the hillslope scale and ii) the routing mechanisms in the channel network. Such an assessment of the relative role of unchannelled-state and channelled-state processes (Rinaldo et al., 1991; Rinaldo et al., 2006a) gives key insights into the relative role of runoff generation processes and of the geomorphology of a catchment. This can also be achieved with virtual modelling experiments with hydrological models that explicitly account for geomorphological dispersion along the channel network. An example is

the work of Nicótina et al. (2008) who assessed the importance of well representing spatial rainfall variability for medium size catchments (a few hundreds to thousands km²) where saturation-excess overland flow dominates (rather than Hortonian flow). They conclude that for rainfall events with a spatial correlation length larger than the hillslope size, an exact representation of the spatial rainfall variability is not required to well represent the hydrologic response - provided that the mean areal rainfall is preserved at each time step. They explain this result by the fact that if the total catchment-scale residence time is controlled by the travel time within the hillslopes, large enough rainfall events sample all possible residence times, independent of the actual spatial rainfall configuration. Their findings were subsequently confirmed by the work of Volpi et al., (2012) amongst others, where a simplified modelling approach based on a geomorphological unit hydrograph was used. While the conclusions were similar, this study also added that spatial variability does not matter “when the integral scale of the excess-rainfall field is much smaller or much larger than the basin drainage area”.

Similar results were obtained in studies that assess the impact of undersampling or of coarse graining an observed rainfall field on the performance of streamflow simulations obtained with more or less complex process-based hydrologic models (Bardossy and Das, 2008; Moulin et al., 2009; Lobligeois et al., 2014; Shah et al., 1996; St-Hilaire et al., 2003; Stisen and Sandholt, 2010; Xu et al., 2013). A key result of these model-based studies is that the hydrologic response depends more on the accurate estimate of the mean areal rainfall than on the actual exact form of the rainfall field, (Obled et al., 1994). However, such model-based studies face the challenge that conceptual hydrological models require recalibration when used with different input fields, which makes disentangling effects from rainfall versus parameters a cumbersome exercise (Bardossy and Das, 2008; Bell and Moore, 2000; Stisen and Sandholt, 2010).

The above hypothesis that the mean areal rainfall might play a more important role for the streamflow response than the actual spatial rainfall pattern is largely based on modelling experiments and remains to be tested in the field. In this paper, we therefore propose to investigate this hypothesis with a data-based framework to analyze the importance of rain gauge density for the event-specific hydrologic response (Ross et al., 2019) of a small, high elevation Alpine headwater catchment (13.4 km²) where the hydrologic processes have been intensely monitored since 2015. Studying such a small catchment has, in addition, the potential to shed new light on the often used assumption that for catchments smaller than a

few tens of km² a single rain gauge is sufficient for reliable runoff prediction. While our analysis focuses here on a small natural headwater catchment, it is noteworthy that the developed rainfall monitoring and data analysis framework might also be of interest for urban hydrology, which deals with similar questions regarding how spatial rainfall patterns, runoff generation processes and flow network geometry lead to peak flows in urban drainage systems (for a review, see the work of Cristiano et al., 2017).

To assess the number of point observations required to properly capture the hydrologic response of our target catchment, we set up a dense rain gauge network made of commercially available and low cost devices. These high-density rain gauge observations (approximately one rain gauge per km²) are then used to answer two key questions:

- i. Which spatial characteristics of the rainfall field explain the timing and the amplitude of the hydrologic response?
- ii. What is the required spatial design of the rain gauge network to capture these characteristics?

To answer these questions, we developed a methodological framework to analyze the rainfall events, the hydrological response, and ultimately the optimal rain gauge density. This framework can be summarized as follows: i) define appropriate metrics to describe the rainfall fields and the hydrological response, ii) understand the relationships between these metrics through correlation analysis, iii) identify the main drivers (i.e. the corresponding metrics) through regression analysis, and iv) use the gained insights to optimize the rain gauge network based on selected metrics. We conclude the analysis with an event-scale modelling of all recorded runoff response events with a semi-distributed model to evaluate the identified rain gauge network configuration.

The remainder of the paper is structured as follows. First, Section 5.2 presents the observational methods and the analysis framework. The results are presented in Section 5.3 and discussed in Section 5.4, with a focus on the impact of rainfall heterogeneity on the streamflow response. Section 5.5 summarizes the main conclusions.

The study area of this study is the Vallon de Nant and is described in detail in the Chapter 2 of this thesis. The Pluvimate drop-counting rain gauges have been described previously in the Chapter 4 (see Section 4.1.8).

5.2 Instruments and methods

5.2.1 Instruments

A network of 12 Pluvimate drop-counting rain gauges was distributed across the Vallon de Nant catchment from 30th June to 4th October 2017 and from July 1st to September 23rd, 2018 to monitor rainfall (see Figure 40 in Chapter 5). Data for the 2018 season are available on Zenodo (Michelon et al., 2020).

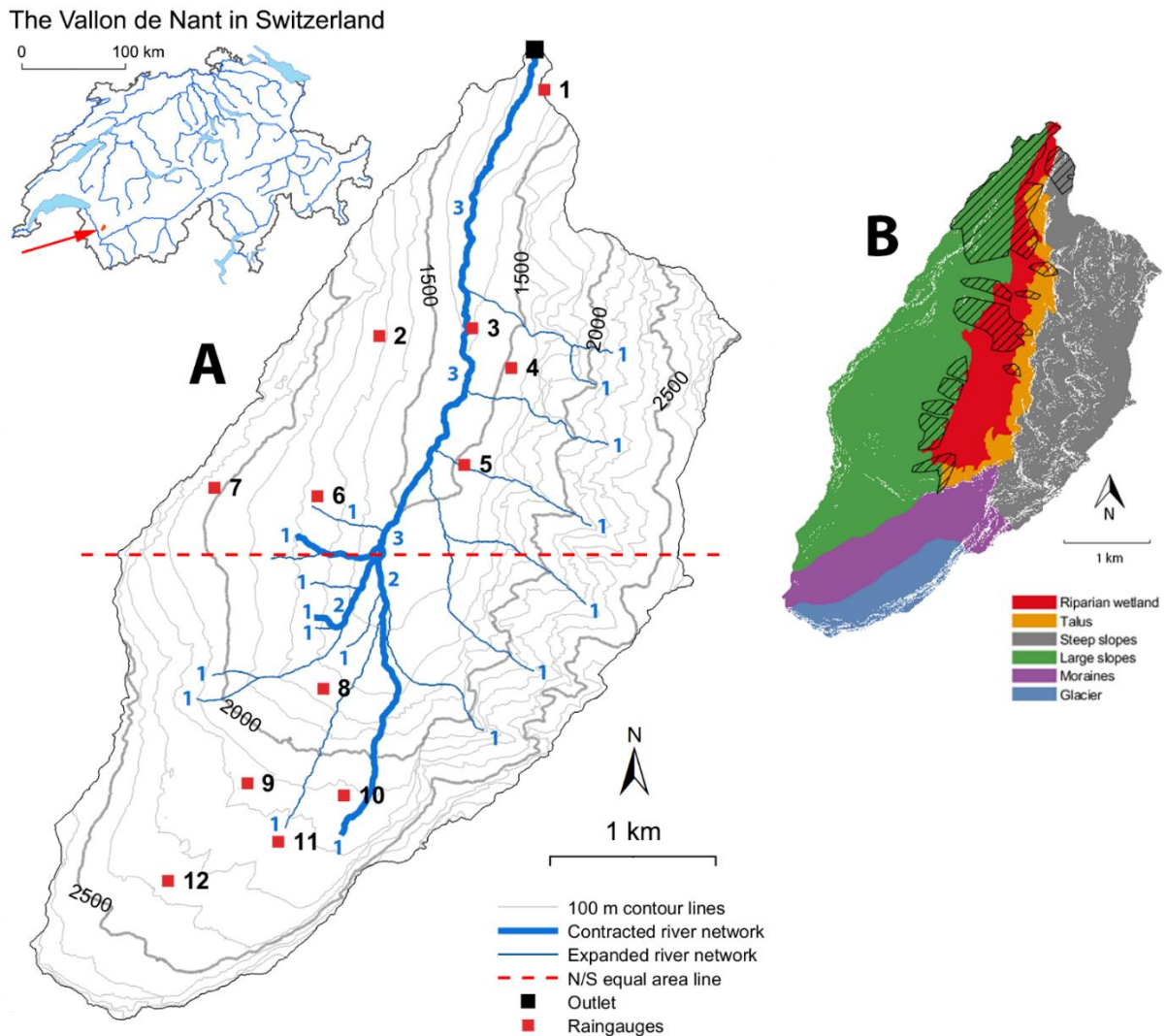


Figure 40. Map of the Vallon de Nant and location of the 12 rain gauges. The streamflow is measured on the main river at the outlet (46.25301 N / 7.10954 E in WGS84 coordinates). The red dashed line splits the catchment area into two parts of equal area. The small numbers next to the streams indicate the Strahler stream order (Strahler, 1957).

The sites were selected to represent the distribution of slope orientations and elevation, but also to meet constraints of accessibility and disturbance risk (livestock, hikers). The distance

between measurement locations within the network ranges from 350 m to 1,550 m (630 m on average), and the greatest distance from any point in the basin to a rain gauge is 1,670 m.

5.2.2 Rainfall event characterization

Event identification

Before further analysis, the rainfall amounts measured by each station were interpolated to a 10 by 10 m grid at a 2 min time step using a high-resolution stochastic approach developed by Benoit et al. (2018a). In a nutshell, it generates an ensemble of stochastic space-time rain fields constrained by the actual observations at the rain gauge locations. The resulting ensemble (here composed of 20 realizations) can be used to analyze spatial rainfall uncertainty or to construct a single rainfall estimator. Following Benoit et al. (2018a), a non-separable and asymmetric covariance function was used to perform the simulations, which allows modelling rainfall advection and diffusion observed in the raw data. Areal rainfall time series are calculated for each of the 20 realization, and from these a single time series (mean and standard deviation) of the areal rainfall.

Using the areal rainfall time series, the rainfall events are identified as periods with rainfall higher than 1 mm separated by at least 90 minutes with rainfall smaller than 1 mm. This duration of 90 minutes corresponds to the delay between the rainfall onset and the streamflow response for the large event recorded on August 23rd (for details see Supplementary Material), which occurred during an otherwise dry period. The streamflow response to the first half-hour of this rainfall event was caused only by rainfall in the southern half of the catchment (stations 8 to 12), corresponding thereby to the most distant event (from the outlet). Accordingly, we assume that this event gives a rough estimate of the catchment's response time (Beven, 2020) i.e. of the time required until the entire catchment contributes to the streamflow response, including the delay caused by runoff transfer to the stream network and from there to the outlet from the hydrologically most distant parts of the catchment. The 90 minutes were therefore selected to maximize the chances of observing a distinct streamflow response for two distinct consecutive rainfall events.

Spatial rainfall pattern metrics

Spatial rainfall patterns are classically characterized with geostatistical tools, including variograms (Berne et al., 2004) or with spatial moments of rainfall (Smith et al., 2002; Zoccatelli et al., 2011; Mei et al., 2014), in particular in presence of observed rainfall fields,

e.g. from radar images. Here we propose to use more hydrological-process oriented metrics that explicitly account for known features of the catchment and the stream network.

To build a first such metric, the catchment is split into two parts of equal area by a west-east line (Figure 40a), delimiting an area close to the outlet in the northern part, and an area farther away in the southern part. This heuristic splitting into two parts is interesting here due to i) the elongated catchment shape and furthermore ii) the clearly distinct stream network organisation in the upper (southern) part of the catchment with more branching than in the northern part (reflected in the Strahler stream order that does not further increase in the northern part, see Figure 1a). Accordingly, we assume the rainfall events falling exclusively on one or the other part of the catchment lead to a distinct streamflow response, with a faster and stronger response for events falling on the northern part (closer to outlet, steeper hillslopes, less storage potential than for the southern part).

The interpolated amounts of rainfall received by the southern and northern parts of the catchment, P_{NORTH} and P_{SOUTH} , are compared and normalized by the total amount of rainfall to create an index of spatial rainfall asymmetry I_{ASYM} :

$$I_{ASYM} = \frac{P_{SOUTH} - P_{NORTH}}{(P_{SOUTH} + P_{NORTH})}, \quad (13)$$

If rainfall is equally distributed between the northern and the southern parts, then $I_{ASYM} = 0$. The extreme values -1 and 1 express rainfall concentration exclusively in the northern or the southern part of the catchment, respectively. A value over -0.33 or 0.33 indicates that the catchment received at least 2 times more rain over one part of the catchment than the other.

To further analyze the relationships between the spatial distribution of rainfall and the streamflow response, we characterize the geomorphological distance of incoming rainfall from the outlet, assuming that this distance should reflect to some degree the timing and the shape of the streamflow response of the catchment: following the terminology of Rinaldo et al. (2006b), transport at the basin scale can be analyzed in terms of travel in the unchannelled state (i.e. in the hillslopes) and travel in the channelled state (i.e. in the stream network).

Accordingly, we estimate for each rainfall event the weighted mean unchannelled distance to the stream network as:

$$D_{HILLS} = \frac{1}{t} \sum_t \frac{\sum_i \sum_j (P(i,j,t) d_{HILLS}(i,j))}{\sum_i \sum_j P(i,j,t)}, \quad (14)$$

where i and j are the coordinates of rainfall location within the grid, $P(i,j,t)$ is the rainfall amount previously calculated using the stochastic method for each of the 10 x 10 meters grid cell at each 2-minute time step t , and $d_{HILLS}(i,j)$ is the distance of this grid cell to the nearest stream network grid cell (following the line of steepest descent in the 2 x 2 m DEM (swissAlti3D, 2012a)).

Similarly, we compute the weighted mean channelled distance between a point of introduction into the stream network and the outlet as:

$$D_{STREAM} = \frac{1}{t} \sum_t \frac{\sum_i \sum_j (P(i,j,t) d_{STREAM}(i,j))}{\sum_i \sum_j P(i,j,t)}, \quad (15)$$

where $d_{STREAM}(i,j)$ is the distance along the stream network from the point of introduction to the outlet. For each cell of the stream network, this distance is calculated once based on the 2 x 2 m DEM.

It is noteworthy that these two metrics, D_{HILLS} and D_{STREAM} correspond to the aforementioned first order spatial rainfall moments, albeit decomposed according to hillslope and stream network distances, similar to what was proposed by Zoccatelli et al. (2015) in their analytical framework to quantify the smoothing of spatial rainfall organisation effects by channel residence time. It would be tempting to use also higher order rainfall moments; however, no significant correlation could be found to retain the streamflow metrics.

In addition to the above two metrics related to the theory of geomorphological dispersion (Rinaldo et al., 2006b), we use the height above the nearest drainage (H_{HAND}) terrain metric (Renno et al., 2008; Gharari et al., 2011; Nobre et al., 2011) to account for the topography. Based on the 2 x 2 m DEM, the normalized terrain heights h_{HAND} are calculated by comparing the elevation of each grid cell to the elevation of the nearest stream network cell in which the water is routed. The mean H_{HAND} value for a rainfall event is given by:

$$H_{HAND} = \frac{1}{t} \sum_t \frac{\sum_i \sum_j (P(i,j,t) h_{HAND}(i,j))}{\sum_i \sum_j P(i,j,t)}. \quad (16)$$

The 3 distance metrics are computed with respect to both the dry and wet river network extent; the network extent to be used per rainfall event is then determined during the rainfall-streamflow response analysis (see Section 5.2.4).

5.2.3 Streamflow response

Identification of streamflow events and fast runoff

The beginning and the end of each streamflow event are identified manually using a data visualization tool (developed in MathWorks MatLab 2017a, see Figure 41 and Figure 42). This choice of a visual expertise was made based on the observation that automatic identification of streamflow events would require almost a case-by-case filtering and parametrization, and thus would not be generalizable. This is partly related to a potentially high signal-to-noise ratio for river stage recordings during sediment transport events, a phenomenon potentially very important after a strong streamflow variation. The result of this visual identification for each streamflow event is displayed in Supplementary Material.

The beginning and the end of the streamflow response determine the initial and final baseflow; the streamflow volume above the straight line connecting these two points is considered here as fast runoff. It is noteworthy that we do not use peak streamflow to characterize streamflow events, for two reasons: i) given the small size of the catchment and the complex temporal distribution of rain intensities, the streamflow response has rarely a single, well identifiable peak (all events are plotted in Figure S5 in Supplementary Material); ii) peak streamflow identification is further complicated by the noise in the stage recordings.

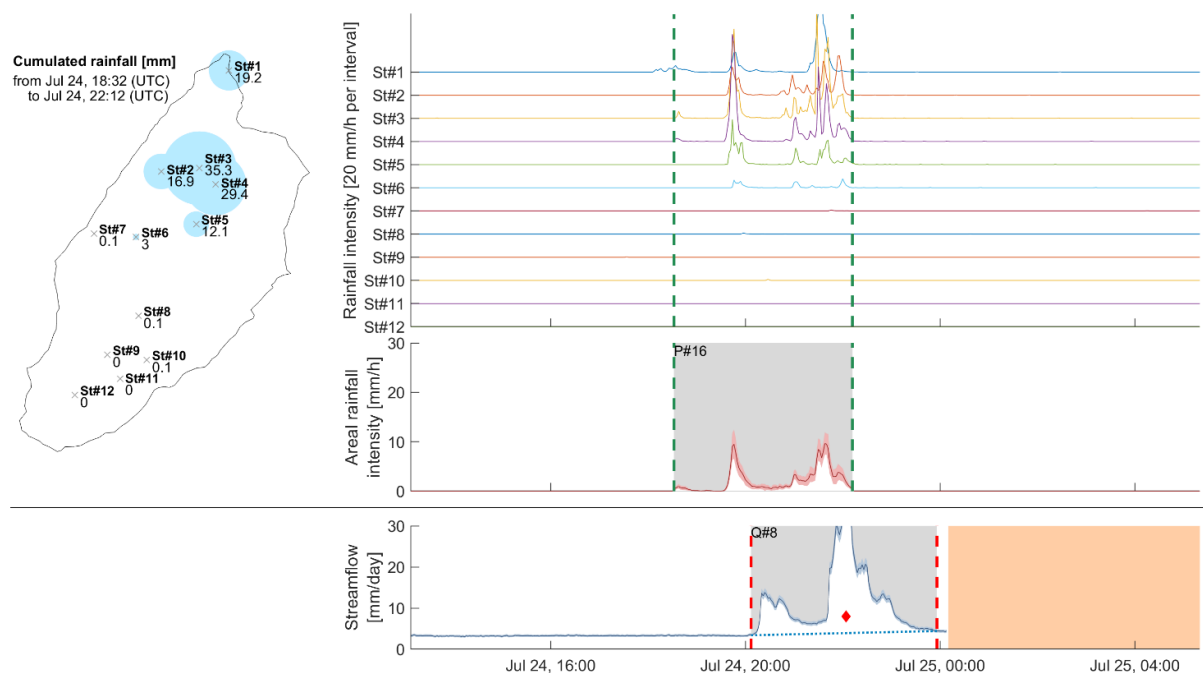


Figure 41. Summary of the recorded rainfall and streamflow for the rainfall event of July 24th 2018 at 6:32 PM (UTC).

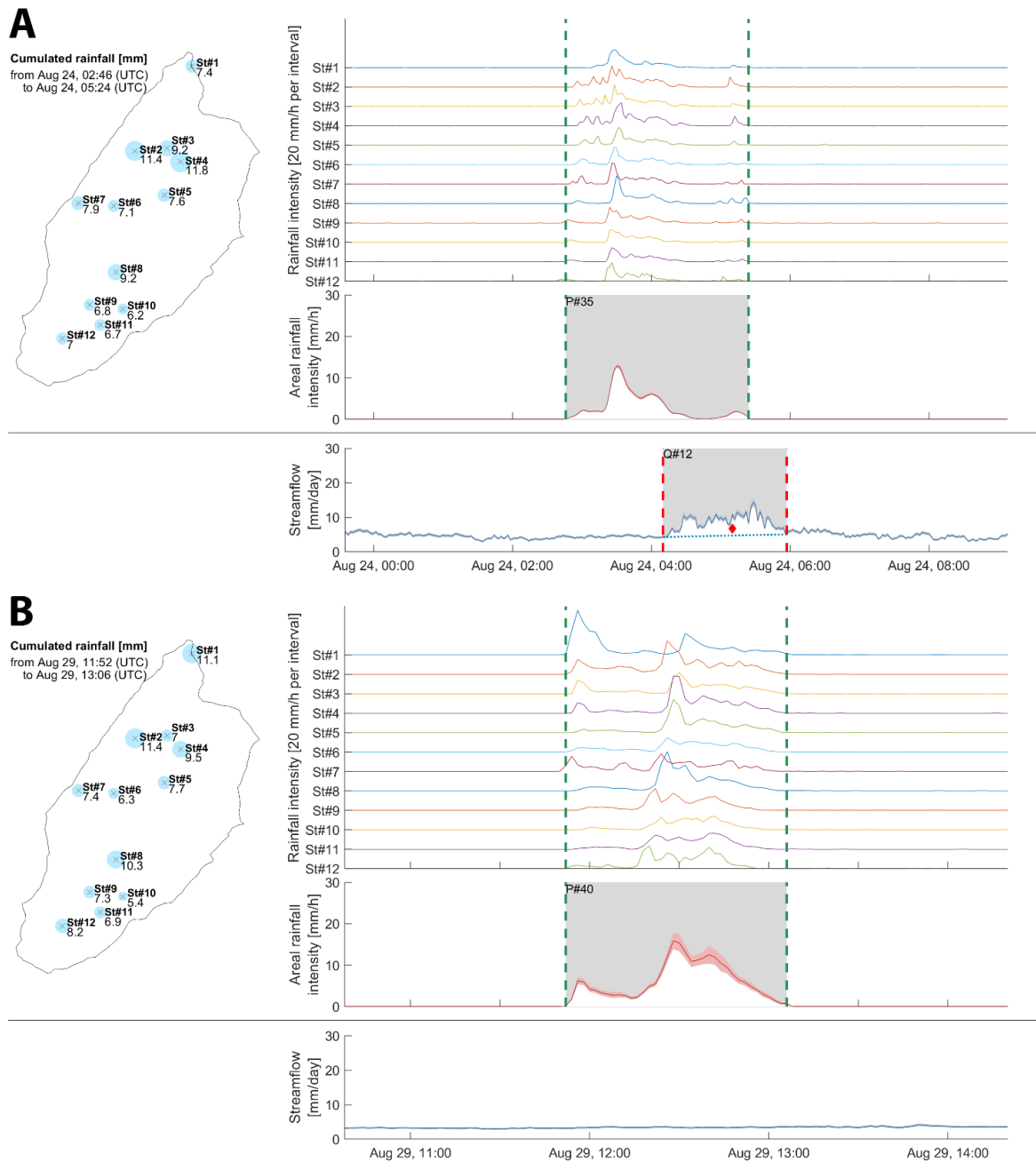


Figure 42. Summary of the recorded rainfall and streamflow for the rainfall events of August 24th 2018 at 2:46 AM (top) and August 29th 2018 at 11:52 AM (bottom).

Streamflow metrics

The key metrics to characterize the streamflow response are the peak flow, the fast streamflow volume, the lag time elapsed between rainfall and streamflow response, and the flatting behaviour. For technical reasons we discarded the peak flow (see Section 5.2.1) and consequently the flatting behaviour. We use the fast streamflow volume through the runoff coefficient (RC), which is obtained by dividing the fast runoff volume by the total rainfall for the given event.

The lag time is usually defined as the elapsed time between the start of excess rainfall (the part of rainfall that causes the streamflow response) and the peak flow (McCuen, 2009). Since the start of excess rainfall is not known, the concept of peak flow is difficult to apply to our observed events (Section 3.3.1) and given the varying shape of our hydrographs, we empirically tested different lag formulations; the lag between 1/3 of the rainfall event volume and 1/3 of the streamflow event volume gives the best results in the regression analysis, and is therefore retained. It is noted $\Delta_{P/Q}$ in the following.

5.2.4 Rainfall-streamflow response characterization

Pseudo-dynamic stream network extent

The extent of the stream network evolves as a function of the catchment wetness conditions. Its minimal and maximal extent (Figure 40a) are determined manually by identifying the uppermost points of the catchment where streamflow was observed in the field during summer baseflow (minimum extent, called *dry state*) and during summer high flow (maximum extent, called *wet state*).

In absence of exact observations of the stream network extent before the start of each streamflow event, we propose here to use a pseudo-dynamic stream network extent which assigns the dry or the wet state to each streamflow. The network state is chosen based on a measure of the initial catchment wetness conditions, which is known to be the major variable explaining the dynamics of the hydrological response to different rainfall events (Penna et al., 2011; Rodriguez-Blanco et al., 2012), in particular through the creation of runoff thresholds (Zehe et al., 2005; Tromp-van Meerveld and McDonnell, 2006) Many studies use the baseflow before the start of a streamflow event as an indicator for the antecedent wetness conditions of the catchment. For snow-influenced catchments with a highly seasonal streamflow regime, this indicator might not reflect the actual wetness conditions. Hence, we rather quantify initial wetness conditions in terms of antecedent rainfall, i.e. using the cumulative rainfall (in mm) that occurred during a period from 1 to 5 days before a given rainfall event. The actual time span is selected based on a correlation analysis between antecedent rainfall over 1 to 5 days and the retained streamflow metrics (Section 5.3.2).

This correlation analysis yields an optimum antecedent wetness indicator corresponding to the rainfall over the 3 days preceding the start of a rainfall event, noted $W_{3\text{days}}$. Using this indicator, the pseudo-dynamic network extent is obtained by assigning the dry network state to rainfall events that have $W_{3\text{days}} < 20$ mm and the wet network state to rainfall events that

show $W_{3\text{days}} \geq 20$ mm. This threshold of 20 mm is selected by maximizing the correlation coefficient between D_{HILLS} and RC (see Section 5.3.2).

Regression analysis

We analyze the relationships between the spatial distribution of rainfall and the hydrological response based on a correlation analysis between the spatial rainfall pattern metrics (Section 5.2.2) and the streamflow metrics (Section 5.2.3) at the event scale, followed by a regression analysis to identify the key variables that best explain the runoff coefficient, RC, and the streamflow lag time, $\Delta_{P/Q}$. All used metrics are summarized in Table 10.

Table 10. List of used metrics, with corresponding parameter name or abbreviation.

Description	Notation, Unit
Rainfall interpolated over entire catchment	P_{ALL} , mm
Rainfall interpolated over north half of catchment	P_{NORTH} , mm
Rainfall interpolated over south half of catchment	P_{SOUTH} , mm
Rainfall event duration	P_{DURATION} , min
Maximum rainfall intensity over the event, $i = \{\text{ALL}, \text{NORTH}, \text{SOUTH}\}$	$P_{\text{max } i}$, mm
Index of spatial asymmetry of rainfall	I_{ASYM} , -
Distance of rainfall spatial center of mass to stream network (along hillslopes)	D_{HILLS} , m
Distance of rainfall spatial center of mass to outlet along the stream network	D_{STREAM} , m
Mean height above the nearest drainage	H_{HAND} , m
Cumulated amount of rainfall for the last X days	$W_{X \text{ days}}$, mm
Streamflow at the start of the streamflow event	Q_{INIT} , mm
Fast streamflow amount	Q_{FAST} , mm
Streamflow response event duration	Q_{DURATION} , min
Rainfall runoff coefficient	RC, -
Lag time between 1/3 of cumulated rainfall and 1/3 of cumulated fast streamflow	$\Delta_{P/Q}$, min

After the initial screening via correlation analysis, we use a pure quadratic regression to further investigate which combination of rainfall pattern metrics and initial wetness condition yields the best prediction of RC and $\Delta_{P/Q}$. Pure quadratic regression (i.e. without multiplication of explanatory variables) is chosen because the small number of observed streamflow events prevents using more complex models. Model selection is performed using the Akaike Information Criterion (AIC)(Akaike, 1974), noted here as I_{AIC} :

$$I_{\text{AIC}} = n \ln \left(\frac{S_{\text{RSS}}}{n} \right) + 2k + C, \quad (17)$$

where n is the number of events, k the number of coefficients, S_{RSS} the residual sum of squares and C a constant that can be ignored when comparing different models based on the same

data set. As we manage small sample sizes (Burnham et al., 2011), we compute and use a corrected version of the AIC (AICc, noted here I_{AICc}):

$$I_{AICc} = I_{AIC} + \frac{2k(k+1)}{n-k-1} \quad (18)$$

For both AIC and AICc, the best model is the one having the lowest score.

5.2.5 Raingauge network configuration analysis

Assuming that the actual rainfall measurement network is sufficient to capture the full spatial distribution of rainfall in the studied catchment, we assess the ability of partial networks to reproduce the identified best explanatory variables. The aim is twofold: i) identifying the best configuration for a future permanent observation network and ii) evaluate the added value of additional rain gauges in a partial network with respect to the identified key metrics (Section 5.3.4 and 5.4.2).

The quality of a partial network configuration is evaluated comparing the value (e.g. total rainfall) by event obtained with the partial network to the reference value obtained with the full network setup. We evaluate all the possible combinations of partial networks composed of less than 12 stations, i.e. 4094 possibilities. Each configuration is evaluated based on the root mean square error (RMSE):

$$RSME := \sqrt{\sum_{t=1}^n \frac{(X_k(t) - X_{ref}(t))^2}{N}}, \quad (19)$$

where X_k is the selected rainfall metric (e.g. rainfall amount) at time step t corresponding to the k -th network configuration, X_{ref} the respective value obtained reference network set-up, and N the number of time steps. The rainfall amounts measured by each station were interpolated to a 10 by 10 m grid at a 2 min time step using the Thiessen polygons method. The interpolation method developed by Benoit et al. (2018a) (see Section 5.2.2) cannot be used in this context because i) it requires at least 5 measuring points to perform adequately and ii) the computation time would be excessive to explore the 4094 combinations of stations for each event.

The best network for each number of stations is the one with the lowest RMSE. A sensitivity analysis is completed by removing from 1 to 3 rainfall events to the 23 events dataset, yielding 2047 datasets evaluated for each partial network configuration. The most frequent network configuration validates the robustness of the result.

5.2.6 Rainfall-runoff model

To further validate the obtained optimal rain gauge network configuration, we set up a semi-distributed, event-based rainfall-runoff model. This model first simulates the mobilization of water at the sub-catchment scale (25 sub-catchments) using a Soil Conservation Service Curve Number (SCS-CN) approach (SCS, 1972). Next, the streamflow response is obtained by convolving the resulting hillslope responses with a travel path distribution derived from the stream network geometry (Schaefli et al., 2014). The subcatchments and the stream network geometry are identified using *TopoToolbox* (<https://topotoolbox.wordpress.com>), in which travel paths correspond to the distance between the bottom part of each sub-catchment and the catchment outlet. In this model we focus on the fast response (i.e. runoff) of the catchment, and baseflow (defined here as the average discharge during the 30 min preceding event start) is subtracted from the actual discharge prior to runoff modeling. The model is calibrated against observed runoff (i.e. discharge - baseflow) through likelihood maximization assuming that the model residuals are normally distributed (e.g. Schaefli et al., 2007). The reference input field for model calibration is the mean of the 20 stochastic rainfall realizations at each time step (note since all realizations are conditioned on the observed precipitation events, this mean preserves the individual observed peaks of precipitation). After calibration the event-based runoff model is applied to the different network configurations to test how rain gauge network geometry influences the simulated runoff response. As the stochastic rainfall interpolation cannot be performed with a number of observation points as low as 3 stations (or less), we use the Thiessen polygons method to interpolate the rainfall fields from the 1 to 3-station rain gauge network obtained during optimal network analysis.

5.3 Results

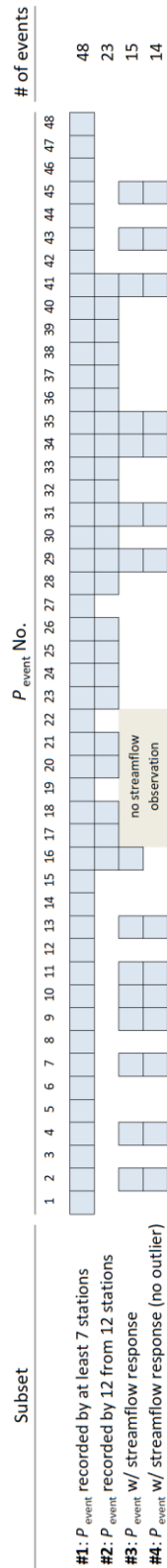
5.3.1 Rainfall events

Areal rainfall and asymmetry

The available 3-month measurements window between July 1st and September 23th 2018 captured 48 rain events (detailed in Supplementary Material) for a total areal rainfall amount of 318 mm. The areal rainfall amount per event ranges from 1 mm to 43.5 mm (mean of 6.6 mm), and event duration ranges from 32 minutes to 10.5 hours (mean of 2.8 hours); these records do not show any evidence of altitude effect on the rainfall amount ($R^2 = 0.06$). Despite the sequential deployment of the 12 rain gauges and other technical issues (see Section 5.2.1), the rainfall events were all measured by at least 7 stations; 36 out of 48 events were recorded

by at least 10 stations and 23 events were recorded by 12 stations. The different subsets used in this study are detailed in Table 11.

Table 11. Summary of the different subsets of rainfall events used within this study. The streamflow response outlier event discarded in subset #4 corresponds to July 24th 2018.



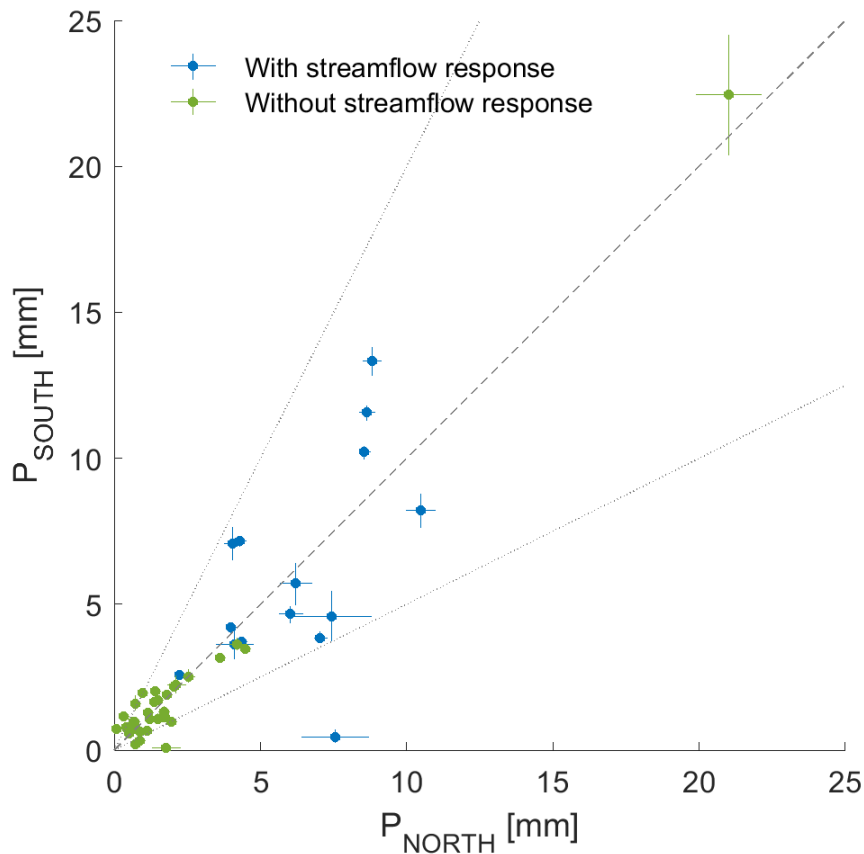


Figure 43. Scatterplot of the rainfall amounts over the northern and the southern parts of the catchment for all 48 rainfall events. The dotted lines show the 1/2 and 2/1 lines which correspond to twice more rainfall in one part of the catchment than in the other or to $|I_{ASYM}| > 0.33$. The highest event is an outlier (event of 6-Aug with 43.5 mm of rainfall in total) and is flagged without streamflow response because the river stage measure was disturbed during this period.

Details for all recorded rainfall events and the corresponding streamflow are shown in summary plots, as illustrated in Figure 41 and Figure 42. Most events show a relatively homogeneous spatial distribution of rainfall (see an example in Figure 42), with only few events showing a strong asymmetry (Figure 43): the correlation between P_{NORTH} and P_{SOUTH} equals 0.91, with a median I_{ASYM} of 0.025. Interestingly, strong spatial asymmetry mainly affects events with low rainfall amounts, with 7 out of 8 events with $|I_{ASYM}| > 0.33$ receiving below 5 mm (Figure 43). For the events that actually triggered a streamflow response, the correlation between P_{NORTH} and P_{SOUTH} is thus significantly higher ($r=0.69$, Table 12).

Table 12. Correlations between rainfall metrics and hydrologic response metrics for event series #4 of Table 2. Absolute values equal or higher than 0.60 are in bold.

	P_{ALL} [mm]	P_{NORTH} [mm]	P_{SOUTH} [mm]	$P_{max\ ALL}$ [mm.h ⁻¹]	$P_{max\ NORTH}$ [mm.h ⁻¹]	$P_{max\ SOUTH}$ [mm.h ⁻¹]	I_{ASYM} [-]	$W_{3\ days}$ [mm]	Q_{UNIT} [mm]	Q_{FAST} [mm]	$P_{DURATION}$ [min]	$Q_{DURATION}$ [min]	$\Delta P/Q$ [min]
P_{ALL} [mm]	-												
P_{NORTH} [mm]	0.89	-											
P_{SOUTH} [mm]	0.94	0.69	-										
$P_{max\ ALL}$ [mm.h ⁻¹]	0.01	0.19	-0.12	-									
$P_{max\ NORTH}$ [mm.h ⁻¹]	0.09	0.33	-0.11	0.96	-								
$P_{max\ SOUTH}$ [mm.h ⁻¹]	0.19	0.19	0.16	0.87	0.78	-							
I_{ASYM} [-]	0.25	-0.20	0.55	-0.42	-0.56	-0.06	-						
$W_{3\ days}$ [mm]	-0.19	-0.30	-0.09	-0.22	-0.27	-0.23	0.18	-					
Q_{UNIT} [mm]	-0.13	0.00	-0.21	0.52	0.54	0.27	-0.28	0.26	-				
Q_{FAST} [mm]	0.77	0.58	0.80	-0.17	-0.16	-0.08	0.43	0.33	-0.01	-			
$P_{DURATION}$ [min]	0.56	0.38	0.62	-0.59	-0.52	-0.48	0.44	0.14	-0.43	0.74	-		
$Q_{DURATION}$ [min]	0.56	0.39	0.61	-0.27	-0.27	-0.17	0.42	0.52	0.11	0.89	0.64	-	
$\Delta P/Q$ [min]	0.13	-0.11	0.29	-0.71	-0.71	-0.58	0.59	0.41	-0.33	0.52	0.81	0.60	-
RC [-]	0.31	0.13	0.40	-0.25	-0.29	-0.22	0.44	0.65	-0.05	0.81	0.67	0.80	0.72

One strong asymmetric and very intense event occurred on July 24th at 6:32 PM (Figure 41). The rainfall map shows a heterogeneous distribution of rainfall, centered close to the outlet in the northern part of the catchment, over 6 out of the 12 stations. One of the rain gauges recorded up to 35.3 mm of rainfall, whereas 1.8 km upstream, half of the stations (on the southern and western parts of the catchment) did not record any rainfall. The interpolated amount of rainfall over the basin was 8.0 ± 1.3 mm, and a fast runoff volume between 28.3 and 32.5 mm was measured, resulting in a runoff coefficient between 3.0 and 4.8 that remains difficult to explain. One possible explanation is that important rainfall amounts fell on the north-eastern part of the catchment, over steep slopes that are difficult to access and were therefore not gauged. This event and its streamflow response are excluded from further analysis involving the hydrological response (see also Section 5.3.2 and the summary of analysed events in Table 11).

Geomorphological and topographical distance metrics

For the 48 recorded rainfall events, the three distance metrics D_{HILLS} , D_{STREAM} and H_{HAND} show significantly different median values if they are computed with respect to the wet network than with respect to the dry network; we can reject for each metric the hypothesis that they have the same median value for the wet state and the dry state with a Wilcoxon rank sum test at level 0.05 (see distributions in Figures S6 and S7 in Supplementary Material). However, each of the distance metrics shows a strong correlation between its values for the wet and for the dry network state (from 0.94 for H_{HAND} to 1.00 for D_{STREAM} , Figure 44).

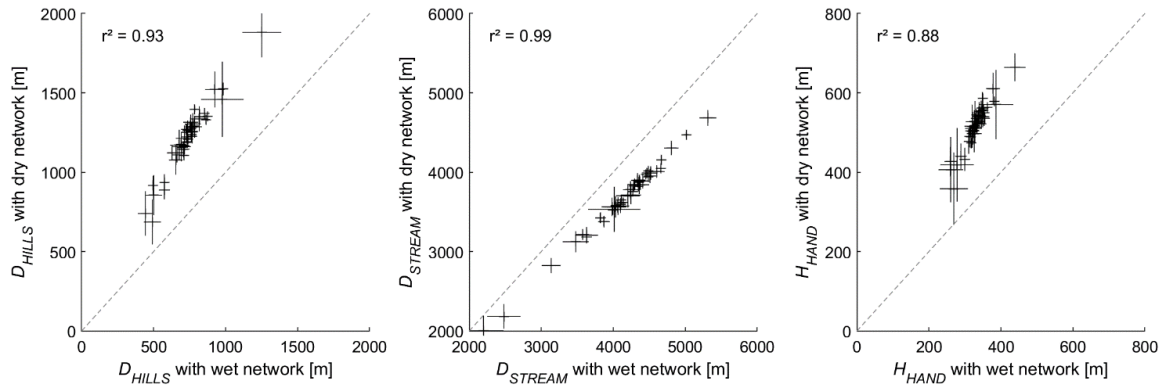


Figure 44. Scatterplots of the distance metrics for the dry network state versus the wet state, for all 48 rainfall events. The bars indicate the standard deviation obtained from the 20 rainfall field realisations. r^2 indicates the linear correlation.

The between-metric correlation for all 48 rainfall events (Supplementary Material, Table S2) ranges for the wet state range from 0.78 ($D_{HILLS} - D_{STREAM}$) to 0.95 ($D_{HILLS} - H_{HAND}$) and for the dry state from 0.70 ($D_{STREAM} - H_{HAND}$) to 0.95 ($D_{HILLS} - H_{HAND}$). Considering only the rainfall events with streamflow response, these correlations are slightly lower (Table 3), but with a clear correlation between D_{HILLS} and H_{HAND} for both the wet and the dry state; accordingly, we do not further use the H_{HAND} metric in this analysis. None of the distance metrics shows a strong correlation (>0.6) with the rainfall spatial distribution metrics, i.e. P_{SOUTH} , P_{NORTH} or I_{ASYM} . They also do not show any correlation higher than 0.6 with the hydrologic response metrics (Table 12). This confirms our hypothesis that the network state needs to be included in a dynamic way (see Section 5.3.2).

Temporal evolution of rainfall metrics

We computed the temporal evolution of the rainfall metrics to unravel potential temporal evolution patterns in I_{ASYM} , D_{HILLS} and D_{STREAM} and their relation to the streamflow response (respectively in Figures S12, S13 and S14 in Supplementary Material). The temporal evolution of the two distance metrics is overall rather flat with no clear fluctuation. There is only one event with a pronounced temporal trend for D_{HILLS} (Q event #1).

For I_{ASYM} , some events show interesting temporal patterns. For example, during the double peak runoff of Figure 41, I_{ASYM} shows an almost constant negative value suggesting that the corresponding double peak rainfall event remained stationary on the northern part of the catchment over its entire duration and therefore caused the double peak streamflow response.

For the first two streamflow events, the I_{ASYM} metric switches from strongly positive to close to zero during the event, implying that the rainfall field moved towards the outlet during the event; in other words, the rainfall cloud follows the overall water movement through the catchment and thereby leads to a stream response concentration. This might explain why these two events are the only ones that show a pronounced single peak streamflow response. However, given the low number of observed events and the diversity of temporal patterns, these insights cannot be further used for a quantitative analysis.

5.3.2 Hydrologic response

Observed streamflow events

For 13 days (6 of the 48 rainfall events), the water stage sensor was disturbed by the proximity of a rock (see Figure 12 F in Chapter 3), resulting in missing streamflow data. For the remaining 42 rainfall events, a streamflow response was observed for 15 of them (see Table 11, Table 12 and Table 13).

Table 13. List of recorded precipitation events with streamflow response (event series #3 of Table 2). Full details are available in Michelin et al. (2021a).

Date	$P_{DURATION}$ [min]	$Q_{DURATION}$ [min]	$\Delta P/Q$ [min]	P_{ALL} [mm]	P_{NORTH} [mm]	P_{SOUTH} [mm]	P_{NORTH}/P_{ALL} [-]	P_{SOUTH}/P_{ALL} [-]	I_{ASYM} [-]	$W_{3\text{ days}}$ [mm]	Stream network	Q_{INIT} [mm]	Q_{FAST} [mm]	RC [-]	D_{HILLS} [m]	D_{STREAM} [m]	H_{HAND} [m]
2-Jul	42	44	24	7.7	4.1	3.6	0.53	0.47	-0.06	3.2	dry	7.9	0.9	0.12	1521	4008	611
3-Jul	40	135	23	12.1	7.4	4.6	0.62	0.38	-0.24	12.7	dry	7.5	8.5	0.71	1336	3842	550
5-Jul	224	309	71	8.2	4.0	4.2	0.49	0.51	0.03	29.8	wet	6.0	6.0	0.74	755	4374	350
6-Jul	478	587	65	20.2	8.6	11.6	0.43	0.57	0.15	40.3	wet	5.8	25.9	1.29	874	4450	355
14-Jul	358	302	49	18.7	10.5	8.2	0.56	0.44	-0.12	0.0	dry	4.5	12.9	0.69	1263	3574	554
15-Jul	136	281	33	10.7	6.0	4.7	0.56	0.44	-0.13	18.9	dry	5.5	9.5	0.89	1122	3377	528
20-Jul	288	228	49	18.8	8.6	10.2	0.46	0.54	0.09	3.4	dry	4.8	14.2	0.76	1282	3823	541
24-Jul	220	229	45	8.0	7.5	0.5	0.94	0.06	0.02	12.2	dry	3.1	30.4	3.78	740	2184	419
14-Aug	204	152	47	11.1	4	7.1	0.37	0.64	0.27	10.2	dry	4.0	7.8	0.70	1286	4305	540
17-Aug	152	109	38	11.9	6.2	5.7	0.52	0.48	-0.04	17.5	dry	3.2	4.9	0.42	1122	3780	490
23-Aug	388	237	47	22.1	8.8	13.3	0.40	0.60	0.20	5.4	dry	2.4	13.5	0.61	1371	3756	563
24-Aug	158	107	40	8.1	4.4	3.7	0.54	0.46	-0.08	29.5	wet	4.1	6.5	0.81	692	4114	320
29-Aug	72	116	48	4.8	2.2	2.6	0.46	0.54	0.07	12.4	dry	3.0	2.3	0.48	1207	3526	524
01-sept	628	341	101	11.4	4.3	7.2	0.38	0.63	0.25	20.4	wet	3.4	16.4	1.44	725	4487	331
13-sept	370	59	45	10.9	7.0	3.8	0.65	0.35	-0.29	0.0	dry	2.6	4.4	0.40	1291	3594	556

The fast streamflow volume during these events, Q_{FAST} , shows a strong correlation with total rainfall and with P_{SOUTH} (Figure 45); however, the event on July 24th with only 8.0 mm of rain and 30.4 mm of fast streamflow falls far away from this relationship, which further motivated the exclusion of this event from the analysis.

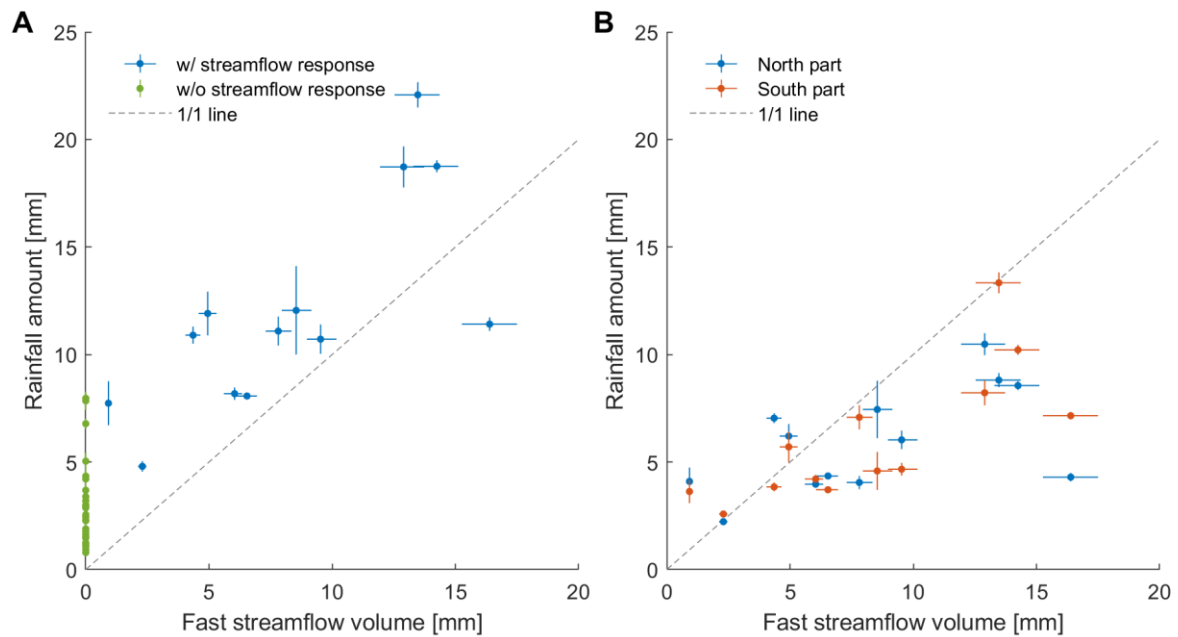


Figure 45. Scatterplots of A) total rainfall amounts versus fast streamflow (highlighting the threshold for streamflow response) and B) of rainfall amounts in the northern and the southern part against fast streamflow (for separation line, see Figure 40a). The bars show the standard deviation of estimated rainfall (Section 5.2.2) and of streamflow. The events of July 24th ($P_{ALL}=8.0$ mm, $Q_{FAST} = 30.4$ mm) and of Aug 6th ($P_{ALL}=43.5$ mm, Q not recorded) are out of the axes in A and in B.

The 14 remaining events are distributed over the entire observation period, covering a wide range of streamflow conditions, which is reflected in the initial streamflow before each event, ranging from 7.9 mm in early July to 2.6 mm by mid-September (Table 13), with an almost linear decrease between the dates (correlation between initial streamflow and day of the year of -0.90, see also Figure S4 in Supplementary Material).

The correlation of this initial flow before events with Q_{FAST} or with the runoff coefficient RC is extremely low (correlation of -0.02 and -0.05), which confirms our hypothesis that antecedent streamflow is not a good proxy for antecedent moisture.

The highest correlation between RC and antecedent precipitation occurs for a time span of 3 days preceding the streamflow event (0.67); this metric, called $W_{3 \text{ days}}$, is thus retained as a proxy for antecedent moisture for further analysis. The role of initial wetness conditions can also be discussed more qualitatively by comparing a pair of rainfall events with very similar spatial patterns and amounts (Figure 42). For the first event (August 24th), the measured rainfall ranges from 6.2 mm to 11.8 mm, corresponding to 8.5 mm of rainfall over the catchment in 2 h 38 min. For the second event (August 29th), the rainfall ranged between 5.4 mm and 11.4 mm, corresponding to 8.4 mm over the catchment during 1 h 14 min. Despite

the similar total amount of rainfall and event duration (during the first event 76 % of the total rain happened for a duration similar to the second event), the first event shows a fast runoff volume of 7.4 mm, whereas for the second event the streamflow response is almost invisible. This difference can be explained by the initial wetness conditions, with 29.5 mm of rainfall during the 3 days preceding the first event, compared to 12.4 mm for the second event.

Streamflow generation processes, RC and lag

The correlation analysis (Table 12) reveals a strong correlation between rainfall amounts and Q_{FAST} (0.77, Table 12). This suggests that streamflow responses are triggered by saturation-excess, rather than by infiltration capacity-excess: If saturation is exceeded, every unit of rainfall leads to a corresponding unit increase of streamflow, which in turn leads to a strong linear correlation between rainfall amounts and fast streamflow volumes. Furthermore, saturation-excess also implies that a longer rainfall event leads to a higher streamflow response volume (once the saturation threshold is reached, all rainfall contributes to streamflow). This is confirmed by the high correlation (0.74) between the rainfall duration $P_{DURATION}$ and Q_{FAST} . If, on the contrary, the driving process was the exceedance of the soil infiltration capacity, then only rainfall intensities above the capacity threshold would trigger a corresponding streamflow increase; small rainfall amounts would trigger almost no response. In this case (infiltration-excess), there would be no linear correlation between rainfall amounts or rainfall duration and streamflow amounts, but a strong correlation between fast streamflow amounts and high or maximum precipitation intensity; positive correlations between Q_{FAST} and $P_{max ALL}$, $P_{max NORTH}$ or $P_{max SOUTH}$ are however all absent (values of -0.17, -0.16 and -0.08, Table 12). In addition, saturation-excess as a main driver of the fast streamflow response is further confirmed by the clear threshold effect for the generation of streamflow as a function of total event rainfall (Figure 45a); a streamflow response only occurs for total rainfall higher than 5 mm

This threshold effect supports the formulation of the lag time $\Delta_{P/Q}$ as the time between one third of the rainfall event volume and one third of the streamflow event volume, since a lag time between the starts of the events would here be misleading. Accordingly, the streamflow events show a relatively strong correlation (0.71, Table 12) between the RC and the lag $\Delta_{P/Q}$: we observe a higher RC when the level of saturation increases; reaching such a higher level of saturation requires more time, which results in a longer lag before a significant amount of streamflow reaches the outlet.

We furthermore find a positive correlation between I_{ASYM} and the lag $\Delta_{P/Q}$ (0.59, Table 12), which supports our initial assumption that negative I_{ASYM} values (corresponding to rainfall concentrated on the northern part, close to the outlet) correspond to low lag times. However, the assumed negative correlation between RC and I_{ASYM} (higher RC values for rainfall events with negative I_{ASYM} values) is not confirmed by the observed data (the correlation is 0.44, Table 12), thereby not confirming our hypothesis that rainfall on the northern catchment part (showing less water storage potential) leads to more fast streamflow.

However, there is also a strong negative correlation between $\Delta_{P/Q}$ and the maximum rainfall intensity over 10 minutes, which is stronger for $P_{max\ NORTH}$ (-0.71, Table 12) than for $P_{max\ SOUTH}$ (-0.58). This probably reflects the fact that in the northern part of the catchment, there is a lack of soil storage capacity due to the large rock walls on the right stream side, which is not compensated by the available soil storage on the left stream side, with ensuing Hortonian (infiltration-excess) streamflow generation processes becoming more important in the northern part than in the southern part of the catchment. This significant difference in streamflow generation processes is also visible in the drainage density, which is higher on the right stream side in the northern part than on the left stream side (Figure 40a).

Dynamic stream network state

As discussed in 4.1.2, the rainfall distance metrics if computed with respect to the dry or the wet stream network state show very low correlations with the streamflow metrics. Accordingly, we attribute either the dry or the wet network state to each streamflow event as a function of the antecedent wetness $W_{3\ days}$, which is used as a measure for the stream network expansion. In the following, we call these new distance metrics “pseudo-dynamic” since only two different states are observed. Setting a $W_{3\ days}$ threshold to 20 mm to discriminate between the dry and the wet state yields correlations between D_{HILLS} – pseudo-dynamic and RC of -0.70 (Figure 46) and between D_{HILLS} – pseudo-dynamic and $\Delta_{P/Q}$ of -0.66 (Table 14). D_{STREAM} – pseudo-dynamic shows correlations of 0.53 and 0.60 with the RC and with the $\Delta_{P/Q}$, and we retain both pseudo-dynamic distances for further analysis.

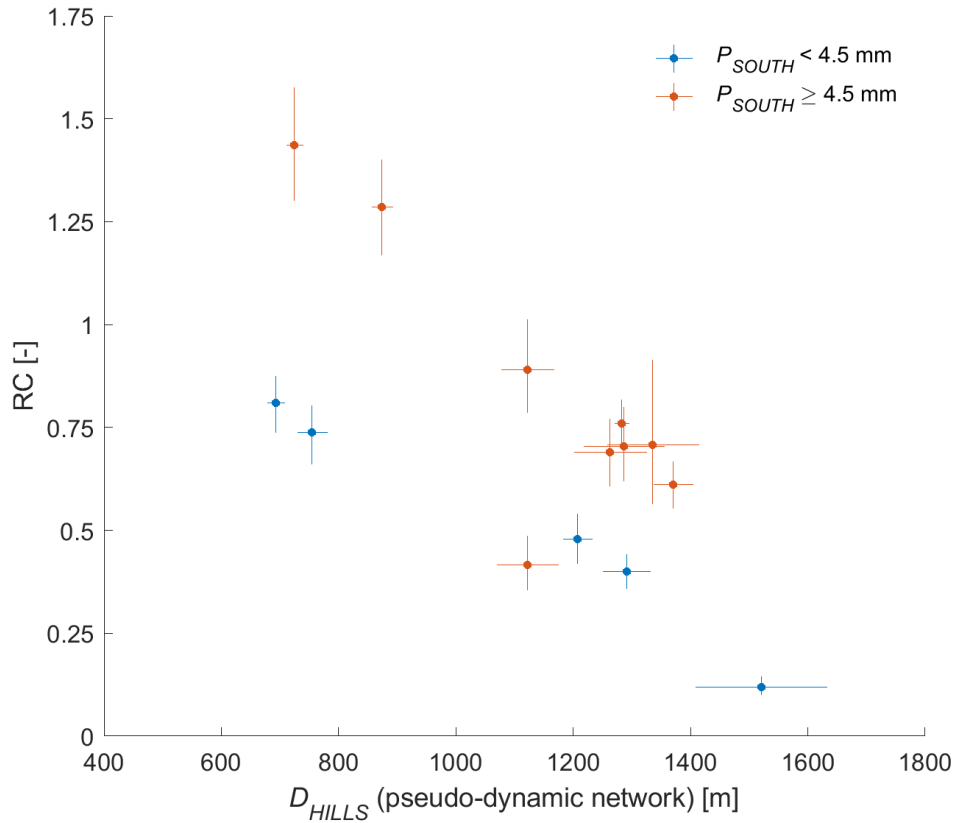


Figure 46. Runoff coefficient against D_{HILLS} , highlighting events with high rainfall amounts in the southern part, i.e. events with $P_{SOUTH} > 4.5$ mm; the July 24th event with $3.02 < RC < 4.85$ and $D_{HILLS} = 740 \pm 140$ m has been discarded (see Section 5.3.1).

Table 14. Correlations between distance metrics for rainfall events with streamflow response (series #4 of Table 2). Absolute values equal or higher than 0.60 are in bold. Correlations for all rainfall events are available in the Table S20 in Supplementary Material.

		D_{HILLS}	D_{HILLS}	D_{STREAM}	D_{STREAM}	H_{HAND}	H_{HAND}	D_{HILLS}	D_{STREAM}	H_{HAND}
River network		Wet	Dry	Wet	Dry	Wet	Dry	Pseudo-dynamic	Pseudo-dynamic	Pseudo-dynamic
D_{HILLS}	Wet	-								
D_{HILLS}	Dry	0.96	-							
D_{STREAM}	Wet	0.59	0.61	-						
D_{STREAM}	Dry	0.54	0.53	0.99	-					
H_{HAND}	Wet	0.91	0.93	0.51	0.44	-				
H_{HAND}	Dry	0.75	0.89	0.40	0.28	0.90	-			
D_{HILLS}	Pseudo-dynamic	0.42	0.45	0.08	0.04	0.51	0.49	-		
D_{STREAM}	Pseudo-dynamic	0.32	0.31	0.75	0.77	0.18	0.09	-0.57	-	
H_{HAND}	Pseudo-dynamic	0.26	0.30	-0.05	-0.10	0.40	0.42	0.98	-0.68	-
RC		-0.20	-0.21	0.10	0.13	-0.28	-0.28	-0.70	0.53	-0.70
$\Delta P/Q$		-0.10	-0.05	0.21	0.21	-0.13	-0.06	-0.66	0.60	-0.68

A sensitivity test showed that setting a $W_{3 \text{ days}}$ threshold of between 12 mm and 20 mm to discriminate between the dry and the wet state yields very similar results, and accordingly, we retain a threshold of 20 mm for $W_{3 \text{ days}}$ to compose the pseudo-dynamic network state. It

should however be kept in mind that these pseudo-dynamic distance metrics represent simply a heuristic solution to overcome the absence of detailed stream network state observations before each event.

5.3.3 Identification of dominant hydrologic drivers via regression analysis

The above correlation analysis results in a range of potential explanatory variables for RC and $\Delta_{P/Q}$ referring to the rainfall amounts, maximum intensity and asymmetry, the pseudo-dynamic rainfall distance metrics and initial wetness conditions ($W_{3 \text{ days}}$). However, according to the correlation analysis, we retain the maximum rainfall intensities as explanatory variables only for $\Delta_{P/Q}$. The tested models, based on one or two explanatory variables, are summarized in Table 15 for RC and in Table 16 for $\Delta_{P/Q}$. The analysis is based on 14 events (after removing the 24 July event, subset #4 of Table 2) and the best models are selected based on their AICc ranking and coefficient of determination (R^2).

Table 15. List of the tested predictors for the RC with a pure quadratic regression, and corresponding statistics: root mean square error (RMSE), coefficient of determination (R^2), variance of residuals (var. residuals), p-value, corrected Akaike criterion (AICc) and AICc ranking. The acceptable p-values (≤ 0.05) and first 3 ranks are highlighted. The analysis is over the 14 events of series #4 of Table 2.

Predictor 1	Predictor 2	RMSE	R^2	var. residuals	p-value	AICc	rank AICc
P_{ALL}	-	0.34	0.14	0.10	0.44	-24.96	17
P_{NORTH}	-	0.36	0.02	0.11	0.88	-23.20	18
P_{SOUTH}	-	0.31	0.28	0.08	0.17	-27.44	12
I_{ASYM}	-	0.33	0.22	0.09	0.25	-26.37	16
$W_{3 \text{ days}}$	-	0.27	0.48	0.06	0.03	-31.90	7
D_{HILLS} (pseudo-dynamic)	-	0.26	0.52	0.06	0.02	-33.00	3
D_{STREAM} (pseudo-dynamic)	-	0.23	0.61	0.04	0.01	-36.13	1
P_{ALL}	I_{ASYM}	0.33	0.35	0.07	0.36	-19.88	19
P_{NORTH}	I_{ASYM}	0.34	0.29	0.08	0.50	-18.53	21
P_{SOUTH}	I_{ASYM}	0.33	0.35	0.07	0.37	-19.84	20
$W_{3 \text{ days}}$	I_{ASYM}	0.25	0.62	0.04	0.05	-27.38	13
D_{HILLS} (pseudo-dynamic)	I_{ASYM}	0.23	0.68	0.04	0.03	-29.55	9
D_{STREAM} (pseudo-dynamic)	I_{ASYM}	0.25	0.62	0.04	0.05	-27.30	14
P_{ALL}	D_{HILLS} (pseudo-dynamic)	0.22	0.70	0.03	0.02	-30.65	8
P_{NORTH}	D_{HILLS} (pseudo-dynamic)	0.26	0.60	0.05	0.06	-26.76	15
P_{SOUTH}	D_{HILLS} (pseudo-dynamic)	0.21	0.74	0.03	0.01	-32.80	4
$W_{3 \text{ days}}$	D_{HILLS} (pseudo-dynamic)	0.24	0.65	0.04	0.04	-28.34	11
P_{ALL}	D_{STREAM} (pseudo-dynamic)	0.20	0.75	0.03	0.01	-33.18	2
P_{NORTH}	D_{STREAM} (pseudo-dynamic)	0.21	0.74	0.03	0.01	-32.55	5
P_{SOUTH}	D_{STREAM} (pseudo-dynamic)	0.21	0.74	0.03	0.01	-32.46	6
$W_{3 \text{ days}}$	D_{STREAM} (pseudo-dynamic)	0.24	0.67	0.04	0.03	-29.10	10

Table 16. As Table 15 but for the lag $\Delta_{P/Q}$.

Predictor 1	Predictor 2	RMSE	R ²	var. residuals	p-value	AICc	rank AICc
$P_{\max \text{ ALL}}$	-	13.07	0.64	144.52	0.00	76.99	3
$P_{\max \text{ NORTH}}$	-	12.70	0.66	136.56	0.00	76.20	2
$P_{\max \text{ SOUTH}}$	-	16.52	0.43	231.05	0.05	83.56	11
I_{ASYM}	-	17.25	0.37	251.75	0.08	84.76	13
$W_{3 \text{ days}}$	-	19.83	0.17	332.65	0.35	88.66	19
D_{HILLS} (pseudo-dynamic)	-	16.28	0.44	224.27	0.04	83.14	10
D_{STREAM} (pseudo-dynamic)	-	13.39	0.62	151.71	0.00	77.67	4
$P_{\max \text{ ALL}}$	I_{ASYM}	11.10	0.79	85.35	0.00	78.72	5
$P_{\max \text{ NORTH}}$	I_{ASYM}	12.89	0.71	115.01	0.02	82.89	8
$P_{\max \text{ SOUTH}}$	I_{ASYM}	10.06	0.83	70.06	0.00	75.95	1
$W_{3 \text{ days}}$	I_{ASYM}	15.86	0.57	174.17	0.08	88.70	20
D_{HILLS} (pseudo-dynamic)	I_{ASYM}	12.97	0.71	116.52	0.02	83.07	9
D_{STREAM} (pseudo-dynamic)	I_{ASYM}	13.83	0.67	132.39	0.03	84.86	15
$P_{\max \text{ ALL}}$	D_{HILLS} (pseudo-dynamic)	14.18	0.65	139.25	0.03	85.57	17
$P_{\max \text{ NORTH}}$	D_{HILLS} (pseudo-dynamic)	13.95	0.67	134.65	0.03	85.10	16
$P_{\max \text{ SOUTH}}$	D_{HILLS} (pseudo-dynamic)	16.57	0.53	190.15	0.12	89.93	21
$W_{3 \text{ days}}$	D_{HILLS} (pseudo-dynamic)	15.65	0.58	169.50	0.07	88.32	18
$P_{\max \text{ ALL}}$	D_{STREAM} (pseudo-dynamic)	11.40	0.78	89.99	0.01	79.46	6
$P_{\max \text{ NORTH}}$	D_{STREAM} (pseudo-dynamic)	11.55	0.77	92.36	0.01	79.82	7
$P_{\max \text{ SOUTH}}$	D_{STREAM} (pseudo-dynamic)	13.37	0.69	123.70	0.02	83.91	12
$W_{3 \text{ days}}$	D_{STREAM} (pseudo-dynamic)	13.82	0.67	132.18	0.03	84.84	14

The best ranked model (in terms of AICc) for RC is a single predictor model using D_{STREAMS} (pseudo-dynamic) as explanatory variable, which yields better results than using antecedent moisture $W_{3 \text{ days}}$ as a single predictor; it should be kept in mind here that the pseudo-dynamic distance metrics also embed information on antecedent moisture conditions (since $W_{3 \text{ days}}$ decides on the moisture state). However, the R^2 becomes considerably higher (0.75) using P_{ALL} and D_{STREAM} (pseudo-dynamic) as explanatory variables. Slightly less good results are obtained with D_{HILLS} (pseudo-dynamic) as a single predictor or in combination with P_{SOUTH} . The fact that D_{STREAM} (pseudo-dynamic) plays a prominent role to explain the RC might be surprising; a possible explanation lies in the fact that the length of instream flow paths is also a metric for runoff storage and exchange within the riparian area, especially in the southern part of the catchment.

For $\Delta_{P/Q}$, the best model (in terms of AICc) has the two explanatory variables $P_{\max \text{ SOUTH}}$ and I_{ASYM} with a R^2 of 0.83 and is considerably better in terms of R^2 than any single predictor model. The best model including a distance metric is $P_{\max, \text{All}}$ in combination with D_{STREAM} ($R^2=0.78$), which underlines the prominent role of D_{STREAM} (pseudo-dynamic) to explain the hydrologic response in this catchment.

5.3.4 Measurement network analysis

Raingauge density analysis

During the observation period, 23 out of 48 events (subset #2, Table 11) were captured by the full network of 12 stations, measuring a total amount of rainfall of 120.7 mm. We tested what a partial rain gauge network (all possible combinations of networks composed with less than 12 stations) would record compared to the full rain gauge network of 12 stations taken as a reference, using the Thiessen polygons method to interpolate the rainfall fields (since, as discussed earlier, the stochastic method cannot be applied to a small station number).

Figure 47a shows, in term of rain gauge density, the number of events having the total amount of rainfall P_{ALL} overestimated or underestimated by a factor 2. We globally observe a misestimation inversely proportional to the rain gauge density, with up to 3 events overestimated by a factor 2 and 8 events underestimated by a factor 2 with the lowest rain gauge density of 0.07 rain gauge per km^2 (1 rain gauge). It is necessary to reach 0.82 rain gauges per km^2 (11 rain gauges) to no longer have events misestimated by a factor 2. In presence of few rain gauges, Figure 47a also shows a strong tendency to underestimate rather than overestimate rainfall amounts. This can be explained by the fact that for a heterogeneous rainfall event, it is more likely to miss a localized important part of the rainfall field rather than to capture it.

Figure 47b presents in the same way the maximum error encountered on the maximum rainfall intensity over 10 minutes $P_{MAX}(10 \text{ min})$. We notice the expected inversely proportional trend, reducing the error if the rain gauge density increases. The figure also shows that in general a low rain gauge density tends to overestimate more than underestimate the $P_{MAX}(10 \text{ min})$. This bias originates from the large footprint associated to each station in presence of a low rain gauge density, increasing the disparities between the observation points while interpolating the rainfall fields.

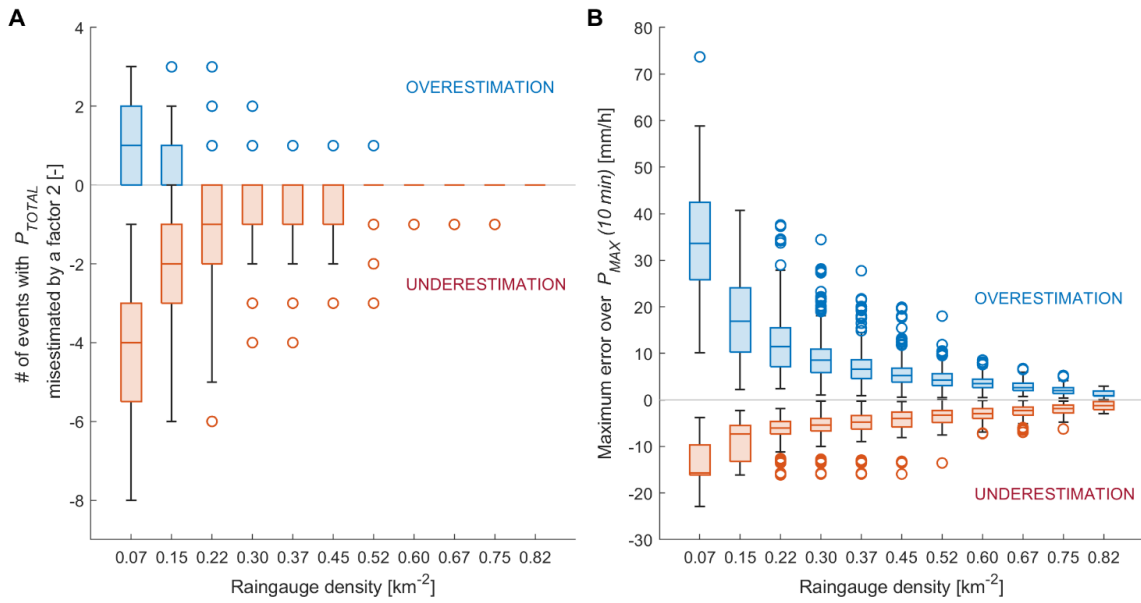


Figure 47. A) Number of rainfall events for which the total amount of rainfall is overestimated or underestimated by a factor 2, according to the rain gauge density, going from 0.07 to 0.82 rain gauges per km^2 (respectively 1 to 11 rain gauges within the catchment). B) Error on the maximum rainfall over 10 minutes $P_{\text{MAX}}(10 \text{ min})$ according to the rain gauge density. For each rain gauge density, all possible combinations of rain gauge networks are tested. The reference value is estimated from the full 12-rain gauge network. The bottom and top of each box are the 25th and 75th percentiles of the sample, the middle line the sample median. The whiskers go up to 1.5 times the interquartile range; values beyond the whiskers (outliers) are marked with circles.

Optimum network identification

Based on the hydrologic driver analysis, we retain P_{ALL} , $P_{\text{max,ALL}}$, I_{ASYM} and D_{STREAM} (pseudo-dynamic) as key metrics for the optimal rain gauge network analysis. Figure 48 shows the best network configurations for 1 to 5 stations and the corresponding RMSE for the select reference metric for the network optimisation (one metric per line).

For a 1-station network, P_{ALL} is best captured when the station is located in the middle of the catchment, while a 2-station network improves substantially the RMSE by arranging the measuring points between the northern and southern parts. Additional stations still improve the RMSE, although to a lesser extent. With a 4-station and 5-station network, the stations tend to align along a north-south transect. For I_{ASYM} and $P_{\text{max,ALL}}$, we see very similar evolution of the spatial patterns as for P_{ALL} for increasing network sizes; for $P_{\text{max,ALL}}$, the RMSE continues however to considerably decrease with the number of stations, which is to be expected for this measure that is more sensitive to spatial-temporal variations of rainfall amount.

For D_{STREAM} as a network optimisation metric, the optimal network configuration first selects stations at the extreme ends of the stream network before organizing along a transect as for

the other metrics, with one lateral station on the left stream side included in the 5-station network as for $P_{\max,ALL}$ (the same) and for I_{ASYM} (a different one).

Considering the small dataset underlying this analysis (23 events), the robustness of the best networks is assessed for two selected metrics (for the P_{ALL} and I_{ASYM}) by re-computing the optimal network if between 1 and 3 events are removed from the dataset. Figure 49 shows how frequent a given configuration is identified as being the optimal solution for networks composed of 1 to 3 stations and clearly confirms the optimal solutions found previously.

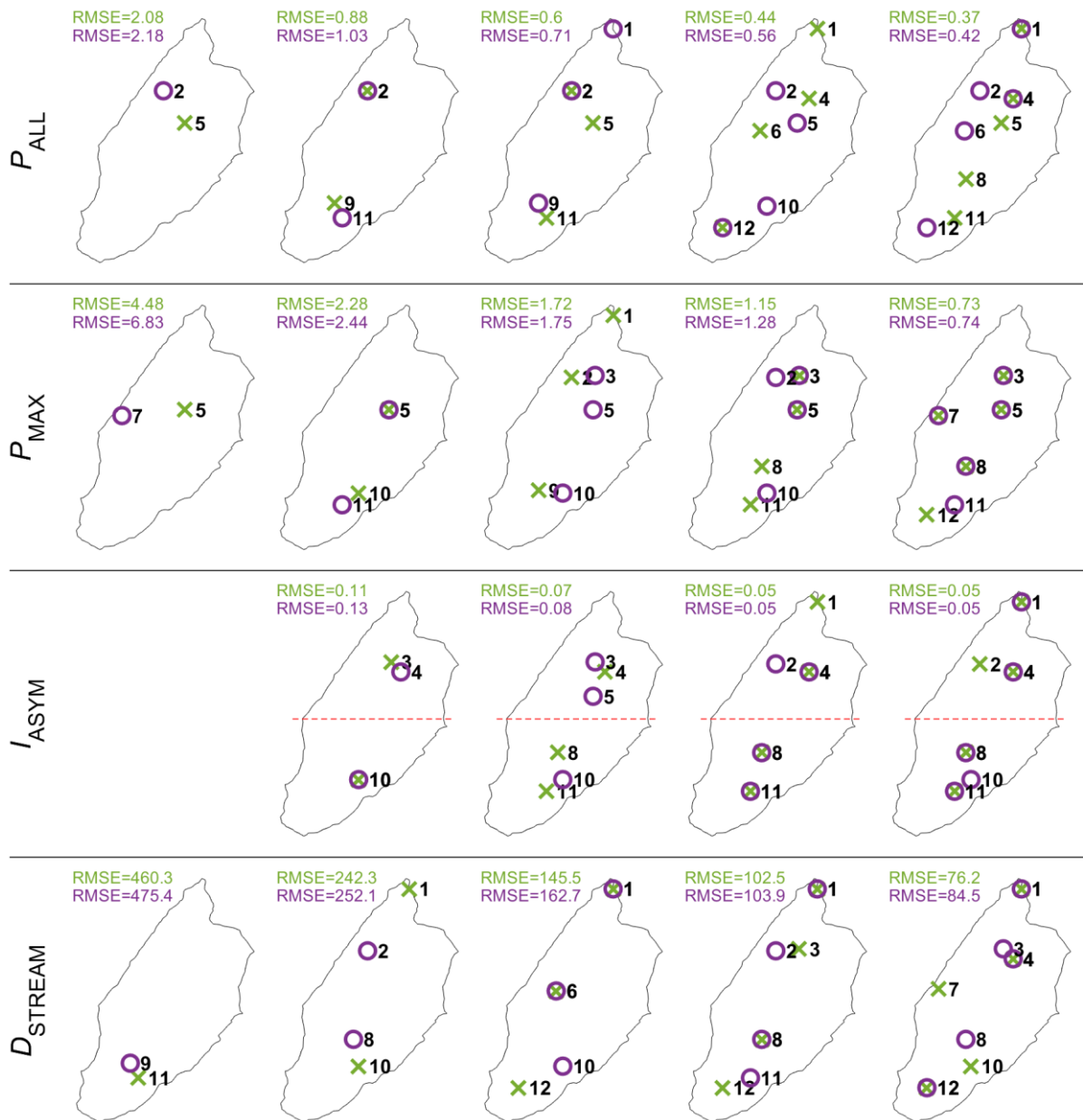


Figure 48. Best (green) and second best (purple) networks and associated RMSE values for 1 to 5 stations resulting from the minimization of the RMSE over 23 events for the P_{ALL} , P_{MAX} , I_{ASYM} and D_{STREAM} . The red dashed line splits the catchments into two parts of equal area.

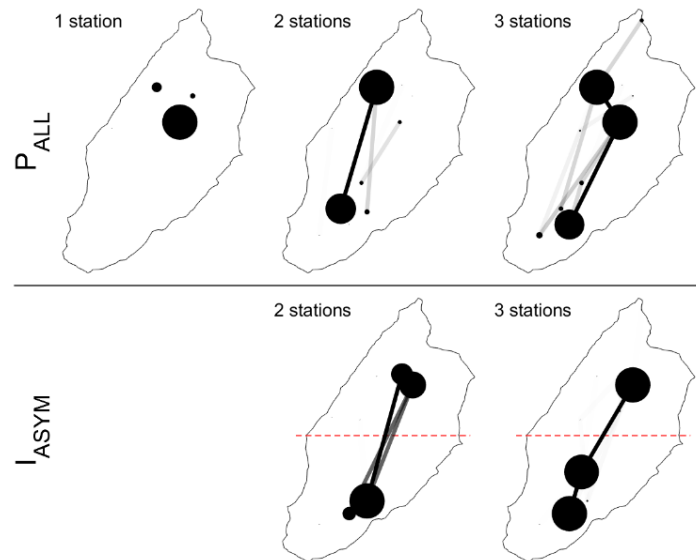


Figure 49. Sensitivity test over the best network from 1 to 3 stations, evaluated by removing from 1 to 3 events over the 23 events (2047 combinations) for the P_{ALL} and I_{ASYM} . The result is presented graphically: larger dots and wider links represent configurations that are found more frequently than others over the different simulations. The red dashed line splits the catchments into two parts of equal area.

Optimum network evaluation

To evaluate this optimum network analysis, we compare in a first step the RC and lag time $\Delta_{P/Q}$ obtained from the full stochastic rainfall field (median field) to the RC and $\Delta_{P/Q}$ values obtained from the best 1-station and 3-station networks and from the worst 3-station network (Figure 50). The corresponding rain gauge densities are 0.07 rain gauge per km^2 for a 1-station network, 0.15 rain gauge per km^2 for a 3-station network and 0.90 rain gauge per km^2 for the full network. For both the RC and $\Delta_{P/Q}$, the dispersion of the values obtained with the reduced rain gauge network decreases from the best 1-station network to the best 3-station network but remains sensibly the same for the worst 3-station network, underlining thereby that a 3-station network can give good results unconditionally to a good location selection.

It is noteworthy that for the lag, even a 1-station network can reproduce this metric correctly for most of the events but can also be completely off (Figure 50). With the best 3-station rain gauge network, the RMSE with respect to the full stochastic rainfall field reduces from 23.18 min to 8.12 min compared to the best 1-station network.

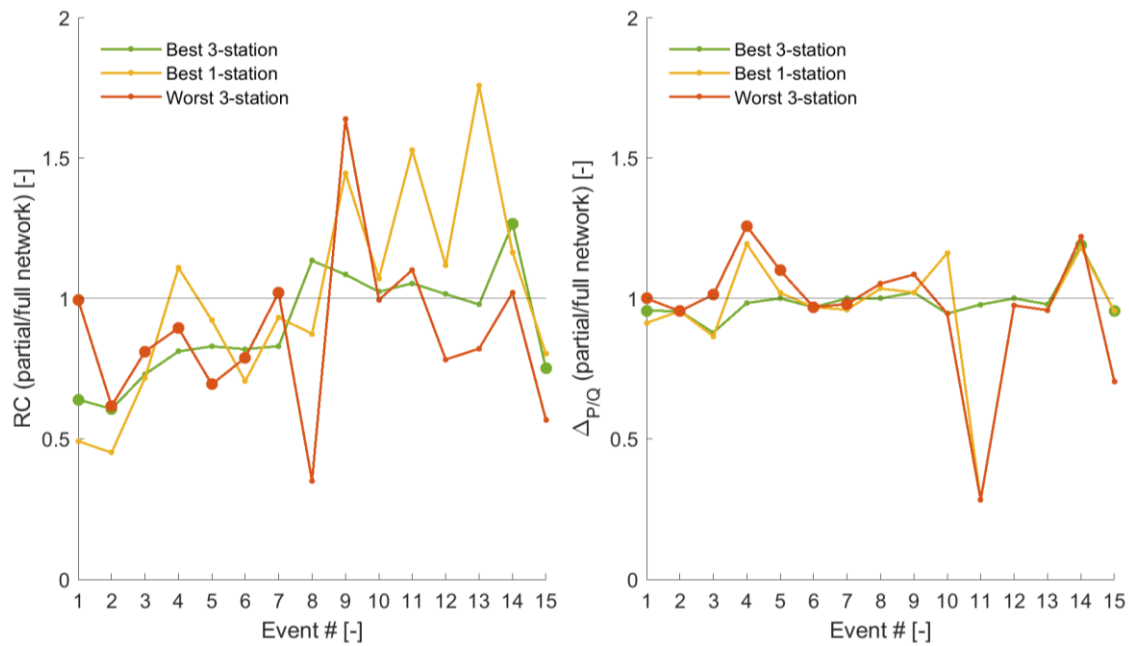


Figure 50. Comparison of streamflow response metrics ratios between a partial network (best 3-station, best 1-station and worst 3-station networks) and the full rain gauge network, using the RC (left) and lag time $\Delta_{P/Q}$ (right). The dataset is subset#4 of Table 2. Larger dots highlight events where events where only 2 of 3 stations were operational (see Section 4.1.1). The lines connect the events to improve readability

In a second evaluation step of the identified optimum rain gauge network, we simulated the event-based streamflow response for the best 1-station network and the best and the worst 3-station network, to compare the result to the simulation with the original rainfall field and thereby obtain a validation on the entire streamflow dynamics rather than on RC or lag only (all simulations are presented in Figures S70 and S71 in Supplementary Material). It is important to point out here that the semi-distributed hydrological model cannot reproduce all observed events equally well as shown by the low correlation coefficients between observed and simulated streamflow in Figure 51. Even with the stochastic generation of rainfall fields, fast streamflow tends to be underestimated with the model; improving the simulation quality for all events would require an in-depth analysis of different subsurface flow mechanisms related also to snow melt and shallow-groundwater recharge, work that is ongoing in this catchment (Beria, 2020b).

Despite of this, we clearly see that the best 1-station network and the worst 3-station network considerably underperform with respect to the full network and that the best 3-station network yields a simulation performance close to the original rainfall field, confirming the results obtained for the summary streamflow response metrics RC and lag.

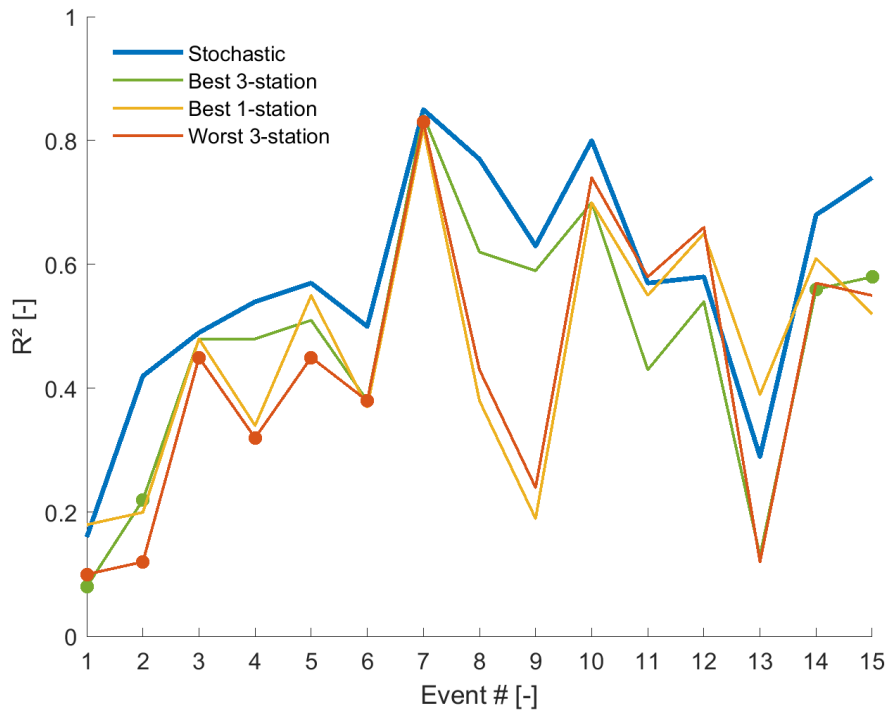


Figure 51. Analysis of 15 rainfall-runoff model events (subset #3, Table 2) with the correlation coefficient between simulated and observed streamflow for different rainfall fields inputs: the stochastic generation of rainfall fields based on all available rain gauge stations, the best 3-stations and the best 1-station network, and the worst 3-stations network. Larger dots highlight events for which only 2 of 3 stations were operational (see Section 4.1.1). The lines connect the events to improve readability.

5.4 Discussion

5.4.1 Spatial heterogeneity of rainfall

One of the key identified metrics to characterize the spatial distribution of rainfall in relation to RC and lag prediction is I_{ASYM} . It splits the catchment into two parts, and aggregates rainfall observations into one value. Among the records showing a strong rainfall asymmetry, 7 out of the 8 events are too small to cause a detectable streamflow response (Figure 43), but one does create a streamflow response although it only rains over half of the 12 rain gauge stations. Despite of this absence of a strong asymmetry in the 14 rainfall events that cause a streamflow response, the regression analysis suggests that the spatial distribution might play an important role for the explanation of the lag time. The importance of this asymmetry predictor can be related to the fact that it captures the key feature of the spatial catchment organisation in terms of distance to the outlet, drainage density and subsurface storage potential.

The second dominant metric of spatial rainfall distribution to predict the RC and the lag is D_{STREAM} (pseudo-dynamic). This suggests that for this catchment, the rainfall distance to the outlet is the overall the dominant predictor for the analyzed streamflow response metrics.

It is noteworthy that this analysis could be affined by investigating different splitting geometries, e.g. by splitting the catchment into west and east parts, thereby separating the large slopes (west) from the steep slopes (east). This and similar spatial asymmetry metrics are case-specific as they rely on the particular geomorphology and topography of the catchment and are thus not directly applicable to other catchments. In particular I_{ASYM} cannot be used as a tool to compare different catchments.

The rainfall distance metrics to the stream network (D_{HILLS}) and along the stream network (D_{STREAM}) were designed here to overcome the limitations of the simple asymmetry measure. The prominent role of D_{STREAM} - pseudo-dynamic to explain the lag time and RC underlines the importance of characterizing the spatial heterogeneity in terms of geomorphological distances to the actual stream network, which requires more detailed network expansion analyses in future studies.

We could expect that in this kind of steep environments, the residence time in hillslopes strongly dominates over residence times in the stream network (Nicotina et al., 2008); the fact that D_{STREAM} outperforms here D_{HILLS} for the prediction of RC and lag time may show that even in steep environments, with a priori fast instream processes and limited storage, the riparian area and related subsurface exchange processes could play a more prominent role. The fact that the travel distance in the stream network explains more of the RC variation than D_{HILLS} might be an indirect effect: the longer the travel distance in the stream network, the more likely are delays due to exchange with groundwater in the riparian area. This implies that along-stream processes might need a better representation in rainfall-runoff models, even for small and steep catchments; to date, these processes are often ignored in rainfall-runoff hydrological models at this scale, or are represented with a simple constant velocity transport term (Schaepli et al., 2014).

However, future work on the role of water residence time in the stream network will necessarily require more detailed field data on the temporal evolution of the stream network. This will in addition open new perspectives to quantify how the stream network extension is imprinted in the streamflow response: in fact, as discussed by Rinaldo et al. (1995), the intrinsic fractal nature of the stream network is not transferred to the streamflow response

and, accordingly, there is potential to infer the stream network extension from observed streamflow records, provided that we have high resolution rainfall data to disentangle the different effects. Finally, we would like to point out here that this result on the prominent role of travel time along the stream network opens interesting new analogies with urban hydrology, where introduction times to the network are typically short (Smith et al., 2013). Future work might show what methods from urban hydrology (Cristiano et al., 2017) could be transposed to the analysis of spatial rainfall variability in small alpine catchments.

5.4.2 Raingauge network density

The selected metrics showed the importance and potential of a high density rain gauge network to capture rain events, and to investigate the dynamics of the hydrologic response. The rain gauge network analysis can then be used as a preliminary investigation to implement a permanent network, composed of fewer stations. The reliability of the study is directly dependent on the number of observed rainfall events, i.e. on deployment duration of the rain gauge network. Despite the small size of the catchment, there could potentially be storms that are not or only partially seen by the rain gauge network.

This possibility of missing localized events is highlighted by the event of July 24th (Section 5.3.1), which was considerably underestimated despite of the high density of the deployed network (1 station for 1.1 km² on average, maximal distance of 1,670 m from a point to a rain gauge). The best partial networks composed of 1, 2 or 3 stations (Section 5.3.4) give for this extremely localized event a total amount of rainfall respectively 12.0 mm, 9.4 mm and 9.2 mm, not far from the 10.6 mm measured with the full network, but these partial networks were trained on the dataset containing the particular event.

With only one station, there is a high risk of totally missing an event, whereas a 2-station network design measuring at least the northern and the southern part of the catchment would i) capture most of the events and ii) give a first estimation of the rainfall spatial distribution.

Overall, the network optimisation analysis with different metrics clearly suggests that to optimally reproduce the hydrologic response in terms of RC and $\Delta_{P/Q}$, we would need to implement at least a three station network in this catchment, organized along a north-south transect, with one of the stations being located in the remote southern part. The north-south organization can be explained by i) the shape of the catchment that also extends longitudinally or ii) a general tendency for rainfall events to move longitudinally, emphasizing the importance, for this case study, to capture spatial configuration of rainfalls over a north-south

transect rather than over a west-east transect and iii) the general increasing trend of elevation along this transect.

5.5 Conclusion

Our analysis of the role of rainfall patterns for the streamflow response is one of the first data-based studies carried out at such a small scale in an Alpine environment. The detailed analysis of 48 events from one summer suggests that spatial rainfall patterns might play a key role to explain the hydrologic response in small Alpine catchments. The novelties of the study include the use of a low-cost rain gauge network to capture rainfall patterns, and the design of a data-based framework to analyze the rainfall-runoff response. The main conclusions from our analysis are:

- A high density rain gauge observation network is a major asset to identify critical areas that are influenced by local rainfall forcing and give an estimation of the rainfall amount errors made by a partial network.
- A detailed analysis of the hydrological response as a function of rainfall patterns and geomorphology requires a rain gauge network specifically designed for this purpose in conjunction with detailed observations of the stream network expansion before events.
- Such a network should take into account the spatial distribution of distances to and along the stream network.
- As shown here, even for small catchments the rainfall distance to the outlet along the stream network might play a key role to explain the hydrologic response. Accordingly, future hydrological modelling studies in small Alpine catchments should investigate the representation of instream transport and storage processes.

The analysis framework developed here is readily transferable to other settings, including natural or even urban catchments. Given the low cost of the deployed rainfall sensor network, the approach has potential for future detailed studies in to-date sparsely gauged catchments.

6 | Studying the dynamic of a high alpine catchment through the scope of multiple natural tracers



Photograph: spring in the Vallon de Nant and melting snowpack.

A version of this chapter (including a description of the catchment, gauging stations and weather stations) is under revision in Hydrology and Earth System Sciences journal:

Michelon, A., Ceperley, N., Beria, H., Larsen, J., Vennemann, T., and Schaepli, B.: Studying the dynamic of a high alpine catchment based on multiple natural tracers, *Hydrol. Earth Syst. Sci. Discuss.* [preprint], <https://doi.org/10.5194/hess-2022-48>, in review, 2022.

Author contributions. AM and NC conceived the field study; AM, NC, HB and JL collected and analyzed the field data; AM, NC and HB did all the lab work; all authors discussed and interpreted the data; AM produced all computations and figures and, together with BS and TV led the writing of the paper.

Abstract

Hydrological processes in high elevation catchments are largely influenced by snow accumulation and melt, as well as summer rainfall input. The use of the stable isotopes of water as a natural tracer has become popular over recent years to characterize water flow paths and storage in such environments, in conjunction with electric conductivity (EC) and water temperature measurements. In this work, we analyzed in detail the potential of year round samples of these natural tracers to characterize hydrological processes in a snow-dominated Alpine catchment. Our results underline that water temperature measurements in springs, groundwater and in-stream are promising to trace flow path depth and relative flow rates. The stable isotopes of water are shown here to be particularly valuable to get insights into the interplay of subsurface flow and direct snowmelt input to the stream during winter and early snow melt periods. Our results underline the critical role of subsurface flow during all melt periods and the presence of snowmelt even during winter base flow. We furthermore discuss why reliably detecting the role of subsurface flow requires year-round water sampling in such environments. A key conclusion of our work is the added value of soil and water temperature measurements to interpret EC and isotope analyses, by giving additional information on snow-free periods and on flow path depths.

6.1 Introduction

Hydrology in Alpine environments is largely dominated by snow accumulation and melt processes compared to summer rainfall, with ensuing high sensitivity to changes in climate (Hanus et al., 2021). For Alpine catchments with a mean elevation above approximately 1,500 masl (Santos et al., 2018), winter snowfall leads to the build-up of a seasonal snowpack, which in the northern hemisphere results in low flow occurring between November and March (Schaefli et al., 2013) and maximum monthly streamflow related to melt between May and August, depending on the depth and extent of the seasonal snowpack and on the degree of glacier cover (Hanus et al., 2021; Muelchi et al., 2021). Given the importance of these cycles of accumulation and melt and the resulting streamflow regime for water resources availability, an important body of literature focuses on quantifying the streamflow regime in such environments, either based on streamflow observations (Blahusiakova et al., 2020; Brunner et al., 2019; Musselman et al.; Hammond and Kampf, 2020) or modelling (Foster et al., 2016; Livneh and Badger, 2020; Muelchi et al., 2020).

Detailed hydrological process studies in high Alpine catchments remain, however, relatively rare even if detailed insights into the fate of rainfall and snowmelt in such catchments are required for model-based extrapolations of their hydrological response into the future, given the likely changes in climate. In addition to logistical challenges, the difficulties to access and continuously monitor in temporally frozen environments requires the development of specific methods and equipment (Rucker et al., 2019), which is certainly one of the main reasons to explain the small number of studies in such places.

Existing field-based studies can be classified according to their focus: i) understanding dominant runoff generation mechanisms during rainfall and snowmelt events (Penna et al., 2016; Engel et al., 2016), including small-scale studies of snowpack flow paths (Webb et al., 2020), ii) understanding the origin of winter low flow (Floriantic et al., 2018), iii) quantification of groundwater or spring recharge (Lucianetti et al., 2020) and seasonal groundwater storage (Arnoux et al., 2020) or iv) understanding the role of glaciers and rock-glaciers in the hydrological response of high elevation catchments (Brighenti et al., 2019; Zuecco et al., 2019; Ohlanders et al., 2013; Penna et al., 2014). A common feature of these studies is the use of natural tracers, such as electric conductivity and/or stable isotope composition of water, for example, to gain new insights into the fate of rainfall and snowfall and related water flow paths and to formulate hypotheses about dominant runoff drivers at specific times of the year, or about the hydrologic response of selected landscape units.

To complement such existing studies, this work attempts to quantify dominant drivers of the hydrologic response of a high elevation catchment throughout the year, i.e. through all streamflow periods, ranging from winter low flow, to different stages of the melt season and the autumn recession. We analyze the observational data from the intensively studied Vallon de Nant catchment in the Swiss Alps (Benoit et al., 2018; Giaccone et al., 2019; Ceperley et al., 2020; Mächler et al., 2021; Michelon et al., 2021a; Thornton et al., 2021a; Beria et al., In revision; Antoniazza et al., Submitted).

This work focuses on what we can learn about water flow paths from stable isotope composition of water, a natural tracer that has been extensively used to characterize hydrological processes related to snow (e.g. Beria et al., 2018). The analysis of stable isotope compositions of water can give insights into different water sources (such as rainfall, snowpack, springs, groundwater), recharge and evaporation processes (e.g. Sprenger et al., 2016); it is complemented here by electrical conductivity measurements that provide additional information on subsurface flow paths and relative water residence times in the subsurface (Cano-Paoli et al., 2019), by temperature measurements of water to trace connectivity between water sources and the atmosphere (Constantz, 2008), and by soil temperature measurements to gain insights into periods of thermal insulation from the seasonal snowcover (Trask et al., 2020).

The specific objective of this work is to examine the dominant hydrological processes that explain the catchment-scale hydrological response during different periods of the year. Key open questions include the origin of winter streamflow (from subsurface storage versus from localized snow melting) (Floriantic et al., 2018; Hayashi, 2020), the dominant runoff processes that drive streamflow generation during early spring snow melt (Brauchli et al., 2017) and later on in the snowmelt season and the role of shallow groundwater in the hillslopes and of alluvial or talus groundwater systems (Hayashi, 2020) in the streamflow generation throughout the year. In addition, the aim is to provide transferable insights into the value of the observed variables for hydrologic process investigations in comparable catchments.

6.2 Case study area

The study area is described in detail in Chapter 2. Figure 52 presents the sampling locations for the analyses presented in this Chapter. The analyses cover the period from 2017 to 2019. The annual average streamflow calculated over 2017 and 2019 is between 0.46 to 0.62 m³ s⁻¹ (3.0 to 4.0 mm day⁻¹) but fluctuates between 0.02 to 0.03 m³ s⁻¹ (0.12 to 0.18 mm day⁻¹) and

2.4 to 3.1 m³ s⁻¹ (15.5 to 19.7 mm day⁻¹). Flood events can cause streamflow from 5.8 to 7.2 m³ s⁻¹ (37.4 to 46.3 mm day⁻¹) over 1 hour and from 6.9 to 8.5 m³ s⁻¹ (44.4 to 54.6 mm day⁻¹) over 10 minutes. The mean temperature of the streamflow at the outlet is 5.0 °C, ranging from 0 °C when the river is frozen during some winter periods to a daily temperature of 10.0 °C during summer. The three years included in the study period show strongly contrasting hydrographs (Figure 53), in terms of total streamflow volume and in terms of seasonal timing, with peak monthly flow varying from June for 2017-2018 and 2018-2019 to July 2016-2017 with a snow rich winter.

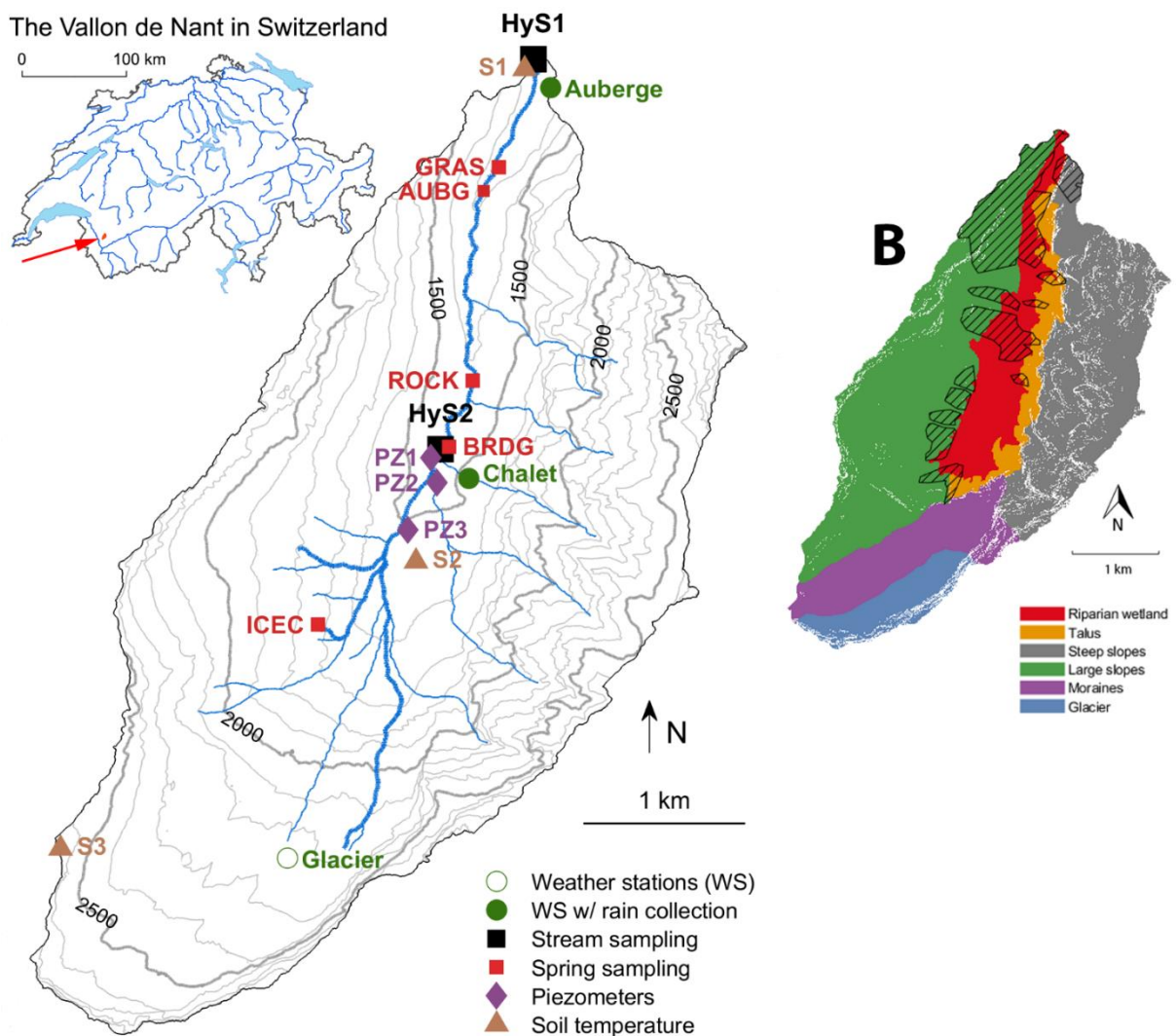


Figure 52. The map A) shows the location of the sampling sites in the Vallon de Nant (outlet at 46.25301°N, 7.10954°E in WGS84). Note that the AUBG spring location shows where the spring is taken, whereas the water from this spring is sampled at the Auberger weather station point, 800 m further north. The topographic map is based on a 2-m digital elevation model (swissAlti3D, 2012a). The stream network shows its full extend during snowmelt periods. 'Soil temperature' shows locations of the sensor network of Vittoz (2021). The map B) identifies the dominant hydrological units of the Vallon de Nant and the hatched area corresponds to forested areas.

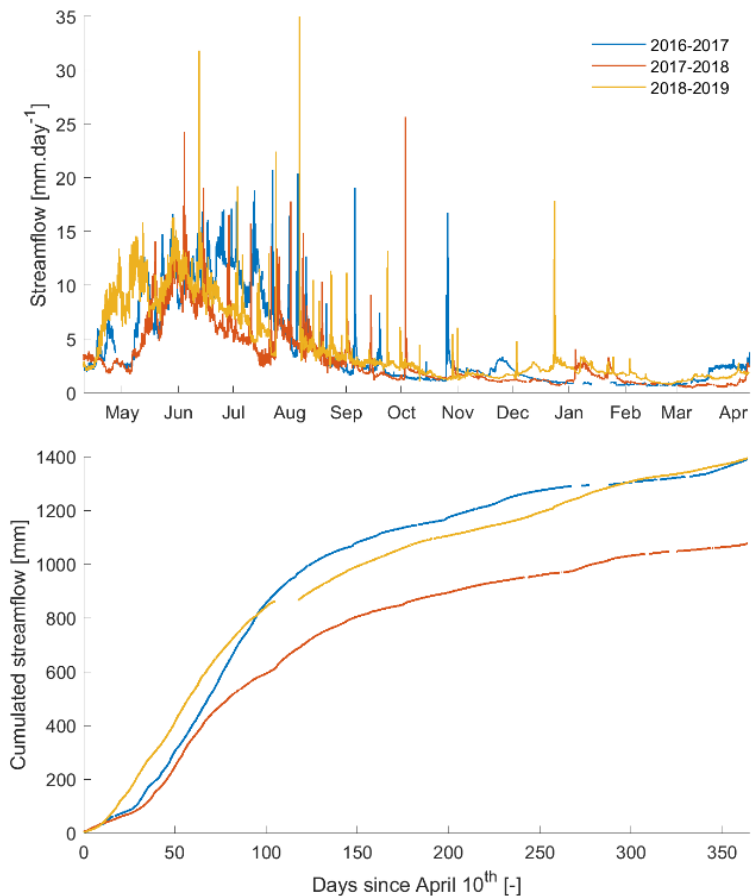


Figure 53. Comparison of the streamflow evolution (on top) and cumulative (bottom) over a year (April 10th to April 9th next year) for 3 years. Note that there are gaps in the data, and 6.4%, 3.2% and 4.6% of the timeseries are missing (respectively in 2016-2017, 2017-2018 and 2018-2019).

6.3 Methods

Below, we describe the hydrological process monitoring equipment and sampling methods deployed during the study period (from 2016 to 2018).

6.3.1 Stable isotopes of water

Water sampling

Water was either sampled manually (grab samples) or via automatic samplers placed at the outlet and an upstream location along the stream (HyS1 and HyS2, see Figure 52) for stable isotope analysis ($\delta^2\text{H}$, $\delta^{17}\text{O}$ and $\delta^{18}\text{O}$). Manual samples were collected from streams, springs and piezometers using 12 mL amber borosilicate glass vials with polypropylene screw-top caps with PTFE-lined silicone septa. Automatic sampling was performed with an ISCO 6712C Compact Portable Sampler with 24 bottles of 500 mL capacity at HyS1 and an ISCO 6712 full-size portable sampler with 24 bottles of 1L capacity at HyS2 (Lincoln, Nebraska, USA).

Automatic samplers were programmed to sample at 6 hours intervals over one week. The automatic sampler was programmed to fill bottles to half of their capacity, 250 mL and 500 mL, respectively, to optimize energy usage and to prevent sample loss due to freezing, while still sampling enough water such to keep fractionation due to evaporation would be insignificant.

A sub-sample of water was then taken manually from each bottle using a 12 mL amber glass vial (either in the laboratory or in the field). Original installation involved the use of pipettes and tubes inside the autosampler bottles similar to those described by von Freyberg et al. (2020), however after some experimentation and due to the alpine and shaded microclimate of the location, fractionation due to evaporation was deemed minimal and additional components resulted in more contamination and less sampling capacity. In case of freezing, the bottles were closed with a cap and moved to a warmer place until the ice fully melted. The same borosilicate glass vials were also used for long-term storage at ambient temperature in the laboratory.

Samples of rainfall were collected at the *Auberge* and *Chalet* meteorological stations (Figure 52) with a 13 cm of diameter plastic funnel, connected to an insulated 2.5 L screw-top bag made of 147 μm PET/NY/LDPE plastic (DaklaPack, Perpignan, France), enclosed in a plastic box. The collected water was well mixed, weighed and sub-sampled using 12 mL amber glass vial once or twice a week from May to November (i.e. outside the snowfall period).

Groundwater was sampled from piezometers installed for a simultaneous hydrogeological study (Thornton et al., 2021a). Prior to water sampling, the piezometers were emptied using a Geotech Peristaltic Pump (Geotech Environmental Equipment, Inc, Denver, Colorado, U.S.A.); and the freshly recharged water was sampled with the same pump and stored in 12 mL amber glass vials.

During winter 2017 and winter 2018, snow samples were collected regularly at two locations. Two different sampling methods were used: i) if distinguishable snow layers were present (visual and textural distinction) each of them was sampled individually, otherwise ii) a single bulk sample of approximately sampled the entire profile was taken.

Snow samples were sealed in alimentary 700 mL zip bags made of 120 μm BOPP/LDPE plastic (DaklaPack, Perpignan, France) after evacuating as much air as possible. The collected snow samples were melted at ambient air temperature (the influence of water vapor from air on the isotopic composition of the sample is discussed in the Appendix 1). A sub-sample of well-

mixed, melted snow was taken manually in the lab from each bag into a 12 mL amber glass vial.

The isotopic composition of the entire snowpack at a given snow pit was obtained with a weighted average of the values of each sampled layer according to depth, as an approximation for the equivalent bulk isotope composition assuming a uniform density.

For vegetation, the isotopic ratio of water is extracted cryogenically from xylem and near-by surface soil collected from two transects of 10 *Larix decidua* individual trees running about 200 m perpendicular to the main stream just below and above 1500 masl during the 2017 and 2018 growing season (Ba, 2019).

6.3.2 Analysis of the isotopic composition of water

Stable isotope composition of water, expressed as the familiar $\delta^2\text{H}$, $\delta^{17}\text{O}$ and $\delta^{18}\text{O}$ notation, were analyzed with a Picarro 2140-i Wavelength-Scanned Cavity Ring Down Spectrometer (Picarro Inc., Santa Clara, California, U.S.A.), using 2.0 mL glass vials closed with screw-top caps with silicone Rubber/TPFE septa filled with 1.8 mL of filtered water. Samples were injected between 6 and 8 times. The first 3 injections were discarded to avoid memory effects. The raw values were then corrected according to a standard curve determined with 3 internal standards, which are regularly calibrated against the international standards of VSMOW (Vienna Standard Mean Ocean Water) and SLAP (Standard Light Antarctic Precipitation) of the IAEA (International Atomic Energy Agency) (Coplen, 1994). Each standard was injected 12 to 15 times, and the last 6 injections were kept. Delta units of isotope compositions (Coplen, 1994) are reported in per mil and the strategy used for the analysis is similar to the one described in the work of Schauer et al. (2016). The median analytical errors obtained with this method are 0.4 ‰ for $\delta^2\text{H}$, 0.01 ‰ for $\delta^{17}\text{O}$, 0.04 ‰ for $\delta^{18}\text{O}$.

Based on these measures, we compute d-excess (Dansgaard, 1964) and ^{17}O -excess (Barkan and Luz, 2005; Landais et al., 2006):

$$\text{d-excess} = \delta^2\text{H} - 8 \cdot \delta^{18}\text{O}, \quad (1)$$

$$^{17}\text{O-excess} = 10^6 \left(\ln \left(\frac{\delta^{17}\text{O}}{1000} + 1 \right) - \lambda_{ref} \cdot \ln \left(\frac{\delta^{18}\text{O}}{1000} + 1 \right) \right). \quad (2)$$

With $\lambda_{ref} = 0.528$ (Meijer and Li, 1998; Barkan and Luz, 2005; Landais et al., 2008). From regression of $\ln(\delta^{17}\text{O}/1000 + 1)$ against $\ln(\delta^{18}\text{O}/1000 + 1)$, we obtain a similar slope for our samples ($\lambda_{ref} = 0.528$), which confirms the universality of this value.

The d-excess and ^{17}O -excess are typically used to investigate the large scale hydrological cycle and oceanic moisture sources (Nyamgerel et al., 2021). Both d-excess and ^{17}O -excess are known to be sensitive to relative humidity during evaporative processes but ^{17}O -excess is supposed to be less temperature sensitive (Surma et al., 2021; Bershaw et al., 2020) than d-excess and can thereby convey additional information on evaporation processes and on climatic conditions (Risi et al., 2010).

To gain insights into local evaporative processes, we compute the line-conditioned excess lc-excess (Landwehr and Coplen, 2006) based on our local meteoric water line LMWL ($\delta^2\text{H} = a \cdot \delta^{18}\text{O} + b$), which significantly deviates from the global meteoric water line GMWL (see Section 0).

$$\text{lc-excess} = \delta^2\text{H} - a \cdot \delta^{18}\text{O} - b. \quad (3)$$

The LMWL is calculated using linear regression between $\delta^{18}\text{O}$ and $\delta^2\text{H}$ of 85 rainfall samples and yields coefficients $a=7.38$ and $b=6.15$.

The median analytical error is 0.4 ‰ for d-excess and lc-excess, and 8 per meg for ^{17}O -excess.

6.3.3 Water temperature and conductivity measures

The water temperature of four springs was recorded every 30 minutes (every 15 minutes for GRAS and ROCK springs) with Hobo temperature loggers (Onset Computer Corporation, Bourne, MA, U.S.A.) for periods between 12 and 21 months. Based on these recordings, we estimate lag times with respect to air temperature and diel and annual amplitudes. The original time resolution of 1 minute for the stream, 30 minutes for piezometers (PZ) and 2 minutes for springs is kept for the diel temperature maximum amplitude but aggregated to 1 day for the annual temperature maximum amplitude (using a 7-day moving average). Lag times are obtained by maximizing cross correlation between the 1-day signal and the one for the reference air temperature signal (at Auberge station). Electrical conductivity (EC) was measured for all collected water samples except snowpack, either directly in the field with a WTW Multi 3510 IDS connected to a WTW TetraCon 925 probe (Xylem Analytics Germany Sales GmbH & Co, Weilheim, Germany) or in the laboratory directly in the 12 mL amber silicate vials using a JENWAY 4510 Conductivity Meter with a 6 mm glass probe (Stone, U.K.). Comparison of duplicate measurements using both probes (compensated in temperature) demonstrated a correlation coefficient of $R^2=0.89$ despite a delay of 23 to 30 months between the in situ and laboratory measurements (see Figure S124 in Supplementary Material).

6.3.4 Additional data sources

Our own data set is complemented by data obtained from an existing sensor network to measure soil temperature (see Figure 52), which was deployed in the context of vegetation research (Vittoz, 2021) and recorded hourly soil temperatures at four locations from July 2009 to November 2018 using GeoPrecision M-Log5W (GeoPrecision GmbH, Ettlingen, Germany) buried at 10 cm depth. The soil temperature can be assumed to be a good proxy for snow cover, making distributed data throughout the catchment area particularly useful to us. Strong diel variations of soil temperature (measured at 10 cm) can in fact be associated with snow-free soils, which are typically exposed to large amplitude air temperature fluctuations and radiative exchanges.

Piezometric data originally collected as part of the work of Thorton et al., (2021) from two locations in the alluvial flood plain (Figure 52) allowed us to characterize the corresponding ground water system.

We obtained a long air temperature time series from a grided product (1 x 1 km grid) from MeteoSwiss (MeteoSwiss, 2019). The gridded data is influenced by of the low number of stations at high elevations (Freudiger et al., 2016) but compared to our own meteorological data, the gridded temperature times series shows a satisfactory level of correlation at a daily scale ($0.96 < R^2 < 0.98$), and is thus useful for gap filling.

6.4 Results

6.4.1 Identification of streamflow periods

To guide the analysis of what might explain the streamflow response during different times of the year, the hydrograph was divided into a series of periods, after smoothing to original 1-min recordings with a 7-day moving average. The retained periods are called baseflow period (B), early melt period (E), melt period (M) and seasonal recession period (R); they are illustrated in Figure 54 along with the hydrograph. The baseflow period extends from the end of September to early spring (mid-March to beginning of April) and shows a streamflow of around 1 mm/d only, which is typical for catchments at comparable elevations (Floriatic et al., 2018). The baseflow exhibits a very slow streamflow decrease throughout the period and almost no diel variations even though some streamflow peaks might occur due to exceptional rainfall events or warm periods (e.g. January 2018). During the early melt period, the streamflow starts increasing to a few mm/d, preceding the main snow melt period. This early melt period lasts several weeks in certain years (e.g. in 2017), with an increase in streamflow

to around 3 mm/d, followed by a plateau that lasts approximately 49 days. In 2018, warming occurred extremely quickly, thus no early melt period existed (Figure 54). This early melt period is rarely explicitly discussed in the literature (for a model-based example, see He et al., 2015), despite the fact that it is a typical pattern and remains challenging to model (see Figure 9 in Brauchli et al., 2017; or Figure 3 in Thornton et al., 2021b).

The melt period is characterized by an increase of the streamflow due to an important water input from snowmelt. Over the course of our observation period, the melt period started at the beginning of May in 2017, and at least a month earlier in 2018 (though this was the year without a clearly visible early melt period). The annual 7-day streamflow maximum marks the start of the seasonal recession period, which for 2017 and 2018 corresponds to the end of May or beginning of June, but only to the end of June in 2016, which was preceded by a very snow-rich winter. The seasonal recession results from a combination of reduced input from snowmelt and evaporation.

6.4.2 Soil temperature

Temporal patterns

The soil temperature data from three different elevations (at 1240 m, 1530 m, and 2640 masl, see Figure 52) shows how the insulation provided by the snow cover dampens the high frequency (diel) air temperature variations (positives and negatives, see Figure 54). Before the start of each winter period, the soil temperature approaches gradually 0 °C, with only a slightly positive temperature that is caused by heat flux from the ground. However, some isolated temperature spikes are observed during winter, most probably due to rain-on-snow events (e.g. the spike during winter 2016 in the green line in Figure 54, representing the lowest elevation). Unfortunately, no other observed tracers are available during these periods to confirm this hypothesis.

The negative temperatures measured during the 2016-2017 winter period by two soil temperature probes (at 1530 m and 2640 masl) are reached due to cold air temperatures associated with an exceptionally dry winter and low snow cover.

The temperature recordings at the three different elevations in Figure 3 show the start of the snow-free period at each measurement location with a sharp warming between March and July (depending on elevation) of more than 5 °C. The start of the snow-free period shows a delay of between 4 (2018) and 8 weeks (2017) between the elevation 1240 m and 1530 masl

Comparing the elevation 1530 m to 2640 masl, the start of the snow free period is delayed by 3.5 (2018) and 8 weeks (2016).

Similarly, the soil temperature time series clearly show the much earlier seasonal snow cover onset in autumn 2016 at the highest elevation as compared to the two lower elevations (12 weeks earlier). In 2017, the seasonal snow cover onset occurred at a similar time at all elevations, visible as a stop of all diel temperature variations, between October 22nd and November 25th, 2017). A summary of snow-free dates as extracted from the temperature recordings is available in the Supplementary Material (Table S24).

Finally, it is noteworthy that, albeit not the focus of this paper, the soil temperature recordings and their co-variation with streamflow show that during summer, rainfall input coincides with cold spells; during autumn, rainfall input coincides with warm spells (e.g. October 2016 and 2017).

Link to streamflow

The soil temperature measurements reveal interesting features with respect to the identified streamflow periods. For all three summers, the soil temperature recordings from the highest elevation show the presence of snow until the start of the recession period, which underscores the late melt of seasonal snow in some areas of the catchment. The start of the two early melt-dominated streamflow periods in 2016 and 2017 corresponds to the disappearance of snow at the lowest soil temperature measurement point. This suggests that this early melt streamflow rise might well be linked to locally complete snow melt and associated water input to the stream at the lowest elevations, during periods when higher up, any potential snow melt is still being retained in the existing snow pack or subsurface.

Soil temperature recession starts at a similar date at all elevations and is in close correspondence with the start of the streamflow baseflow periods; i.e. significant decrease of soil temperature only starts when the streamflow recession period is already well advanced. In the winter of 2016/2017, winter streamflow fluctuations are reflected in the soil temperature, whereas the mid-winter streamflow rise in January 2018 is not visible in any of the soil temperature recordings, which may be due to errors in recording river stage caused e.g. by accumulated sediments.

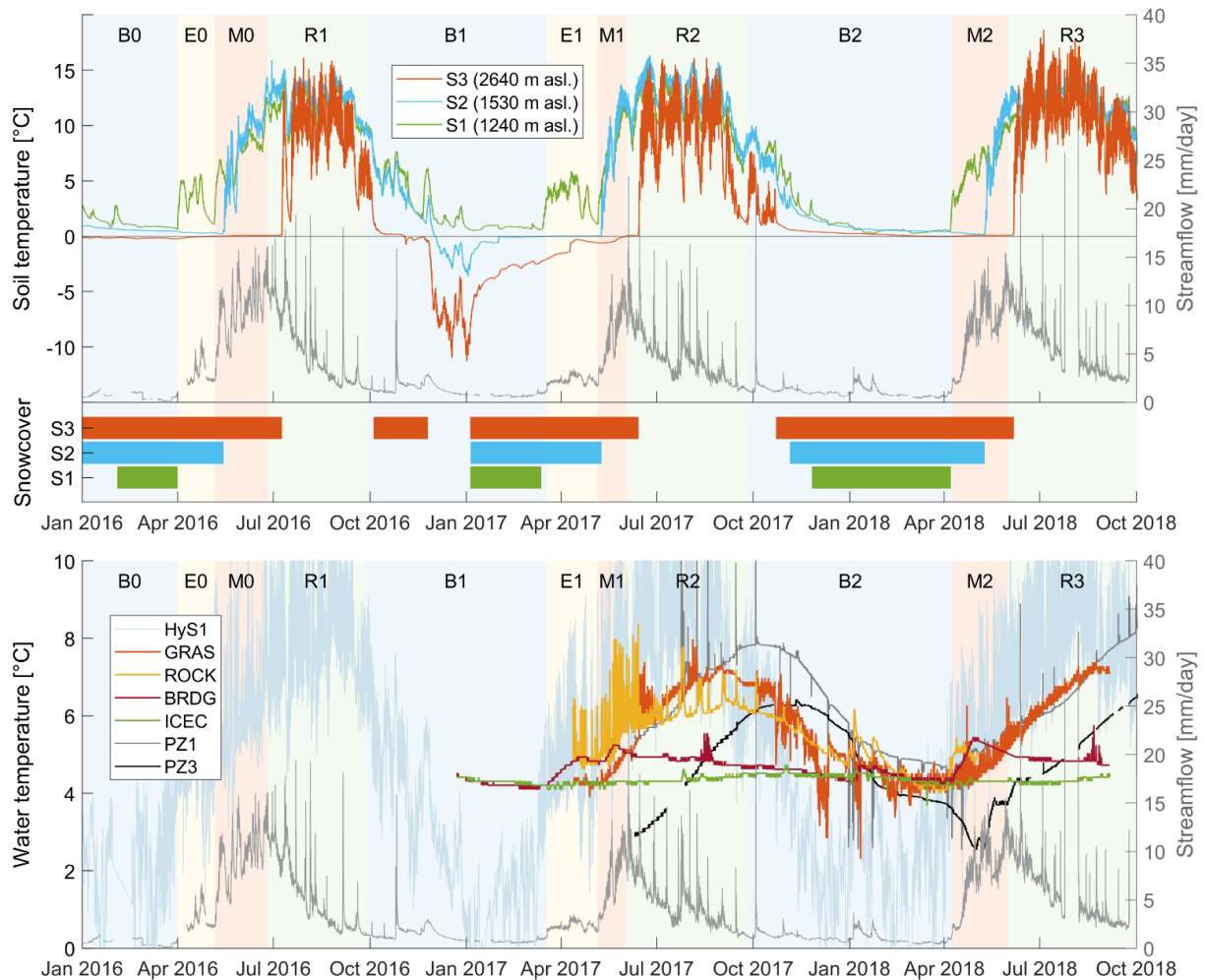


Figure 54. Evolution of soil temperature (top) at 3 locations within the Vallon de Nant catchment and (bottom) of the stream at the outlet, 4 springs and groundwater at 2 locations between January 2016 and October 2018. A summary of dates is available in the Supplementary Material, .

6.4.3 Water temperature

Influence of air temperature on stream temperature

Average recorded stream temperature at the outlet corresponds to 5.0 °C, which is slightly higher than the average recorded air temperature at mean elevation 2,012 m asl, which equals 3.1 °C. The fluctuations of the water temperature at the catchment outlet (HyS1, Figure 52) are correlated with the variations of the air temperature ($R^2 = 0.87$ between water temperature and air temperature at the Auberge weather station) and the annual cycle shows no lag with respect to air temperature. This can be explained by the fact that the in-stream travel time is long enough for atmospheric heat exchange to exert a strong influence on water temperatures (Gallice et al., 2015). The importance of the instream atmospheric heat exchange is also supported by the high annual and diel temperature amplitudes (Table 17), in

close correspondence to the observed air temperature amplitudes over the year (between 17.5 and 19.5 °C at the lower elevations, with a 30-day moving average).

Spring temperature

Regarding the temperature recordings in the sampled water sources (springs and groundwater), they show varying correlations with air temperature at the Auberge station (Table 17); PZ1 has the strongest correlations ($R^2=0.80$) and ICEC the weakest ($R^2=0.56$).

The GRAS spring is a permanent source of water but is small in volume, with an outflow of only a few liters per minute (personal observation). The temperature is recorded directly in the outflowing water, the sensor might thus heat up by atmospheric heat exchange in case of very low outflow rates. This most probably explains some strong sub-daily temperature fluctuations of the GRAS (and ROCK) springs (Figure 54). Despite these diel fluctuations, the GRAS temperature signal does not seem to react to the summer rainfall events (visible as peaks on the streamflow), whereas ROCK shows a reaction.

The shape of the temperature signal of the BRDG spring differs from the sinusoidal shape of the GRAS and ROCK springs (the shape of the air temperature variations). The BRDG spring signal shows a constant temperature during winter, with an increase during the early melt and melt periods, with e.g. a temperature rise from 4.3 °C to 5.4 °C over 3 weeks at the beginning of M2. The temperature rise stops around the time when soil temperature at mid-elevation shows snow disappearance (blue bar in Figure 54) and then recedes to winter base temperature. These two patterns (strong reaction during melt at low elevations, return to a base temperature during winter) suggest that the BRDG spring is fed by snowmelt from low elevations (from the right bank riparian area where it is located) during spring and by groundwater the rest of the year.

All spring temperatures converge at around 4.3 °C at the end of B2 (the only winter period measured in all springs), which corresponds to the almost constant temperature of ICEC spring (annual amplitude of 0.4 °C, Table 17).

The two piezometers that access the groundwater (PZ1 and PZ3) are both located in the alluvial floodplain where the stream meanders. During intense rainfall events, PZ1 shows strong positive temperature excursions, which can even exceed streamflow temperature in summer; its winter anomalies are smaller. The annual cycle of the PZ1 temperature reaches its maximum temperature of 7.9 °C with a delay of 74 days (2.5 months) after the air maximum

and exceeds the maximum recorded in the springs by 1.5 °C. The strong delay of the annual cycle together with the warm temperatures and relatively small amplitude dampening compared to ROCK and GRAS springs suggests that it is influenced by a large storage volume which induces the delay and is closely connected to heat input from the surface.

PZ3 shows the same annual temperature amplitude as PZ1 but has an even longer delay (21 days with respect to PZ1) and has a negative offset of 1.5 °C of its maxima (6.4 °C for PZ3) compared to PZ1, possibly related to the higher elevation and more northern aspect of its source area (PZ3 is located 30 m higher, in the more north-facing part of the catchment). PZ3 has, however an average temperature of 4.8 °C closer to the one of the springs.

A distinctive feature of PZ3 is its temperature decrease during M2, in phase (but in opposite direction) with the streamflow increase. This suggests a direct, relatively important cold input during snow melt, resulting from a high hydrologic connectivity of PZ3 to snowmelt water (either directly or via exfiltration from the stream) and a low storage volume during this time of the year.

Flowpath depth estimation

We can use a simple analytical temperature model with sinusoidal initial conditions (e.g. Elias et al., 2004) to compute a rough depth that would correspond to such a lag L (for details see Appendix 2). With a typical thermal diffusivity of soil of $5.56 \cdot 10^{-7} \text{ m}^2/\text{s}$ (Elias et al., 2004) a lag of 41 days would correspond to a depth of 1.7 m, a lag of 39 days to 1.6 m. The dampening depths estimated for the other water sources are reported in Table 17. They should however be interpreted with care as i) the presence of an insulating snowpack on the hillslopes prevents heat advection during winter, thereby further increasing temperature lags and amplitude dampening in the subsurface, and ii) the model is only based on heat conduction and does not account for advection that could be locally important during snowmelt inputs.

Such limitation is reached at BRDG, as the temperature variation over the year (0.9 °C) happens over few weeks during melt periods (M1 and M2); this variation shows a strong reactivity to the snowmelt input but the resulting estimation of flowpath depth (0.2 m) is obviously erroneous. At this time, the maximum air temperature is not reached yet (during R2 and R3) and the expected heat signal transferred from air by conduction later in the year is finally not visible.

All subsurface water temperatures except one have a dampened annual cycle and a positive lag compared with streamflow temperature, which can be explained by the delay resulting from heat conduction (depending on the soil's thermal diffusivity D) and advection with water flow. The one exception is BRDG, for which lag estimation fails. The lags are furthermore coherent with the dampening: stronger lags correspond to stronger dampening and are associated with deeper depths.

Table 17. Statistics on temperature time series recorded in the stream, piezometers, and springs. The dampening depth estimated for the BRDG spring () is biased because of a positive anomaly of temperature due to snowmelt input (see text).*

Water source	Mean T [°C]	Max T [°C]	Annual T amplitude [°C]	Max. diel T amplitude [°C]	Cross corr. w/ air T		Dampening depth [m]	Snowmelt anomaly	Rainfall anomaly
					Lag [days]	Max corr. [-]			
Stream	5.0		8.8	11.4	0	0.92	-	-	-
PZ1	6.3	7.8	3.8	4.0 (punctually)	79	0.80	3.2	No	Yes
PZ3	4.8	6.3	3.7	0.5 (punctually)	105	0.68	4.3	Negative	No
GRAS	5.5	7.4	3.0	2.4	41	0.76	1.7	No	Yes
ROCK	5.4	6.7	2.5	2.9	39	0.76	1.6	Positive	yes
BRDG	4.7	5.6	0.9	0.9	6	0.68	0.2*	Positive	No
ICEC	4.3	4.7	0.4	0.6 (noise)	133	0.54	5.4	No	No

6.4.4 Electrical conductivity

The electrical conductivity of all samples is high compared to what we could expect in an Alpine environment (Cano-Paoli et al., 2019). The median value of 216 $\mu\text{S}/\text{cm}$ in the streamflow samples at the outlet (Figure 55 F) is not significantly different from the streamflow samples of the upper subcatchment (HyS2, median EC of 215 $\mu\text{S}/\text{cm}$); assuming a spatial homogeneity between flow path depth and flow velocity, this similarity suggests a similar flow path length distribution. The temporal evolution of EC in the stream shows a typical seasonal pattern (Penna et al., 2014; Cano-Paoli et al., 2019), with a decrease in EC during the melt season. A similar pattern was observed by Chiaudani et al. (2019) for a large aquifer in Italy, who explained that it results from the large amount of melt water that recharges into the aquifer and creates a decrease of electrical conductivity, resulting from a combined effect of volume increase and dilution. This dilution effect is obtained because any recharging water has a shorter subsurface residence time than old water and accordingly a lower ionic content and thus EC (Cano-Paoli et al., 2019). We furthermore observed a certain time lag between the seasonal cycles in EC and streamflow cycle (Figure 57), which was previously shown by Cano-Paoli et al. (2019). On an event-scale basis, a similar lag between streamflow and EC has been previously observed and is explained by the well-known delay

between the transmission of pressure waves (leading to discharge increase) and the actual arrival of newly recharged water (Chiudani et al., 2019). This event-scale lag will ultimately lead to a shift of the seasonal cycle of streamflow and EC.

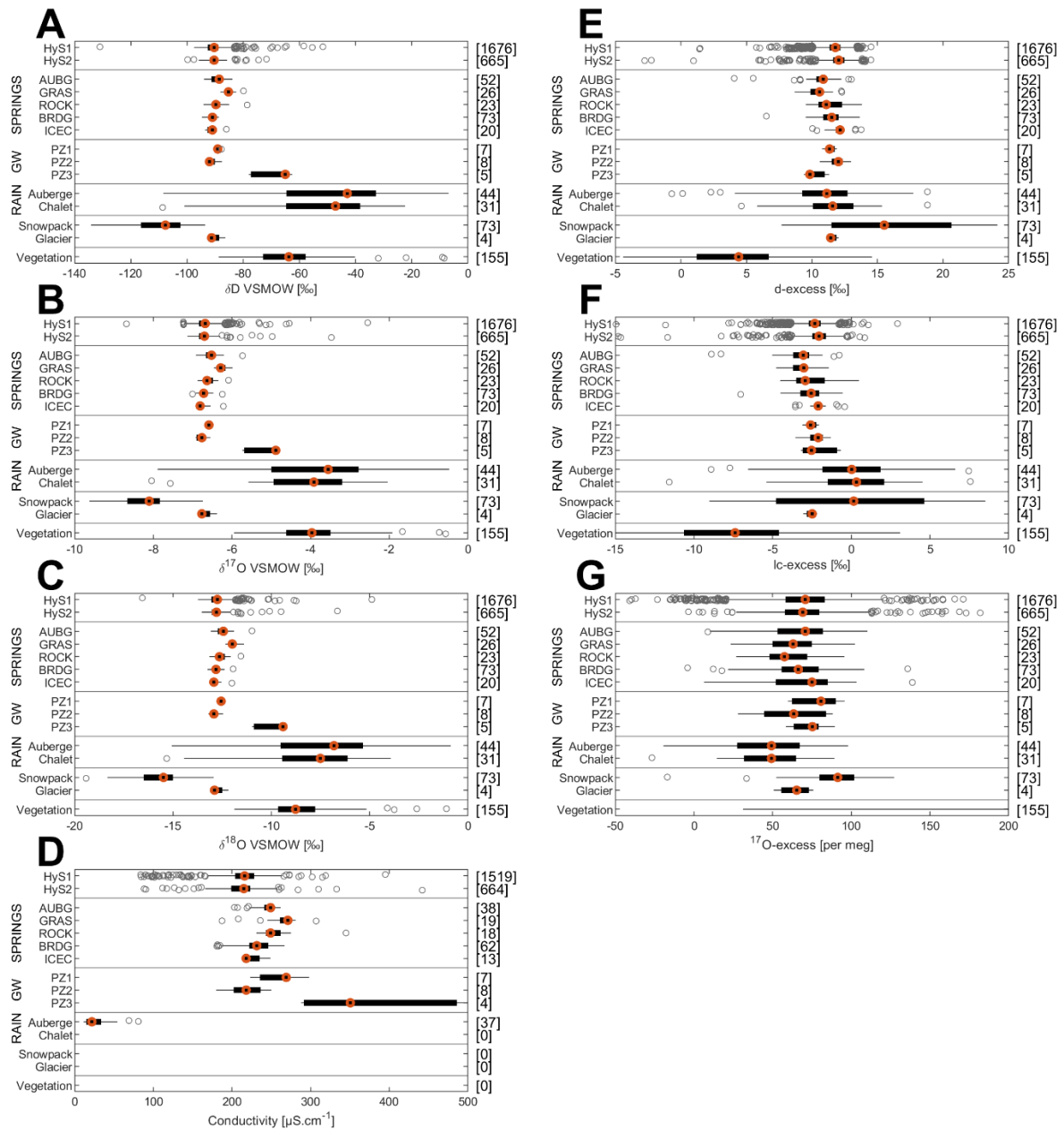


Figure 55. Range of $\delta^2\text{H}$, $\delta^{17}\text{O}$, $\delta^{18}\text{O}$, conductivity, $d\text{-excess}$, $lc\text{-excess}$ and $^{17}\text{O}\text{-excess}$ for stream, springs, groundwater, rainfall, snowpack, glacier and vegetation water samples. The left and right end of each box show the 25th and 75th percentiles, and the middle point is the median. The whiskers go up to 1.5 times the interquartile range; values beyond the whiskers (outliers) are marked with circles. The values on the right y-axis of the figures are the number of samples in each category. Note that there are no conductivity measurements for snowpack and vegetation water samples. For $^{17}\text{O}\text{-excess}$ the values of vegetations samples are out of the box (median 572 ‰, 25th and 75th percentiles are 374 ‰ and 742 ‰, resp., and whiskers are from 31 ‰ to 8329 ‰).

All springs, except ICEC have higher EC values than the stream or the groundwater. Higher EC values point towards longer flow paths in the subsurface, either vertically or laterally (Cano-Paoli et al., 2019), or alternatively longer residence times of the water, hence lower flow rates. The spring with the highest EC (GRAS, median EC of 271 $\mu\text{S}/\text{cm}$) shows the least temperature dampening, and vice-versa, the spring with the lowest EC (ICEC, median 211 $\mu\text{S}/\text{cm}$) shows the most dampening (where high amounts of dampening indicates deep flow paths in the subsurface). Assuming an homogeneous underlying geology, the only possible explanation of EC signals in conjunction with the temperature signals is thus that low EC values of subsurface water result from short flow paths in the shallow subsurface (GRAS spring), and relatively high EC values result from longer and deep flow paths (ICEC).

6.4.5 Stable isotopes of water

Ranges of $\delta^2\text{H}$, $\delta^{17}\text{O}$ and $\delta^{18}\text{O}$

The overall observed ranges of isotopic compositions ($\delta^2\text{H}$, $\delta^{17}\text{O}$ and $\delta^{18}\text{O}$ values), d-excess, lc-excess, ^{17}O -excess and EC of all water samples are summarized in Figure 55 and their temporal evolution is shown in Figure 56, Figure 57 and Figure 58.

The sampled rain water has a lapse rate of 0.84 ‰/(100m) for $\delta^2\text{H}$ and 0.128 ‰/(100m) for $\delta^{18}\text{O}$, which is approximately half the isotopic lapse rates of precipitation observed in Switzerland (e.g. Beria et al., 2018), with an ensuing higher median value at the lower Auberge weather station.

This lapse rate does not show up in the stream water (Figure 55 a, b, c). A rough computation (see also Appendix 3) shows that the distribution of elevations connected to HyS1 is not sufficiently different from the distribution at HyS2 to lead to a significant off-set of the isotopic values at the two streamflow sampling locations, despite the isotopic lapse rate. This most likely also explains the similar median isotopic values of all sampled water bodies, except the GRAS spring, with a significantly higher median value. This suggests that this spring might receive water only from a small low elevation subcatchment and not from the high rock walls located next to it.

The median $\delta^{18}\text{O}$ value of all streamflow samples equals -12.7 ‰, which is in line with the slightly lower values observed for the Rhone in Porte de Scex (Schurch et al., 2003), of which Vallon de Nant is a headwater catchment (albeit one with relatively low elevations compared to other headwater catchments of the Rhone).

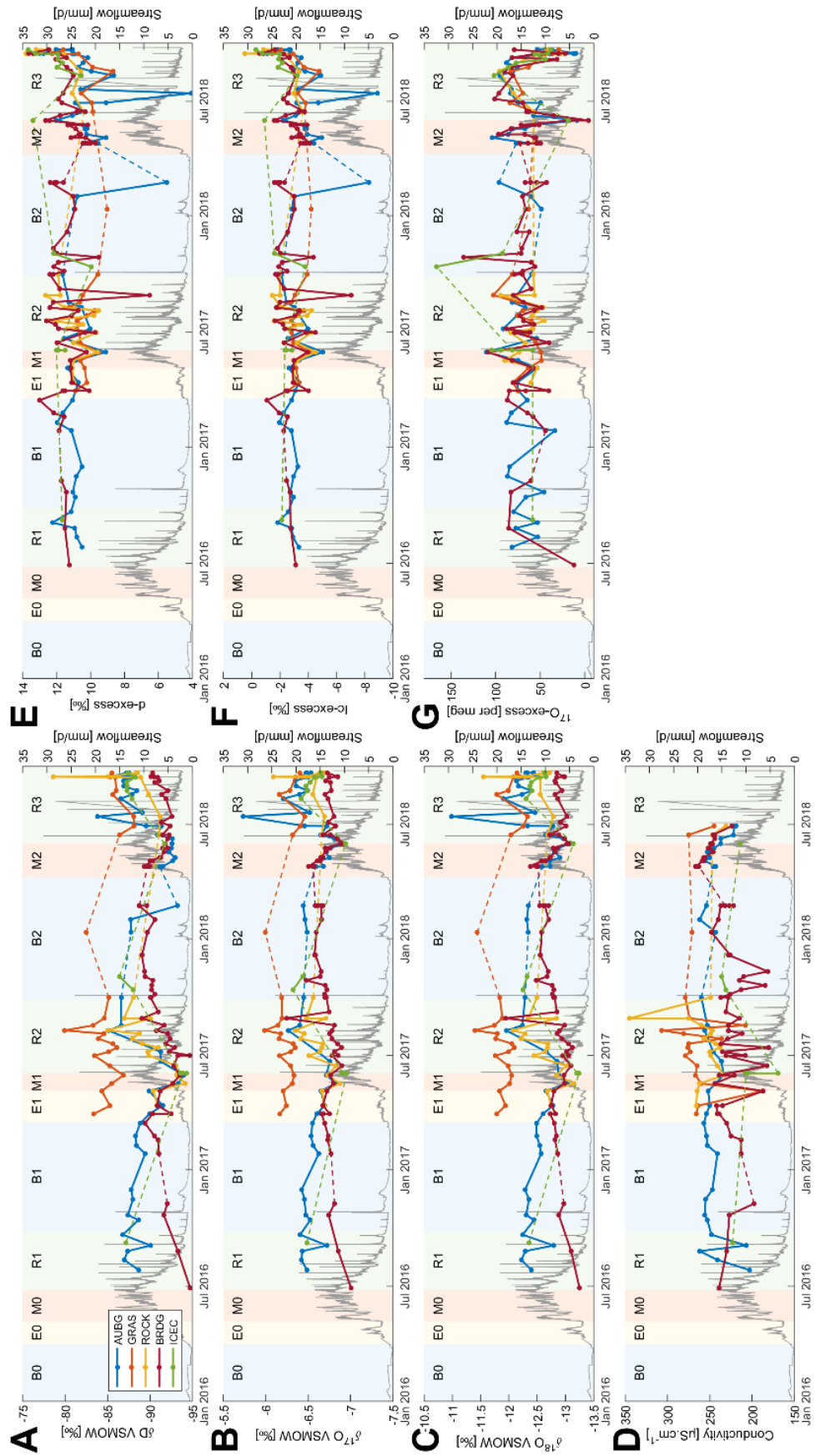


Figure 56. Time series of $\delta^2\text{H}$, $\delta^{17}\text{O}$, $\delta^{18}\text{O}$, conductivity, d -excess, lc -excess and ^{17}O -excess for 5 springs (location on map Figure 52 A).

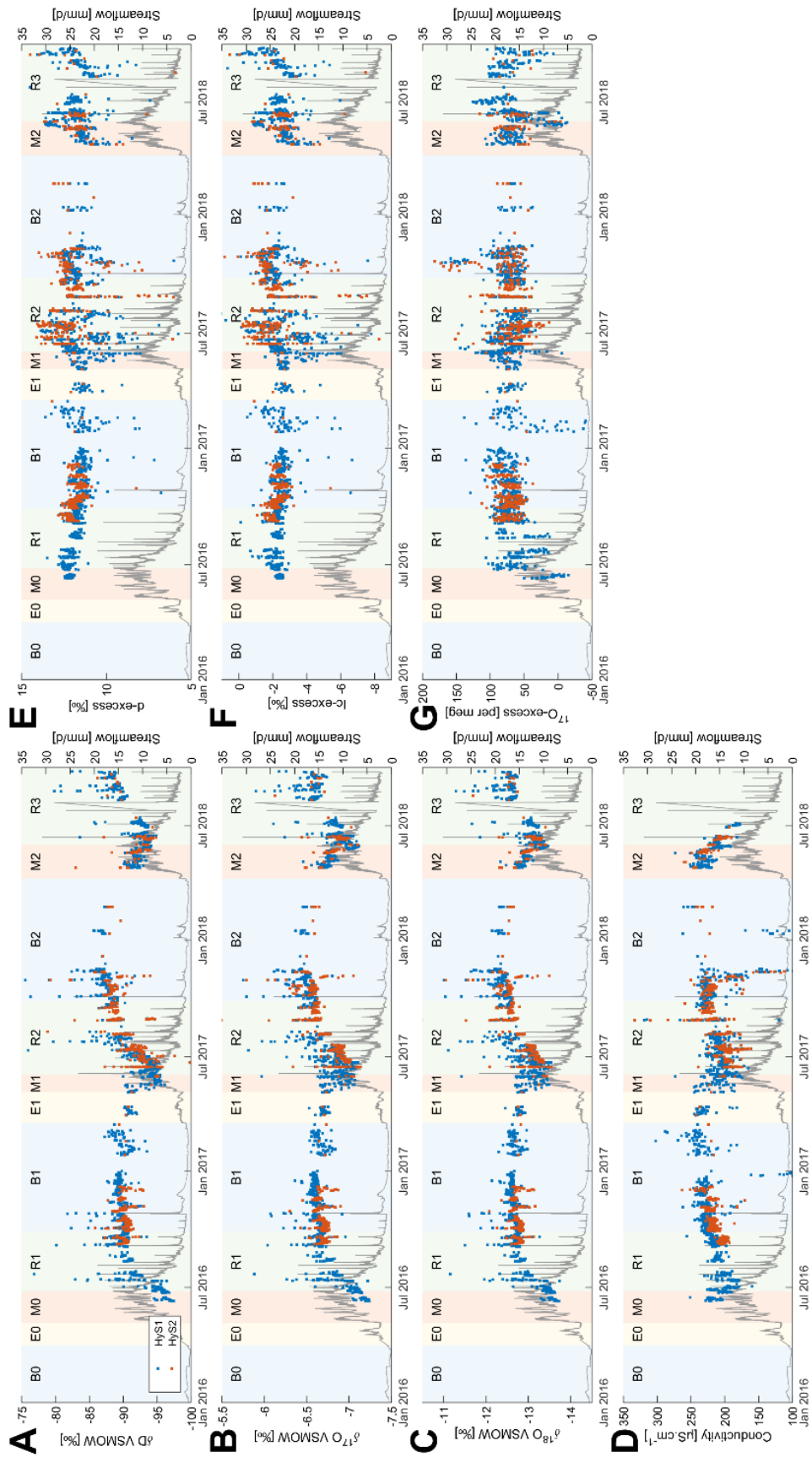


Figure 57. Time series of $\delta^2\text{H}$, $\delta^{17}\text{O}$, $\delta^{18}\text{O}$, conductivity, d-excess, l-excess and ^{17}O -excess at the Vallon de Nant outlet HyS1 and at the upper subcatchment HyS2 (location on map Figure 52 A).

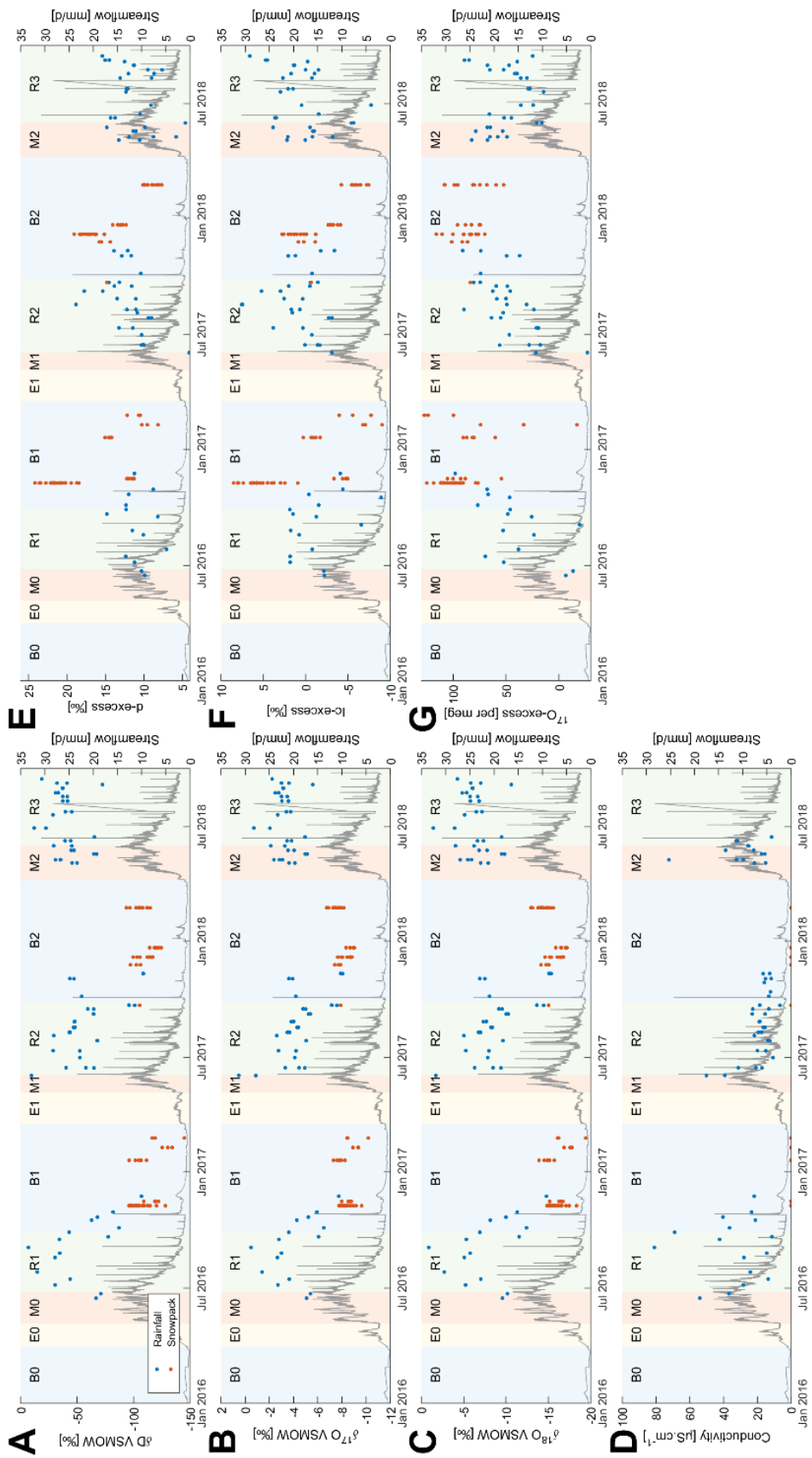


Figure 58. Time series of $\delta^2\text{H}$, $\delta^{17}\text{O}$, $\delta^{18}\text{O}$, conductivity, d -excess, lc -excess and ^{17}O -excess for rainfall (from Auberge and Chalet weather stations, location on map Figure 52 A) and snowpack. Note that the conductivity of snowpack has not been measured.

Dynamics of $\delta^2\text{H}$, $\delta^{17}\text{O}$ and $\delta^{18}\text{O}$ in springs

The fluctuations of the isotopic composition from 6 springs monitored between July 2016 and September 2018 is discussed qualitatively based on the streamflow periods (see Figure 56). The relative variations being similar between $\delta^2\text{H}$, $\delta^{17}\text{O}$ and $\delta^{18}\text{O}$, only the $\delta^{18}\text{O}$ variations are commented hereafter.

Despite some variability, the AUBG spring $\delta^{18}\text{O}$ values remain relatively constant ($\delta^{18}\text{O}$ between -12.8 ‰ and -12.2 ‰) during the 2016 streamflow recession R1 and then slowly decrease throughout the 2016/2017 baseflow period B1. Meanwhile, the BRDG spring starts with more depleted isotopic values (-13.3 ‰) but get enriched in the heavy isotopes through R1 and B1 to finally have a similar composition during the 2017 early melt period (E1) compared to the AUBG (and ROCK) springs, also with a subsequent decreasing trend in the heavy isotopes.

The 2017 minimum isotopic values of the AUBG, ROCK and BRDG springs are reached around the time of 2017 maximum streamflow and then diverge during the 2017 recession period (R2), increasing at a different rate: the δ -values of AUBG and ROCK springs increase quickly (+1.0 ‰ in 3 months), while the BRDG spring values only initiates a slow increase that will continue throughout winter (B2).

The beginning of the 2018 melt period was exceptionally fast, without an early melt period. The springs sampling started 3 weeks after it's the beginning of the early melt period, with a significant part of the snowpack having melted already. As during M1, the isotopic composition of the AUBG and BRDG springs over this period shows a constant decrease in the heavy isotopes until the 2018 streamflow maximum. At the inverse of R1, the BRDG composition then remains constant during the recession, while the AUBG spring increases quickly in the δ -values.

The pattern repeats during the 2018 melt period (M2) with a decrease in δ -values, which then diverge at different rates. Again, the BRDG spring δ -values increases slowly, while for the AUBG and ROCK springs the increase is faster.

The ICEC spring, located on the western slopes (Figure 52), tends to follow the same isotopic pattern as the AUBG spring. Although, because of its lower sampling rate, points are missing at the critical moments during the melting periods, and so we cannot discuss the differences in timing. It can be pointed out also that ICEC shows higher isotopic values compared to BRDG even if it is located at a higher elevation. This can be explained by the higher maximum

elevation of the mountain ridge upstream of BRDG compared to ICEC (see Figure 52), which most certainly leads to a higher snowfall proportion for BRDG.

As discussed earlier, the GRAS spring behaves differently from other springs, with higher δ -values than all the others in 2017. EC and temperature measurements indicate that this spring has relatively shallow flow paths and its δ -values also suggest a larger proportion of rainfall-derived water (which has a higher average δ -values than snowmelt).

Dynamics of $\delta^2\text{H}$, $\delta^{17}\text{O}$ and $\delta^{18}\text{O}$ in streamflow

The temporal evolution of the isotopic ratios in the streamflow shows high $\delta^2\text{H}$ values during winter baseflow, close to the median value of all sampled subsurface water bodies, and a significant decrease in the heavy isotopes during the melt periods.

Streamflow is thus largely fed by recent (isotopically light) snowmelt during the melt period; the decrease of the δ -values is proportional to the amount of snowmelt, with a larger decrease in 2017 compared to 2018.

The early melt period does not decrease the δ -values, which suggests that during this period, the streamflow is composed of previously stored groundwater and not of recent, mid-winter snowmelt at hydrologically close areas (e.g. in the floodplain or the riparian area), as is assumed in some models (Schaefli et al., 2014).

d-excess

The sampled rainfall has a median d-excess of 11.3 ‰, which is in the range of published values for rainfall in the Swiss Alps (Leuenberger and Ranjan, 2021). The snowpack samples have a median value of 15.5 ‰. Values from the Swiss Alps (Grimsel, Schotterer et al. (2004)) show similarly high d-excess values in winter. High d-excess from snowpack is caused by the assumed source of winter precipitation, the Mediterranean Sea (Froehlich et al., 2002). Secondary evaporative process happening within the snowpack or on the snowpack surface led to a further shifting away of the isotopic ratios from the GMWL, i.e. to a decrease of the d-excess values. Since we did not sample fresh snowfall but from the snowpack, we can safely assume that the original fresh snow in our catchment could have even higher d-excess values. Secondary evaporation effects also explain the low d-excess values for the glacier ice samples.

The surface and subsurface water samples show d-excess median values close to that of rainfall and considerably lower than the median value for snow. The apparent surface and subsurface water samples bias towards the d-excess value of rain can be explained by

secondary evaporation (from the soil or vegetation); the soil water that remains (and that ultimately recharges groundwater and the streams) thus has a lower d-excess value than either rainfall or meltwater. This process also explains the low d-excess values of xylem water in vegetation.

The above illustrates that d-excess values are rather difficult to interpret in terms of local scale process information ; the significant difference between the values for rainfall and snow pack indicates some potential to quantify snowfall and rainfall proportions in streamflow but secondary evaporative processes prevent a straight forward estimate. For ice melt, d-excess values are too close to those of rainfall for providing further insights into its importance in streamflow.

LC-excess

Figure 55 F shows the computed LC-excess values. The range of values for the rainfall samples are related to the spread around the evaporation line. We see that the median value of the snowpack samples is close to the reference for rainfall (0 ‰), which is in line with the findings Beria et al. (2020) who reviewed snowpack data for entire snow seasons and does often not show a significant deviation from median values for the reference precipitation value. On average, secondary snow evaporation does not appear to be important in our catchment. The xylem water samples from larch trees show the expected low LC-excess values due to strong evaporation effects.

All subsurface water and stream samples have a negative median value, indicating that all recharged water in this catchment has undergone evaporation, albeit at degrees that vary in space and time. Compared to other subsurface samples, the ICEC spring samples seem to be less affected by evaporation (has a higher LC-excess value), which agrees with the fact that the area upstream of this spring is occupied by only low growing vegetation (meadow and shrubs) and that for this spring the rainfall is directly exfiltrated.

¹⁷O-excess

Our computed ¹⁷O-excess values of rainfall (Figure 55 G) are much higher than the few published values in Switzerland, which range from 6.5 per meg (Leuenberger and Ranjan, 2021) to 18 per meg (Affolter et al., 2015) for low and high elevation locations. There are no published values for snowfall or snowpack for Switzerland, but values between 17 and 62 per meg for freshly precipitated snow on Mount Zugspitze (German Alps, 2,962 masl) are found

in the work of Surma et al. (2021). Our values for snow have a median value of 91.3 per meg and are significantly higher than for rainfall (49.2 per meg).

The difference between rainfall, snowpack and glacier observed for $\delta^2\text{H}$, $\delta^{17}\text{O}$ and $\delta^{18}\text{O}$ is also visible with ^{17}O -excess, but not with d-excess. ^{17}O -excess could potentially be useful to distinguish between rainfall, snowpack and ice melt but secondary evaporative processes complicate a direct interpretation.

Given that the local and global reference lines for ^{17}O are very similar (see Section 6.3.1), it is tempting to interpret the spatial differences in ^{17}O -excess values; the median values of all sampled water show a coherent picture, with subsurface and stream water having intermediate values between rainfall and snow samples and thus being a mix thereof. As for d-excess, we can however not draw any direct conclusions on mixing ratios since rainfall and snowfall undergo further evaporative processes during recharge.

Furthermore, the temporal dynamic of ^{17}O -excess in springs does not show additional information compared to d-excess. Given the lack of reference data at comparable sites, we cannot elaborate further at this stage.

6.5 Discussion

Below we discuss how the above findings contribute to answer our research questions on the origin of streamflow and on the role of subsurface flow.

6.5.1 Origin of winter streamflow

The streamflow in the studied catchment shows the typical seasonal recession leading to an almost constant winter baseflow between January and March. It is tempting to assume that such catchments are essentially dormant during winter (Schaeferli et al., 2013) without any liquid water input, and thus to use the constant end of winter baseflow to infer total storage (Cochand et al., 2019). However, we observed diverging isotopic ratios in two springs, showing either an enrichment in heavy isotopes (AUBG) or an enrichment in light isotopes (BRDG) during winter (Figure 56). Such an enrichment by light isotopes can only be explained by the presence of winter melt processes feeding light isotopes throughout the winter to the respective groundwater system.

The result is also supported by the relatively constant EC value of the AUBG spring: in absence of any inflow, we would expect a gradual aging of the water and thus an increase of EC. Therefore, assuming the water is not saturated with regards to the ionic charge, a constant

value suggests a permanent new water input (with low EC) during winter. Thus, in the Vallon de Nant, winter base flow is the combined result of the long seasonal recession and some small input during winter; whether this input is related to air-induced snowmelt or ground heat melt (Schaefli, 2016) remains to be investigated.

6.5.2 Dominant runoff processes driving streamflow generation during early spring snow melt

The start of the two early melt streamflow periods corresponds to the disappearance of snow at the lowest soil temperature measurement point (1,240 masl). This suggests that this early melt streamflow rise might well be linked to local snowmelt water input to the stream at the lowest elevation. At the same period, at higher elevations, the snow cover is still in place (according to the soil temperature observations). It is unknown whether snow melt is already occurring at these higher elevations during the early melt period since potential snow melt might most probably be retained in the existing snowpack or in the subsurface.

Furthermore, the streamflow increases at the beginning of E1, but that the decrease of EC is delayed (Figure 56), suggesting that older water (with high EC) is pushed into the stream at the beginning of E1. This is consistent with the unchanged isotopic composition of streamflow during E1, showing that streamflow input is dominated by groundwater during this period.

6.5.3 Dominant runoff processes during melt periods

Although the $\delta^2\text{H}$, $\delta^{17}\text{O}$ and $\delta^{18}\text{O}$ annual medians of AUBG, ROCK, BRDG and ICEC show an enrichment in the light isotopes with elevation (Figure 55), these values are difficult to compare due to the number of samples and the sampling dates that vary by source. However, we notice in Figure 56 that the isotopic compositions of these 4 water sources converge towards a common value during M1 (around -93.5 ‰ for $\delta^2\text{H}$, -6.8 ‰ for $\delta^{17}\text{O}$ and -13.0 ‰ for $\delta^{18}\text{O}$), which suggests that the entire subsurface is flushed with snowmelt that either comes from a similar elevation range or that sampled all elevation ranges in a similar way.

The higher EC values in the stream compared to the springs during the melt period (Figure 56, Figure 57) are unexpected: it suggests that there is a significant amount of subsurface water reaching the stream that has a higher EC value than all sampled springs. This result however underlines the importance of subsurface flow paths during melt periods.

The positive temperature anomalies (during summer rainfall events) observed during M2 (ROCK) shows the existence of fast surface flowpaths but are not enough to explain the high EC values at this period.

6.5.4 Dominant runoff processes during the seasonal recession

The divergence of the isotopic composition of the four springs (AUBG, ROCK, GRAS and BRDG) after the melt period (due to increased summer rainfall contributions) give clues, qualitatively, either about their respective reservoir size or about their respective relative permeabilities and/or outflow rates: a smaller increase in δ -values indicates hereby a larger reservoir or slower flow rates/permeabilities (e.g. BRDG); a relatively rapid increase in values is associated to a small reservoir size or to high permeabilities/flow rates (e.g., AUBG).

The EC increase of springs and streamflow during R2 shows the prevalence of deeper flowpaths, as the stream water get less diluted by the shallow and faster flowpaths (low EC) from snowmelt contribution.

6.5.5 Interplay of shallow groundwater in the hillslopes and of alluvial or talus groundwater systems

During M2, both BRDG and PZ3 temperature signals are correlated with streamflow variations, but the positive temperature anomaly measured at BRDG suggests a snowmelt input that is heated up before infiltration (due to heat exchange during surface runoff), while the negative temperature anomaly for PZ3 suggests the melted snow is directly infiltrating. Indeed, the subcatchment area of BRDG collects snowmelt from the nearby riparian area and steep slopes facing west that are exposed to sun radiation, while the temperature anomaly for PZ3 begins with the melt period start and ends approximately when the area is free of snow (200 m from soil temperature sensor at 1,530 masl), which suggest a local infiltration of snowmelt. The water temperature is usually influenced by ground temperature, but the high hydraulic conductivity in the area of PZ3 probably does not allow time for the water temperature to reach equilibrium. This temporary (6 weeks) and local snowmelt input is superimposed on a longer scale pattern that leads to 74 days of lag between PZ3 and air temperature. This suggest that we have here a groundwater system that is very well connected to surface water during the melt period, but with a much more dampened response later in the year.

The PZ1 (470 m to the north) reacts in a different way: the 58 days of lag indicate a shallower flow path, but without temperature anomaly during the melt period. Short-term temperature anomalies (positive during the summer, negative during the winter) associated with rainfall events suggest local incursions of surface water, which is however in contradiction with the absence of temperature anomalies during the melting period. One possible explanation is that the stored water volume is small enough (with water levels between 0.8 and 2.4 m below the surface, see Supplementary Material, Figure S125) during R2 and B2 to react quickly to local

surface inputs, while during M2 the stored volume is high enough (with water level between 0.1 and 1.0 m below the surface) to not show short term reactions to melt water input.

The average temperature difference between PZ1 and PZ3 (mean 6.3°C and 4.8 °C over the year) can most likely be explained by their respective subcatchments: PZ1 (left bank) collects water from the grassy slopes of the west side of the valley (facing east), while through PZ3 (right bank) flows water from the south (facing north), with more shaded areas and snowpack remaining later in the year.

At the end of B2, the 4 springs tend to converge to a temperature around 4.3°C and if we limit ourselves only to this variable, we could think that this is pointing toward a common aquifer feeding them during baseflow. The shift of the PZ1 and PZ3 temperatures (+0.4 °C and -0.5 °C) at the end of baseflow could be explained by a calibration issue. The fact that streamflow isotopes during B2 are close to the median value of all sampled water sources suggests that our spatial sampling was good enough to represent the main water sources during baseflow.

The available EC measurements clearly suggest that the subsurface flowpath distributions are very similar in the upper part of the catchment (HyS2) and in the lower part of the catchment (HyS1). This is supported by the fact that the isotopic lapse rate observed in rain water does not show up in streamflow.

The isotopic composition of GRAS is quite different from that of the other sources (mean values of -85.3 ‰ for $\delta^2\text{H}$, -6.3 ‰ for $\delta^{17}\text{O}$ and -12.0 ‰ for $\delta^{18}\text{O}$). The absence of a temperature anomaly during the melt period suggests a large and well-mixed source of water. The high thermal connectivity with the surface could then be explained by a shallow flowpath over a certain distance before the water exits at the source. However, we still cannot explain why the temperature signal shows a variation induced by rainfall, whereas there is no variation due to snowmelt input.

6.5.6 Transferable insights into the value of the observed variables for hydrologic process investigations in comparable catchments.

Water sources temperature and shallow soil temperature

Although temperature is not a conservative tracer, temperature measurements of springs are very useful to estimate flowpath depth. However, the underlying assumption that heat transfer is essentially driven by conduction might not always be verified (Kane et al., 2001),

and anomalies between measured and modelled temperature (pure sinusoid) could be related to heat transport with subsurface water flows (i.e. to advection phenomena).

At shallow depth (10 cm), the soil temperature is strongly influenced by air temperature, and the present analysis of soil temperature at different elevations shows that it is a good proxy for the detection of snow cover. Early melt starts when the soil temperature at low elevation (1,240 masl) rises, showing that snow is melting in the area close to the outlet (1,200 masl). The temperature sensor, albeit not intended for this use, seems to be well positioned to detect the onset of early melt for the melting seasons in 2016 and 2017 (no early melt in 2018).

For the other soil temperature recordings, there is no direct link to the streamflow dynamics. The time elapsed between the snowmelt onset on the next higher soil temperature site (1,530 masl) and the beginning of the melting period varies significantly but is always positive (8 days in 2016, 3 days in 2017 and 51 days in 2018). The large variations of this lag time tend to indicate that the snowpack disappearance might not be a good proxy for actual snowpack melt outflow. Indeed, the underlying assumption is that snowpack disappearance might follow a similar pattern from one year to the other, but it does not consider the area which is actively melting and supplying melted snow, nor snowpack thickness.

A larger number of soil temperature sensors would provide an interesting perspective to identify more precisely the relative contributions of the different landscape units, elevations, and terrain aspects. This could be particularly promising in combination with satellite images for snow cover mapping.

Isotopic composition of springs and stream water

Stable isotopes of water are particularly promising to track the co-existence of seasonal baseflow and winter melt within springs and shallow groundwater. However, this requires year-round time series to understand which locations become enriched in heavy isotopes with time throughout the winter and which ones become depleted. This year-round monitoring is particularly important since, as we have shown, many subsurface signals are likely to see a “reset” during the main melt period.

The range of isotopic composition for each source informs on the relative snowmelt proportions from their respective subcatchments. Without evidence of a strong isotopic lapse rate in snowfall, the differences measured can be explained by the variation of snowfall amounts with elevation.

The relative proximity of some water sources monitored in this study underlines that spatial proximity does not necessarily imply similar behaviours (in terms of temperature or isotopic composition), as we see noticeable differences between the sources due to the different characteristics of their subcatchments (i.e. flowpath depth, hydraulic conductivity, slope, aspect).

LC-excess values might reveal some additional insights in future work, in combination with future analyses of soil water isotopes (to give insights into evaporation effects).

At this stage, it is not clear either what the value of ^{17}O -excess is for hydrological purposes and the question whether it conveys local scale information remains open. These measures would have probably been more relevant if fresh snow was sampled instead of the snowpack. Even if we cannot draw any interesting conclusions, the publication of these values will nevertheless be useful for future work.

The added value of EC

EC allows a qualitative estimation of the water age, but the difficulty to characterize the different physical and geochemical properties of soils (influencing EC) do not allow an intercomparison of absolute EC values between the sources. However, the variations at a given source may inform on the snowmelt input (low EC) or the flowpath dynamic (old water pushed by water input). Especially in catchments that, similarly to ours, show little elevational gradients in the isotopic ratios of different water sources, EC represents an extremely valuable tracer to observe in addition to isotopes and water temperature, i.e. when having changes in EC which are not following the changes in the isotopic composition.

6.6 Conclusion

We presented a detailed study on the interplay of hydrological processes across all streamflow seasons of a high Alpine catchment, with the help of temperature recordings and measurements of EC and of stable isotopes of water. The combined use of these three natural tracers has been shown to be very promising to analyze the temporal succession of surface and subsurface runoff contributions to streamflow, specifically around the “reset” of the isotopic composition during the melt period. The range of the isotopic composition of each source also informs on the relative proportions of snowmelt.

Our study of the isotopic composition of streamflow as well as of EC values suggest that i) subsurface flow plays a prominent role throughout all stages of the melt period and that ii)

winter streamflow might be partially fed by winter snowmelt and not by groundwater alone. Subsurface flow and winter melt might thus require more specific attention during future hydrologic model development.

Water temperature recordings have been shown to be particularly useful to trace the subsurface water, specifically the relative depth of different subsurface water sources and how well the reservoirs are connected to the atmospheric heat input; it has a particular added value when it is measured jointly with EC because it disentangles shallow flow paths from deeper flow paths (which both can lead to a high EC signal). These results show the interest of monitoring the temperature of each potential water source, as this measure is simple and gives solid insights about the water flowpaths. In particular, temperature recordings in springs together with elevation distributed soil temperature monitoring is extremely powerful. However, future monitoring strategies should pay more attention to EC monitoring to obtain estimates of the water age.

Much laboratory time was devoted here to the measurement of $\delta^{17}\text{O}$ and ^{17}O -excess, without providing conclusive insights in their added value for local-scale snow hydrological processes studies, except some potential to distinguish glacier melt from snowmelt. This is partly also due to absence of relevant reference data. We hope that the full value of the $\delta^{17}\text{O}$ data set presented here will be unravelled in the future.

Appendix 6 - 1: Influence of air on the isotopic composition of a water sample ($\delta^2\text{H}$, $\delta^{17}\text{O}$ and $\delta^{18}\text{O}$) within a sealed container

The purpose of this calculation is to estimate how the isotopic composition of a water sample locked up together with some air in a sealed container will be altered by the water vapor of the air. This configuration may happen i.e. with snow sampling as snow density ranging from 0.55 to 0.83 suggests that at least 17 % to 45 % of the volume in the container is ambient air from the sampling site. To make these calculations we consider the conditions in which the samples will be analysed; we take the ambient temperature of 25.3 °C for which we know the isotopic fractionation factor between vapor and liquid phases of water for $\delta^2\text{H}$, $\delta^{17}\text{O}$ and $\delta^{18}\text{O}$. At this temperature the samples are in a liquid phase, and in equilibrium with the air of their container.

Following Mook et al. (2008), the isotopic fractionation of water between two phases at the equilibrium is written as a reaction between the liquid l and vapor v phases of H_2O as:



where * marks the heavy isotopic form of the molecule that may contain ^2H , ^{17}O or ^{18}O , and δ^* its isotopic composition in per mil. At a given temperature T , the isotopic fractionation factor of water between liquid and vapor $\alpha_{l/v}$ is the equilibrium constant of the Equation 1:

$$\alpha_{l/v}(T) = \frac{[\text{H}_2\text{O}^*_l][\text{H}_2\text{O}]_v}{[\text{H}_2\text{O}]_l[\text{H}_2\text{O}^*_v]} = \frac{\delta^*_l/1000+1}{\delta^*_v/1000+1} \quad (21)$$

As we know i) the amount of liquid water in the container and its initial isotopic composition, ii) the amount of ambient air captured in the container and its initial isotopic composition, and that we can deduce iii) the total amount of heavy isotopes in the total amount of water, we can solve the Equation 2 as a second order equation.

The calculations are made for two extreme amounts of air vapor saturation, namely air without any water vapor and air fully saturated with water vapor. For the last one we take the partial pressure of water at 25°C $P=3169.9$ Pa (Haynes et al., 2017):

The value of the fractionation factor of water ^2H and ^{18}O between 0 and 100°C are (Majoube, 1971):

$$\ln \alpha_{l/v}^2(T) = 24.844 \cdot 10^3/T^2 - 76.248/T - 52.612 \cdot 10^{-3} \quad (22)$$

$$\ln \alpha_{l/v}^{18}(T) = 1.137 \cdot 10^3/T^2 - 0.4156/T - 2.0667 \cdot 10^{-3} \quad (23)$$

From Equations 3 and 4 we compute ${}^2\alpha_{l/v}(T = 25.3\text{ }^\circ\text{C}) = 1.0789$ and ${}^{18}\alpha_{l/v}(T = 25.3\text{ }^\circ\text{C}) = 1.0135$.

For ${}^{17}\text{O}$ we will take the experimental values given by Barkan and Luz (2005) at 25.3 °C: ${}^{17}\alpha_{l/v} = 1.00496 \pm 0.00002$.

For each stable water isotope, the values are calculated for 2 extreme sample isotopic composition from our database ($\delta^2\text{H} = -180\text{ ‰}$ and 5 ‰ , $\delta^{17}\text{O} = -12\text{ ‰}$ and 0 ‰ , $\delta^{18}\text{O} = -30\text{ ‰}$ and 5 ‰). The range of the isotopic composition of ambient air is based on records reported by Wei et al. (2019) for Rietholzbach, Switzerland (755 masl) from August to December 2011: the $\delta^2\text{H}$ air values range between -239.79 ‰ and -73.48 ‰ , and $\delta^{18}\text{O}$ values range between -31.41 ‰ and -9.94 ‰ . No reference value is available for $\delta^{17}\text{O}$, so a range between -30 and 0 ‰ has been chosen arbitrarily.

The Figure 59 shows the changes of the sample isotopic composition for $\delta^2\text{H}$, $\delta^{17}\text{O}$ and $\delta^{18}\text{O}$. These values have been completed for different amounts of air (ratios of sample volume over container volume).

The constant error for dry air corresponds to the case where the water vapor in air originates via evaporation of the water sample.

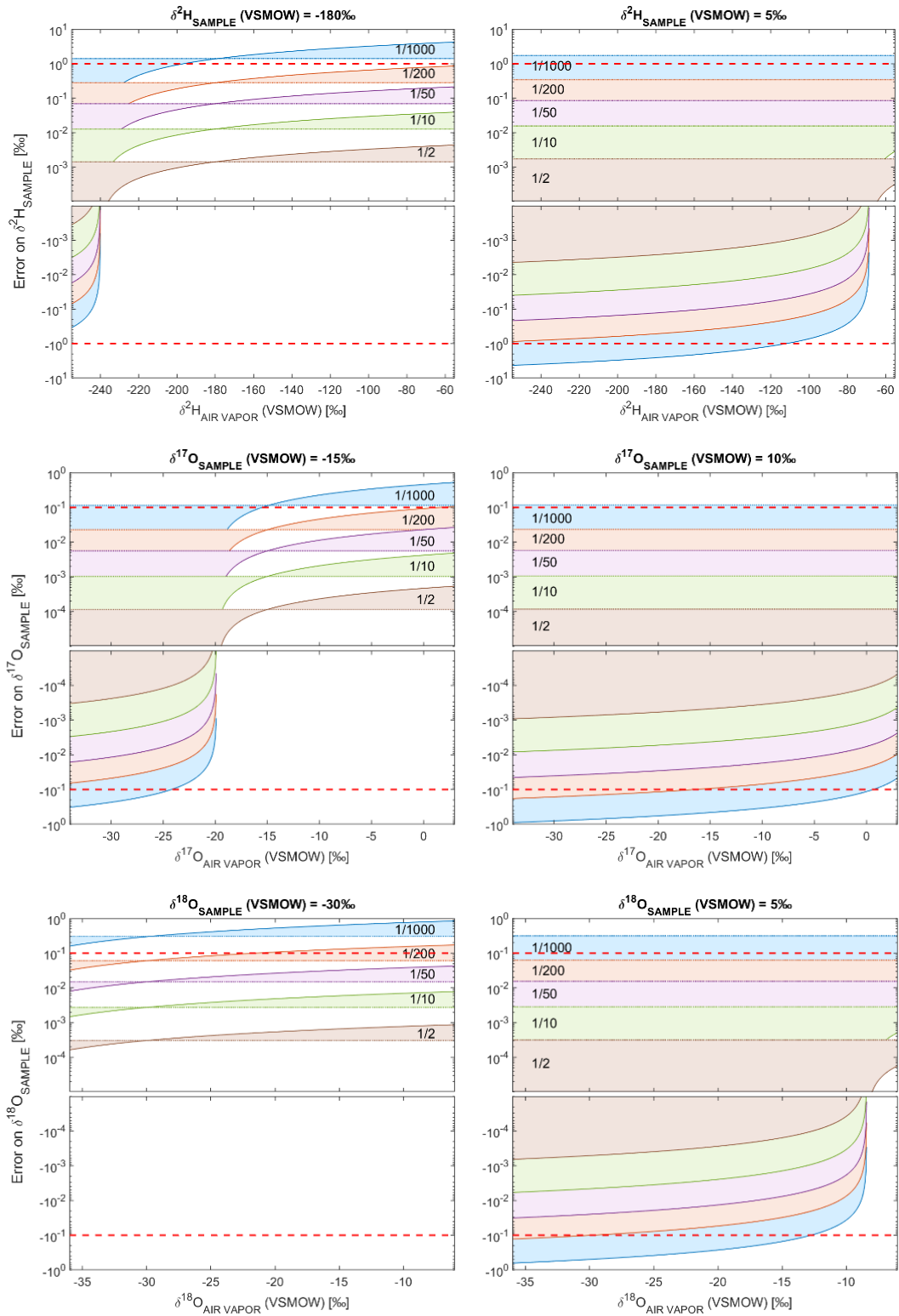


Figure 59. Changes in $\delta^2\text{H}$, $\delta^{17}\text{O}$ and $\delta^{18}\text{O}$ of a water sample depending on the initial isotopic composition of the water vapor of the air locked up with the sample. The results are completed for saturated air (continuous line) and dry air (dashed line), for ratios of sample volume over container volume from 1/2 to 1/1000. The red dashed line represents the detection limit of the measuring device.

Appendix 6 - 2: Estimate of water flow depth based on a soil temperature model

The estimate of the water flow depth is based on the soil temperature model presented in the work of Elias et al. (2004), assuming the water temperature measured at the spring/piezometer being equal to the soil temperature at the mean water flow depth. The evolution with time t of soil temperature T at the surface (depth $z=0$) corresponds to air temperature, and is characterized by the mean air temperature T_a and its amplitude A :

$$T(z=0, t) = T_a + A \sin(\omega t + \varphi), \quad (4)$$

with ω the radial frequency (in rad/s) and φ a phase constant (in rad). The heat transfer into the soil is dampened by D , the dampening depth coefficient (in m) expressed as a function of K (in m^2/s) the soil thermal diffusivity:

$$D = \sqrt{\frac{2K}{\omega}}, \quad (5)$$

giving the soil temperature at depth z :

$$T(z, t) = T_a + A \exp\left(-\frac{z}{D}\right) \sin\left(\omega t - \left(\frac{z}{D}\right) + \varphi\right), \quad (6)$$

The lag time L between air temperature and soil temperature at a given depth z is then:

$$L(z) = \frac{z}{\omega D}. \quad (7)$$

The depth is approached using the *fminsearch* function in MatLab, reducing the error between the observed lag time and the modeled lag time. Although the thermal diffusivity of soil is influenced by i) water volumetric content, ii) volume fraction of solids, and iii) air-filled porosity (Ochsner et al., 2001), we retain for this computation a unique value of thermal diffusivity of soil for all the points, using the typical value of $5.56 \cdot 10^{-7} \text{ m}^2/\text{s}$ (Elias et al., 2004). The sinusoidal air temperature is based on time series from a grided product (1 x 1 km grid) from MeteoSuisse (Schaepli, 2021). The results are presented in Table 18 and Figure 60.

Table 18. Characteristics of the sinusoidal air and water temperatures used for the soil temperature model, and characteristics of the soil temperature at the estimate depth corresponding to the water temperature.

Water sources	Measured air T [°C]		Measured water T [°C]		Air/Water lag time [d]	Modelized soil T [°C]		Modelized Soil depth [m]
	mean	amplitude	mean	amplitude		mean	amplitude	
PZ1	5.8	10	6.3	3.8	79	6	5.1	3.2
PZ3	5.8	10	4.8	3.7	105	4.5	3.3	4.3
GRAS	6.3	10	5.5	3	41	5.3	9.9	1.7
ROCK	6.3	10	5.4	2.5	39	5.2	10.2	1.6
BRDG	5.8	10	4.7	0.9	6	5	18	0.2
ICEC	5.8	10	4.3	0.4	133	4.2	2	5.4

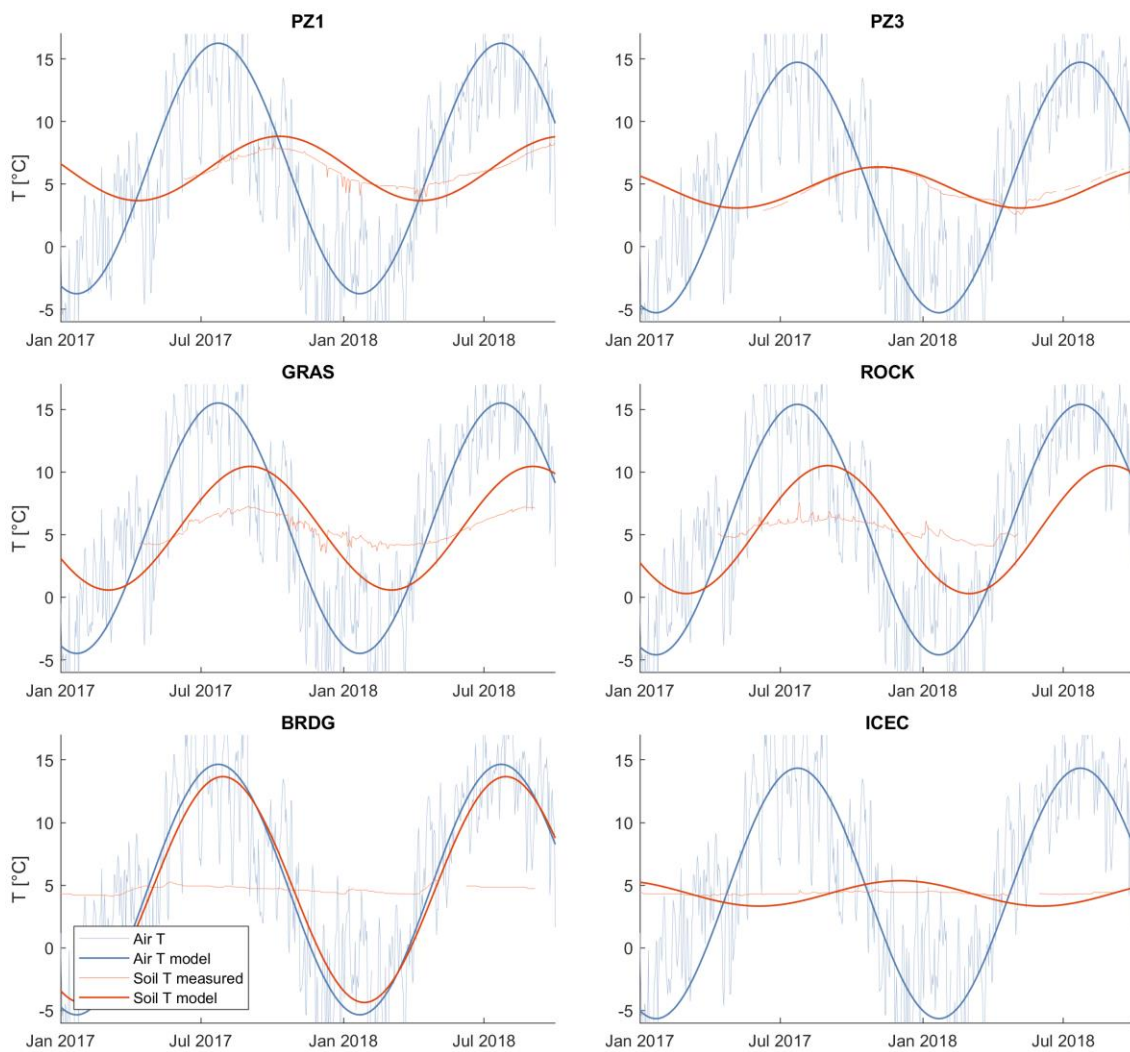


Figure 60. Measured and modeled air and soil temperature for 2 piezometers (PZ1 and PZ2) and 4 springs (GRAS, ROCK, BRDG and ICEC).

Appendix 6 - 3: Lapse rate estimation

An isotopic lapse rate of 1.9 ‰/100/m for $\delta^2\text{H}$ and 0.27 ‰/100/m for $\delta^{18}\text{O}$ is calculated for Switzerland based on data from the Global Network of Isotopes in Precipitation (GNIP) between 1966 and 2014 (Beria et al., 2018). This lapse rate is twice the lapse rate we compute from our precipitation water samples between the Auberge and Chalet stations: 0.84 ‰/100/m for $\delta^2\text{H}$ and 0.13 ‰/100/m for $\delta^{18}\text{O}$.

We make the hypothesis of a homogeneous rainfall input having such a lapse rate over the catchment (which is unrealistic regarding runoff, but conceivable at longer time scale, involving baseflow), and we estimate that a difference of isotopic composition of the streamflow water should appear between the two hydrological stations over the main river even for our lower lapse rates. We focus on 2 periods for which we have a large number of stream water samples for both HyS1 and HyS2 (from November 5th, 2016 to December 7th, 2016 and June 13th, 2017 to November 15th, 2017).

The water collected by the whole catchment should be depleted by 0.87 ‰ in the heavy isotopes for $\delta^2\text{H}$ and 0.14 ‰ for $\delta^{18}\text{O}$. This difference is in the order of magnitude of the processing error (see section 3.6), and so should not be further commented following the stated hypothesis. The weak difference is due to the fact that the mean elevation is too close between the upper subcatchment and the whole catchment, respectively 2196 m and 2165 masl.

7 | Discussion



Photograph: view in direction of the Dent Favre (2,916 masl), with late snowpack the steep slopes over (on the top part), alluvial cone (on the left), and the moraine area (on the right).

7.1 Preliminary remarks

The work of this thesis touched upon a wide variety of topics related to hydro-meteorological process observations and analysis in the Vallon de Nant catchment, which stands exemplarily for high elevation head water catchments that make up the hydrological behavior of the Alps. Since hydrological research in that catchment started with the beginning of this thesis, it is too early to draw a complete picture of dominant processes in that catchment. First important insights were, however, gained into how the different landscape units interact and how their interaction explains the hydrological response at the catchment scale. The process insights are of course site-specific; they give hints into what aspects deserve more attention in following research and particularly to project the hydrological behavior into the future with the help of models.

In addition to process insights, this work gives suggestions on how to advance field-based research in similar catchments. Accordingly, the first part of this discussion is dedicated to a critical discussion of the deployed hydro-meteorological measurement techniques.

7.2 Part 1: Hydro-meteorological measurements

7.2.1 Measuring streamflow and other variables at the outlet

Most of the analyses in this thesis, as well as of other studies carried out in the Vallon de Nant, rely on the streamflow measurement at the outlet. Time-lapse images showed that often the stream water is concentrated into one or two channels moving across the weir section, but the river stage is measured at a unique point in the middle of the weir, which does not account for such variations. The assumption of constant water height across the weir section is rarely satisfied, leading to considerable overestimation or underestimation of the streamflow. Note that this error may also affect the rating curve during the salt gauging measures. The following solutions are proposed:

- Correct the river stage measured at the middle point by measuring manually water height profiles across the weir section (as proposed in Chapter 3). The efficiency of this method is proportional to the amount and regularity of the profile measures, and obviously will be time consuming.
- Correct the river stage measured at the middle point using time-lapse image analysis to estimate back the water height profile. However, with situations such as those presented in Section 3.3, the overestimation by a factor 1.6 to 1.9 is due to a variation

of 5 cm along the profile, and such accuracy is unlikely to be reached based on image analysis.

- Improve the measurement across the river section using at least 2 measurement points. The cost and technical realization remains reasonable, and allows i) a continuous integration of the river stage profile and a good accuracy of the streamflow estimate, ii) to avoid biases due to streamflow perturbations (e.g. big rock) at distances too short upstream of the sensor (which leads to an irregular water height on the weir), and iii) study the stream bed dynamics across the section related to the sediment transport measures.
- Build a low flow channel. However, this would impact the sediment transport method used so far. An alternative could be to build this narrow section gauging station downstream and separate the river bed dynamic and sediment transport measurements (actual gauging station) from the streamflow measure. In both cases, the cost and amount of work is important.

The accuracy of the streamflow estimate should be a priority concern as it impacts many studies in the Vallon de Nant, requiring a good accuracy on streamflow, in particular during low flows.

The measurement of additional variables such as electric conductivity is also a challenge at the location of the gauging station, due to i) the river bed dynamic upstream of the gauging station, ii) the high variation of the river stage in the area downstream of the gauging station and iii) the potentially high accumulation of sediment downstream of the gauging station. It is thus difficult to find a location where sensors remain continuously immersed without being buried in sediments. A proposition would be to move the temperature, conductivity, and turbidity sensors 150 m upstream, below a road bridge, where the river section is narrow and water height sufficient even at low flow.

The use of a camera to keep track of the river state at the gauging station would be of interest and is a low cost quality check that could be recommended systematically, including if possible nighttime capabilities to capture rainfall-induced flood events, typically happening during evenings and nights (because of late afternoon thunderstorms).

New studies on wood log transportation started at the end of this thesis, and a time-lapse camera taking a picture of the stream during the day and at night at the gauging station replaced the time-lapse camera used in this thesis.

7.2.2 Identification of stream network extent and along stream gauging

The stream network extent plays a major role for the streamflow response at the outlet, both for high flow events (Chapter 5) as for the seasonal recession. To date, only two stream network extents have been identified and could be roughly related to a wet and a dry state (based on antecedent moisture conditions over the past 3 days, see Chapter 5). A better description of the stream network extent can be achieved in the future with different solutions:

- Use a basic electrical resistance (ER) sensor (Assendelft and van Meerveld, 2019) recording presence/absence of water in stream bed at multiple points in tributaries. This method requires time for setting up sensors and collecting results, with a high risk of losing sensors in the unstable river beds, but easy to set up.
- Use time-lapse cameras to visually appreciate if a stream is flowing or not. The requirements for equipment and power supply are higher than the previous method, but the experience at the outlet gauging station is encouraging and shows the benefits of using pictures (they contain a large amount of information).
- These efforts should be directed particularly toward temporary tributaries, mainly located on the steep slopes, where storage capacity is small.

Along stream gaugings shed light on lateral inputs and tributary contributions and thereby also on the water storage and release potential of the hillslopes connected to different stream network sections. These measures become approximative for points where the calculated upstream area (from DEM) and the actual upstream area (not necessarily matching the topography) differ strongly. The measure is also more difficult in the floodplain area, where the braided river moves regularly. Measurements have shown water recirculation in the floodplain area and have been confirmed by the complete disappearance of the main stream during some low flow periods. It appears then that this area plays an important role in mixing inputs (local snowmelt infiltration, upstream flow, groundwater storage) and delineate the extent of this area should be more important than measuring its intrinsic variability.

7.2.3 Weather station network

The deployment in the Vallon de Nant of a new weather station network working year-round was challenging due to the extreme weather conditions of the high mountain environment, but also due to the specific constraints of the study site, namely the lack of power supply in shadowed areas, the radio communication between the stations in a curve shaped valley, the

connection to a remote server to access the data, and the need for sensors and dataloggers to work with a reduced maintenance throughout winter.

The solution adopted (see Chapter 4) showed that the constraints of i) low maintenance, ii) power supply requirements, and iii) communication intra- and extra-catchment have been addressed. The major issues at the origin of data gaps are structural failures at the Glacier weather station (Figure 61), which was not strong enough to resist the snowpack accumulations (up to 4.5 m height). The 20° slope at the site caused i) uneven tensions on cables (deforming and breaking poles), and ii) flowing snowpack that no structure with a reasonable size could resist. The options for suitable locations to set up a weather station in the Vallon de Nant are few (visibility, accessibility, avalanche exposition) and we have not found another potential site for a weather station at this range of elevation in the catchment.



Figure 61. State of the Glacier weather station in spring 2017 (A), spring 2018 (B) and spring 2019 (C).

The Glacier weather station has been dismantled in 2021, and a new solution of weather station network is in discussion at the time of writing this thesis to continue weather data records for the actual and future studies in the area. The new solution will also have to cope with the closure of the Sensorscope company (making the DS3 dataloggers) in 2021.

7.2.4 Precipitation measures

The Lufft sensor showed, despite discrepancies when compared with official wind-sheltered sensors, their ability to work with a very low maintenance and in situations with low power configurations in Alpine environments.

The 3 stations measuring precipitations all year-round have been completed during this thesis by a high density raingauge network (12 stations) for 3 months (summer) to record rainfall. Neither the temporary 12-station network nor the permanent 3-station network have established the existence of a lapse rate of precipitations. Longer time series are needed to confirm the homogeneous spatial field of precipitation, but the result is not aberrant. Indeed, the synoptic winds causing precipitations originate mainly from the west, rising air to high

elevation to enter the catchment, and the basin width on this axis may not be sufficient (approx. 3 km) to observe orographic effects on such a short distance. However, it remains possible that this effect exists but has not been seen, not even by the high-density raingauge network, which did not have a measuring point within the steep slopes area on the eastern side of the catchment (i.e. storm event of 24 July 2018 in Chapter 5).

7.2.5 Snow cover and snowmelt observations

In this study, the identification of snow covered areas is done: i) based on satellite images, and ii) using soil temperature sensors. In the Vallon de Nant, the snowcover area identification from satellite images is particularly difficult due to the presence of large shadow areas caused by the relief. The proposed method (see Chapter 4) depends on visual assessment and for this reason its reproducibility is questionable. However, at the time of this thesis, no better methods have been brought to our attention.

The low frequency of snowcover maps is due to availability of satellite images over the area (every 5 days for Sentinel-2 satellite), coupled to the occurrence of a clear sky to correctly see the ground (less common in winter). The low frequency of snowcover maps is problematic for snowmelt periods, as an important part of snowmelt may happen during periods as short as a few days (e.g. in spring 2018). The shallow soil temperature sensors are very good proxy for snowcover presence at a given place and can help to fill gaps between satellite images.

It should be noted, however, that the occurrence of snowcover onset cannot be accurately identified neither by satellite images (rare clear sky during snowfall periods), nor by the soil temperature sensors as the temperature drop when soil get covered by snow is not as sharp as during snowmelt.

For modelling or data analysis purposes, areas with potential snowmelt (with temperature > 0 °C) could be identified from measured temperature and an air temperature gradient, but the existence of a remanent cold pool effect at the valley bottom could make such an estimate difficult. There is a need for a more accurate description of the vertical profile of temperature and for a more detailed study of cold air accumulation. Overlaying a snow cover map with a potential snowmelt map indicates the potential areas of meltwater inputs, both during the melt periods when the snowmelt is important (see Section 6.5.3) and during the baseflow period to identify areas which could deliver a small but constant snowmelt (see Section 6.5.1).

Based on an accurate air temperature estimate, the correlation between the positive daily temperatures (positive degree-day model, see e.g. Braithwaite (1995)) and the snowmelt rate

measured by the lysimeters could indicate if a simple temperature-index model is sufficient to explain the snowmelt rate in this catchment (or at least in some parts), or if additional variables (i.e. solar radiation) are needed.

7.2.6 Flow depth and flow path deduced from water sources temperature

We showed that the water temperature flowing through the ground (although it is not a conservative tracer), may convey useful information on flow depth and flow paths. Information on flow depth can be obtained by fitting the delayed air temperature using a conductive soil temperature model (water temperature is induced by soil temperature). Information on flow paths can be deduced by interpreting anomalies of temperature due to advection (i.e. colder water input from snowmelt, warmer input from surface runoff water) assuming that water keeps (at least partially) its temperature from the soil surface.

Conductive heat transfer of soils is also recorded by shallow soil temperature sensors. The variations of temperature give clues on the soil being covered by snow (no or few temperature variations, converging to 0°C), or free of snow (faster variations of temperature).

A study of the temperature derivative, or the use of additional sensors (i.e. surface temperature, deeper depth), could provide information on the different thermal properties of the soil, which could contribute to explain the different snowmelt rates measured across the catchment (see Section 4.2.1).

7.3 Part 2: What did we learn about the hydrology of the Vallon de Nant

In the Vallon de Nant, precipitation is mainly coming from the west and are probably not influenced (orographic effect) by the ridge that delimits the basin to the west (2,294 masl for the Pointe des Savolaires), but the higher peaks on the east side (2810 m and 3015 masl for the Petit Muveran and Grand Muveran) may at least have an influence on summer rainfall events (see Section 5.2.3).

Despite the absence of a strong orographic effect and despite the small catchment size (13.4 km²), the exact spatial variability of the rainfall fields might play an important role for the hydrologic response: this work showed in fact that the distance to the outlet, the drainage density and the subsurface storage potential varies between the north and south parts of the catchment. The stream network extent plays thus a major role in streamflow response at the outlet by reducing, dynamically, the distance between hillslopes and the stream network, and thereby also the lag time between the input peak and the streamflow response peak at the

outlet. The direction of rainfall movement relative to the stream network also has an impact on the stream response at the outlet.

The catchment gets entirely covered by snow in winter, with a snowpack that could exceed 4.5 m of thickness. During the cold period, the snowpack in the lower part of the catchment (between 1,253 m and 1,530 masl) releases water during winter e.g. when positive temperatures are reached and during rainfall events (short periods). Even when air temperature remains negative, a continuous snowmelt rate is observed at all elevations (0.30 mm/d at 1,780 masl and 0.02 mm/d at 2,136 masl), feeding the groundwater with fresh water. Subsurface water is shown to receive at least locally water inputs even during winter.

The first, usually small streamflow increase lasting sometimes several weeks (early melt from mid-March to early-May in 2017) is due to a complete snowcover melt at the lowest elevation (near the outlet), most probably completed by snowmelt release from the snow pack higher up. The streamflow during this early melt period is at least partly composed of subsurface water, that is the snowmelt pushes older water stored in the soils into the stream.

During the melt period, the snowpack melts quickly and a large amount of meltwater rises the water table, connecting the different groundwater systems and leading to a high connectivity of subsurface water to surface input during summer. This is visible in the fact that intense rainfall events that punctuate summer snowmelt, lead to temperature fluctuations in the shallow subsurface.

During this main melt period, the δ -values of stable isotopes of all subsurface water sources show a decrease toward a common low value, indicating a flushing of the entire system with snowmelt. The snowmelt can follow different pathways: we observed direct infiltration (PZ2), surface runoff (BRDG), or groundwater flow (GRAS, ROCK, ICEC, PZ1), including relatively deep flow (roughly estimated to 5.4 m, ICEC). Note that the identification of flow paths is largely based on water temperature; the memory of this tracer is limited to the last flow path and can thus not see a surface runoff followed up by a deep flowpath.

During the seasonal recession, the along-stream gaugings show a relatively constant contribution (in space) from all connected areas in the lower part of the catchment, where there is a single main stream. This can most probably be explained by the fact that all areas connected to the main stream have a relatively similar elevation distribution (which is a particularity of the catchment). This is also supported by the fact that the isotopic lapse rate

that is clearly present in rainfall is not visible in the isotopic composition of the waters sampled in the stream at two different locations.

Despite of this, the groundwater systems show different behaviors during the seasonal recession. During this period, the stable isotope compositions of water indicates that the subsurface reservoirs with a large capacity or with a smaller flow rate (i.e. BRDG, ICEC) are less sensitive to rainfall inputs than reservoirs having a small capacity or a higher flow rate (i.e. AUBG, ROCK). The seasonal streamflow recession thus results from the recession of different subsurface water systems with different recession behavior. Detailed event-scale recession analysis could shed light on how they are linked to the seasonal streamflow recession, but this is left for future research.

7.4 Part 3: Outlook for hydrological research in the Vallon de Nant

7.4.1 Avenues for future research in the Vallon de Nant

The present research did not include any work on evaporation and transpiration processes in the catchment and almost everything remains to be done in this field. Such work might also include the study of stable isotope compositions from soil water and shed further light on the spatial distribution of isotope compositions for the subsurface water. Future work on evaporation and transpiration (including evaporation from snow) will be a key component to advance our understanding of the recession of individual snowmelt and rainfall events but also of the seasonal recession. Such a focus on the seasonal recession is of particular interest to gain insights into the possible future occurrence of autumn droughts (Muelchi et al., 2021a).

Future work could also focus more specifically on generation of snowmelt induced high flow events, and thereby contribute to further advance the work on sediment dynamics, which is ongoing in the Vallon de Nant (Antoniazza et al., Submitted).

Efforts might also be devoted to study the glacier melt contribution to streamflow and to explore the hydrological processes involved in the moraine area; these two areas have not been included in the present study due to lack of time.

How snowmelt patterns interact with the stream network extent remains open to date but presents an interesting avenue for future research. This could also include the more detailed analysis of snow cover outflow, eventually with the help of lysimeters as attempted here (but not completed due to a lack of time).

7.4.2 Recommendations for future hydrological processes studies in ungauged Alpine headwater catchments

The absence (or limited amount) of historical hydrometeorological records for the Vallon de Nant at the beginning of this study is comparable to the situation of many snow-dominated headwaters catchments in Alpine environments. Based on our measurements and the findings specific to our study area, we can nevertheless formulate the following recommendations to obtain information on the internal dynamic of an ungauged basin. The installation of a gauging station at the outlet is necessary for the main hydrological period identifications, but the streamflow quantification itself does not come first in the list of priorities to investigate flowpaths.

- Our work shows that a good starting point is the characterization of water sources. Such a study starts best at the end of the recession period with an extensive inventory and sampling of all springs of the catchment, during a day after a long period without any precipitation input. During such a period, it is expected that the springs have the highest discriminant power in terms of water temperature, EC, and stable isotope composition. Clusters of springs with identical parameters can then be identified to choose one spring within each group to be monitored continuously using a temperature/EC probe.
- The maximum stream network extent should be identified right after an intense rainfall event, and main tributaries could be instrumented with ER sensors (flow/no flow) during snow-free periods (no avalanche risk).
- At the end of the recession period and in dry conditions again, along-stream gauging gives information about the lateral input to the main stream, and the possible areas with water exfiltration/recirculation. The measure can be repeated after rainfall events i) to identify the input of different tributaries with uneven area contribution, and ii) to identify the lateral input from subsurface flow along sections without tributaries.
- Shallow soil temperature sensors can be setup at different elevations and for various slope aspects. Satellite images allow one to estimate the areas having the most variable snowcover and give indications on areas where a better description of the snowline recession is required (i.e. on areas where more soil temperature sensors could be installed).
- Precipitation recording (and if possible, sampling) should start at least at two locations, as far apart as possible from one another in terms of distance and elevation, jointly

with air temperature measure. The spatial variability of precipitation can be explored with less efforts through rainfall measurements during summer, using a high-density raingauge network deployed across the most extensive range of elevations and slope aspects, including the highest elevation points to capture eventual orographic effects. The permanent weather station network can then be adapted accordingly.

- Air temperature sensors could complete the weather station network to give a good estimate of the temperature gradient for snowmelt areas. A higher number of sensors could be deployed at lower elevation to identify cold air accumulation. The number of sensors can be reduced in a second time based on this first analysis.
- Lysimeters require large efforts to setup but are the only way to infer directly the snowmelt rate and identify the active parts of the catchment during winter. The sampling of meltwater, if possible, provides a precious source of information.
- The sampling of springs and streamflow at the outlet should ideally follow the same frequency: during baseflow, a monthly water sample is sufficient to give a trend of the isotopic composition (but a more intensive sampling could allow to capture rain-on-snow events), and a high frequency sampling (every few hours) is necessary during the early-melt and melt periods to capture the fast changes of water properties. Concerning the rainfall events, for places equipped with automated water samplers, the sampling during and after rainfall events can be driven either by a raingauge or a water stage sensor.
- The sampling of rainfall is easily done by collecting rain water in a sealed plastic bag, ideally changed after each rainfall event. To obtain a full picture of precipitation isotopes, fresh snowfall would ideally be sampled i.e. by taking grab samples along a topographical transect during a ski trip. However, this remains to be challenging in most places (avalanche risk). If electricity is available, a heating tipping bucket could at least provide some samples of fresh snow fall. However, as shown in this work, snowpack samples might well be a good alternative since during winter (i.e. before the snowpack reaches an isothermal state), deeper snowpack layers preserve the d-values of the fresh snowfall.

A year of measurements with this setup provides a good picture of the hydrological processes of a catchment. These first results will indicate what additional measures might be required (weather stations, lysimeters), and which sensors could be removed (soil temperature, air temperature). The analysis of data of a single year should however keep in mind that some dynamics might be modified during years with an important snow pack or during dry years.

8 | General conclusion



Photograph: one of the many Alpine salamanders (*Salamandra atra*) that populate the Vallon de Nant

The objective of this PhD thesis was to investigate the hydrological processes across the various landscape units of the Vallon de Nant, a small (13.4 km²) snow-dominated Alpine headwater catchment in the western Swiss Alps. The extremely challenging fieldwork resulted in three remarkable datasets, an all year-round record of precipitation at three locations between 1,253 masl and 2,136 masl, the characterization of rainfall fields using a temporary high density raingauge network (12 stations), and the collection of 2861 water samples (mainly stream, springs, rainfall, and snowpack water) analyzed for EC and the triple stable isotopes of water ($\delta^2\text{H}$, $\delta^{17}\text{O}$ and $\delta^{18}\text{O}$). These datasets are now available for other studies and have been complemented by a wide variety of meteorological and hydrological measurements to provide information on the water flowpaths at the scale of identified hydrological units and during the key streamflow periods (winter base flow, early and main melt period, seasonal recession). The impressive isotope data set, in particular, offers a large number of avenues to study individual events, as well as the variability of this tracer for the distinct surface and ground waters and ensuing uncertainties in such a high elevation catchment.

This work was motivated by three main research questions. The first question was to know what spatial and temporal resolution would be necessary to capture the rainfall variability in order to explain the hydrological response of the catchment. The detailed analysis of 48 summer rainfall events measured by a high-density raingauge network (1 station for 1.1 km²) suggests that spatial rainfall patterns might play a key role to explain the hydrologic response in small Alpine catchments, induced by the variable drainage density, distance to the outlet, and subsurface storage potential.

The second research question was to identify the dominant hydrological processes and the related surface and subsurface flowpaths of the different hydrological units in the catchment. This question led, among others, to the monitoring of water temperature in several springs and piezometers and the analyses (EC and stable isotope compositions of water) of a large number of water samples. The combination of these tracers showed the predominance of subsurface flow during all seasons and, during the snow melt period, the activation of shallower flowpaths followed by rainfall.

Finally, the last question discussed the additional insights from the stable isotope compositions of water compared to traditional temperature and EC tracers. It was shown that in this catchment, flowpath depth and connectivity information was mainly conveyed by temperature. EC data conveyed complementary information on water age and thus has the

potential to give additional insights into subsurface flow path length. Unlike temperature and EC, stable water isotope compositions are not influenced by the soil properties and show the history of water phase change processes that happened in the air. Sampled in the streamflow, they are an important source of information on the prevalence of recent snowmelt water (versus older subsurface water) during different stages of the melt season, without being influenced by soil properties (like EC). The rate of isotopic composition variation can also provide information on either on reservoir size or flow rates. For this study, the ^{17}O -excess gives the same insights as the d-excess, and then the question whether there are secondary evaporations in the catchment or whether it is measurable at this scale remains open.

The datasets and findings from this thesis are the foundation for upcoming studies and for the improvements of hydrological models in comparable catchments, and any future work can now capitalize to better plan new campaigns.

For the Vallon de Nant, many open questions remain concerning the evaporation and transpiration processes due to the vegetation cover, as well as the role of the glacier and moraine areas in the upper part of the catchment, as all may have a strong influence during the melt and recession periods.

References

Affolter, S., Hauselmann, A. D., Fleitmann, D., Hauselmann, P., and Leuenberger, M.: Triple isotope (δD , $\delta O-17$, $\delta O-18$) study on precipitation, drip water and speleothem fluid inclusions for a Western Central European cave (NW Switzerland), *Quaternary Sci Rev*, 127, 73-89, DOI 10.1016/j.quascirev.2015.08.030, 2015.

Akaike, H.: A new look at the statistical model identification, *IEEE Transactions on Automatic Control*, 19, 716-723, 10.1109/TAC.1974.1100705, 1974.

Antoniazza, G., Nicollier, T., Boss, S., Mettra, F., Badoux, A., Schaepli, B., Rickenmann, D., and Lane, S. N.: Hydrological drivers of bedload transport in an Alpine watershed, *Earth and Space Science Open Archive*, 46, doi:10.1002/essoar.10507461.1, 2021.

Antoniazza, G., Nicollier, T., Boss, S., Mettra, F., Badoux, A., Schaepli, B., Rickenmann, D., and Lane, S.: Hydrological drivers of bedload transport in an Alpine watershed, *Water Resources Research*, <https://www.essoar.org/doi/abs/10.1002/essoar.10507461.1>, Submitted.

Arduino: Arduino Nano, available at <https://docs.arduino.cc/hardware/nano> (last access: 6 September 2021), 2021.

Arnoux, M., Brunner, P., Schaepli, B., Mott, R., Cochand, F., and Hunkeler, D.: Low-flow behavior of alpine catchments with varying quaternary cover under current and future climatic conditions, *Journal of Hydrology*, 125591, <https://doi.org/10.1016/j.jhydrol.2020.125591>, 2020.

Assendelft, R. S., and van Meerveld, H. J. I.: A Low-Cost, Multi-Sensor System to Monitor Temporary Stream Dynamics in Mountainous Headwater Catchments, *Sensors*, 19, 10.3390/s19214645, 2019.

Ba, R.: Origines et quantification de l'eau utilisée par *Larix decidua* dans un bassin versant de haute montagne (Vallon de Nant – Suisse), Master Thesis, University of Lausanne, Switzerland, 50, 2019.

Badoux, H.: Aperçu géologique du Vallon de Nant. La Thomasia, Jardin alpin de Pont de Nant., Lausanne, 37-43, 1991.

Bard, A., Renard, B., Lang, M., Giuntoli, I., Korck, J., Koboltschnig, G., Janza, M., d'Amico, M., and Volken, D.: Trends in the hydrologic regime of Alpine rivers, *Journal of Hydrology*, 529, 1823-1837, 10.1016/j.jhydrol.2015.07.052, 2015.

Bardossy, A., and Das, T.: Influence of rainfall observation network on model calibration and application, *Hydrol Earth Syst Sc*, 12, 77-89, DOI 10.5194/hess-12-77-2008, 2008.

Barkan, E., and Luz, B.: High precision measurements of O-17/O-16 and O-18/O-16 ratios in H₂O, *Rapid Commun Mass Sp*, 19, 3737-3742, 10.1002/rcm.2250, 2005.

Barnett, T. P., Adam, J. C., and Lettenmaier, D. P.: Potential impacts of a warming climate on water availability in snow-dominated regions, *Nature*, 438, 303-309, 10.1038/nature04141, 2005.

Barnhart, T. B., Molotch, N. P., Livneh, B., Harpold, A. A., Knowles, J. F., and Schneider, D.: Snowmelt rate dictates streamflow, *Geophys Res Lett*, 43, 8006-8016, 10.1002/2016gl069690, 2016.

Bell, V. A., and Moore, R. J.: The sensitivity of catchment runoff models to rainfall data at different spatial scales, *Hydrol Earth Syst Sc*, 4, 653-667, DOI 10.5194/hess-4-653-2000, 2000.

Beniston, M., Farinotti, D., Stoffel, M., Andreassen, L. M., Coppola, E., Eckert, N., Fantini, A., Giacomoni, F., Hauck, C., Huss, M., Huwald, H., Lehning, M., Lopez-Moreno, J. I., Magnusson, J., Marty, C., Moran-Tejeda, E., Morin, S., Naaim, M., Provenzale, A., Rabatel, A., Six, D., Stotter, J., Strasser, U., Terzago, S., and Vincent, C.: The European mountain cryosphere: a review of its current state, trends, and future challenges, *Cryosphere*, 12, 759-794, 10.5194/tc-12-759-2018, 2018.

Benoit, L., Allard, D., and Mariethoz, G.: Stochastic Rainfall Modeling at Sub-kilometer Scale, *Water Resources Research*, 54, 4108-4130, 10.1029/2018WR022817, 2018.

Berghuijs, W. R., Woods, R. A., & Hrachowitz, M.: A precipitation shift from snow towards rain leads to a decrease in streamflow. *Nature Climate Change*, 4, 583-586. <https://doi.org/10.1038/nclimate2246>, 2014.

Beria, H., Larsen, J. R., Ceperley, N. C., Michelon, A., Vennemann, T., and Schaeffli, B.: Understanding snow hydrological processes through the lens of stable water isotopes, *Wires Water*, 5, 10.1002/wat2.1311, 2018.

Beria, H., Larsen, J. R., Michelon, A., Ceperley, N. C., and Schaeffli, B.: HydroMix v1.0: a new Bayesian mixing framework for attributing uncertain hydrological sources, *Geosci. Model Dev.*, 13, 2433-2450, 10.5194/gmd-13-2433-2020, 2020.

Beria, H., Benoit, L., Michelon, A., Mariéthoz, G., and Schaeffli, B.: Improving hydrologic model realism by using stable water isotopes Hydrological Processes, In revision.

Berne, A., and Krajewski, W. F.: Radar for hydrology: Unfulfilled promise or unrecognized potential?, *Adv Water Resour*, 51, 357-366, 10.1016/j.advwatres.2012.05.005, 2013.

Bershaw, J., Hansen, D. D., and Schauer, A. J.: Deuterium excess and O-17-excess variability in meteoric water across the Pacific Northwest, USA, *Tellus B*, 72, 10.1080/16000889.2020.1773722, 2020.

Beven, K. J.: A history of the concept of time of concentration, *Hydrol. Earth Syst. Sci.*, 24, 2655–2670, <https://doi.org/10.5194/hess-24-2655-2020>, 2020.

Blahusiakova, A., Matouskova, M., Jenicek, M., Ledvinka, O., Kliment, Z., Podolinska, J., and Snopkova, Z.: Snow and climate trends and their impact on seasonal runoff and hydrological drought types in selected mountain catchments in Central Europe, *Hydrol. Sci. J.-J. Sci. Hydrol.*, 65, 2083-2096, 10.1080/02626667.2020.1784900, 2020.

Blume, T., Zehe, E., and Bronstert, A.: Rainfall-runoff response, event-based runoff coefficients and hydrograph separation, *Hydrol. Sci. J.-J. Sci. Hydrol.*, 52, 843-862, 10.1623/hysj.52.5.843, 2007.

Bocquet, G., and Thomas, A.: Mesures hydrologiques et climatologiques en haute montagne : les handicaps du milieu *Revue de Géographie Alpine Année 1989 77-1-3*, 95-104, 1989.

Böll, A.: Wildbach- und Hangverbau, Berichte der Eidgenössischen Forschungsanstalt für Wald, Schnee und Landschaft, 343, Eidgenössische Forschungsanstalt für Wald Schnee und Landschaft, Birmensdorf, 123 p. pp., 1997.

Bormann, K. J., Brown, R. D., Derksen, C., and Painter, T. H.: Estimating snow-cover trends from space, *Nature Climate Change*, 8, 923-927, 10.1038/s41558-018-0318-3, 2018.

Braithwaite, R. J.: Positive Degree-Day Factors for Ablation on the Greenland Ice-Sheet Studied by Energy-Balance Modeling, *J Glaciol*, 41, 153-160, Doi 10.3189/S0022143000017846, 1995.

Bras, R. L., and Rodriguez-Iturbe, I.: RAINFALL NETWORK DESIGN FOR RUNOFF PREDICTION, *Water Resour Res*, 12, 1197-1208, 10.1029/WR012i006p01197, 1976a.

Bras, R. L., and Rodriguez-Iturbe, I.: NETWORK DESIGN FOR ESTIMATION OF AREAL MEAN OF RAINFALL EVENTS, *Water Resour Res*, 12, 1185-1195, 10.1029/WR012i006p01185, 1976b.

Brauchli, T., Trujillo, E., Huwald, H., and Lehning, M.: Influence of Slope-Scale Snowmelt on Catchment Response Simulated With the Alpine3D Model, *Water Resour Res*, 53, 10723-10739, 10.1002/2017wr021278, 2017.

Brighenti, S., Tolotti, M., Bruno, M. C., Engel, M., Wharton, G., Cerasino, L., Mair, V., and Bertoldi, W.: After the peak water: the increasing influence of rock glaciers on alpine river systems, *Hydrological Processes*, 33, 2804-2823, 10.1002/hyp.13533, 2019.

Brunner, M. I., Farinotti, D., Zekollari, H., Huss, M., and Zappa, M.: Future shifts in extreme flow regimes in Alpine regions, *Hydrol. Earth Syst. Sci.*, 23, 4471-4489, 10.5194/hess-23-4471-2019, 2019.

Burnham, K. P., Anderson, D. R., and Huyvaert, K. P.: AIC model selection and multimodel inference in behavioral ecology: some background, observations, and comparisons, *Behav Ecol Sociobiol*, 65, 23-35, 10.1007/s00265-010-1029-6, 2011.

Cano-Paoli, K., Chiogna, G., and Bellin, A.: Convenient use of electrical conductivity measurements to investigate hydrological processes in Alpine headwaters, *Sci. Total Environ.*, 685, 37-49, 10.1016/j.scitotenv.2019.05.166, 2019.

Ceperley, N., Michelon, A., Escoffier, N., Mayoraz, G., Boix Canadell, M., Horgby, A., Hammer, F., Antoniazza, G., Schaepli, B., Lane, S., Rickenmann, D., and Boss, S.: Salt gauging and stage-discharge curve, Avançon de Nant, outlet Vallon de Nant catchment, Zenodo, 10.5281/zenodo.1154798, 2018.

Ceperley, N., Zuecco, G., Beria, H., Carturan, L., Michelon, A., Penna, D., Larsen, J., and Schaepli, B.: Seasonal snow cover decreases young water fractions in high Alpine catchments, *Hydrological Processes*, 34, 4794-4813, <https://doi.org/10.1002/hyp.13937>, 2020.

Chacon-Hurtado, J. C., Alfonso, L., and Solomatine, D. P.: Rainfall and streamflow sensor network design: a review of applications, classification, and a proposed framework, *Hydrol Earth Syst Sc*, 21, 3071-3091, 10.5194/hess-21-3071-2017, 2017.

Cherix, D., and Vittoz, P.: Synthèse et conclusions aux Journées de la biodiversité 2008 dans le Vallon de Nant, Biodiversité du Vallon de Nant, Mémoire de la Société vaudoise des Sciences naturelles, 23, 225-240, 2009.

Chiaudani, A., Di Curzio, D., and Rusi, S.: The snow and rainfall impact on the Verde spring behavior: A statistical approach on hydrodynamic and hydrochemical daily time-series, *Sci. Total Environ.*, 689, 481-493, [10.1016/j.scitotenv.2019.06.433](https://doi.org/10.1016/j.scitotenv.2019.06.433), 2019.

Cochand, M., Christe, P., Ornstein, P., and Hunkeler, D.: Groundwater Storage in High Alpine Catchments and Its Contribution to Streamflow, *Water Resour Res*, 55, 2613-2630, [10.1029/2018wr022989](https://doi.org/10.1029/2018wr022989), 2019.

Constantz, J.: Heat as a tracer to determine streambed water exchanges, *Water Resources Research*, 44, <https://doi.org/10.1029/2008WR006996>, 2008.

Coplen, T. B.: Reporting of Stable Hydrogen, Carbon, and Oxygen Isotopic Abundances, *Pure Appl Chem*, 66, 273-276, DOI [10.1351/pac199466020273](https://doi.org/10.1351/pac199466020273), 1994.

Coquelin, C.: Projet d'installation d'un réseau de stations météorologiques dans le Vallon de Nant, Mémoire de Master en Géosciences et Environnement, Université de Lausanne, 82, 2008.

Dansgaard, W.: Stable Isotopes in Precipitation, *Tellus*, 16, 436-468, 1964.

Dutoit, A.: La Végétation de l'étage Subalpin Du Vallon de Nant, PhD Thesis, University of Lausanne, Switzerland, 131, 1983.

Elias, E. A., Cichota, R., Torriani, H. H., and de Jong van Lier, Q.: Analytical soil-temperature model: correction for temporal variation of daily amplitude, *Soil Science Society of America Journal*, 68, 784-788, <https://doi.org/10.2136/sssaj2004.7840>, 2004.

Engel, M., Penna, D., Bertoldi, G., Dell'Agnese, A., Soulsby, C., and Comiti, F.: Identifying run-off contributions during melt-induced run-off events in a glacierized alpine catchment, *Hydrological Processes*, 30, 343-364, [10.1002/hyp.10577](https://doi.org/10.1002/hyp.10577), 2016.

Engel, M., Notarnicola, C., Endrizzi, S., and Bertoldi, G.: Snow model sensitivity analysis to understand spatial and temporal snow dynamics in a high-elevation catchment, *Hydrological Processes*, 31, 4151-4168, [10.1002/hyp.11314](https://doi.org/10.1002/hyp.11314), 2017.

Engel, M., Penna, D., Bertoldi, G., Vignoli, G., Tirlor, W., and Comiti, F.: Controls on spatial and temporal variability in streamflow and hydrochemistry in a glacierized catchment, *Hydrol. Earth Syst. Sci.*, 23, 2041-2063, [10.5194/hess-23-2041-2019](https://doi.org/10.5194/hess-23-2041-2019), 2019.

Fischer, M., Huss, M., Barboux, C., and Hoelzle, M.: The new Swiss Glacier Inventory SGI2010: relevance of using high-resolution source data in areas dominated by very small glaciers, *Arctic, Antarctic, and Alpine Research*, 46, 933-945, 2014.

Floriancic, M. G., van Meerveld, I., Smoorenburg, M., Margreth, M., Naef, F., Kirchner, J. W., and Molnar, P.: Spatio-temporal variability in contributions to low flows in the high Alpine Poschiavino catchment, *Hydrological Processes*, 32, 3938-3953, [doi:10.1002/hyp.13302](https://doi.org/10.1002/hyp.13302), 2018.

Foehn, A., García Hernández, J., Schaeffli, B., and De Cesare, G.: Spatial interpolation of precipitation from multiple rain gauge networks and weather radar data for operational applications in Alpine catchments, *Journal of Hydrology*, 563, 1092-1110, [10.1016/j.jhydrol.2018.05.027](https://doi.org/10.1016/j.jhydrol.2018.05.027), 2018a.

Foehn, A., Hernandez, J. G., Schaeffli, B., and De Cesare, G.: Spatial interpolation of precipitation from multiple rain gauge networks and weather radar data for operational applications in Alpine catchments, *Journal of Hydrology*, 563, 1092-1110, 2018b.

Foster, L. M., Bearup, L. A., Molotch, N. P., Brooks, P. D., and Maxwell, R. M.: Energy budget increases reduce mean streamflow more than snow-rain transitions: using integrated modeling to isolate climate change impacts on Rocky Mountain hydrology, *Environ. Res. Lett.*, 11, 10, 10.1088/1748-9326/11/4/044015, 2016.

Freudiger, D., Frielingsdorf, B., Stahl, K., Steinbrich, A., Weiler, M., Griessinger, N., and Seibert, J.: The Potential of meteorological gridded datasets for hydrological modeling in alpine basins, *Hydrol Wasserbewirts*, 60, 353-367, 10.5675/HyWa_2016,6_1, 2016.

Froehlich, K., Gibson, J. J., and Aggarwal, P. K.: Deuterium excess in precipitation and its climatological significance, International Atomic Energy Agency (IAEA) 2002.

Gallice, A., Schaefli, B., Lehning, M., Parlange, M. B., and Huwald, H.: Stream temperature prediction in ungauged basins: review of recent approaches and description of a new physics-derived statistical model, *Hydrol Earth Syst Sc*, 19, 3727-3753, 10.5194/hess-19-3727-2015, 2015.

Germann, U., Galli, G., Boscacci, M., and Bolliger, M.: Radar precipitation measurement in a mountainous region, *Q J Roy Meteor Soc*, 132, 1669-1692, 10.1256/qj.05.190, 2006.

Germann, U., Boscacci, M., Gabella, M., and Sartori, M.: Peak Performance: Radar design for prediction in the Swiss Alps, *Meteorological Technology International*, 42-45, 2015.

Gharari, S., Hrachowitz, M., Fenicia, F., and Savenije, H. H. G.: Hydrological landscape classification: investigating the performance of HAND based landscape classifications in a central European meso-scale catchment, *Hydrol Earth Syst Sc*, 15, 3275-3291, 10.5194/hess-15-3275-2011, 2011.

Giaccone, E., Luoto, M., Vittoz, P., Guisan, A., Mariéthoz, G., and Lambiel, C.: Influence of microclimate and geomorphological factors on alpine vegetation in the Western Swiss Alps, *Earth Surf Proc Land*, 44, 3093– 3107, 10.1002/esp.4715, 2019.

Giaccone, E.: Geomorphological characteristics as predictors for vegetation models in alpine environment, PhD Thesis, University of Lausanne, Switzerland, 164, 2020.

Grand, S., Rubin, A., Verrecchia, E. P., and Vittoz, P.: Variation in Soil Respiration across Soil and Vegetation Types in an Alpine Valley, *Plos One*, 11, 10.1371/journal.pone.0163968, 2016.

Guastini, E., Zuecco, G., Errico, A., Castelli, G., Bresci, E., Preti, F., and Penna, D.: How does streamflow response vary with spatial scale? Analysis of controls in three nested Alpine catchments, *J Hydrol*, 570, 705-718, 10.1016/j.jhydrol.2019.01.022, 2019.

Gunther, D., Markel, T., Essery, R., and Strasser, U.: Uncertainties in Snowpack Simulations-Assessing the Impact of Model Structure, Parameter Choice, and Forcing Data Error on Point-Scale Energy Balance Snow Model Performance, *Water Resour Res*, 55, 2779-2800, 10.1029/2018wr023403, 2019.

Hammond, J. C., Saavedra, F. A., and Kampf, S. K.: Global snow zone maps and trends in snow persistence 2001-2016, *Int J Climatol*, 38, 4369-4383, 10.1002/joc.5674, 2018.

Hammond, J. C., and Kampf, S. K.: Subannual Streamflow Responses to Rainfall and Snowmelt Inputs in Snow-Dominated Watersheds of the Western United States, *Water Resour Res*, 56, 10.1029/2019WR026132, 2020.

Hanus, S., Hrachowitz, M., Zekollari, H., Schoups, G., Vizcaino, M., and Kaitna, R.: Future changes in annual, seasonal and monthly runoff signatures in contrasting Alpine catchments in Austria, *Hydrology and Earth System Sciences*, 25, 3429-3453, 10.5194/hess-25-3429-2021, 2021.

Hayashi, M.: Alpine Hydrogeology: The Critical Role of Groundwater in Sourcing the Headwaters of the World, *Groundwater*, 58, 498-510, 10.1111/gwat.12965, 2020.

Haynes, W. M., Lide, D. R., and Bruno, T. J.: CRC handbook of chemistry and physics, Boca Raton, Florida : CRC Press/Taylor & Francis, 2017.

He, Z. H., Tian, F. Q., Gupta, H. V., Hu, H. C., and Hu, H. P.: Diagnostic calibration of a hydrological model in a mountain area by hydrograph partitioning, *Hydrology and Earth System Sciences*, 19, 1807-1826, 2015.

Heimo, A., Calpini, B., Konzelmann, T., and Suter, S.: SwissMetNet: The New Automatic Meteorological Network of Switzerland, CIMO/TECO Conference, Geneva, 4-6 December 2006, extended abstract, 9 pp. in: WMO/TD-No. 1354, 2006.

Henn, B., Newman, A. J., Livneh, B., Daly, C., and Lundquist, J. D.: An assessment of differences in gridded precipitation datasets in complex terrain, *J Hydrol*, 556, 1205-1219, 10.1016/j.jhydrol.2017.03.008, 2018.

Horgby, A., Canadell, M. B., Utseth, A. J., Vennemann, T. W., and Battin, T. J.: High-Resolution Spatial Sampling Identifies Groundwater as Driver of CO₂ Dynamics in an Alpine Stream Network, *J Geophys Res-Biogeophys*, 124, 1961-1976, 10.1029/2019jg005047, 2019a.

Horgby, A., Gomez-Gener, L., Escoffier, N., and Battin, T. J.: Dynamics and potential drivers of CO₂ concentration and evasion across temporal scales in high-alpine streams, *Environ. Res. Lett.*, 14, 10.1088/1748-9326/ab5cb8, 2019b.

Huggenberger, P.: Faltenmodelle und Verformungsverteilung in Deckenstrukturen am Beispiel der Morcles-Decke (Helvetikum der Westschweiz), Ph.D. Thesis, ETH-Zürich, Switzerland, 326, 10.3929/ethz-a-000365939, 1985.

Huss, M., Bookhagen, B., Huggel, C., Jacobsen, D., Bradley, R. S., Clague, J. J., Vuille, M., Buytaert, W., Cayan, D. R., Greenwood, G., Mark, B. G., Milner, A. M., Weingartner, R., and Winder, M.: Toward mountains without permanent snow and ice, *Earth's Future*, 5, 418-435, 10.1002/2016ef000514, 2017.

ISO: International Standard Atmosphere ISO 2533:1975, 1975.

Jobard, S.: Retour d'expérience sur l'instrumentation d'un glacier du Baounet : quels apports de la traçabilité des mesures environnementales ?, Collection EDYTEM Cahiers de géographie, 8, 10.3406/edyte.2009.1082, 2009.

Kane, D. L., Hinkel, K. M., Goering, D. J., Hinzman, L. D., and Outcalt, S. I.: Non-conductive heat transfer associated with frozen soils, *Global Planet Change*, 29, 275-292, Doi 10.1016/S0921-8181(01)00095-9, 2001.

Kaser, G., Grosshauser, M., and Marzeion, B.: Contribution potential of glaciers to water availability in different climate regimes, *P Natl Acad Sci USA*, 107, 20223-20227, 10.1073/pnas.1008162107, 2010.

Landais, A., Barkan, E., Yakir, D., and Luz, B.: The triple isotopic composition of oxygen in leaf water, *Geochim Cosmochim Acta*, 70, 4105-4115, 10.1016/j.gca.2006.06.1545, 2006.

Landais, A., Barkan, E., and Luz, B.: Record of delta O-18 and O-17-excess in ice from Vostok Antarctica during the last 150,000 years, *Geophys Res Lett*, 35, 10.1029/2007gl032096, 2008.

Landwehr, J. M., and Coplen, T. B.: Line-conditioned excess: a new method for characterizing stable hydrogen and oxygen isotope ratios in hydrologic systems, *International Conference on Isotopes in Environmental Studies, Aquatic Forum, Monte-Carlo, Monaco, 25–29 October 2004, IAEA, Vienna*, 132–135, 2006.

Lane, S. N., Borgeaud, L., and Vittoz, P.: Emergent geomorphic-vegetation interactions on a subalpine alluvial fan, *Earth Surf Proc Land*, 41, 72-86, 10.1002/esp.3833, 2016.

Laternser, M., and Schneebeli, M.: Long-term snow climate trends of the Swiss Alps (1931-99), *Int J Climatol*, 23, 733-750, 10.1002/joc.912, 2003.

Leuenberger, M. C., and Ranjan, S.: Disentangle Kinetic From Equilibrium Fractionation Using Primary (delta O-17, delta O-18, delta D) and Secondary (Delta O-17, d(ex)) Stable Isotope Parameters on Samples From the Swiss Precipitation Network, *Frontiers in Earth Science*, 9, 10.3389/feart.2021.598061, 2021.

Li, S. N., Levin, N. E., and Chesson, L. A.: Continental scale variation in O-17-excess of meteoric waters in the United States, *Geochim Cosmochim Acta*, 164, 110-126, 10.1016/j.gca.2015.04.047, 2015.

Linsbauer, A., Huss, M., Hodel, E., Bauder, A., Fischer, M., Weidmann, Y., Bärtschi, H., and Schmassmann, E.: The new Swiss Glacier Inventory SGI2016: From a topographical to a glaciological dataset, *Frontiers in Earth Science*, in review, 2021.

Livneh, B., and Badger, A. M.: Drought less predictable under declining future snowpack, *Nature Climate Change*, 10, 452-+, 10.1038/s41558-020-0754-8, 2020.

Lobligeois, F., Andreassian, V., Perrin, C., Tabary, P., and Loumagne, C.: When does higher spatial resolution rainfall information improve streamflow simulation? An evaluation using 3620 flood events, *Hydrology and Earth System Sciences*, 18, 575-594, 10.5194/hess-18-575-2014, 2014.

Lucianetti, G., Penna, D., Mastorillo, L., and Mazza, R.: The Role of Snowmelt on the Spatio-Temporal Variability of Spring Recharge in a Dolomitic Mountain Group, Italian Alps, *Water*, 12, 26, 10.3390/w12082256, 2020.

Mächler, E., Salyani, A., Walser, J. C., Larsen, A., Schaefli, B., Altermatt, F., and Ceperley, N.: Environmental DNA simultaneously informs hydrological and biodiversity characterization of an Alpine catchment, *Hydrol. Earth Syst. Sci.*, 1-30, 10.5194/hess-25-735-2021, 2021.

Majoube, M.: Fractionnement en oxygène 18 et en deutérium entre l'eau et sa vapeur, *J. Chim. Phys.*, 68, 1423-1436, 1971.

Mayoraz, G.: Mesure du débit et du transport sédimentaire total dans un bassin versant des Alpes suisses, *Mémoire de Master en Géosciences et Environnement, Université de Lausanne*, 106, 2018.

Mei, Y. W., Anagnostou, E. N., Stampoulis, D., Nikolopoulos, E. I., Borga, M., and Vegara, H. J.: Rainfall organization control on the flood response of mild-slope basins, *Journal of Hydrology*, 510, 565-577, 10.1016/j.jhydrol.2013.12.013, 2014.

Meijer, H. A. J., and Li, W. J.: The use of electrolysis for accurate delta O-17 and delta O-18 isotope measurements in water, *Isot Environ Health S*, 34, 349-369, Doi 10.1080/10256019808234072, 1998.

MeteoSwiss: Documentation of MeteoSwiss Grid-Data Products: Daily Precipitation (final analysis): RhiresD, 2019.

Michelon, A., Benoit, L., Beria, H., Ceperley, N., and Schaepli, B.: A 2-minute rainfall (12 locations) and discharge time series at the Vallon de Nant catchment, Switzerland, for 2018 summer seasons (Version v2.0), Zenodo, <https://doi.org/10.5281/zenodo.3946242>, 2020.

Michelon, A., Benoit, L., Beria, H., Ceperley, N., and Schaepli, B.: Benefits from high-density rain gauge observations for hydrological response analysis in a small alpine catchment, *Hydrol. Earth Syst. Sci.*, 25, 2301-2325, 10.5194/hess-25-2301-2021, 2021a.

Michelon, A., Schaepli, B., Ceperley, N., and Beria, H.: Weather dataset from Vallon de Nant, Switzerland (from 16 August 2016 to 14 October 2018), Zenodo, <https://doi.org/10.5281/zenodo.5518942>, 2021b.

Michelon, A., Ceperley, N., Beria, H., Larsen, J., Vennemann, T., and Schaepli, B.: Studying the dynamic of a high alpine catchment based on multiple natural tracers, *Hydrol. Earth Syst. Sci. Discuss.* [preprint], <https://doi.org/10.5194/hess-2022-48>, in review, 2022.

Mook, W. G.: Environmental isotopes in the hydrological cycle – Principles and applications, UNESCO, Paris, 1, 2000.

Moulin, L., Gaume, E., and Obled, C.: Uncertainties on mean areal precipitation: assessment and impact on streamflow simulations, *Hydrol Earth Syst Sc*, 13, 99-114, DOI 10.5194/hess-13-99-2009, 2009.

Muelchi, R., Rössler, O., Schwanbeck, J., Weingartner, R., and Martius, O.: Future runoff regime changes and their time of emergence for 93 catchments in Switzerland, *Hydrol. Earth Syst. Sci. Discuss.*, 2020, 1-25, 10.5194/hess-2020-516, 2020.

Muelchi, R., Rossler, O., Schwanbeck, J., Weingartner, R., and Martius, O.: River runoff in Switzerland in a changing climate - runoff regime changes and their time of emergence, *Hydrology and Earth System Sciences*, 25, 3071-3086, 10.5194/hess-25-3071-2021, 2021a.

Muelchi, R., Rossler, O., Schwanbeck, J., Weingartner, R., and Martius, O.: River runoff in Switzerland in a changing climate - changes in moderate extremes and their seasonality, *Hydrol Earth Syst Sc*, 25, 3577-3594, 10.5194/hess-25-3577-2021, 2021b.

Munoz-Villers, L. E., and McDonnell, J. J.: Runoff generation in a steep, tropical montane cloud forest catchment on permeable volcanic substrate, *Water Resour Res*, 48, 10.1029/2011wr011316, 2012.

Musselman, K. N., Addor, N., Vano, J. A., and Molotch, N. P.: Winter melt trends portend widespread declines in snow water resources, *Nature Climate Change*, 17, 10.1038/s41558-021-01014-9,

Musselman, K. N., Clark, M. P., Liu, C. H., Ikeda, K., and Rasmussen, R.: Slower snowmelt in a warmer world, *Nature Climate Change*, 7, 214-+, 10.1038/Nclimate3225, 2017.

Musselman, K. N., Lehner, F., Ikeda, K., Clark, M. P., Prein, A. F., Liu, C. H., Barlage, M., and Rasmussen, R.: Projected increases and shifts in rain-on-snow flood risk over western North America, *Nature Climate Change*, 8, 808-+, 10.1038/s41558-018-0236-4, 2018.

Musselman, K. N., Addor, N., Vano, J. A., and Molotch, N. P.: Winter melt trends portend widespread declines in snow water resources, *Nature Climate Change*, 11, 418-+, 10.1038/s41558-021-01014-9, 2021.

Nicótina, L., Alessi Celegon, E., Rinaldo, A., and Marani, M.: On the impact of rainfall patterns on the hydrologic response, *Water Resour Res*, 44, W12401, 10.1029/2007WR006654, 2008.

Nikolopoulos, E. I., Anagnostou, E. N., Borga, M., Vivoni, E. R., and Papadopoulos, A.: Sensitivity of a mountain basin flash flood to initial wetness condition and rainfall variability, *J Hydrol*, 402, 165-178, 10.1016/j.jhydrol.2010.12.020, 2011.

Nitu, R., Roulet, Y.-A., Wolff, M., Earle, M., Reverdin, A., Smith, C., Kochendorfer, J., Morin, S., Rasmussen, R., Wong, K., Alastrué, J., Arnold, L., Baker, B., Buisán, S., Collado, J. L., Colli, M., Collins, B., Gaydos, A., Hannula, H.-R., Hoover, J., Joe, P., Kontu, A., Laine, T., Lanza, L., Lanzinger, E., Lee, G. W., Lejeune, Y., Leppänen, L., Mekis, E., Panel, J.-M., Poikonen, A., Ryu, S., Sabatini, F., Theriault, J., Yang, D., Genthon, C., van den Heuvel, F., Hirasawa, N., Konishi, H., Nishimura, K., and Senese, A.: WMO Solid Precipitation Intercomparison Experiment (SPICE) (2012 - 2015), IOM Report, 131, available at: https://library.wmo.int/doc_num.php?explnum_id=5686 (last access: 31 October 2021), 2018.

Nobre, A. D., Cuartas, L. A., Hodnett, M., Renno, C. D., Rodrigues, G., Silveira, A., Waterloo, M., and Saleska, S.: Height Above the Nearest Drainage - a hydrologically relevant new terrain model, *J Hydrol*, 404, 13-29, 10.1016/j.jhydrol.2011.03.051, 2011.

Nogues-Bravo, D., Araujo, M. B., Errea, M. P., and Martinez-Rica, J. P.: Exposure of global mountain systems to climate warming during the 21st Century, *Global Environ Chang*, 17, 420-428, 10.1016/j.gloenvcha.2006.11.007, 2007.

Nyamgerel, Y., Han, Y., Kim, M., Koh, D., and Lee, J.: Review on Applications of O-17 in Hydrological Cycle, *Molecules*, 26, 10.3390/molecules26154468, 2021.

Obled, C., Wendling, J., and Beven, K.: The sensitivity of hydrological models to spatial rainfall patterns - an evaluation using observed data, *Journal of Hydrology*, 159, 305-333, 1994.

Ochsner, T. E., Horton, R., and Ren, T. H.: A new perspective on soil thermal properties, *Soil Science Society of America Journal*, 65, 1641-1647, DOI 10.2136/sssaj2001.1641, 2001.

OFEV: Impacts des changements climatiques sur les eaux et les ressources en eau. Rapport de synthèse du projet « Changement climatique et hydrologie en Suisse » (CCHydro), *Connaissance de l'environnement*, 76, 2012.

Ohlanders, N., Rodriguez, M., and McPhee, J.: Stable water isotope variation in a Central Andean watershed dominated by glacier and snowmelt, *Hydrol. Earth Syst. Sci.*, 17, 1035-1050, 10.5194/hess-17-1035-2013, 2013.

Passey, B. H., and Ji, H. Y.: Triple oxygen isotope signatures of evaporation in lake waters and carbonates: A case study from the western United States, *Earth Planet Sc Lett*, 518, 1-12, 10.1016/j.epsl.2019.04.026, 2019.

Pechlivanidis, I. G., McIntyre, N., and Wheeler, H. S.: The significance of spatial variability of rainfall on simulated runoff: an evaluation based on the Upper Lee catchment, UK, *Hydrol. Res.*, 48, 1118-1130, 10.2166/nh.2016.038, 2017.

Penna, D., Tromp-van Meerveld, H. J., Gobbi, A., Borga, M., and Dalla Fontana, G.: The influence of soil moisture on threshold runoff generation processes in an alpine headwater catchment, *Hydrol Earth Syst Sc*, 15, 689-702, 10.5194/hess-15-689-2011, 2011.

Penna, D., Engel, M., Mao, L., Dell'Agnese, A., Bertoldi, G., and Comiti, F.: Tracer-based analysis of spatial and temporal variations of water sources in a glacierized catchment, *Hydrol. Earth Syst. Sci.*, 18, 5271-5288, 10.5194/hess-18-5271-2014, 2014.

Penna, D., van Meerveld, H. J., Zuecco, G., Fontana, G. D., and Borga, M.: Hydrological response of an Alpine catchment to rainfall and snowmelt events, *Journal of Hydrology*, 537, 382-397, 10.1016/j.jhydrol.2016.03.040, 2016.

Penna, D., Engel, M., Bertoldi, G., and Comiti, F.: Towards a tracer-based conceptualization of meltwater dynamics and streamflow response in a glacierized catchment, *Hydrol Earth Syst Sc*, 21, 23-41, 10.5194/hess-21-23-2017, 2017.

Penna, D., and van Meerveld, H. J.: Spatial variability in the isotopic composition of water in small catchments and its effect on hydrograph separation, *Wires Water*, 6, 33, 10.1002/wat2.1367, 2019.

Planet: Planet Application Program Interface: In Space for Life on Earth, San Francisco, CA, 2017.

Renno, C. D., Nobre, A. D., Cuartas, L. A., Soares, J. V., Hodnett, M. G., Tomasella, J., and Waterloo, M. J.: HAND, a new terrain descriptor using SRTM-DEM: Mapping terra-firme rainforest environments in Amazonia, *Remote Sens Environ*, 112, 3469-3481, 10.1016/j.rse.2008.03.018, 2008.

Rinaldo, A., Marani, M., and Rigon, R.: Geomorphological dispersion, *Water Resour Res*, 27, 513-525, 1991.

Rinaldo, A., Vogel, G. K., Rigon, R., and Rodriguez-Iturbe, I.: Can One Gauge the Shape of a Basin, *Water Resour Res*, 31, 1119-1127, Doi 10.1029/94wr03290, 1995.

Rinaldo, A., Banavar, J. R., and Maritan, A.: Trees, networks, and hydrology *Water Resour Res*, 42, W06D07 10.1029/2005WR004108, 2006a.

Rinaldo, A., Botter, G., Bertuzzo, E., Uccelli, A., Settin, T., and Marani, M.: Transport at basin scales: 1. Theoretical framework, *Hydrol Earth Syst Sc*, 10, 19-29, DOI 10.5194/hess-10-19-2006, 2006b.

Risi, C., Landais, A., Bony, S., Jouzel, J., Masson-Delmotte, V., and Vimeux, F.: Understanding the O-17 excess glacial-interglacial variations in Vostok precipitation, *J Geophys Res-Atmos*, 115, 10.1029/2008jd011535, 2010.

Rodriguez-Blanco, M. L., Taboada-Castro, M. M., and Taboada-Castro, M. T.: Rainfall-runoff response and event-based runoff coefficients in a humid area (northwest Spain), *Hydrolog Sci J*, 57, 445-459, 10.1080/02626667.2012.666351, 2012.

Ross, C. A., Ali, G., Spence, C., Oswald, C., and Casson, N.: Comparison of event-specific rainfall-runoff responses and their controls in contrasting geographic areas, *Hydrol Process*, 33, 1961-1979, 10.1002/hyp.13460, 2019.

Roth, D.: Analyse microclimatique du Vallon de Nant, Mémoire de Master en Géosciences et Environnement, Université de Lausanne, 192, 2011.

Rowley, M. C., Grand, S., and Verrecchia, E. P.: Calcium-mediated stabilisation of soil organic carbon, *Biogeochemistry*, 137, 27-49, 10.1007/s10533-017-0410-1, 2018.

Rucker, A., Zappa, M., Boss, S., and von Freyberg, J.: An optimized snowmelt lysimeter system for monitoring melt rates and collecting samples for stable water isotope analysis, *J. Hydrol. Hydromech.*, 67, 20-31, 10.2478/johh-2018-0007, 2019.

Santos, A. C., Portela, M. M., Rinaldo, A., and Schaeffli, B.: Analytical flow duration curves for summer streamflow in Switzerland, *Hydrol Earth Syst Sc*, 22, 2377-2389, 10.5194/hess-22-2377-2018, 2018.

Schaeffli, B., Rinaldo, A., and Botter, G.: Analytic probability distributions for snow-dominated streamflow, *Water Resour Res*, 49, 1-13, 10.1002/2012WR020234, 2013.

Schaeffli, B., Nicotina, L., Imfeld, C., Da Ronco, P., Bertuzzo, E., and Rinaldo, A.: SEHR-ECHO v1.0: a Spatially Explicit Hydrologic Response model for ecohydrologic applications, *Geosci Model Dev*, 7, 2733-2746, 10.5194/gmd-7-2733-2014, 2014.

Schaeffli, B.: Snow hydrology signatures for model identification within a limits-of-acceptability approach, *Hydrological Processes*, 30, 4019-4035, 10.1002/hyp.10972, 2016.

Schaeffli, B.: Average daily air temperature, precipitation and relative sunshine duration for Vallon de Nant catchment, extracted from gridded MeteoSwiss data (1961-2020), Zenodo, <https://doi.org/10.5281/zenodo.5420415>, 2021.

Schauer, A. J., Schoenemann, S. W., and Steig, E. J.: Routine high-precision analysis of triple water-isotope ratios using cavity ring-down spectroscopy, *Rapid Commun Mass Sp*, 30, 2059-2069, 10.1002/rcm.7682, 2016.

Schmieder, J., Garvelmann, J., Marke, T., and Strasser, U.: Spatio-temporal tracer variability in the glacier melt end-member How does it affect hydrograph separation results?, *Hydrological Processes*, 32, 1828-1843, 10.1002/hyp.11628, 2018.

Schotterer, U., Stichler, W., and Ginot, P.: The Influence of Post-Depositional Effects on Ice Core Studies: Examples From the Alps, Andes, and Altai, Springer Netherlands 2004.

Schurch, M., Kozel, R., Schotterer, U., and Tripet, J. P.: Observation of isotopes in the water cycle - the Swiss National Network (NISOT), *Environ Geol*, 45, 1-11, 10.1007/s00254-003-0843-9, 2003.

Schwanghart, W., and Scherler, D.: TopoToolbox 2 – MATLAB-based software for topographic analysis and modeling in Earth surface sciences, *Earth Surface Dynamics*, 2, 1-7, 10.5194/esurf-2-1-2014, 2014.

SFOE: Aperçu de la consommation d'énergie en suisse au cours de l'année 2020, available at: <https://www.bfe.admin.ch/bfe/fr/home/approvisionnement/statistiques-et-geodonnees/statistiques-de-lenergie/statistique-globale-de-l-energie.html> (last access: 1 November 2021), Swiss Federal Office for Energy, Bern, 2021.

Shah, S. M. S., Oconnell, P. E., and Hosking, J. R. M.: Modelling the effects of spatial variability in rainfall on catchment response .1. Formulation and calibration of a stochastic rainfall field model, *Journal of Hydrology*, 175, 67-88, 10.1016/s0022-1694(96)80006-0, 1996.

Sideris, I. V., Gabella, M., Erdin, R., and Germann, U.: Real-time radar-rain-gauge merging using spatio-temporal co-kriging with external drift in the alpine terrain of Switzerland, *Q J Roy Meteor Soc*, 140, 1097-1111, 10.1002/qj.2188, 2014.

Singh, V. P.: Effect of spatial and temporal variability in rainfall and watershed characteristics on stream flow hydrograph, *Hydrol Process*, 11, 1649-1669, 10.1002/(sici)1099-1085(19971015)11:12<1649::Aid-hyp495>3.0.Co;2-1, 1997.

Sodemann, H., and Zubler, E.: Seasonal and inter-annual variability of the moisture sources for Alpine precipitation during 1995-2002, *Int J Climatol*, 30, 947-961, 10.1002/joc.1932, 2010.

Sohrabi, M. M., Tonina, D., Benjankar, R., Kumar, M., Kormos, P., and Marks, D.: Role of temporal resolution of meteorological inputs for process-based snow modelling, *Hydrological Processes*, 32, 2976-2989, 10.1002/hyp.13242, 2018.

Sprenger, M., Leistert, H., Gimbel, K., and Weiler, M.: Illuminating hydrological processes at the soil-vegetation-atmosphere interface with water stable isotopes, *Reviews of Geophysics*, 54, 2015RG000515, 10.1002/2015RG000515, 2016.

St-Hilaire, A., Ouarda, T., Lachance, M., Bobee, B., Gaudet, J., and Gignac, C.: Assessment of the impact of meteorological network density on the estimation of basin precipitation and runoff: a case study, *Hydrological Processes*, 17, 3561-3580, 10.1002/hyp.1350, 2003.

Stisen, S., and Sandholt, I.: Evaluation of remote-sensing-based rainfall products through predictive capability in hydrological runoff modelling, *Hydrol Process*, 24, 879-891, 10.1002/hyp.7529, 2010.

Surma, J., Assonov, S., and Staubwasser, M.: Triple Oxygen Isotope Systematics in the Hydrologic Cycle,, *Reviews in Mineralogy and Geochemistry*, 401–428, <https://doi.org/10.2138/rmg.2021.86.12>, 2021.

swissAlti3D: The digital elevation model of Switzerland, 2012a.

swissAlti3D, S.: available at: <https://www.swisstopo.admin.ch/fr/geodata/height/alti3d.html> (last access: 1 July 2020), 2012b.

Tarboton, D. G., Bras, R. L., and Puente, C. E.: Combined hydrologic sampling criteria for rainfall and streamflow, *Journal of Hydrology*, 95, 323-339, [https://doi.org/10.1016/0022-1694\(87\)90009-6](https://doi.org/10.1016/0022-1694(87)90009-6), 1987.

Tetzlaff, D., and Uhlenbrook, S.: Significance of spatial variability in precipitation for process-oriented modelling: results from two nested catchments using radar and ground station data, *Hydrol Earth Syst Sc*, 9, 29-41, DOI 10.5194/hess-9-29-2005, 2005.

Thornton, J. M., Mariethoz, G., and Brunner, P.: A 3D geological model of a structurally complex Alpine region as a basis for interdisciplinary research, *Sci Data*, 5, 10.1038/sdata.2018.238, 2018.

Thornton, J. M.: Fully-integrated hydrological modelling in steep, snow-dominated, geologically complex Alpine terrain, PhD Thesis, University of Neuchâtel, Switzerland, 2020.

Thornton, J. M., Brauchli, T., Mariethoz, G., and Brunner, P.: Efficient multi-objective calibration and uncertainty analysis of distributed snow simulations in rugged alpine terrain, *Journal of Hydrology*, 126241, <https://doi.org/10.1016/j.jhydrol.2021.126241>, 2021a.

Thornton, J. M., Therrien, R., Mariéthoz, G., Linde, N., and Brunner, P.: Simulating fully-integrated hydrological dynamics in complex Alpine headwaters, *EarthArXiv*, pre-print, doi.org/10.31223/X5RG7Q, 2021b.

Trask, J. C., Devine, S. M., and Fogg, G. E.: Soil temperature survey in a mountain basin, *Geoderma*, 367, 114202, <https://doi.org/10.1016/j.geoderma.2020.114202>, 2020.

Tromp-van Meerveld, H. J., and McDonnell, J. J.: Threshold relations in subsurface stormflow: 2. The fill and spill hypothesis, *Water Resour Res*, 42, 10.1029/2004wr003800, 2006.

Viglione, A., Chirico, G. B., Woods, R., and Blöschl, G.: Generalised synthesis of space-time variability in flood response. An analytical framework, *Journal of Hydrology*, 394, 198-212, 10.1016/j.jhydrol.2010.05.047, 2010.

Vittoz, P.: Permanent.Plot.ch – a database for Swiss permanent vegetation plots, *Biodiversity & Ecology*, 4, 337-337, 2012.

Vittoz, P.: Soil temperature series in Vallon de Nant catchment, Switzerland, Zenodo, <http://doi.org/10.5281/zenodo.4715669>, 2021.

Viviroli, D., Durr, H. H., Messerli, B., Meybeck, M., and Weingartner, R.: Mountains of the world, water towers for humanity: Typology, mapping, and global significance, *Water Resour Res*, 43, 10.1029/2006wr005653, 2007.

Volpi, E., Di Lazzaro, M., and Fiori, A.: A simplified framework for assessing the impact of rainfall spatial variability on the hydrologic response, *Advances in Water Resources*, 46, 1-10, <https://doi.org/10.1016/j.advwatres.2012.04.011>, 2012.

von Freyberg, J., Knapp, J. L. A., Rücker, A., Studer, B., and Kirchner, J. W.: Technical note: Evaluation of a low-cost evaporation protection method for portable water samplers, *Hydrol. Earth Syst. Sci.*, 24, 5821-5834, 10.5194/hess-24-5821-2020, 2020.

Webb, R. W., Wigmore, O., Jennings, K., Fend, M., and Molotch, N. P.: Hydrologic connectivity at the hillslope scale through intra-snowpack flow paths during snowmelt, *Hydrological Processes*, 34, 1616-1629, 10.1002/hyp.13686, 2020.

Wei, Z. W., Lee, X., Aemisegger, F., Benetti, M., Berkelhammer, M., Casado, M., Caylor, K., Christner, E., Dyroff, C., Garcia, O., Gonzalez, Y., Griffis, T., Kurita, N., Liang, J., Liang, M. C., Lin, G. H., Noone, D., Gribanov, K., Munksgaard, N. C., Schneider, M., Ritter, F., Steen-Larsen, H. C., Vallet-

Coulomb, C., Wen, X. F., Wright, J. S., Xiao, W., and Yoshimura, K.: A global database of water vapor isotopes measured with high temporal resolution infrared laser spectroscopy, *Sci Data*, 6, 10.1038/sdata.2018.302, 2019.

Wever, N., Comola, F., Bavay, M., and Lehning, M.: Simulating the influence of snow surface processes on soil moisture dynamics and streamflow generation in an alpine catchment, *Hydrol Earth Syst Sc*, 21, 4053-4071, 10.5194/hess-21-4053-2017, 2017.

Woods, R., and Sivapalan, M.: A synthesis of space-time variability in storm response: Rainfall, runoff generation, and routing, *Water Resour Res*, 35, 2469-2485, Doi 10.1029/1999wr900014, 1999.

Würzer, S., Wever, N., Juras, R., Lehning, M., and Jonas, T.: Modelling liquid water transport in snow under rain-on-snow conditions – considering preferential flow, *Hydrol. Earth Syst. Sci.*, 21, 1741-1756, 10.5194/hess-21-1741-2017, 2017.

Xu, H. L., Xu, C. Y., Chen, H., Zhang, Z. X., and Li, L.: Assessing the influence of rain gauge density and distribution on hydrological model performance in a humid region of China, *Journal of Hydrology*, 505, 1-12, 10.1016/j.jhydrol.2013.09.004, 2013.

Yang, D. Q.: Double Fence Intercomparison Reference (DFIR) vs. Bush Gauge for "true" snowfall measurement, *Journal of Hydrology*, 509, 94-100, 10.1016/j.jhydrol.2013.08.052, 2014.

Zampieri, M., Scocimarro, E., Gualdi, S., and Navarra, A.: Observed shift towards earlier spring discharge in the main Alpine rivers, *Sci. Total Environ.*, 503, 222-232, 10.1016/j.scitotenv.2014.06.036, 2015.

Zehe, E., Becker, R., Bardossy, A., and Plate, E.: Uncertainty of simulated catchment runoff response in the presence of threshold processes: Role of initial soil moisture and precipitation, *Journal of Hydrology*, 315, 183-202, 10.1016/j.jhydrol.2005.03.038, 2005.

Zemp, M., Huss, M., Thibert, E., Eckert, N., McNabb, R., Huber, J., Barandun, M., Machguth, H., Nussbaumer, S. U., Gartner-Roer, I., Thomson, L., Paul, F., Maussion, F., Kutuzov, S., and Cogley, J. G.: Global glacier mass changes and their contributions to sea-level rise from 1961 to 2016 (vol 568, pg 382, 2019), *Nature*, 577, E9-E9, 10.1038/s41586-019-1889-5, 2020.

Zillgens, B., Merz, B., Kirnbauer, R., and Tilch, N.: Analysis of the runoff response of an alpine catchment at different scales, *Hydrol Earth Syst Sc*, 11, 1441-1454, DOI 10.5194/hess-11-1441-2007, 2007.

Zoccatelli, D., Borga, M., Chirico, G. B., and Nikolopoulos, E. I.: The relative role of hillslope and river network routing in the hydrologic response to spatially variable rainfall fields, *Journal of Hydrology*, 531, 349-359, 10.1016/j.jhydrol.2015.08.014, 2015.

Zuecco, G., Carturan, L., De Blasi, F., Seppi, R., Zanoner, T., Penna, D., Borga, M., Carton, A., and Dalla Fontana, G.: Understanding hydrological processes in glacierized catchments: Evidence and implications of highly variable isotopic and electrical conductivity data, *Hydrological Processes*, 33, 816-832, 10.1002/hyp.13366, 2019.

Supplementary Material

Supplementary material - Chapter 2

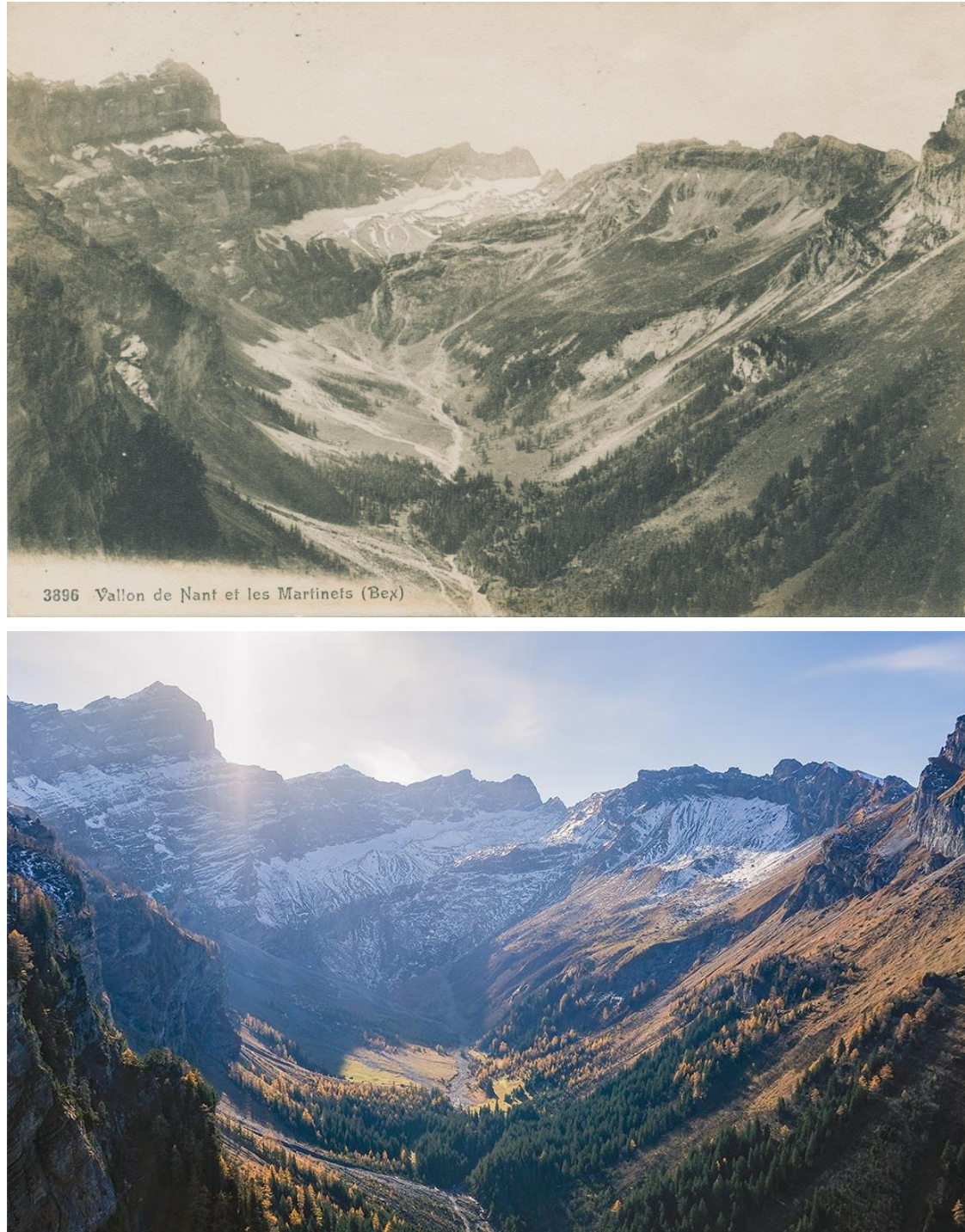


Figure S62. Comparison of vegetation cover between a historical picture (1912 or before, on top) and an actual picture (2017, on bottom). Credit for the top picture: Robert di Salvo.

Supplementary material - Chapter 4

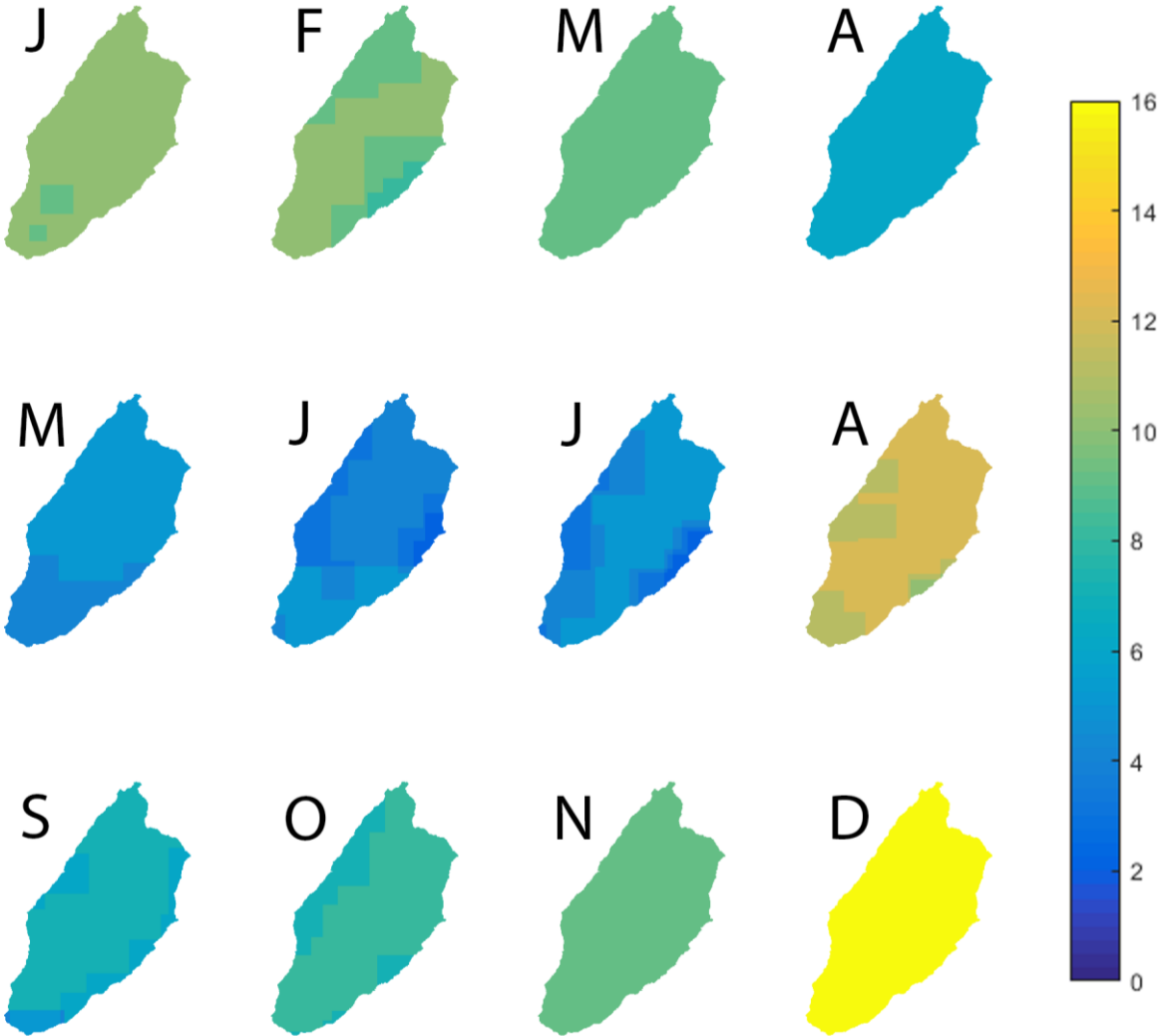


Figure S63. Maps showing the number of images used to compute the snowcover maps. The square shapes are due to the removal of a part of an image with clouds.

Supplementary material - Chapter 5

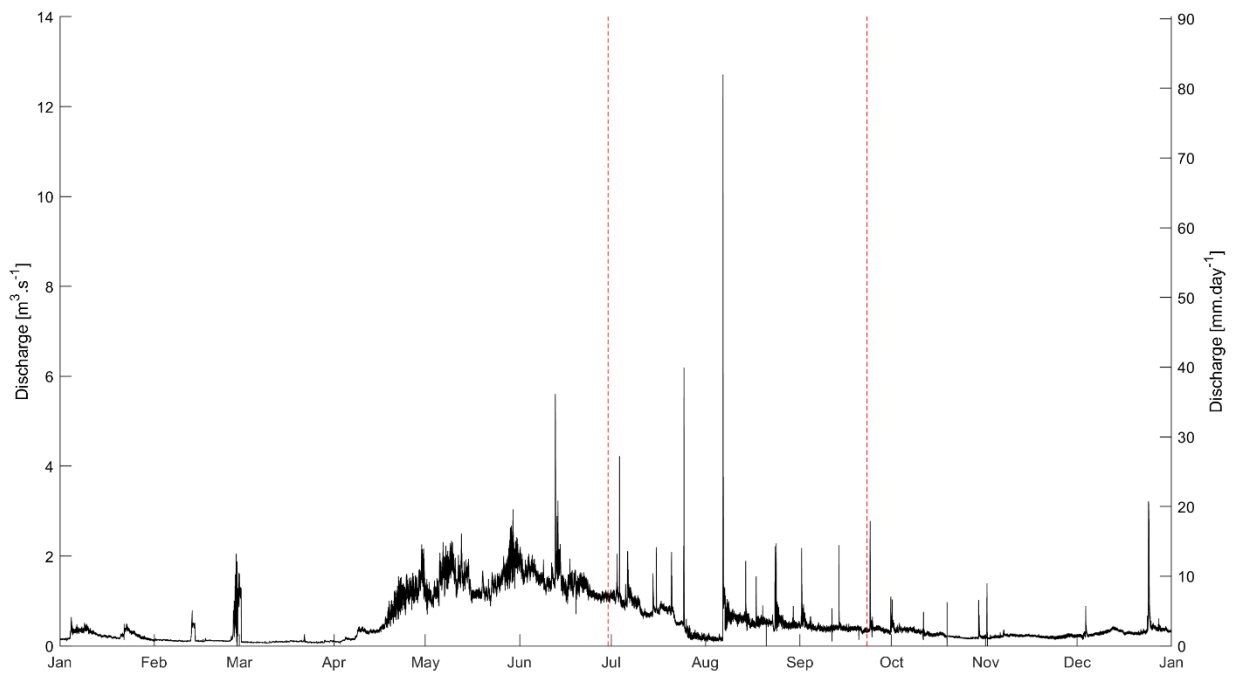


Figure S64. River discharge measured at the Vallon de Nant outlet (in $m^3.s^{-1}$ and $mm.day^{-1}$) over 2018. The study period (from July 1st 2018 to September 23th 2018) is marked out by the two red dashed lines.

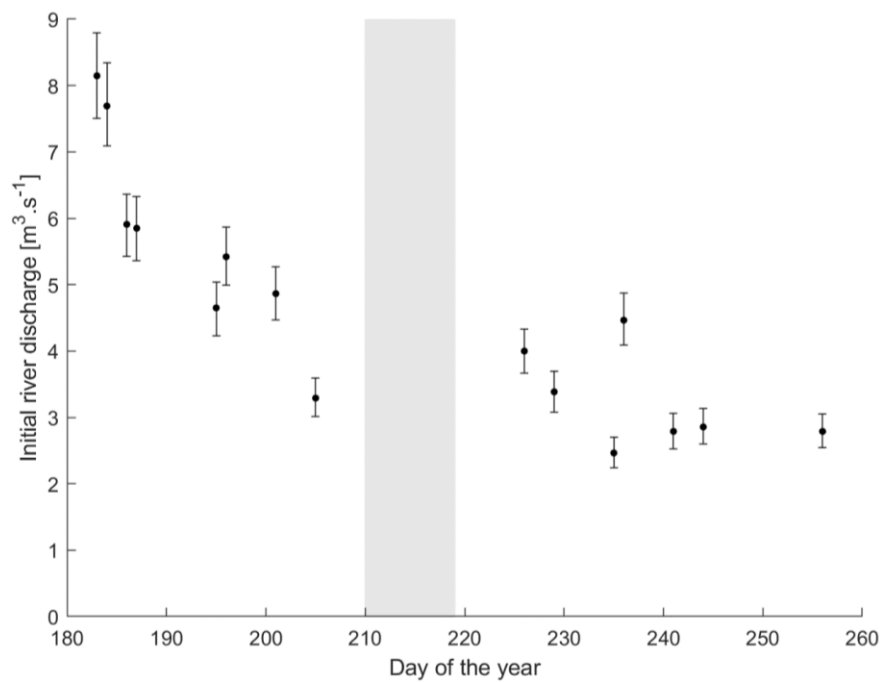


Figure S65. Initial streamflow for the 15 rainfall events causing a river reaction as function of the day of the year. The grey area corresponds to the period when the streamflow gauge readings were perturbed and thus discarded from the present analysis.

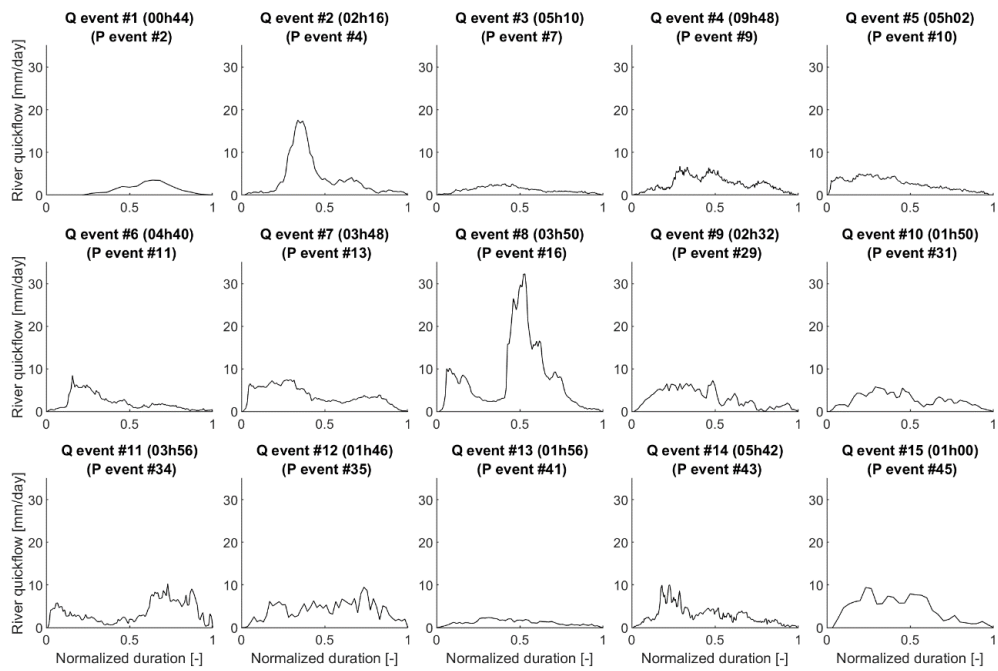


Figure S66. River quickflow for 15 rainfall events (P event) causing a noticeable river reaction (Q event). The length of events is normalized.

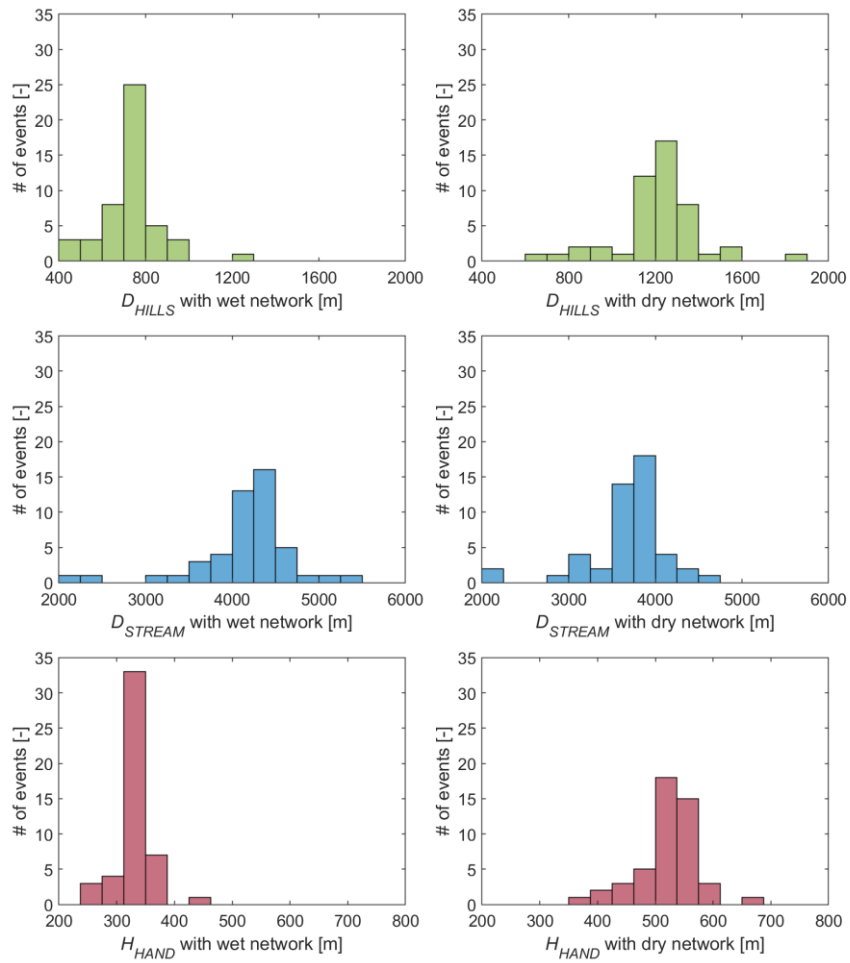


Figure S67. Distribution of the distance metrics D_{HILLS} , D_{STREAM} and H_{HAND} for all 48 rainfall events.

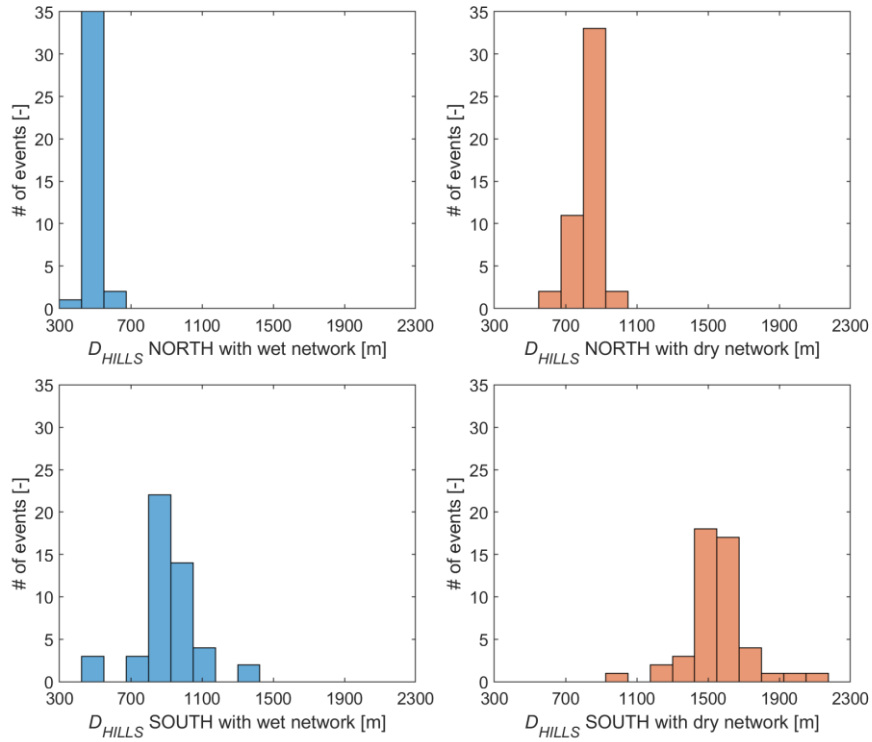


Figure S68. Distribution of D_{HILLS} for the northern part (left column) and the southern part (right column) of the catch men, with respect to the wet network (top row) and the dry network (bottom row). The median of the wet distances are 329 m shorter than the dry distances in the northern part (top), in the southern part (bottom) they are 634 m shorter.

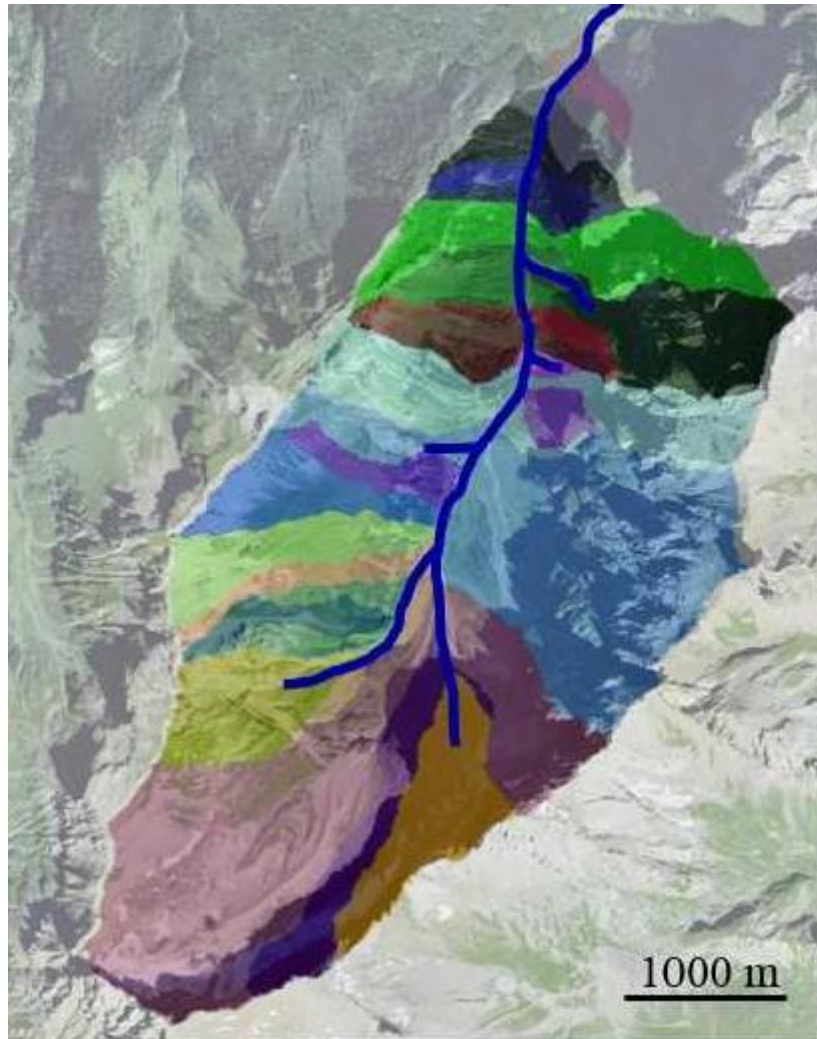


Figure S69. Map of the Vallon de Nant (Map data from www.map.geo.admin.ch, © CNES, Spot Image, swisstopo, NPOC) showing the 25 subcatchments and the stream network geometry used for the modelization.

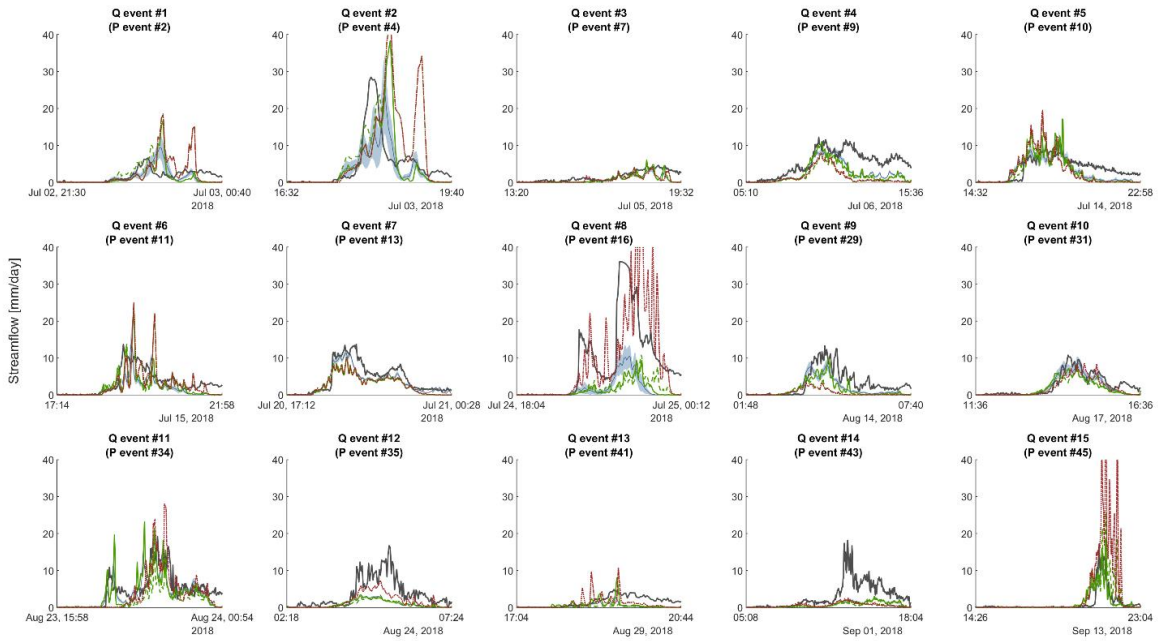


Figure S70. Results of simulation. For each of the 15 events having a streamflow reaction is plotted the observed streamflow (black curve), the simulated streamflow based on stochastic rainfall fields (blue curve and band), the simulated streamflow based on the best 3-station and 1-station network (respectively with plain and dashed green curves), and the simulated streamflow based on the worst 3-station network (dotted red curve).

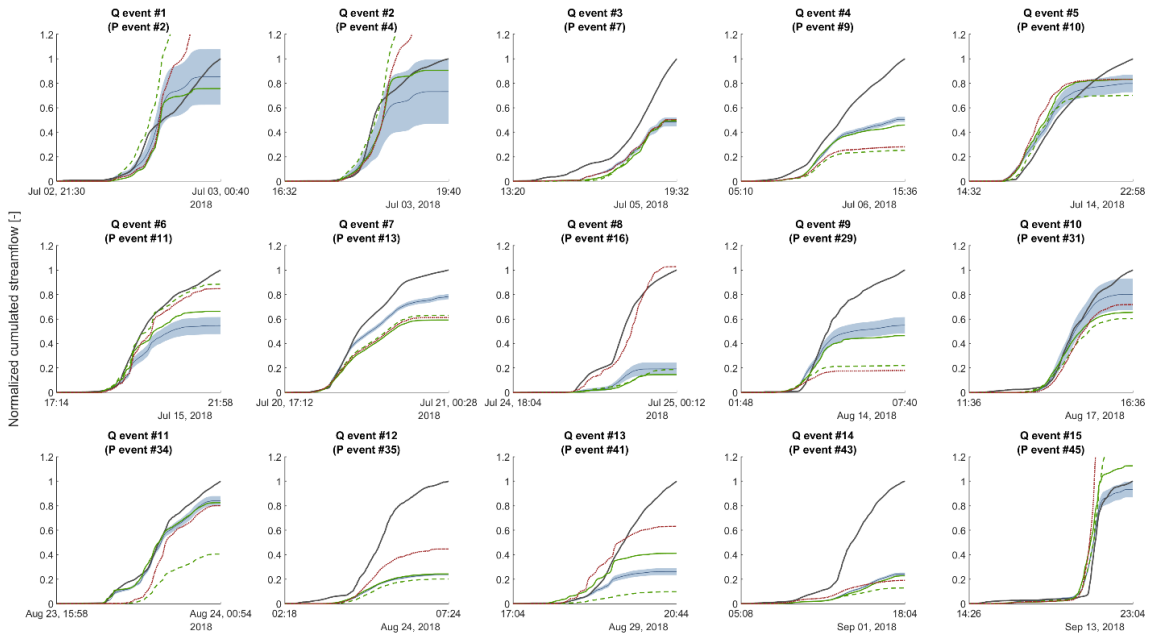


Figure S71. Cumulated results of simulation. For each of the 15 events having a streamflow reaction is plotted the cumulated observed streamflow (black curve), the cumulated simulated streamflow based on stochastic rainfall fields (blue curve and band), the cumulated simulated streamflow based on the best 3-station and 1-station network (respectively with plain and dashed green curves), and the cumulated simulated streamflow based on the worst 3-station network (dotted red curve). The amounts of streamflow are normalized by the cumulated amount of observed streamflow.

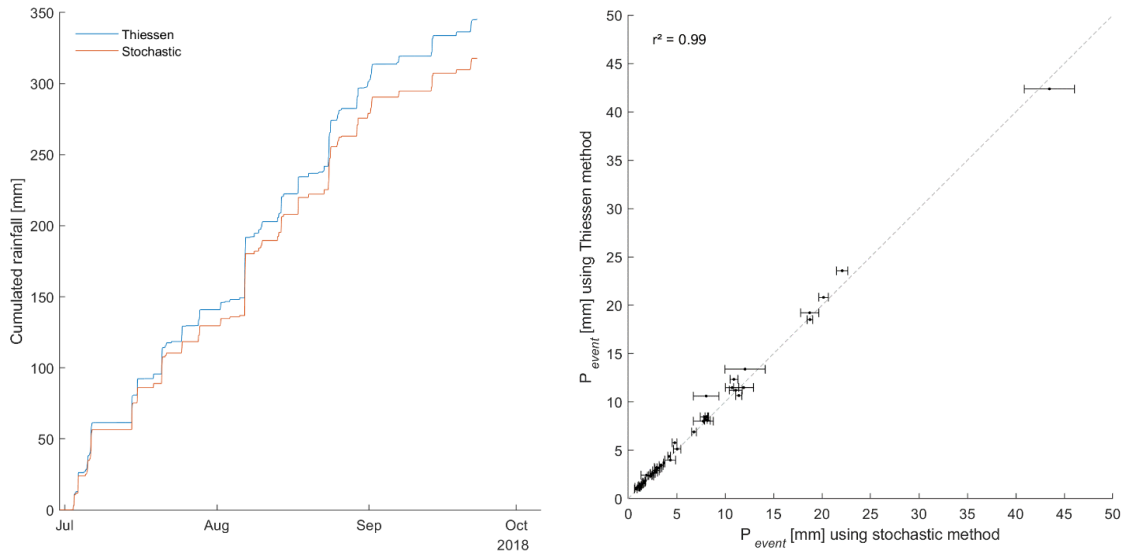


Figure S72: Deviation between the two spatial rainfall interpolation methods used in this paper, in terms of cumulated rainfall (left) and per event (right).

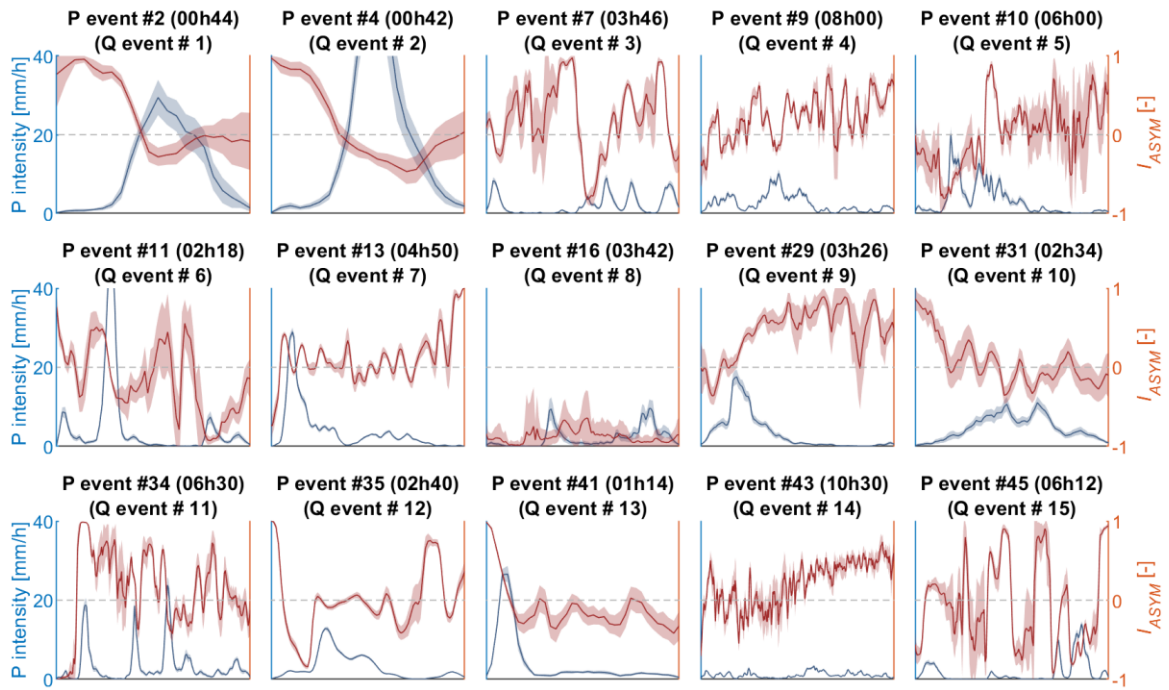


Figure S73. Evolution of rainfall intensity and I_{ASYM} for the 15 rainfall events (P event) associated with a river reaction (Q event).

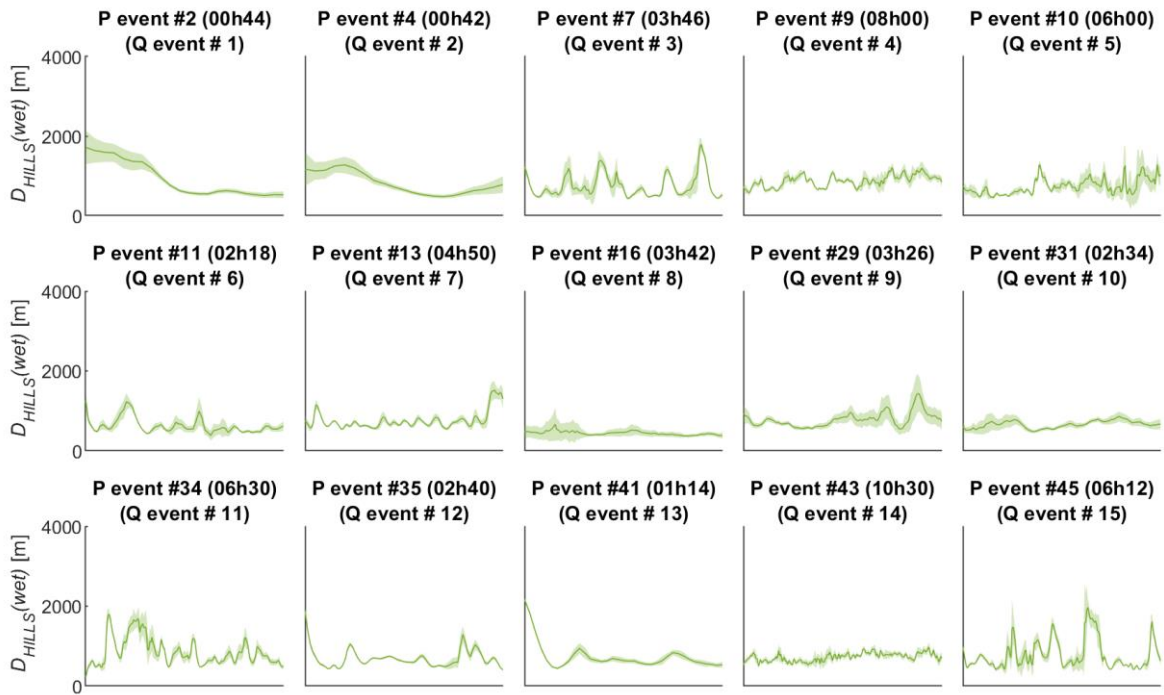


Figure S74. Evolution of D_{HILLS} for the 15 rainfall events (P event) associated with a river reaction (Q event).

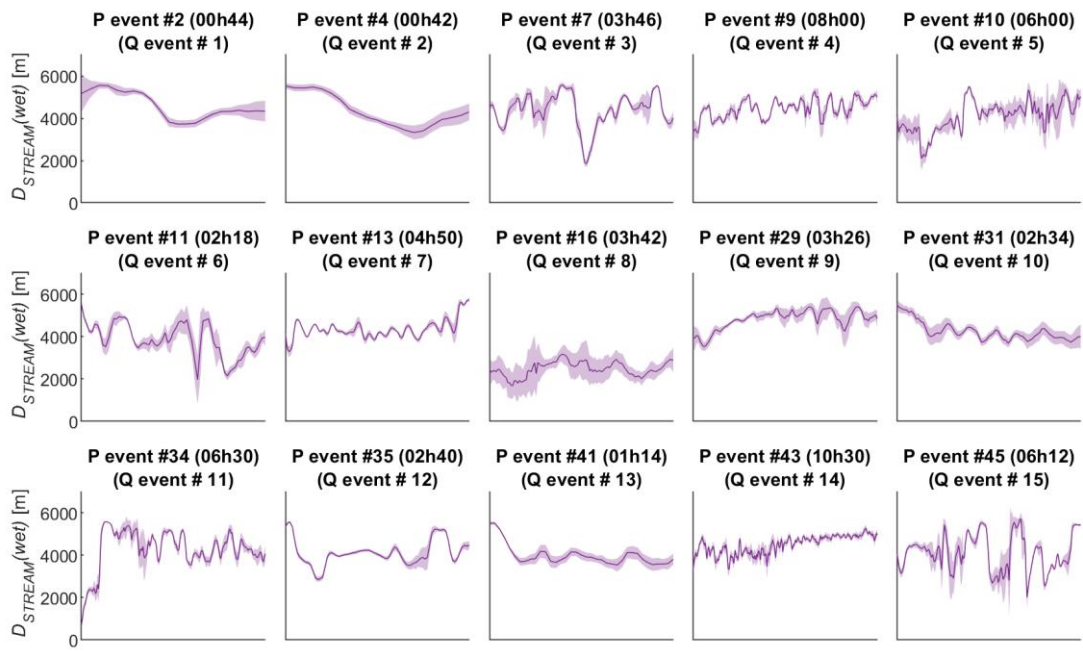


Figure S75. Evolution of D_{STREAM} for the 15 rainfall events (P event) associated with a river reaction (Q event).

Table S19. Distance metrics for each streamflow event with respect to the extended (wet) and the retracted (dry) network and the combined distance if a threshold of antecedent precipitation of 20 mm is applied.

Network	D_{HILLS} [m]			D_{STREAM} [m]			H_{HAND} [m]		
	wet	dry	pseudo-dynamic	wet	dry	pseudo-dynamic	wet	dry	pseudo-dynamic
2-Jul-18	925	1521	1521	4604	4008	4008	378	611	611
3-Jul-18	817	1336	1336	4361	3842	3842	350	550	550
5-Jul-18	755	1287	755	4374	3842	4374	350	557	350
6-Jul-18	874	1352	874	4450	3972	4450	355	536	355
14-Jul-18	736	1263	1263	4100	3574	3574	345	554	554
15-Jul-18	628	1122	1122	3871	3377	3377	326	528	528
20-Jul-18	758	1282	1282	4348	3823	3823	336	541	541
24-Jul-18	443	740	740	2481	2184	2184	278	419	419
14-Aug-18	784	1286	1286	4806	4305	4305	354	540	540
17-Aug-18	662	1122	1122	4240	3780	3780	313	490	490
23-Aug-18	854	1371	1371	4273	3756	3756	362	563	563
24-Aug-18	692	1155	692	4114	3651	4114	320	503	320
29-Aug-18	739	1207	1207	3995	3526	3526	336	524	524
01-sept-18	725	1271	725	4487	3941	4487	331	545	331
13-sept-18	782	1291	1291	4103	3594	3594	352	556	556

Table S20. Correlations between distance metrics for all the rainfall events (subset #1, Table 4 in the main text). Absolute values equal or over 0.60 are in bold.

		D_{HILLS}	D_{HILLS}	D_{STREAM}	D_{STREAM}	H_{HAND}	H_{HAND}	D_{HILLS}	D_{STREAM}	H_{HAND}
	River network	<i>Wet</i>	<i>Dry</i>	<i>Wet</i>	<i>Dry</i>	<i>Wet</i>	<i>Dry</i>	<i>pseudo-dynamic</i>	<i>pseudo-dynamic</i>	<i>pseudo-dynamic</i>
D_{HILLS}	<i>Wet</i>	-								
D_{HILLS}	<i>Dry</i>	0.97	-							
D_{STREAM}	<i>Wet</i>	0.78	0.87	-						
D_{STREAM}	<i>Dry</i>	0.76	0.85	1.00	-					
H_{HAND}	<i>Wet</i>	0.95	0.95	0.70	0.68	-				
H_{HAND}	<i>Dry</i>	0.87	0.95	0.79	0.75	0.94	-			
D_{HILLS}	<i>pseudo-dynamic</i>	0.51	0.57	0.42	0.38	0.57	0.63	-		
D_{STREAM}	<i>pseudo-dynamic</i>	0.72	0.77	0.92	0.93	0.61	0.65	0.04	-	
H_{HAND}	<i>pseudo-dynamic</i>	0.28	0.36	0.22	0.18	0.40	0.48	0.96	-0.18	-

Table S21. For the 23 events measured by the full network setup: number of stations wrong by a factor 2 compared to the average of all the stations.

P event No.	Number of stations wrong by a factor 2
16	9
17	0
18	0
20	4
21	7
23	11
24	1
25	0
26	0
28	4
29	2
30	0
31	0
32	7
33	0
34	1
35	0
36	2
37	2
38	4
39	11
40	0
41	1

Table S22. For the 23 events measured by the full network setup: number of events for which the station is wrong by a factor 2 compared to the average of all the stations.

Station No.	Number of events for which the station is wrong by a factor 2
1	8
2	2
3	5
4	5
5	3
6	4
7	8
8	6
9	7
10	4
11	7
12	7

Detail of all the 48 rainfall events measured over the observation period (Figure S76 to Figure S123)

Each of the following figure presents:

- On the left, a map with the 12 rain gauge locations shows the total amount of rainfall recorded by each station during the event (a red cross is displayed in case of missing data).
- On top is plotted the rainfall intensity recorded by each of the 12 rain gauges (the y-axis scale between 2 stations is 20 mm/h). The rainfall event extent is marked out by green dashed lines.
- Below is shown the areal rainfall intensity (and uncertainty) calculated for the catchment using the stochastic method. The rainfall event extent is marked out by green dashed lines.
- Below the horizontal line the zoomed hydrogram shows a detailed view of the river discharge (and uncertainty). In case a river reaction is associated, the discharge event extent is marked out by red dashed lines. Between these vertical lines is drawn a line joining the initial and final baseflow, separating the streamflow fed by the baseflow (under the line) to the fast streamflow (over the line). The red square shows the center of mass of the fast streamflow part. The shaded orange areas correspond to periods the river streamflow data are not available.
- At the bottom is shown the general hydrogram over the whole observation period (July 1st to September 23th). The red dashed lines mark out the period the other plots are focusing on. The shaded orange areas correspond to periods the river streamflow data are not available.

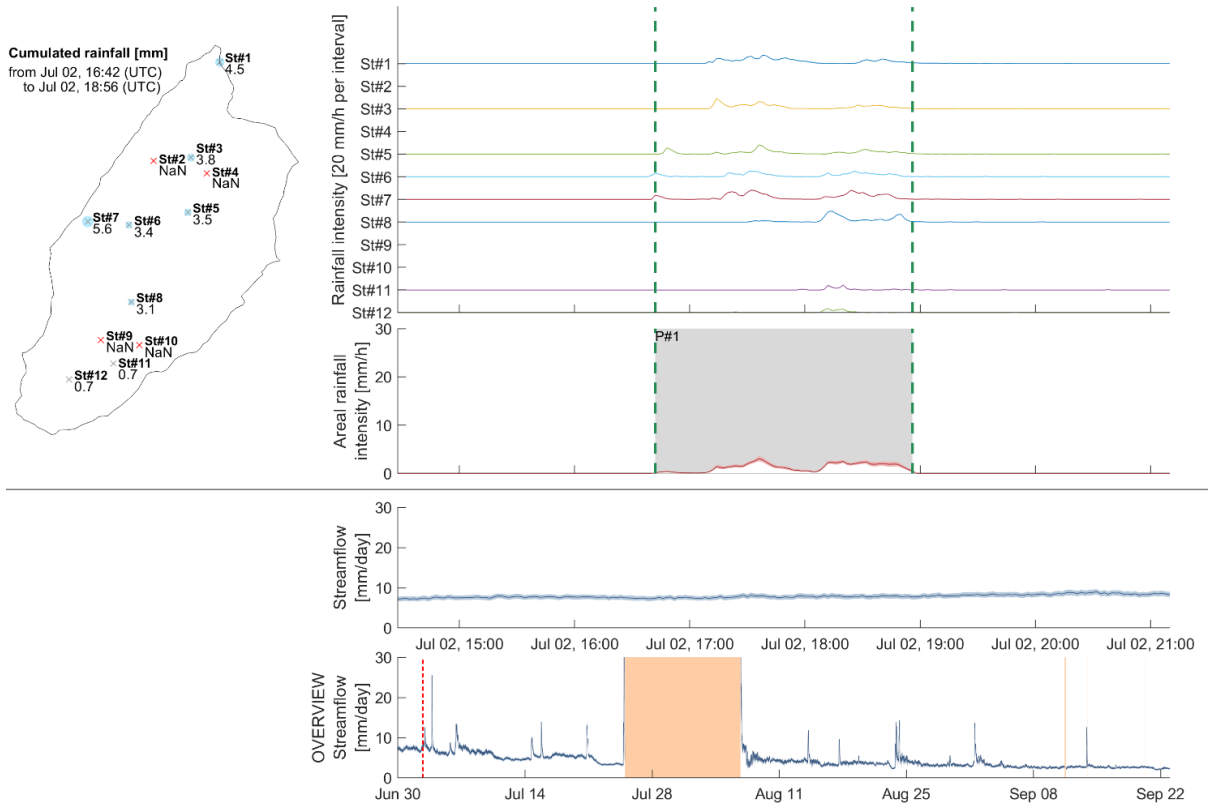


Figure S76. Precipitation event No. 1 from July 2nd 04:42 PM to July 2nd 06:56 PM

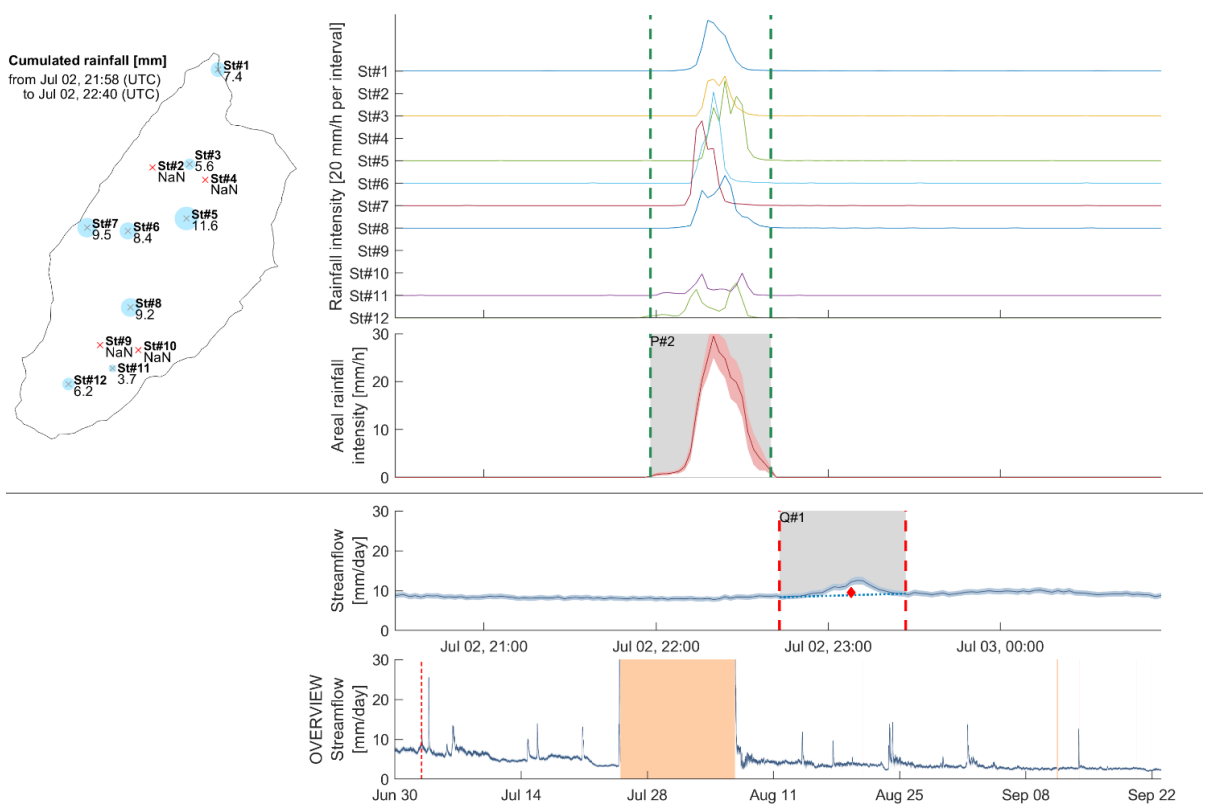


Figure S77. Precipitation event No. 2 from July 2nd 09:58 PM to July 2nd 10:40 PM and discharge event No. 1 from July 2nd 10:43 PM to July 2nd 11:27 PM

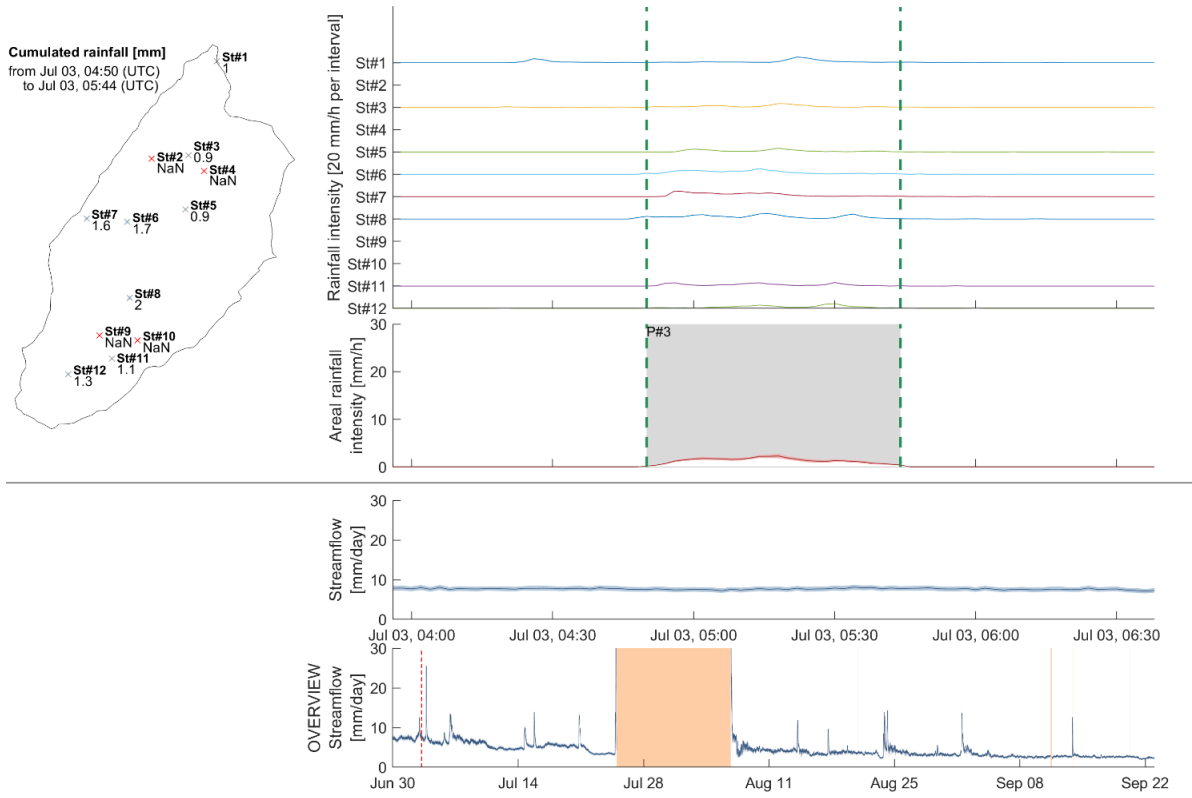


Figure S78. Precipitation event No. 3 from July 3rd 04:50 AM to July 3rd 05:44 AM

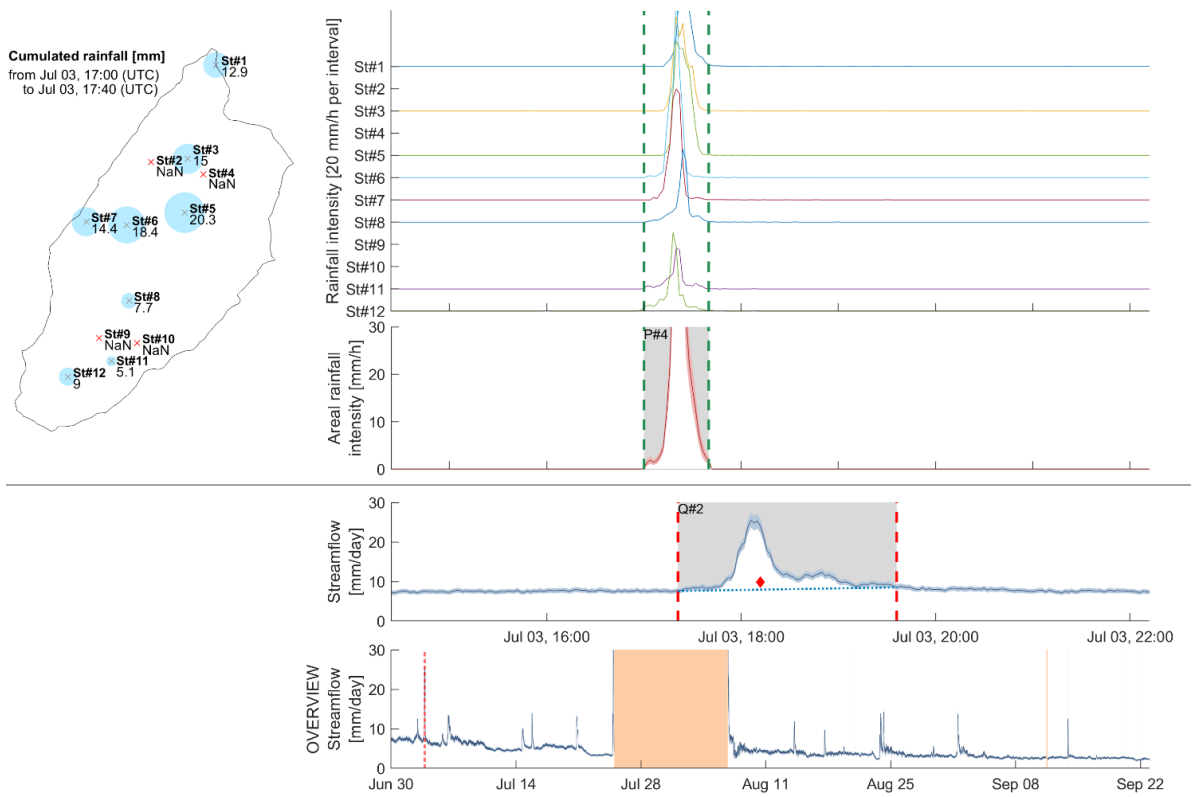


Figure S79. Precipitation event No. 4 from July 3rd 05:00 PM to July 3rd 05:40 PM and discharge event No. 2 from July 3rd 05:21 PM to July 3rd 07:36 PM

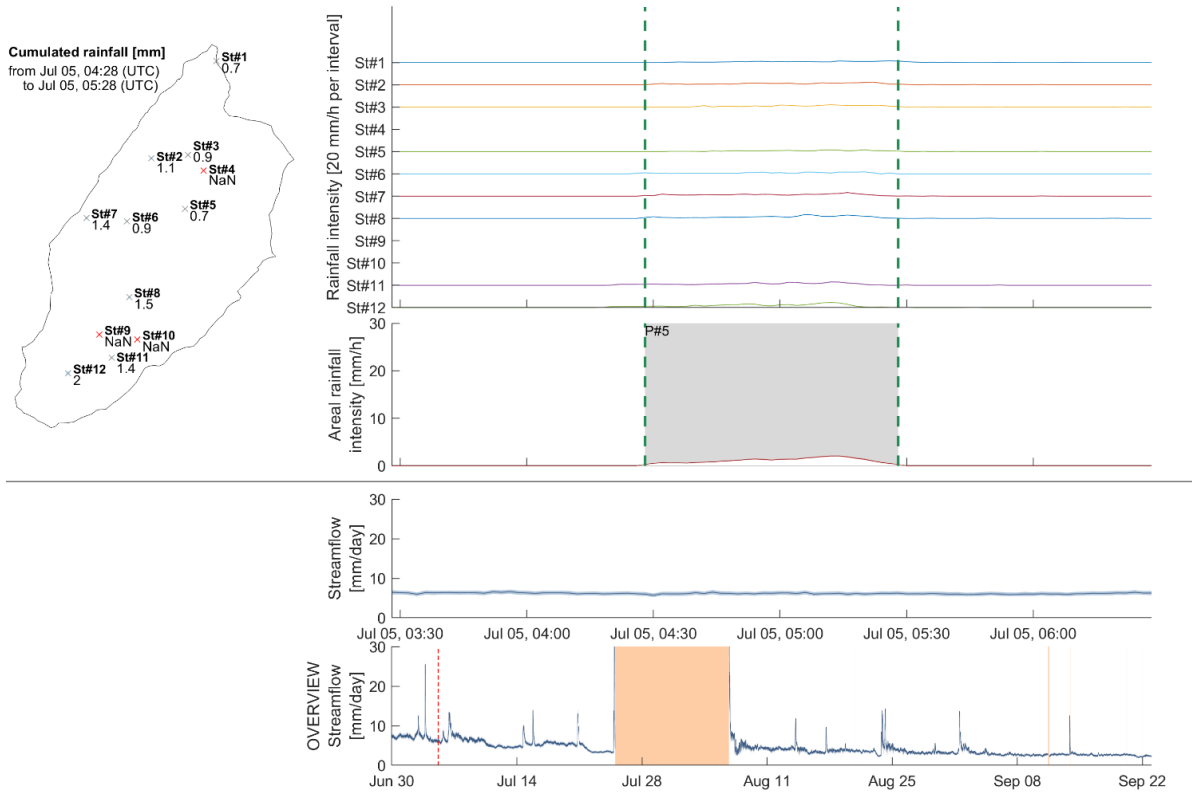


Figure S80. Precipitation event No. 5 from July 5th 04:28 AM to July 5th 05:28 AM

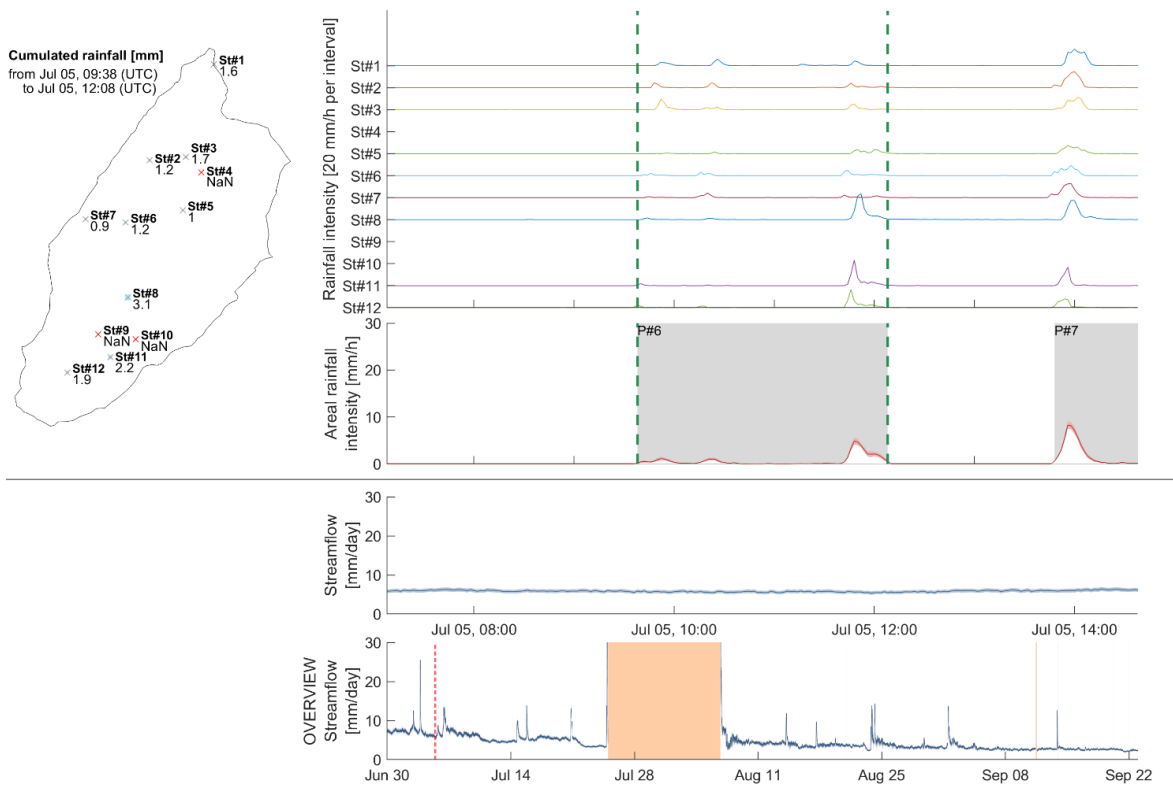


Figure S81. Precipitation event No. 6 from July 5th 09:38 AM to July 5th 12:08 PM

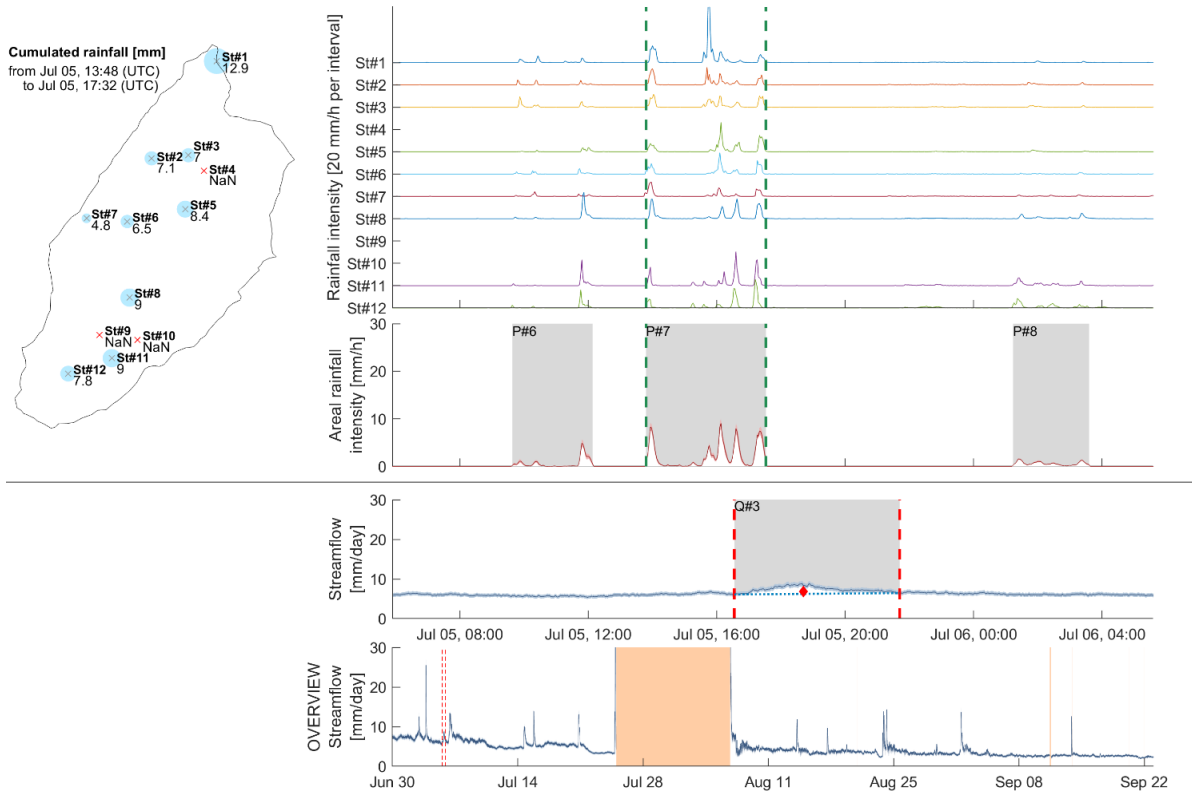


Figure S82. Precipitation event No. 7 from July 5th 01:48 PM to July 5th 05:32 PM and discharge event No. 3 from July 5th 04:33 PM to July 5th 09:42 PM

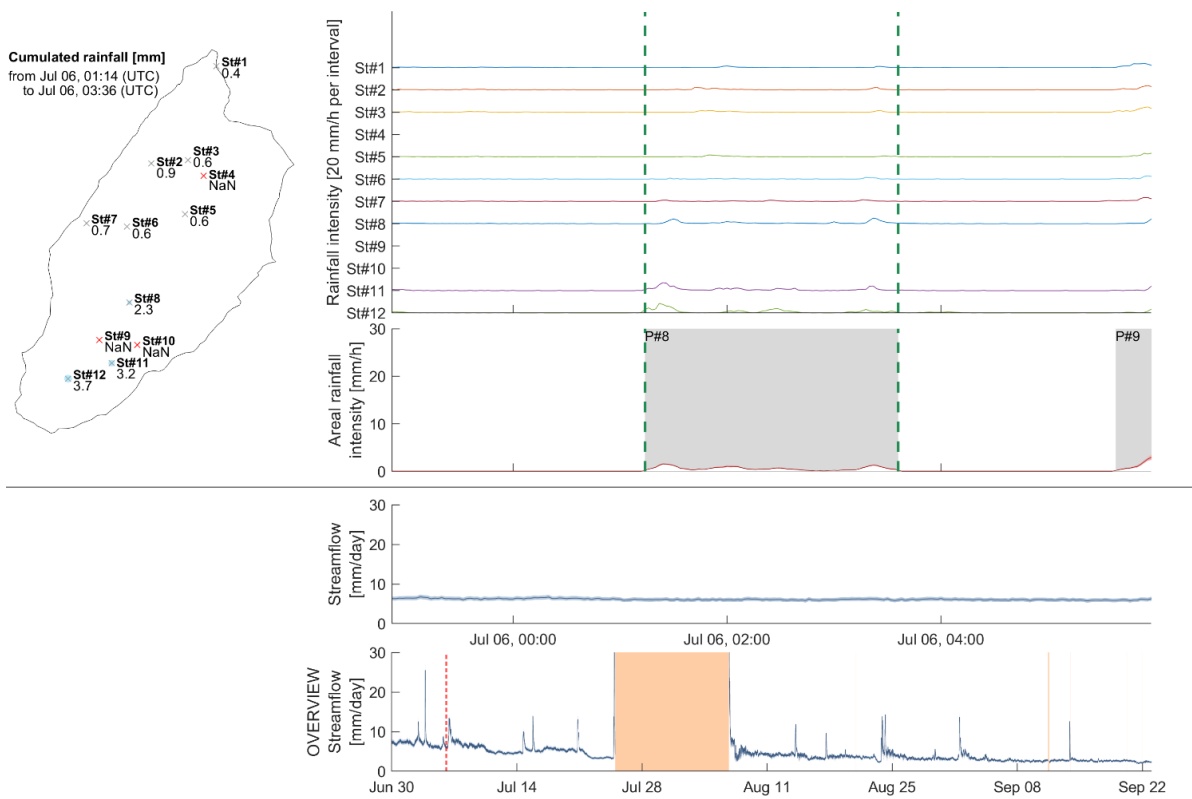


Figure S83. Precipitation event No. 8 from July 6th 01:14 AM to July 6th 03:36 AM

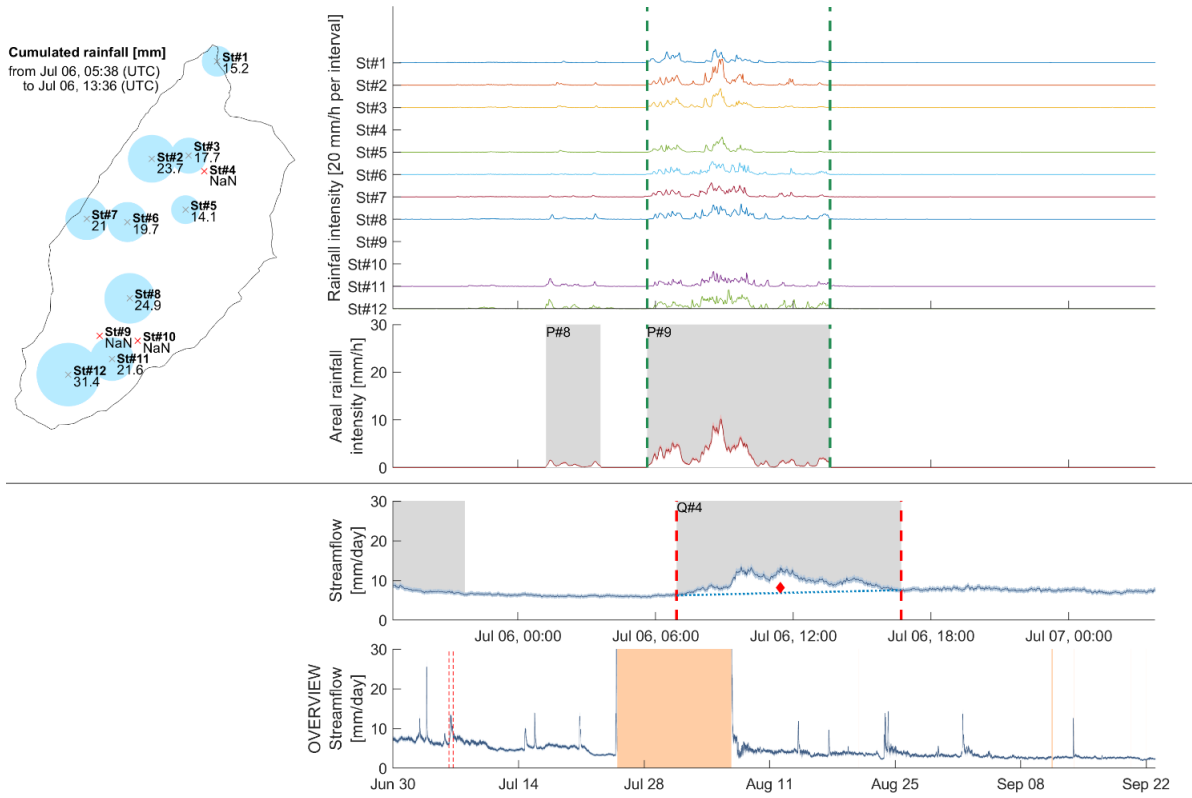


Figure S84. Precipitation event No. 9 from July 6th 05:38 AM to July 6th 01:36 PM and discharge event No. 4 from July 6th 06:55 AM to July 6th 04:42 PM

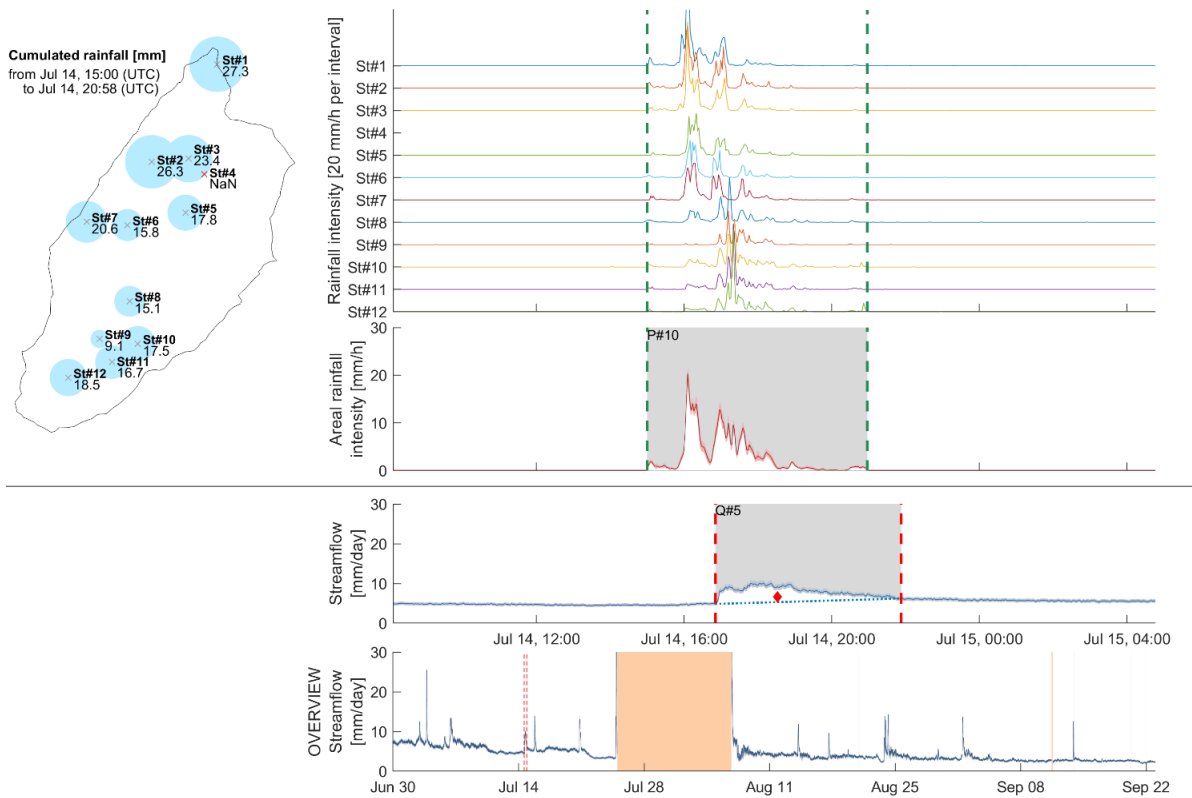


Figure S85. Precipitation event No. 10 from July 14th 03:00 PM to July 14th 08:58 PM and discharge event No. 5 from July 14th 04:51 PM to July 14th 09:53 PM

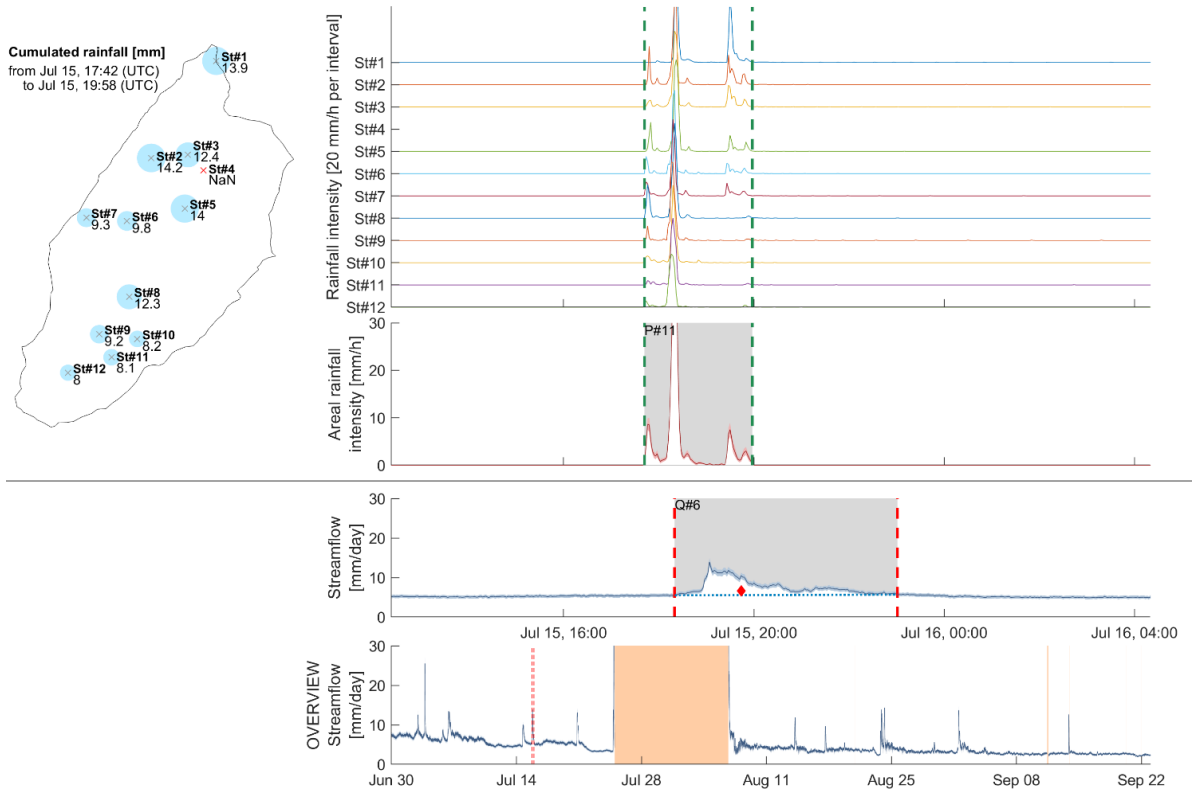


Figure S86. Precipitation event No. 11 from July 15th 05:42 PM to July 15th 07:58 PM and discharge event No. 6 from July 15th 06:20 PM to July 15th 11:01 PM

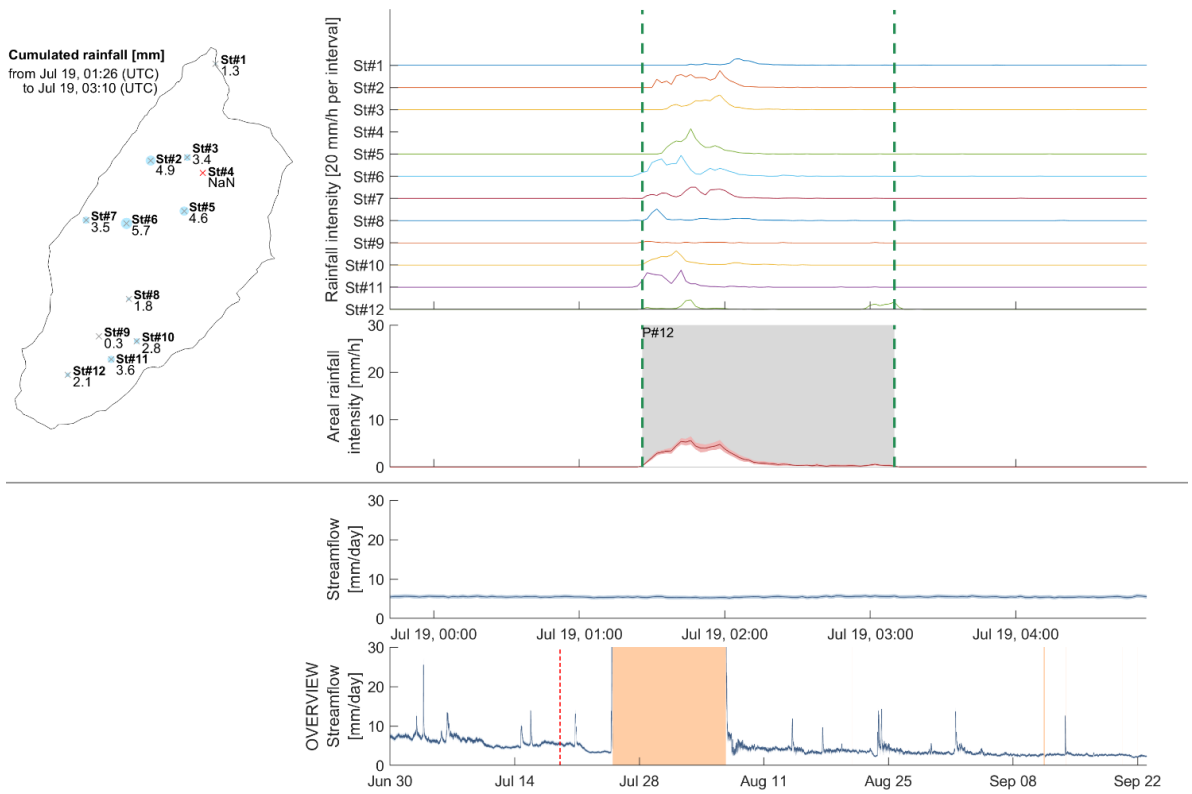


Figure S87. Precipitation event No. 12 from July 19th 01:26 AM to July 19th 03:10 AM

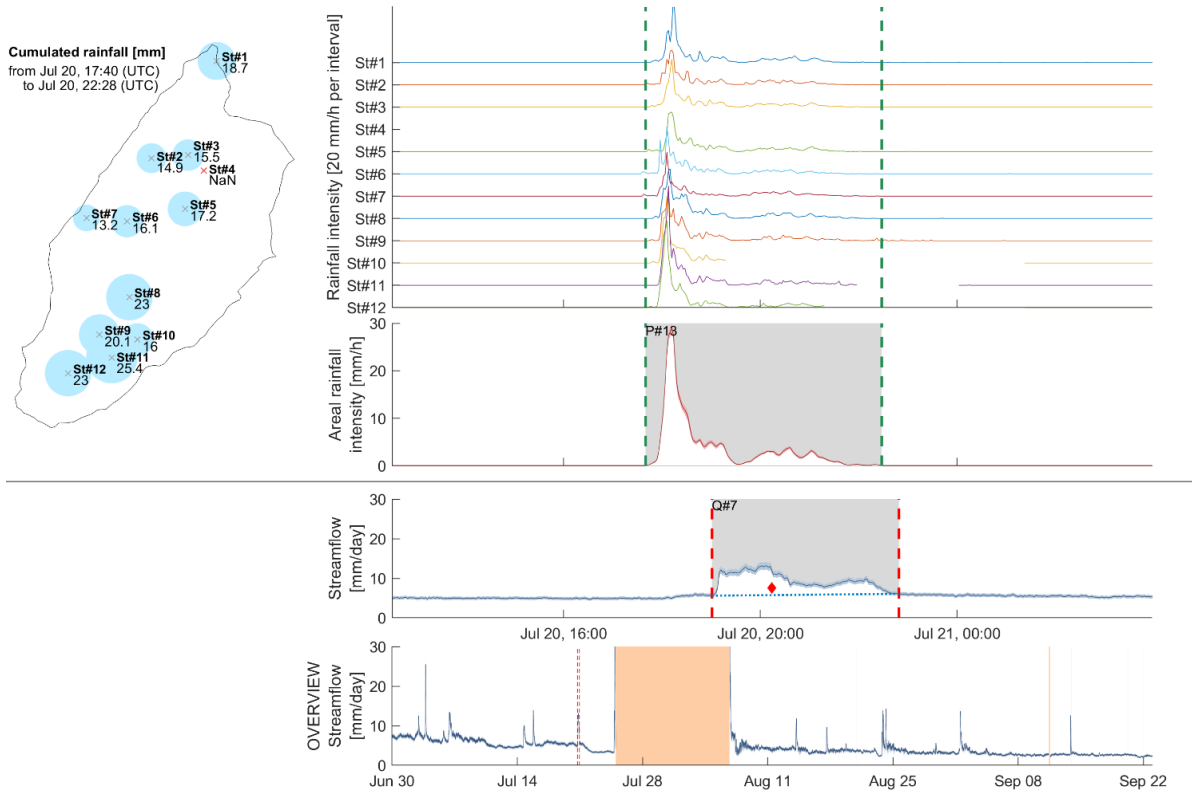


Figure S88. Precipitation event No. 13 from July 20th 05:40 PM to July 20th 10:28 PM and discharge event No. 7 from July 20th 07:01 PM to July 20th 10:49 PM

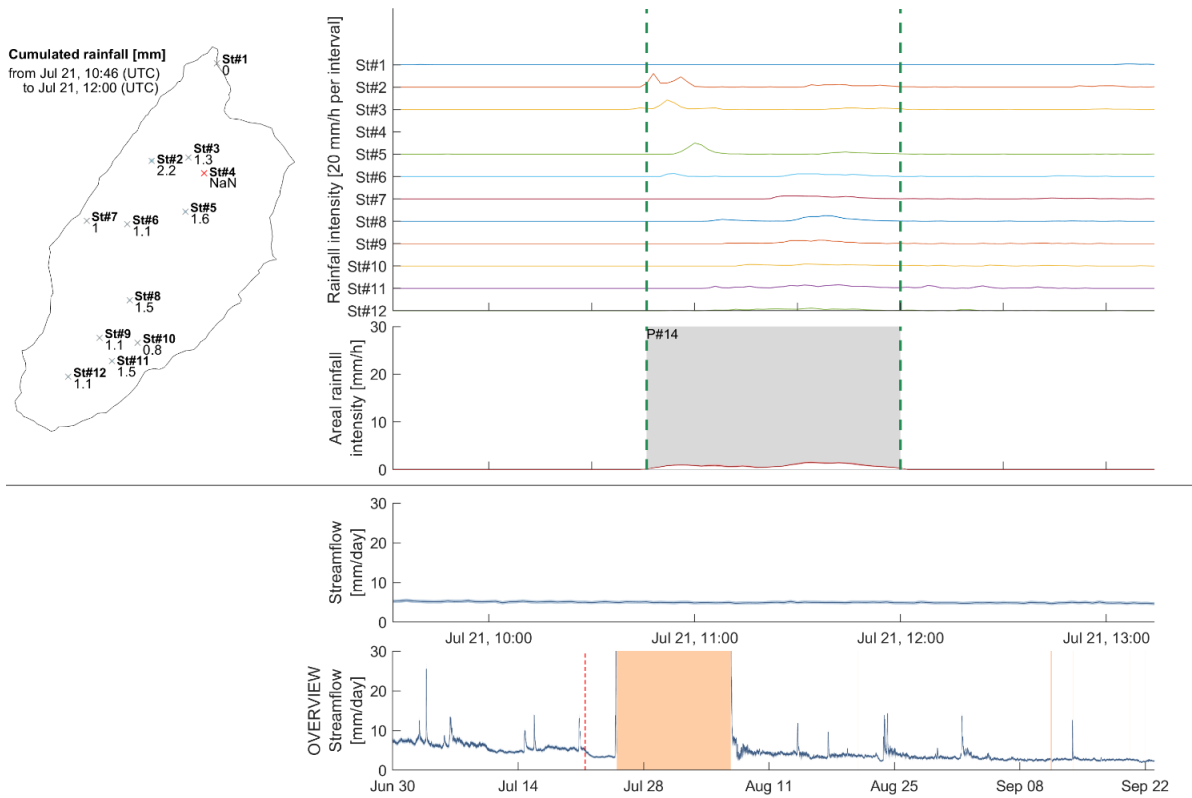


Figure S89. Precipitation event No. 14 from July 21st 10:46 AM to July 21st 12:00 PM

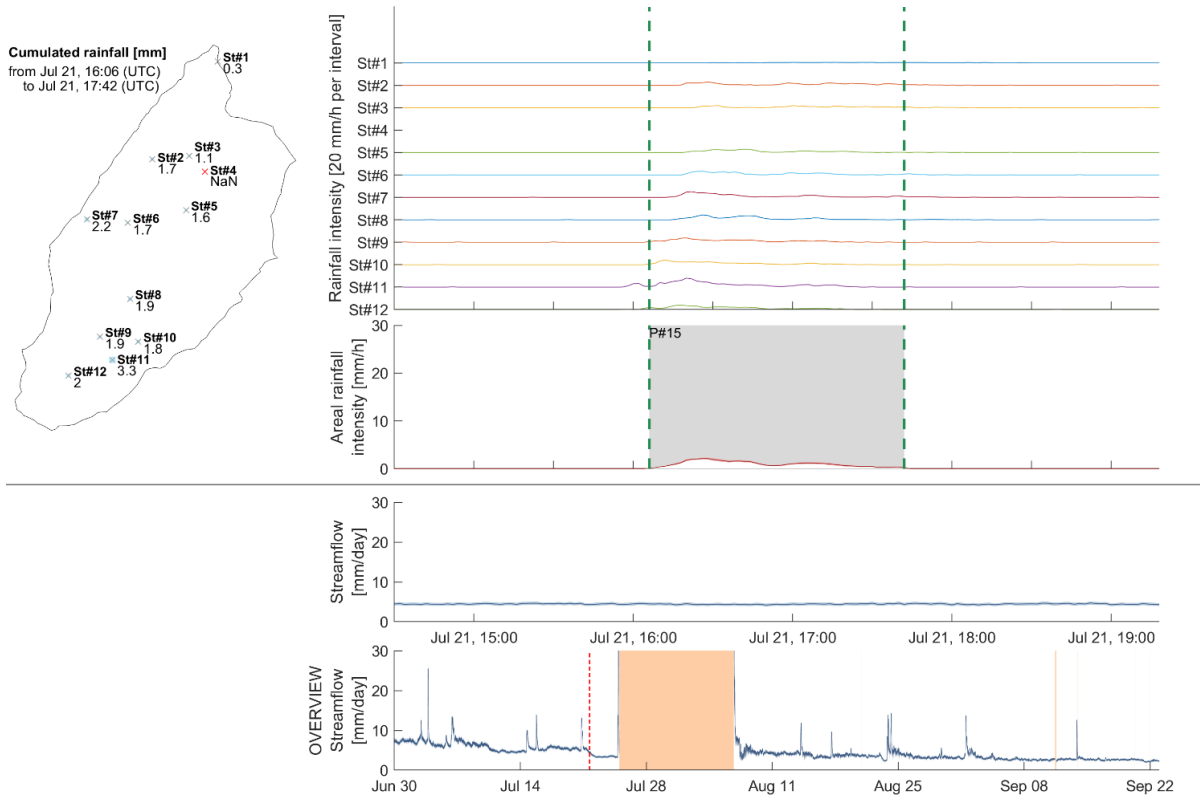


Figure S90. Precipitation event No. 15 from July 21st 04:06 PM to July 21st 05:42 PM

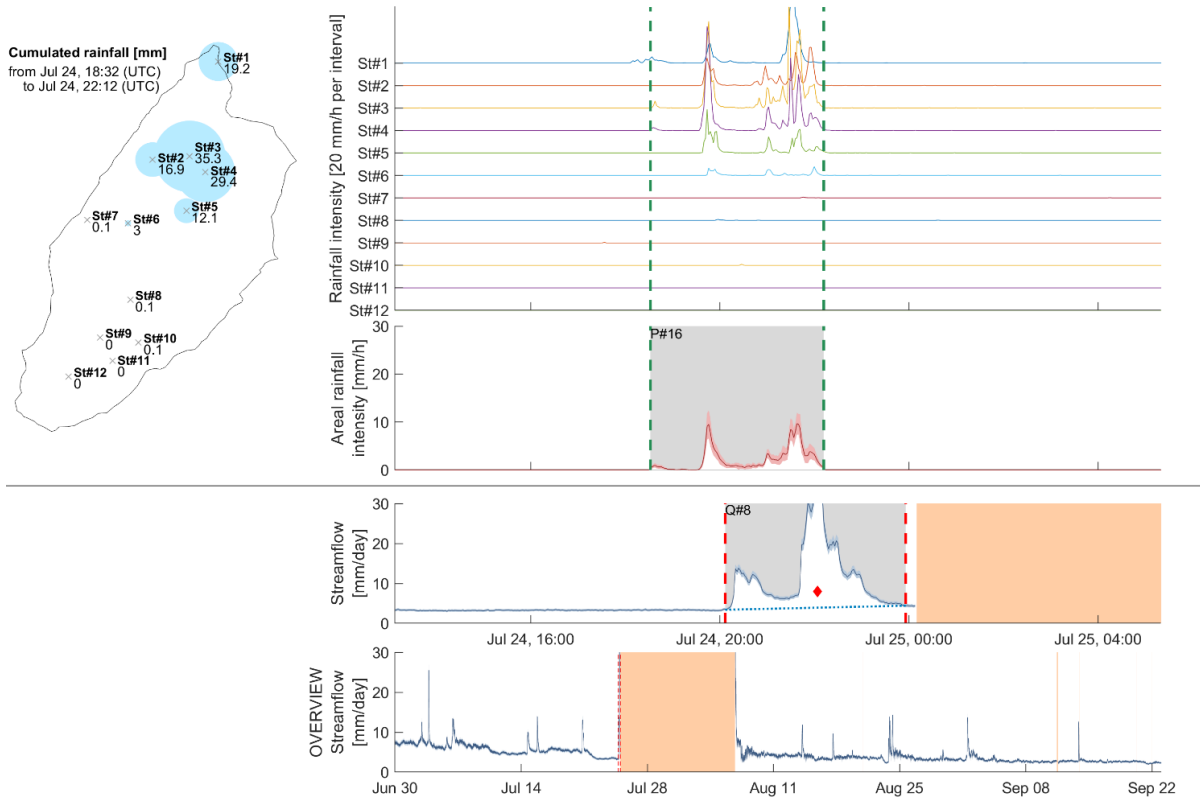


Figure S91. Precipitation event No. 16 from July 24th 06:32 PM to July 24th 10:12 PM and discharge event No. 8 from July 24th 08:07 PM to July 24th 11:56 PM

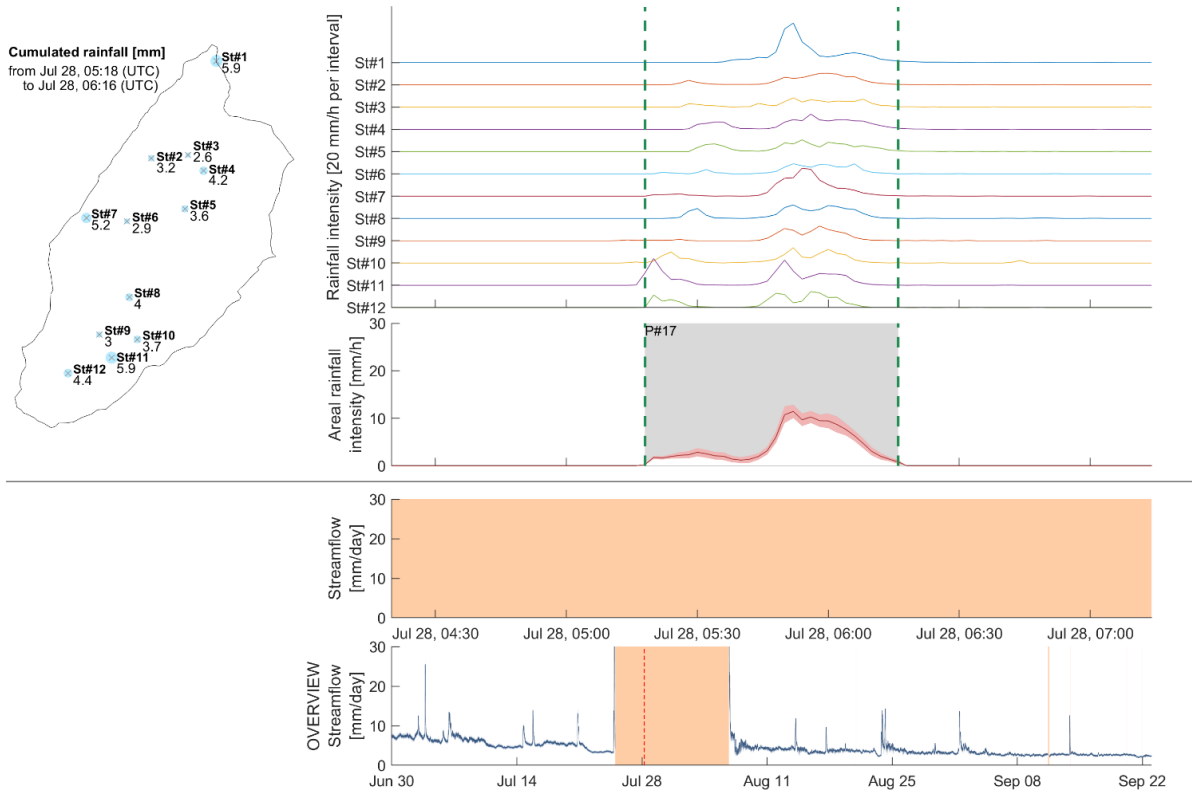


Figure S92. Precipitation event No. 17 from July 28th 05:18 AM to July 28th 06:16 AM

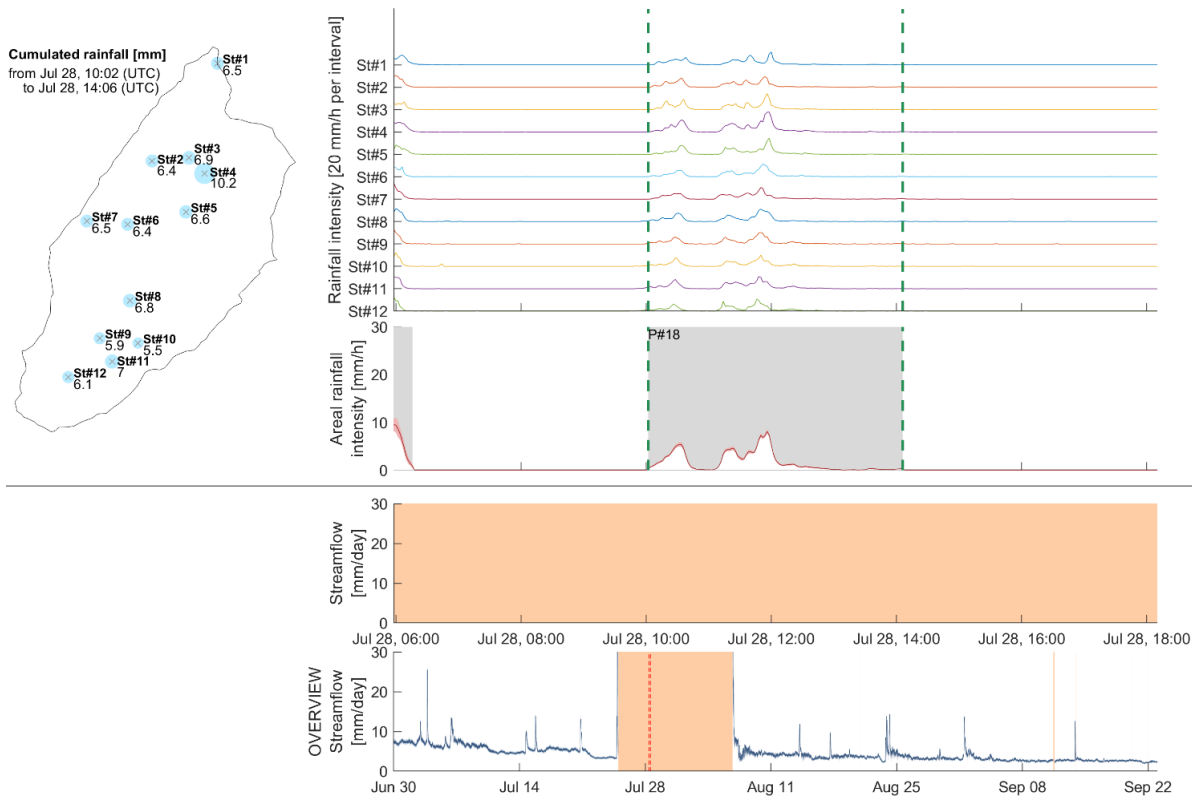


Figure S93. Precipitation event No. 18 from July 28th 10:02 AM to July 28th 02:06 PM

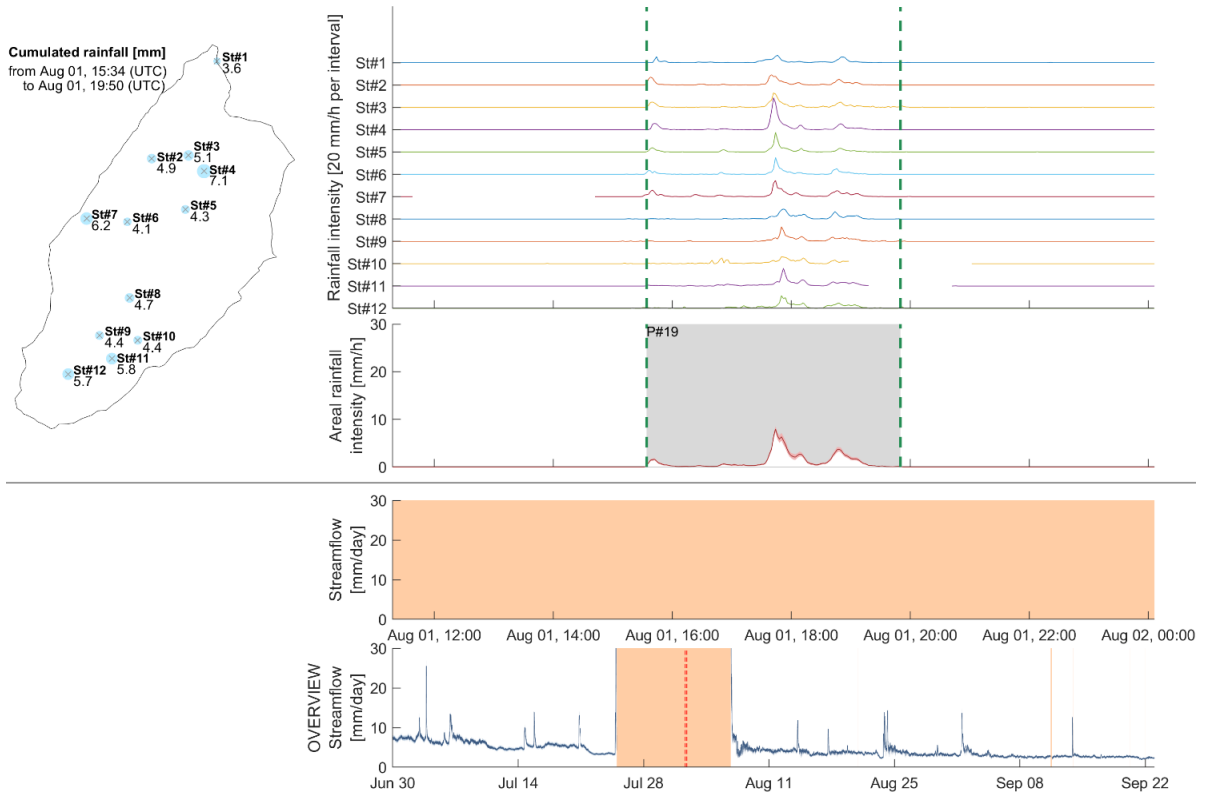


Figure S94. Precipitation event No. 19 from August 1st 03:34 PM to August 1st 07:50 PM

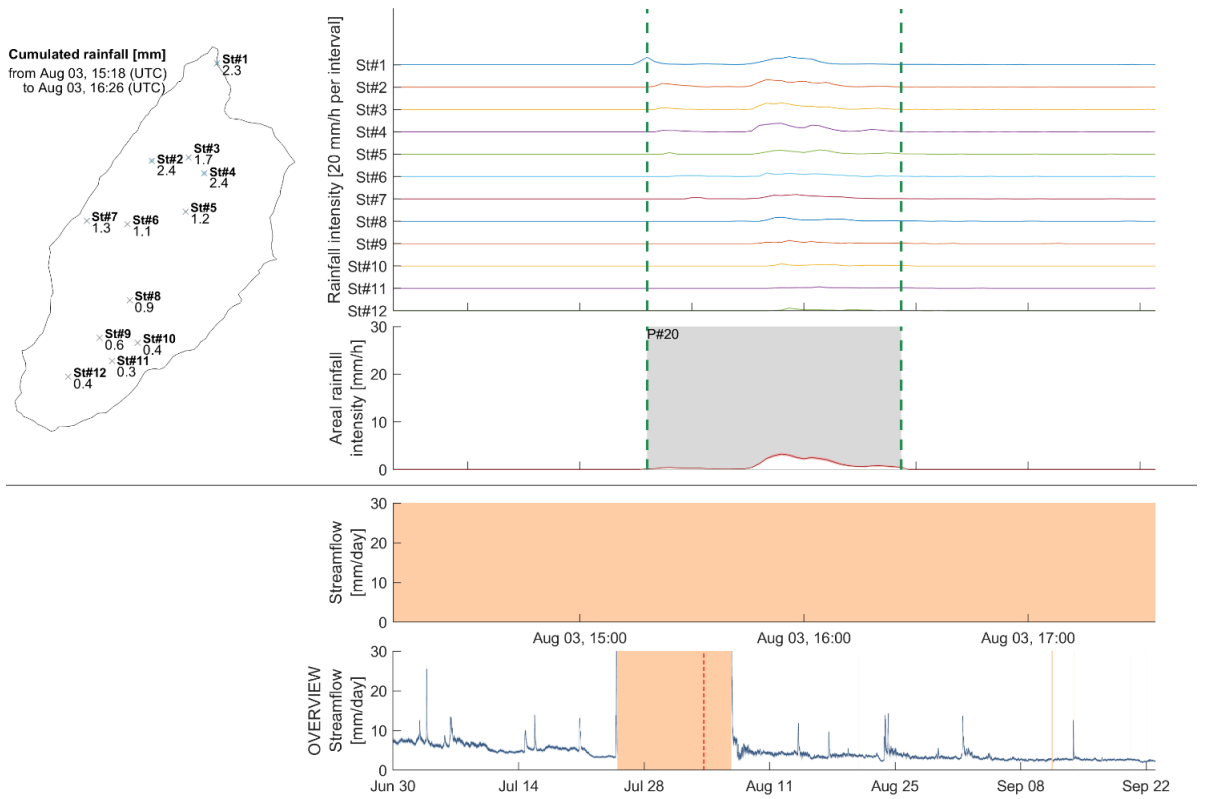


Figure S95. Precipitation event No. 20 from August 3rd 03:18 PM to August 3rd 04:26 PM

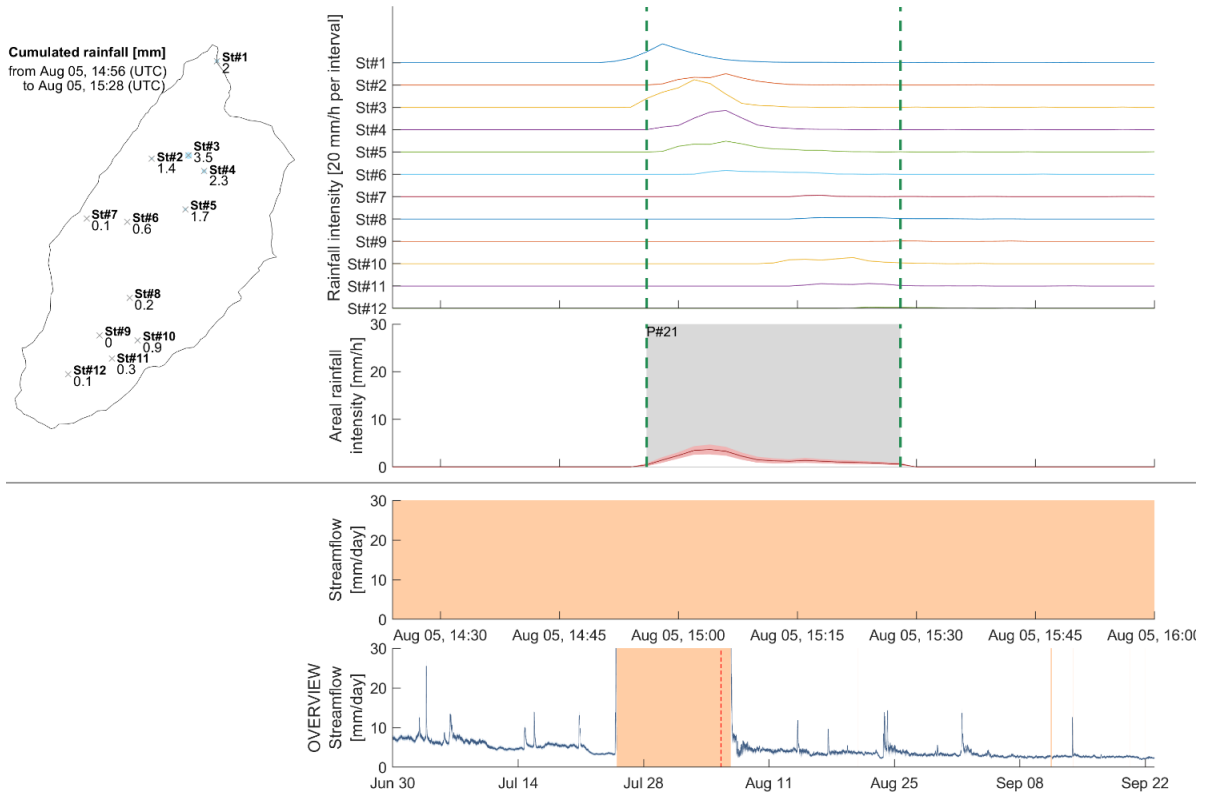


Figure S96. Precipitation event No. 21 from August 5th 02:56 PM to August 5th 03:28 PM

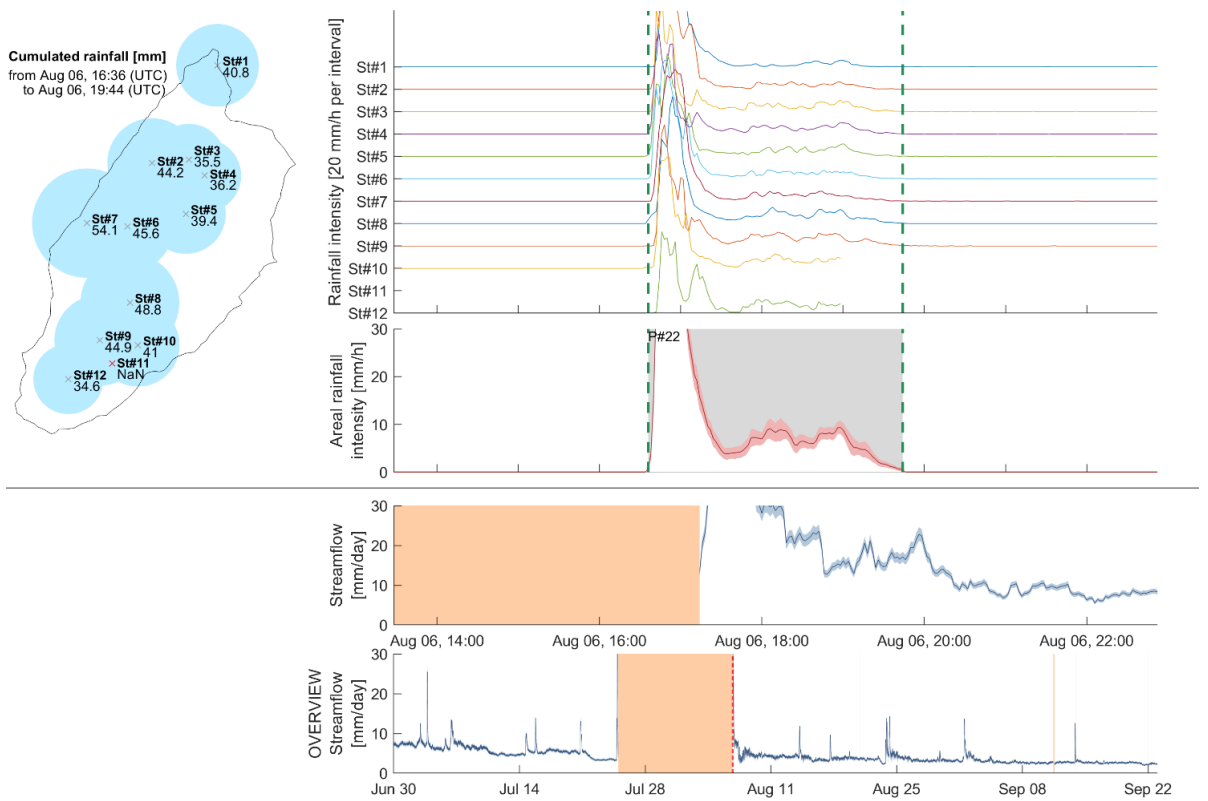


Figure S97. Precipitation event No. 22 from August 6th 04:36 PM to August 6th 07:44 PM

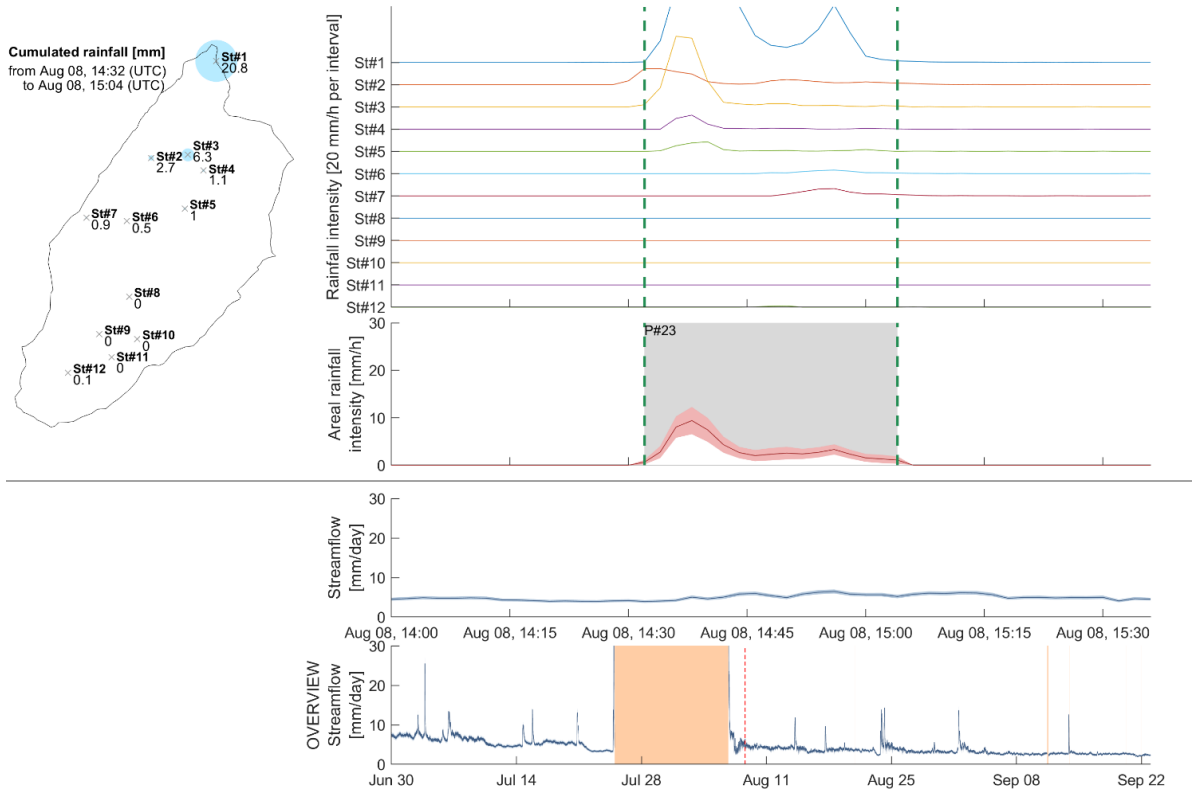


Figure S98. Precipitation event No. 23 from August 8th 02:32 PM to August 8th 03:04 PM

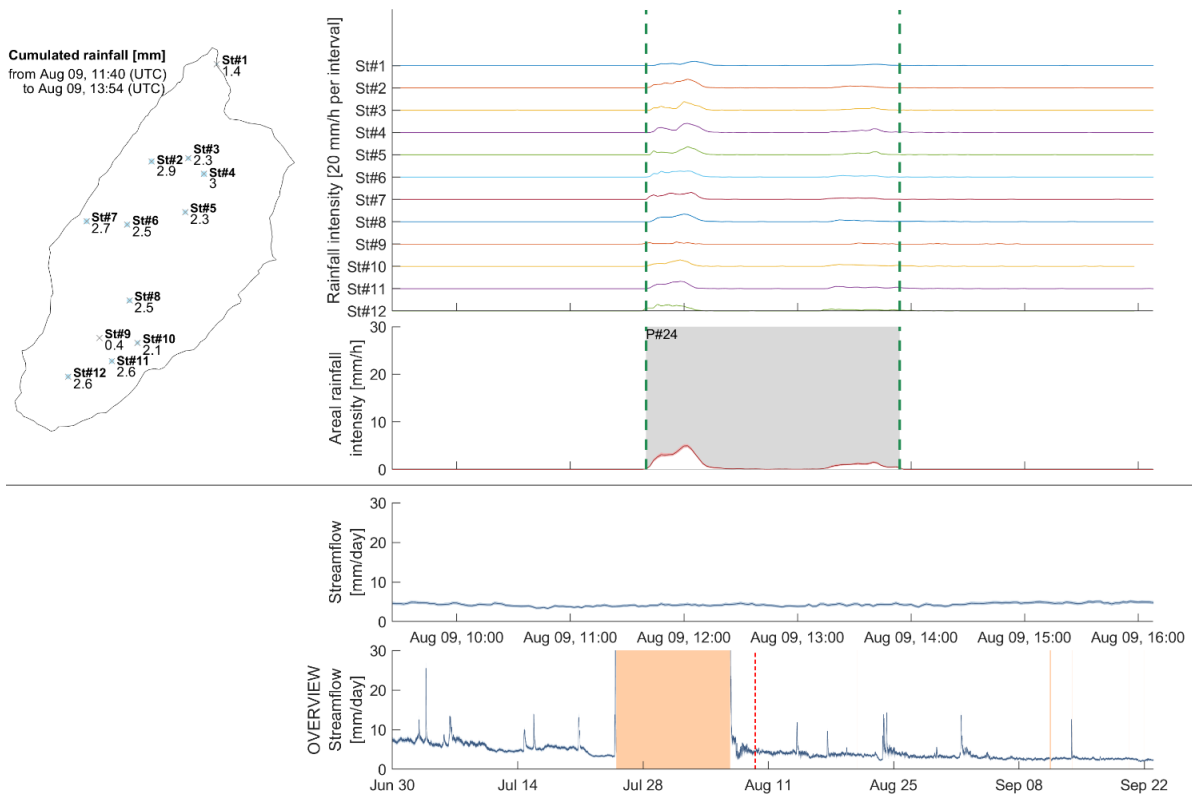


Figure S99. Precipitation event No. 24 from August 9th 11:40 AM to August 9th 01:54 PM

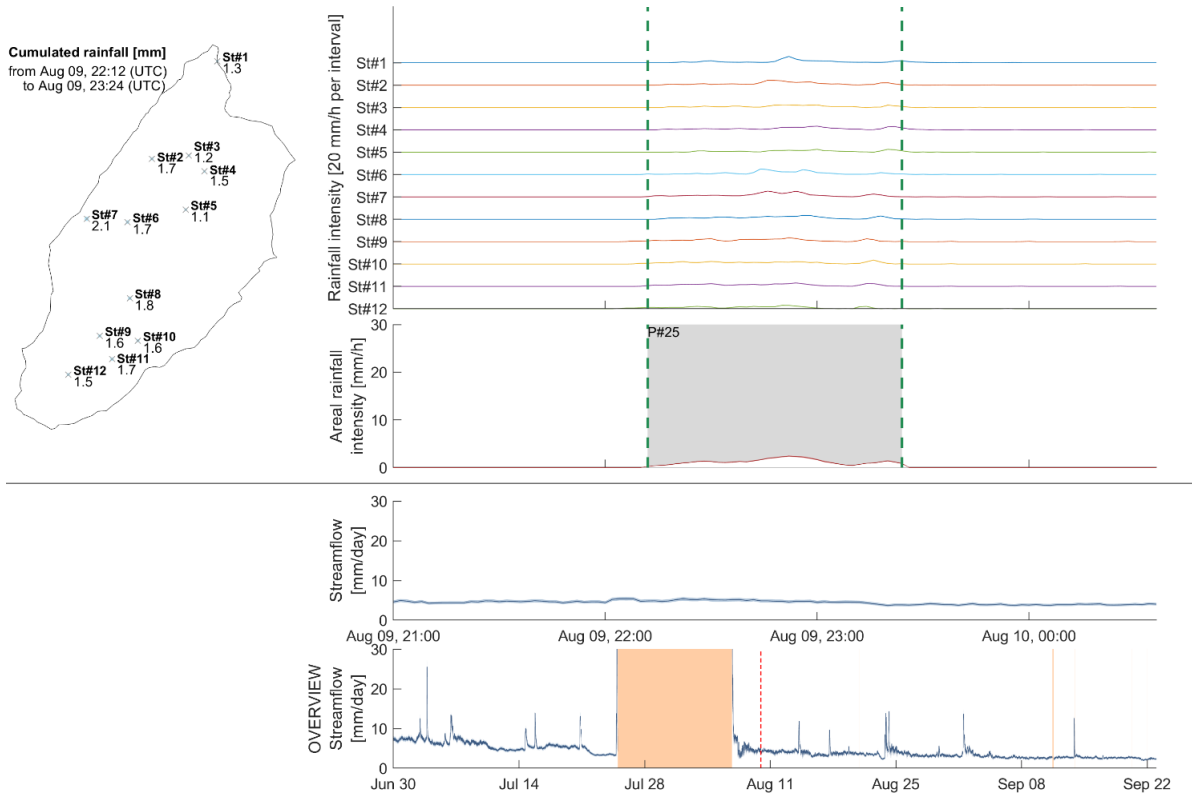


Figure S100. Precipitation event No. 25 from August 9th 10:12 PM to August 9th 11:24 PM

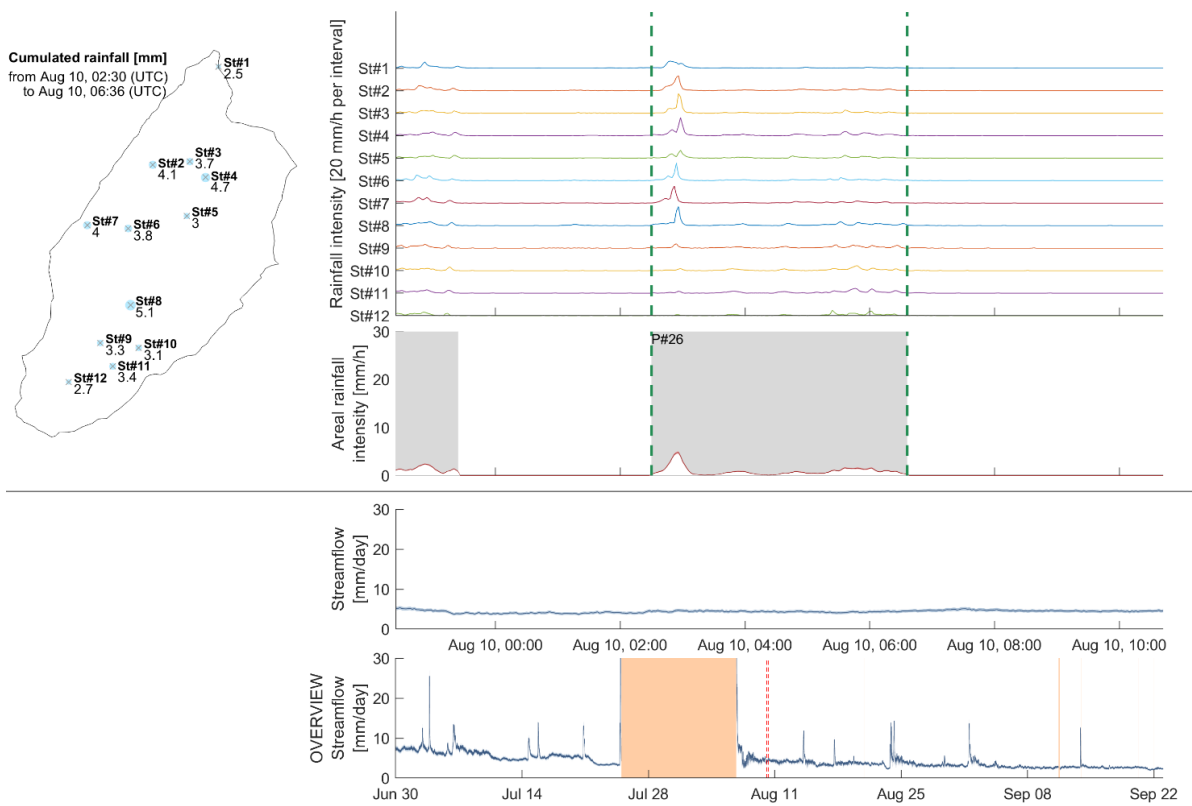


Figure S101. Precipitation event No. 26 from August 10th 02:30 AM to August 10th 06:36 AM

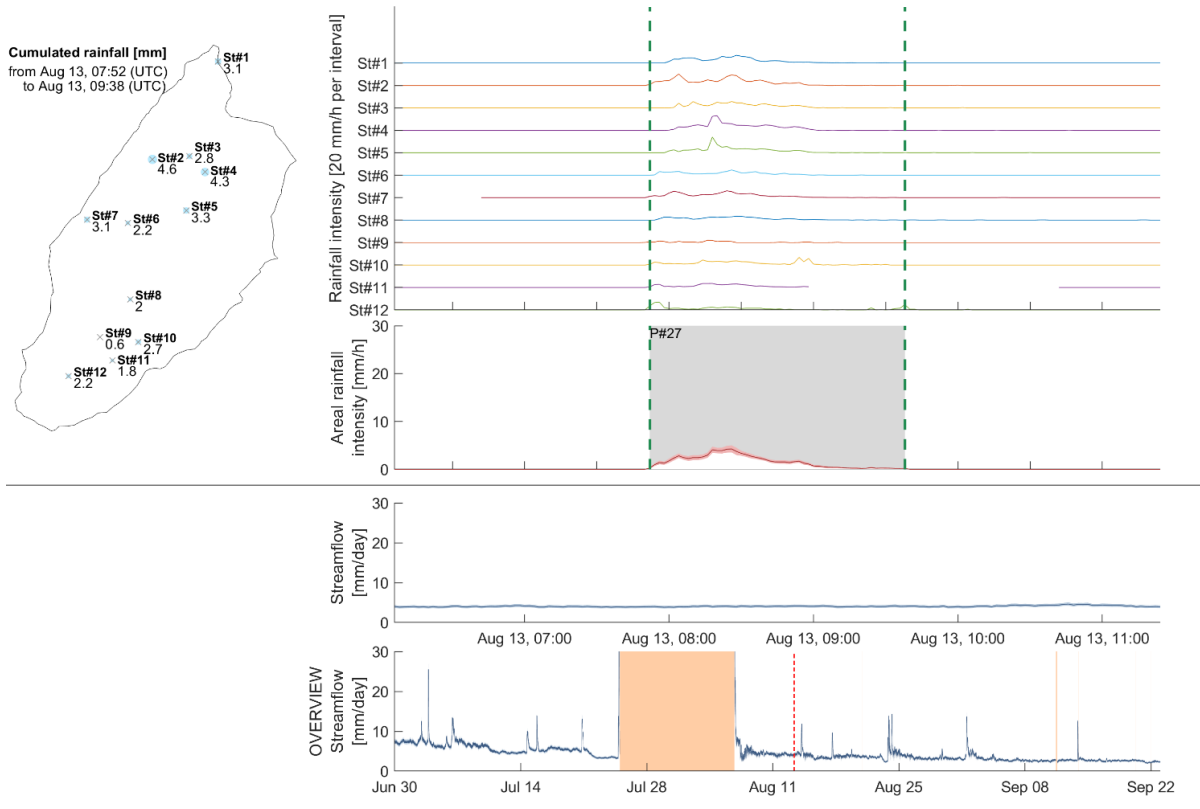


Figure S102. Precipitation event No. 27 from August 13th 07:52 AM to August 13th 09:38 AM

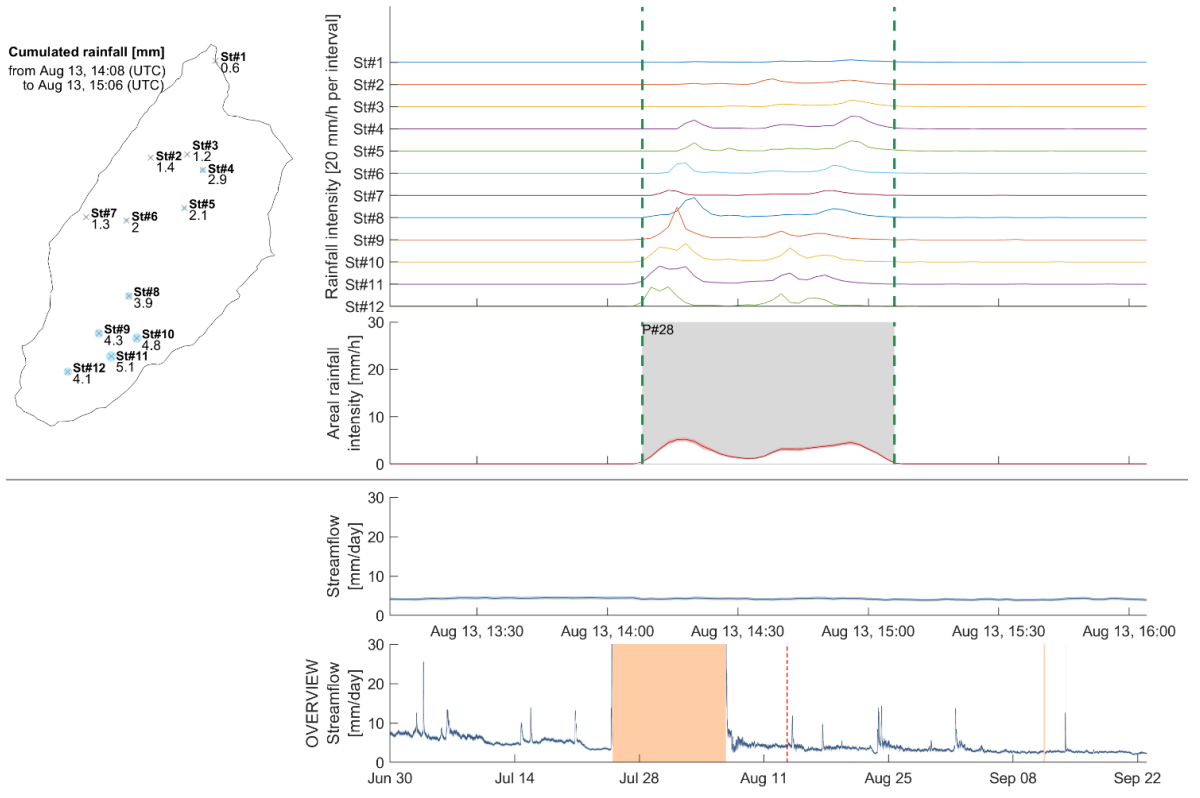


Figure S103. Precipitation event No. 28 from August 13th 02:08 PM to August 13th 03:06 PM

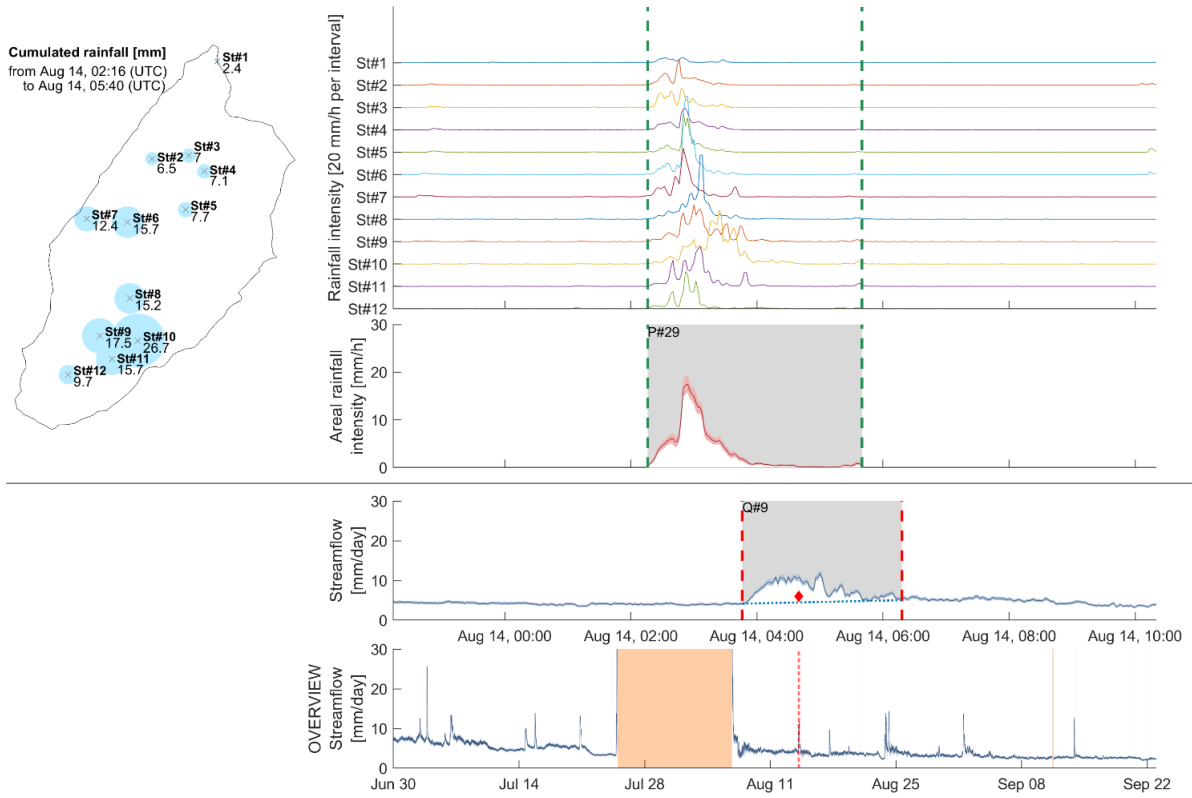


Figure S104. Precipitation event No. 29 from August 14th 02:16 AM to August 14th 05:40 AM and discharge event No. 9 from August 14th 03:46 AM to August 14th 06:18 AM

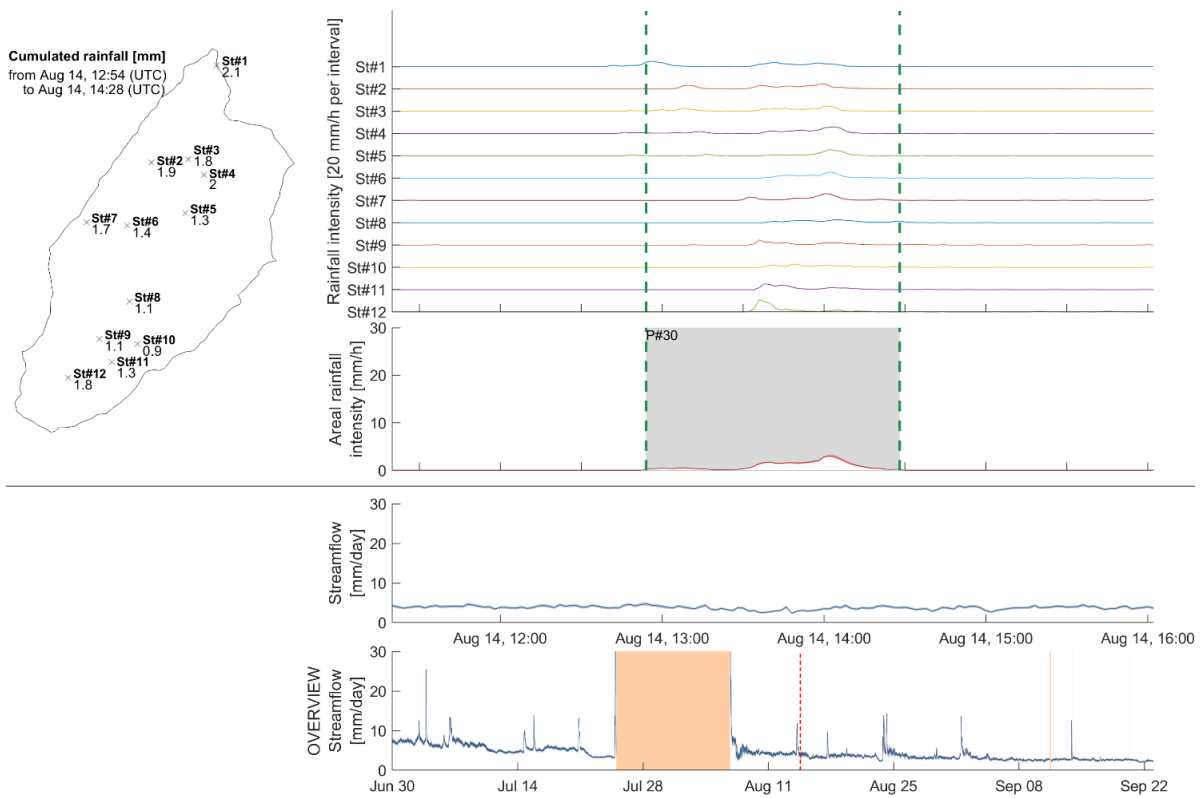


Figure S105. Precipitation event No. 30 from August 14th 12:54 PM to August 14th 02:28 PM

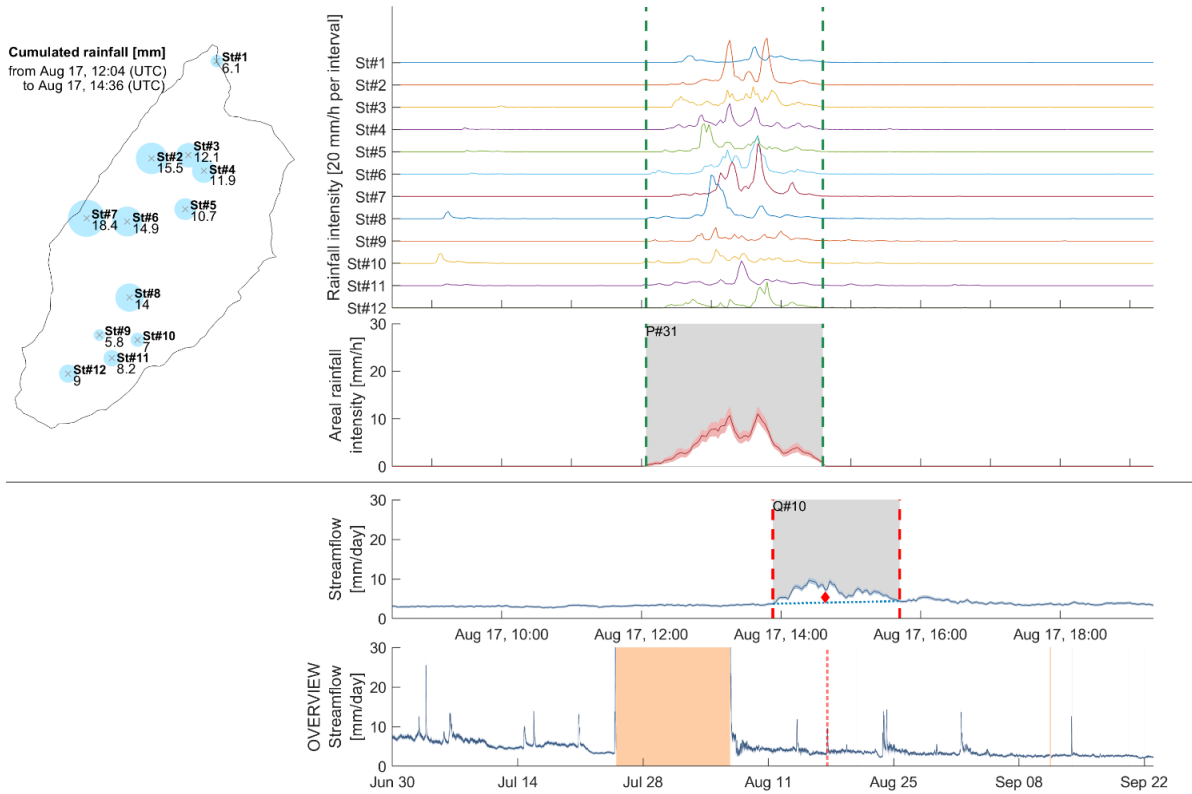


Figure S106. Precipitation event No. 31 from August 17th 12:04 PM to August 17th 02:36 PM and discharge event No. 10 from August 17th 01:53 PM to August 17th 03:42 PM

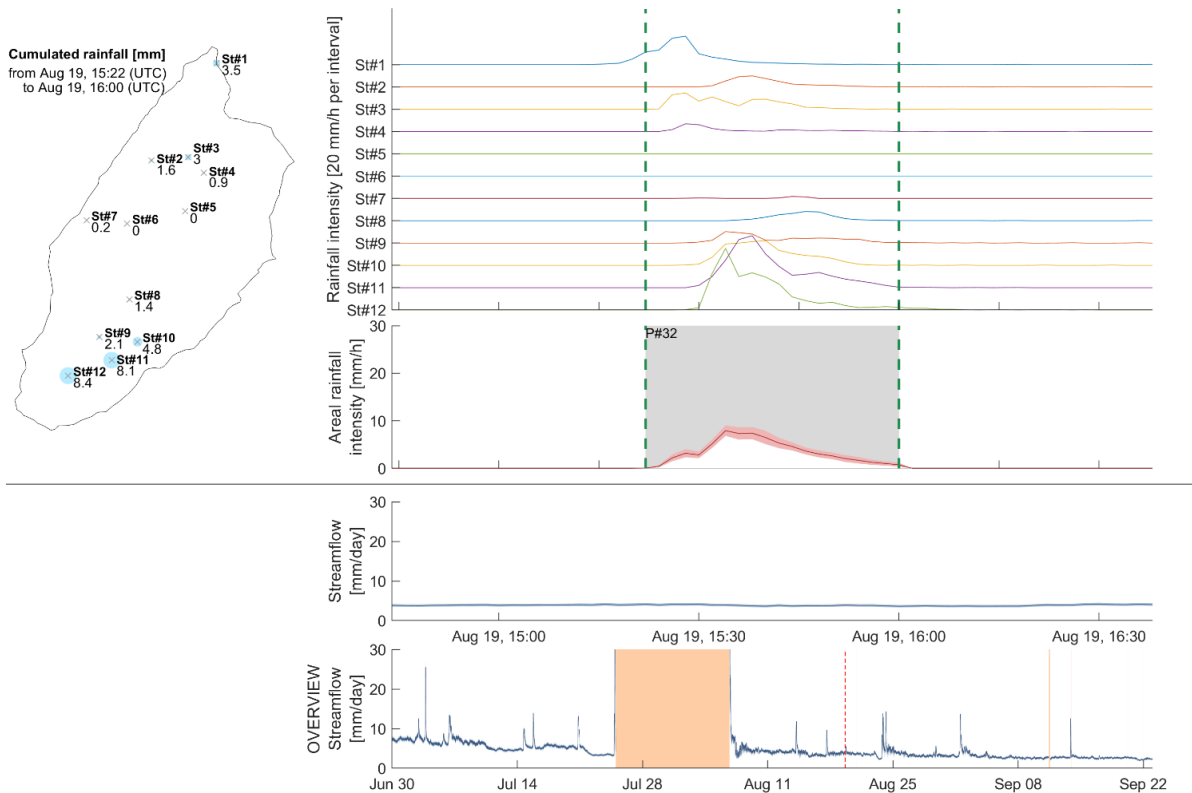


Figure S107. Precipitation event No. 32 from August 19th 03:22 PM to August 19th 04:00 PM

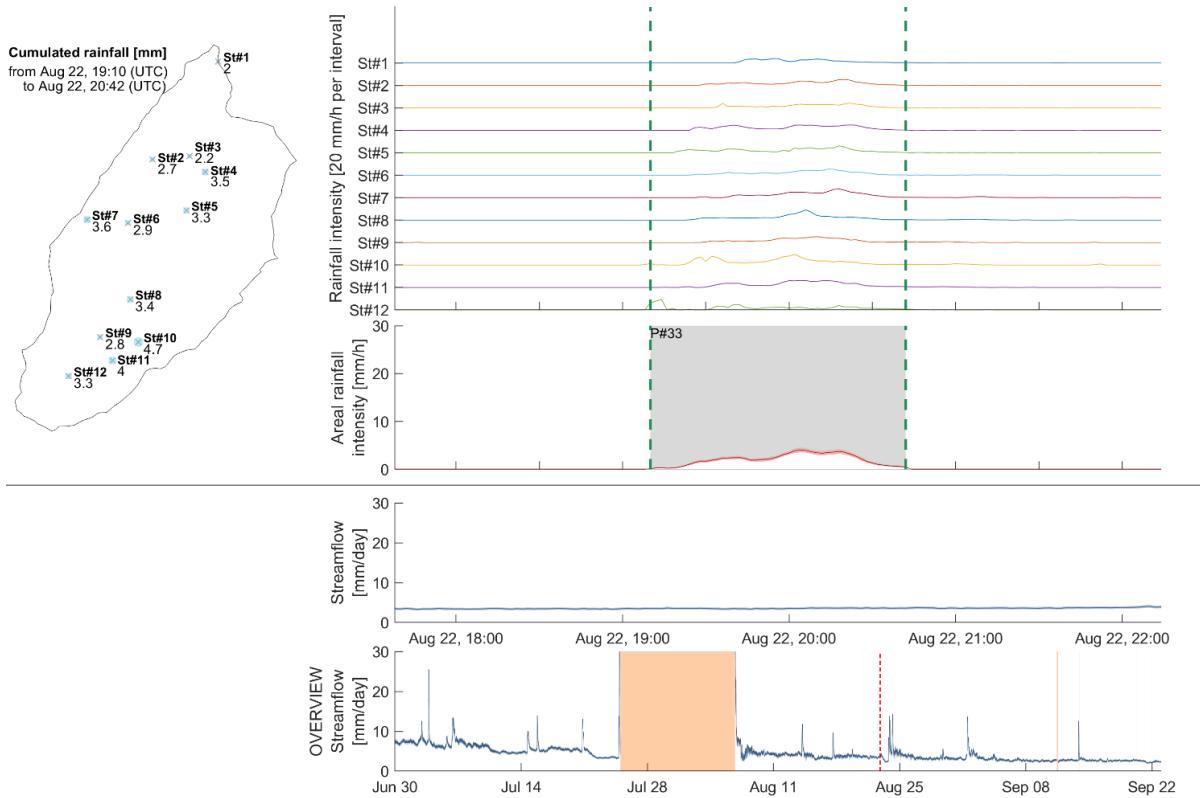


Figure S108. Precipitation event No. 33 from August 22nd 07:10 PM to August 22nd 08:42 PM

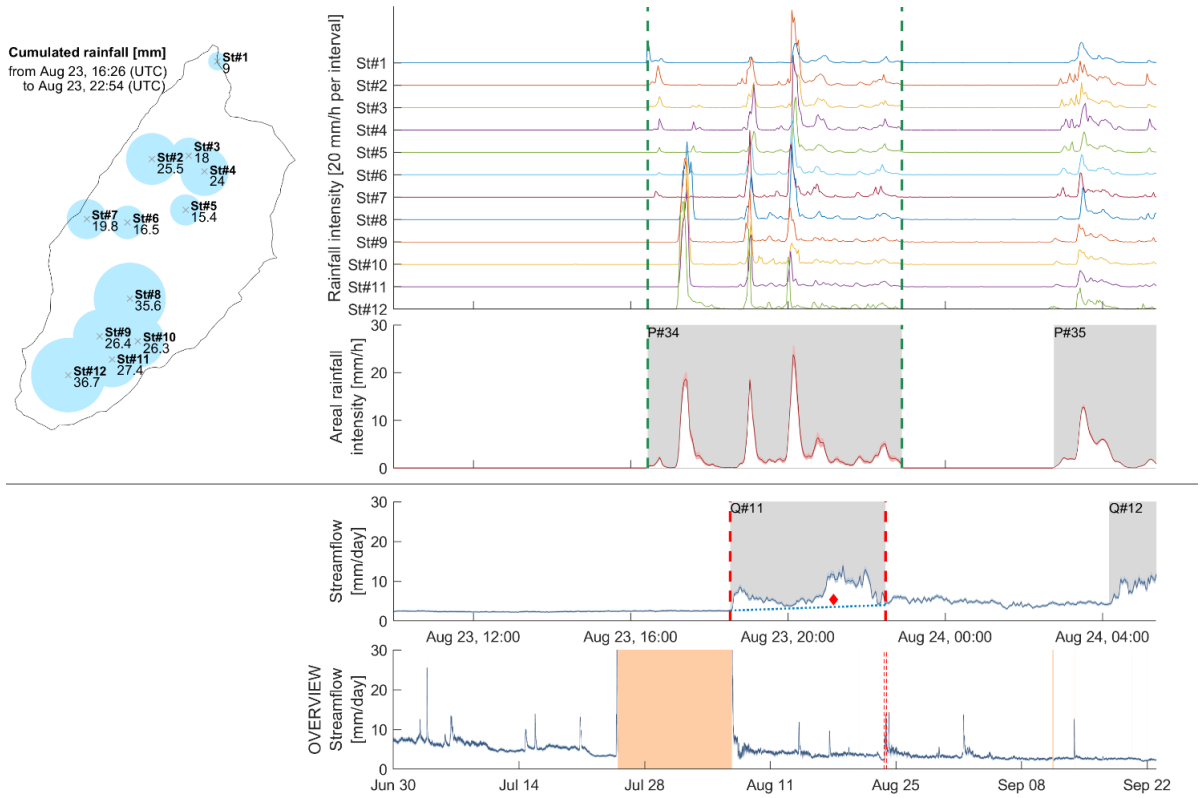


Figure S109. Precipitation event No. 34 from August 23rd 04:26 PM to August 23rd 10:54 PM and discharge event No. 11 from August 23rd 06:32 PM to August 23rd 10:29 PM

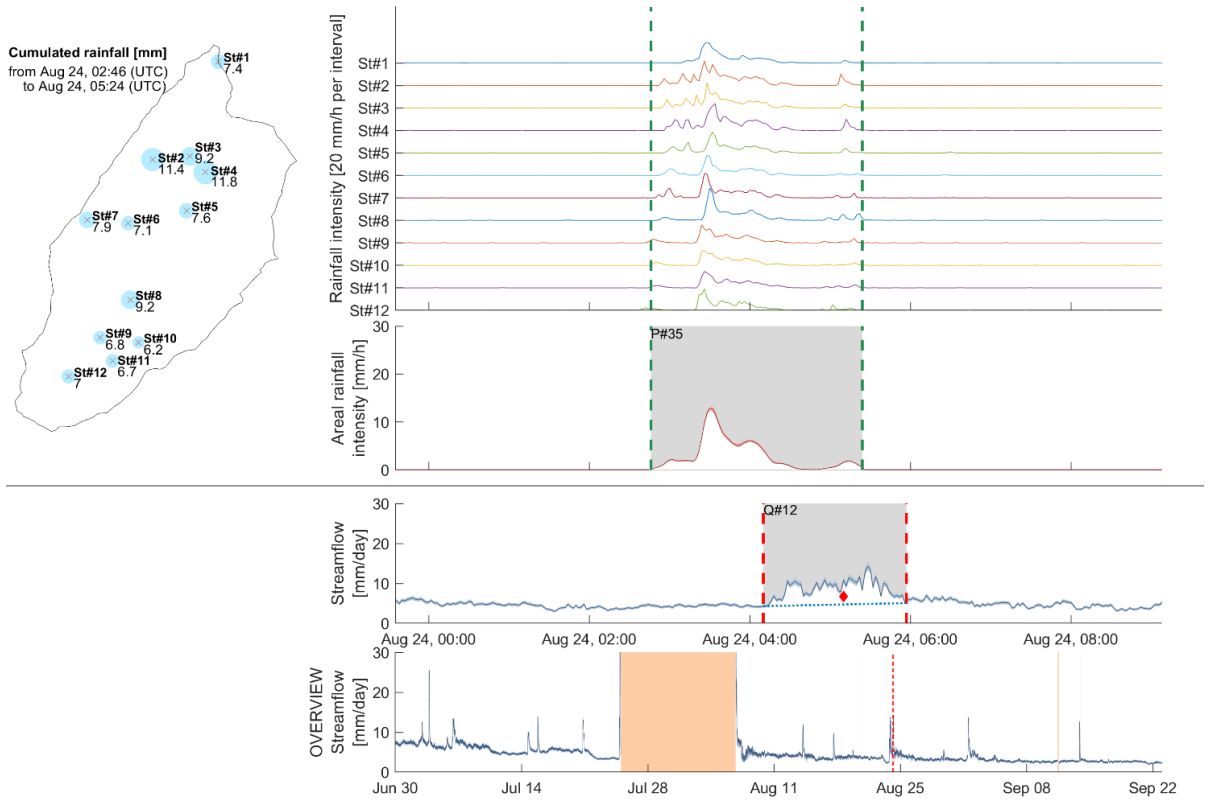


Figure S110. Precipitation event No. 35 from August 24th 02:46 AM to August 24th 05:24 AM and discharge event No. 12 from August 24th 04:10 AM to August 24th 05:57 AM

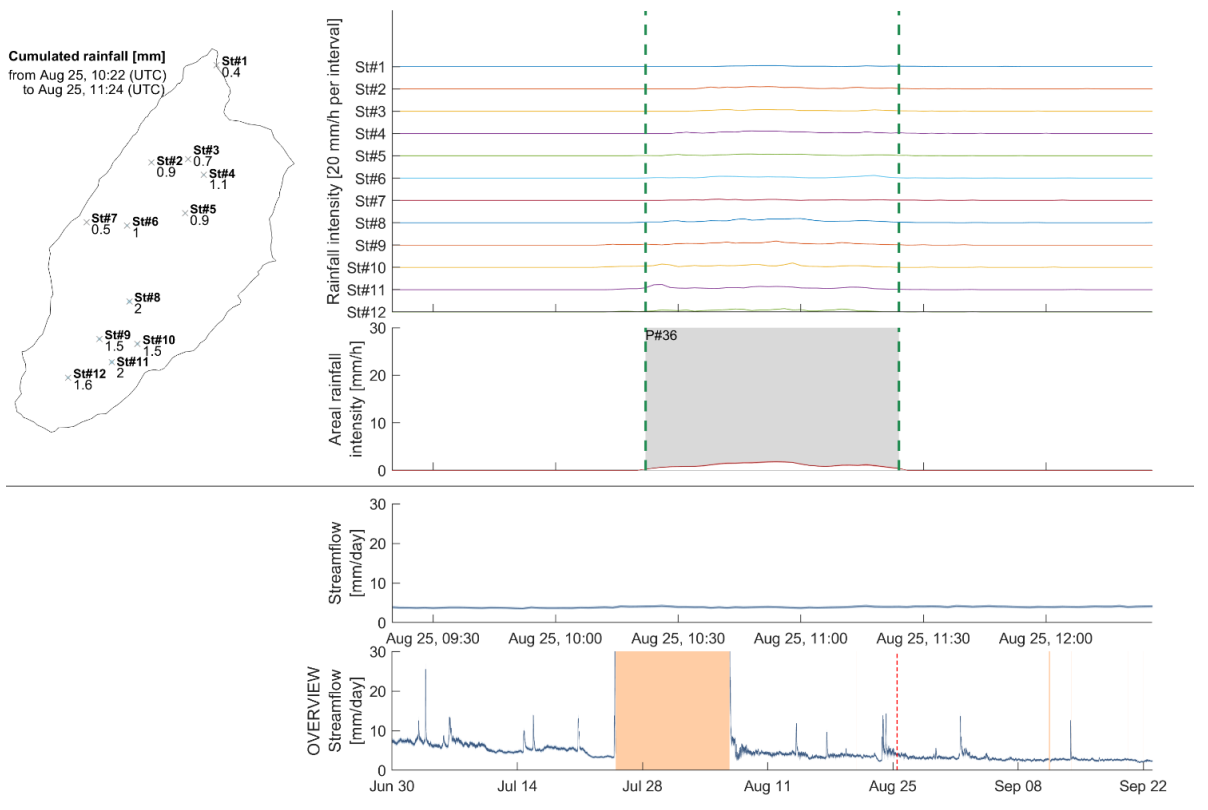


Figure S111. Precipitation event No. 36 from August 25th 10:22 AM to August 25th 11:24 AM

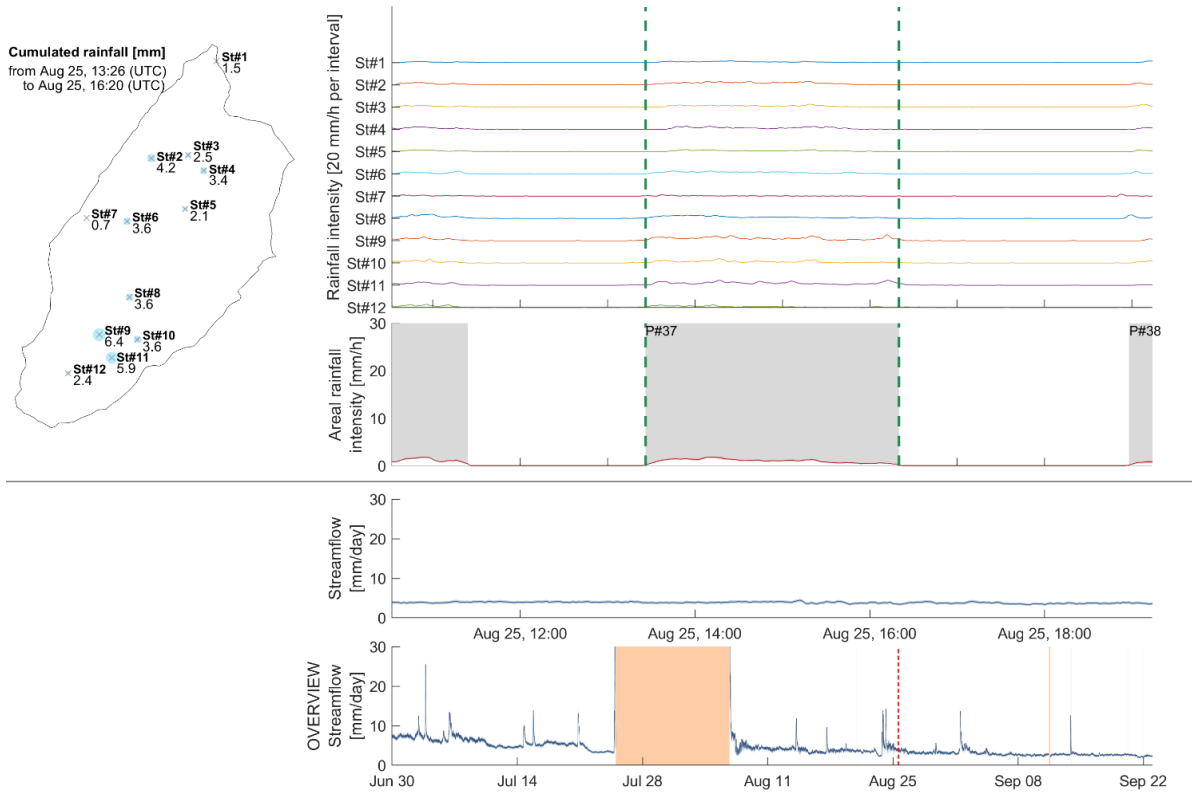


Figure S112. Precipitation event No. 37 from August 25th 01:26 PM to August 25th 04:20 PM

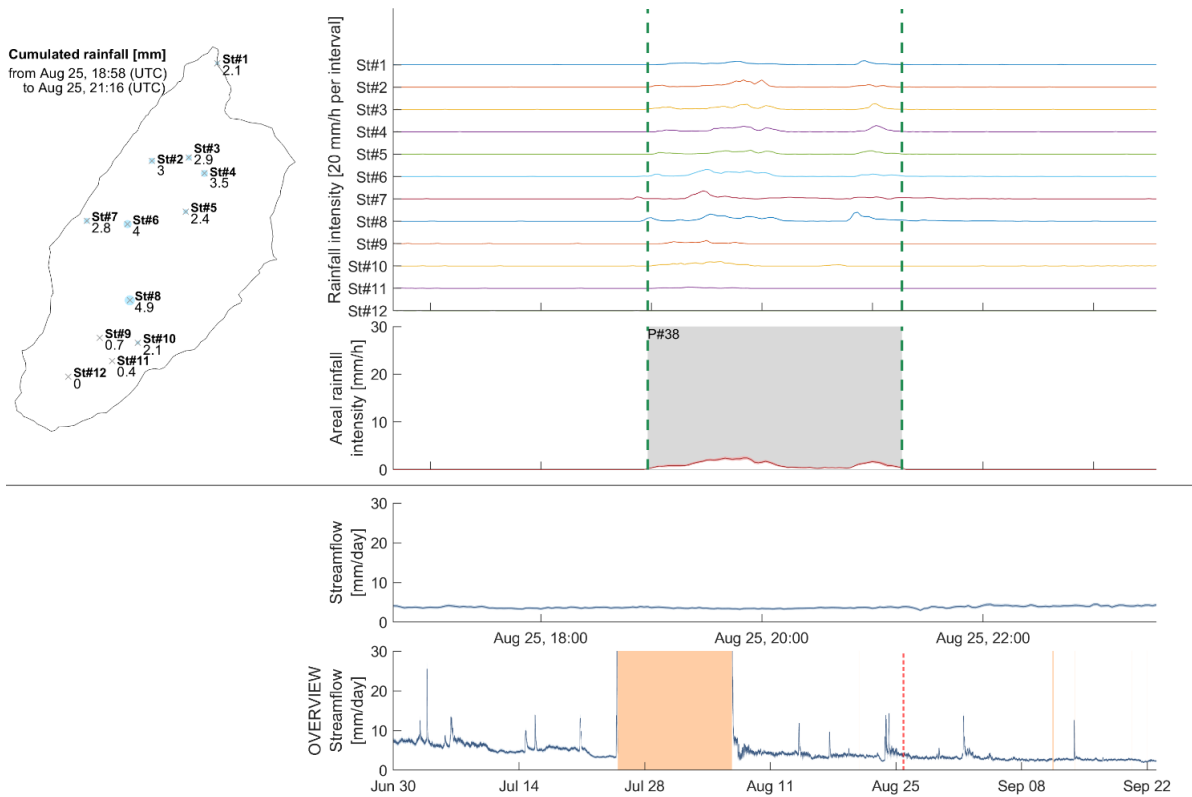


Figure S113. Precipitation event No. 38 from August 25th 06:58 PM to August 25th 09:16 PM

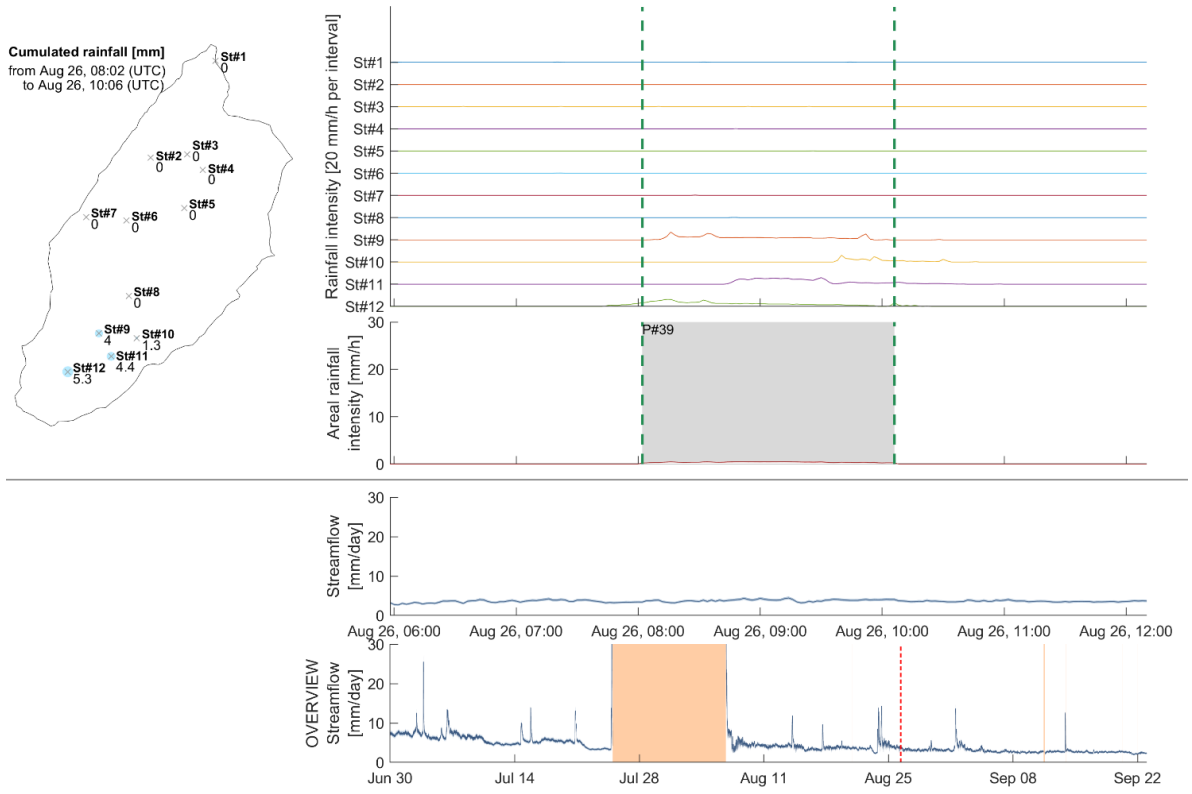


Figure S114. Precipitation event No. 39 from August 26th 08:02 AM to August 26th 10:06 AM

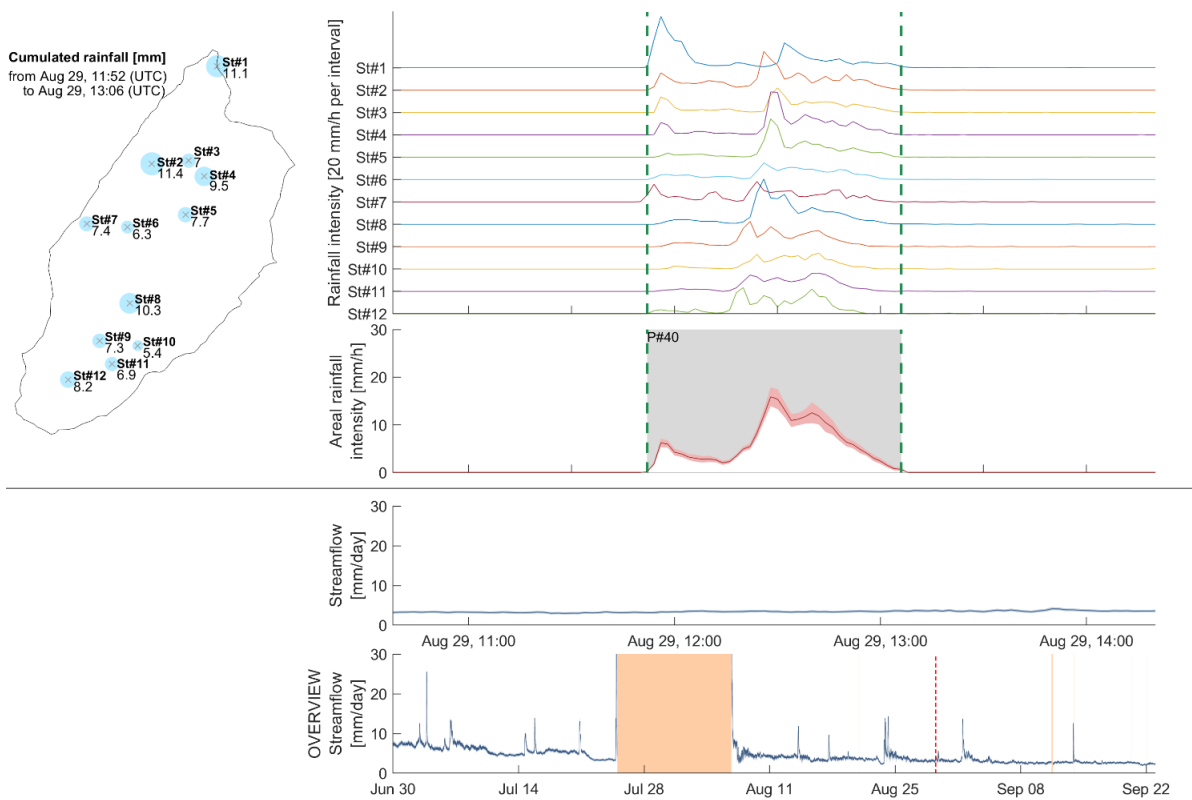


Figure S115. Precipitation event No. 40 from August 29th 11:52 AM to August 29th 01:06 PM

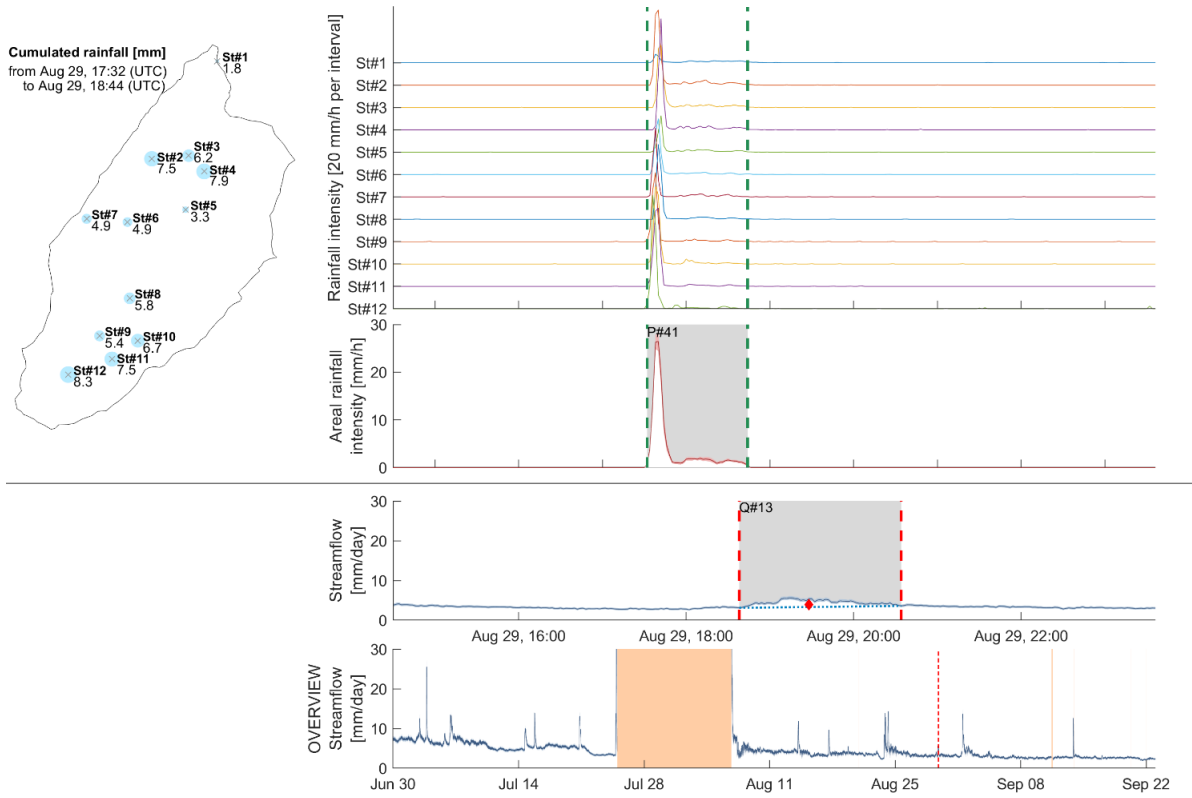


Figure S116. Precipitation event No. 41 from August 29th 05:32 PM to August 29th 06:44 PM and discharge event No. 13 from August 29th 06:38 PM to August 29th 08:34 PM

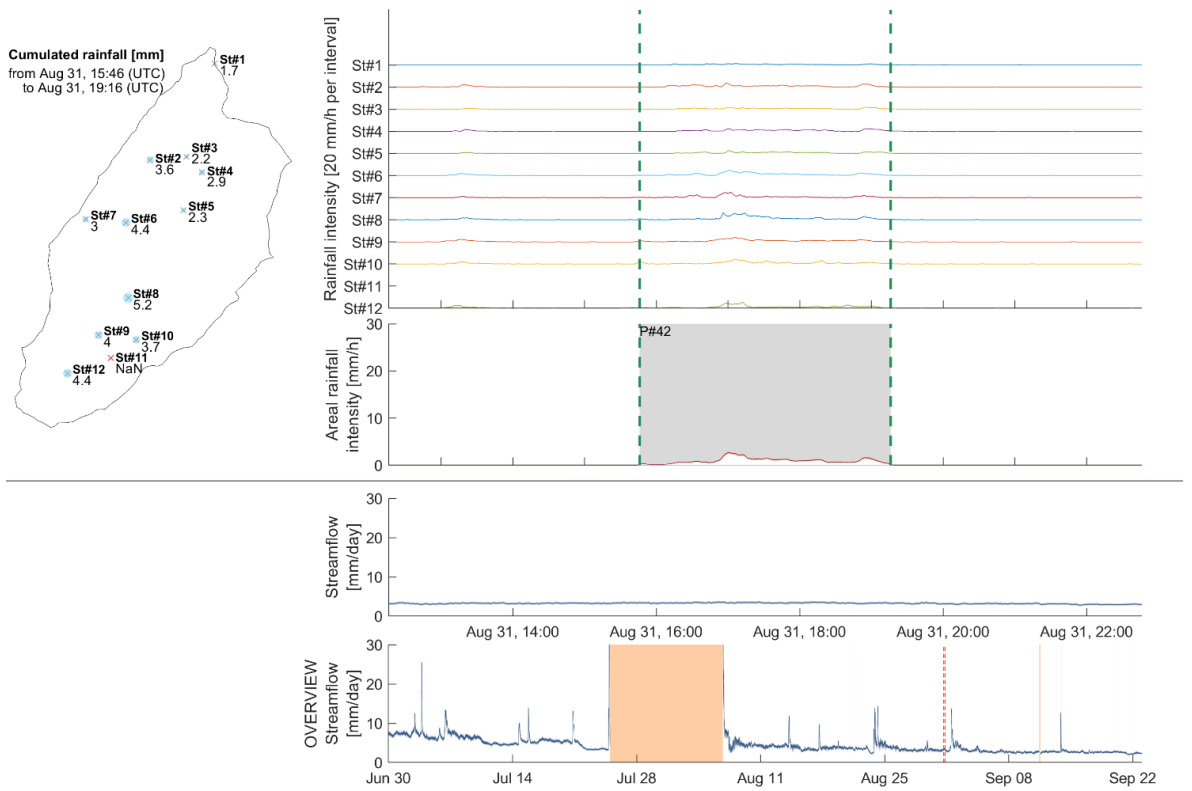


Figure S117. Precipitation event No. 42 from August 31st 03:46 PM to August 31st 07:16 PM

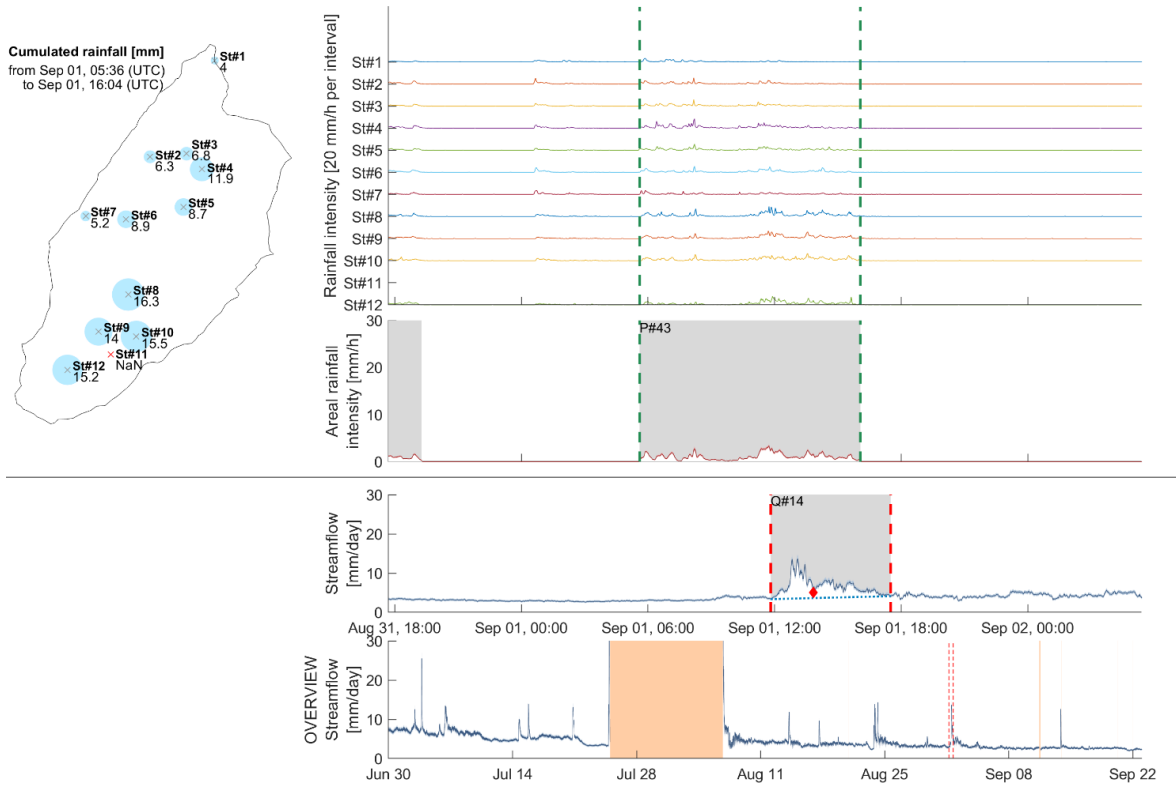


Figure S118. Precipitation event No. 43 from September 1st 05:36 AM to September 1st 04:04 PM and discharge event No. 14 from September 1st 11:49 AM to September 1st 05:30 PM

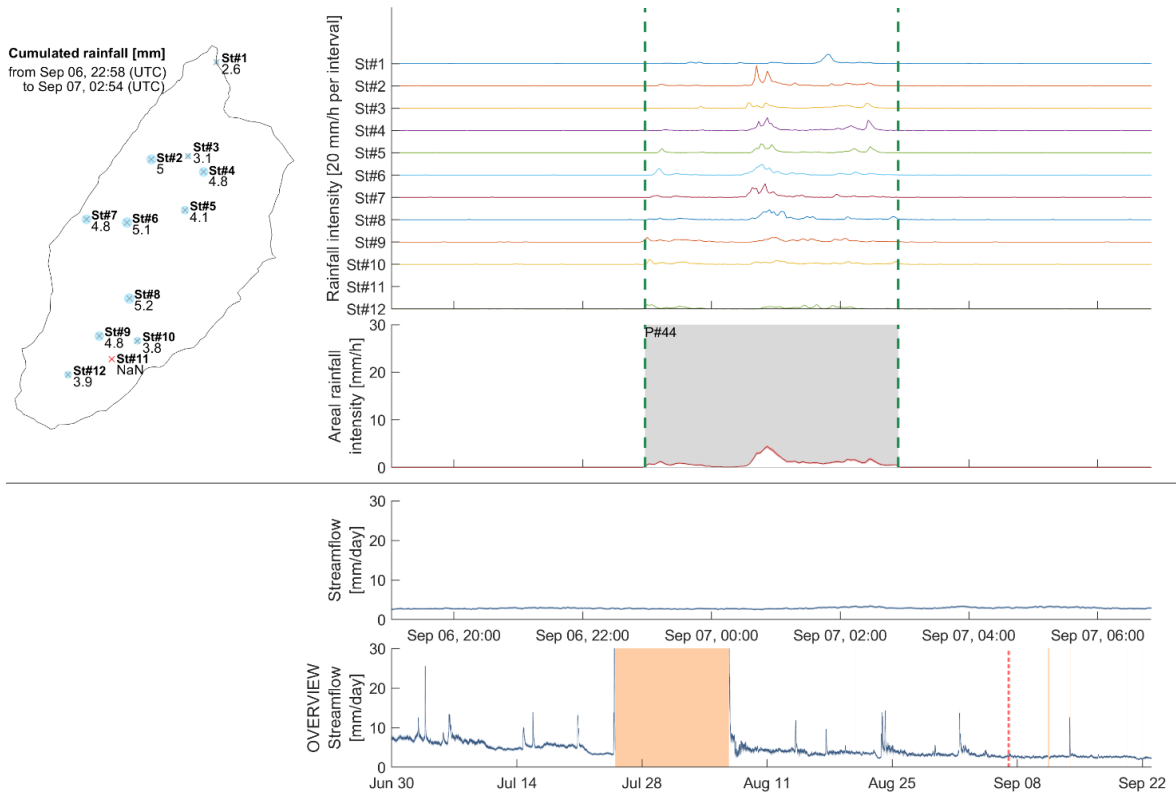


Figure S119. Precipitation event No. 44 from September 6th 10:58 PM to September 7th 02:54 AM

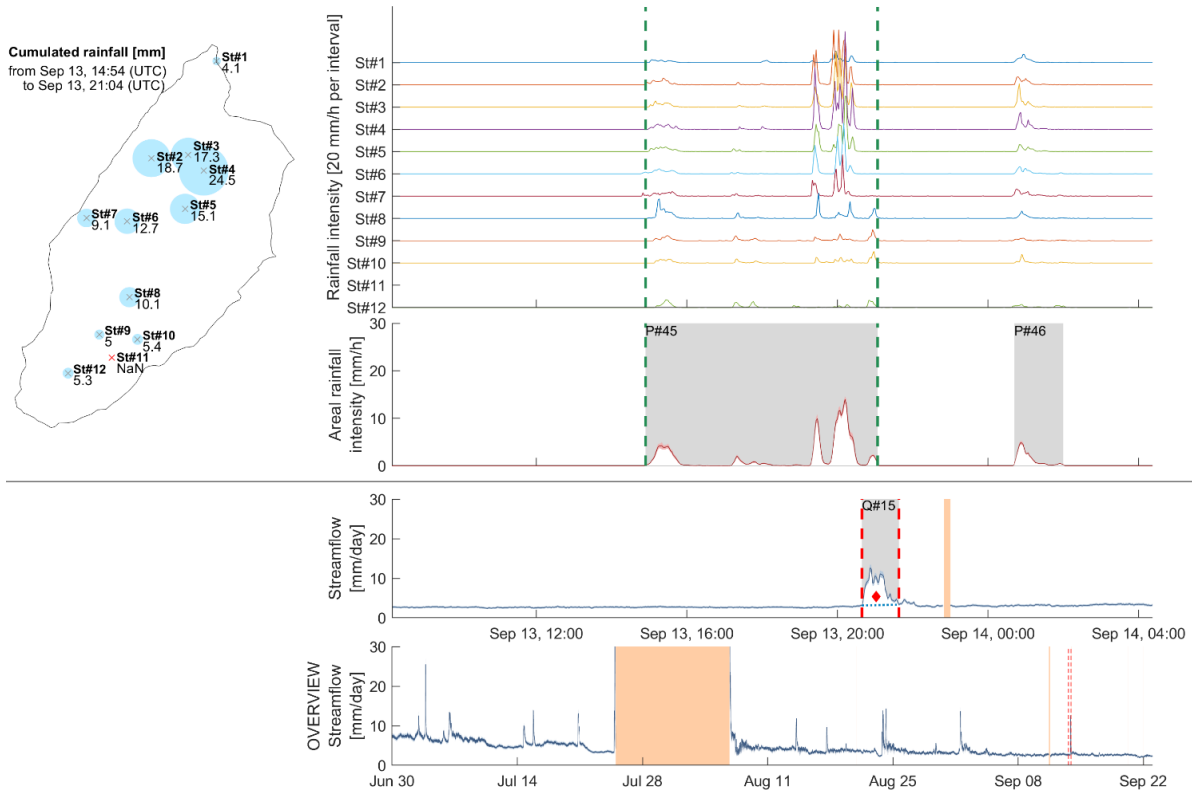


Figure S120. Precipitation event No. 45 from September 13th 02:54 PM to September 13th 09:04 PM and discharge event No. 15 from September 13th 08:39 PM to September 13th 09:38 PM

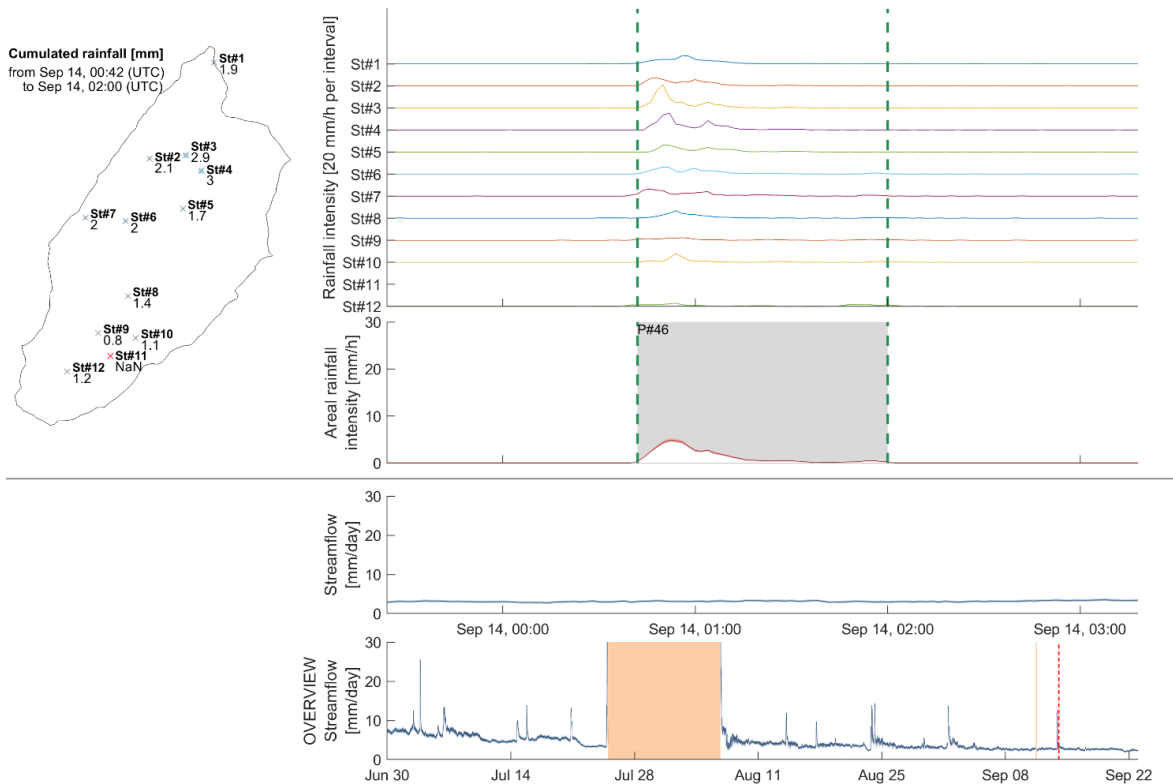


Figure S121. Precipitation event No. 46 from September 14th 12:42 AM to September 14th 02:00 AM

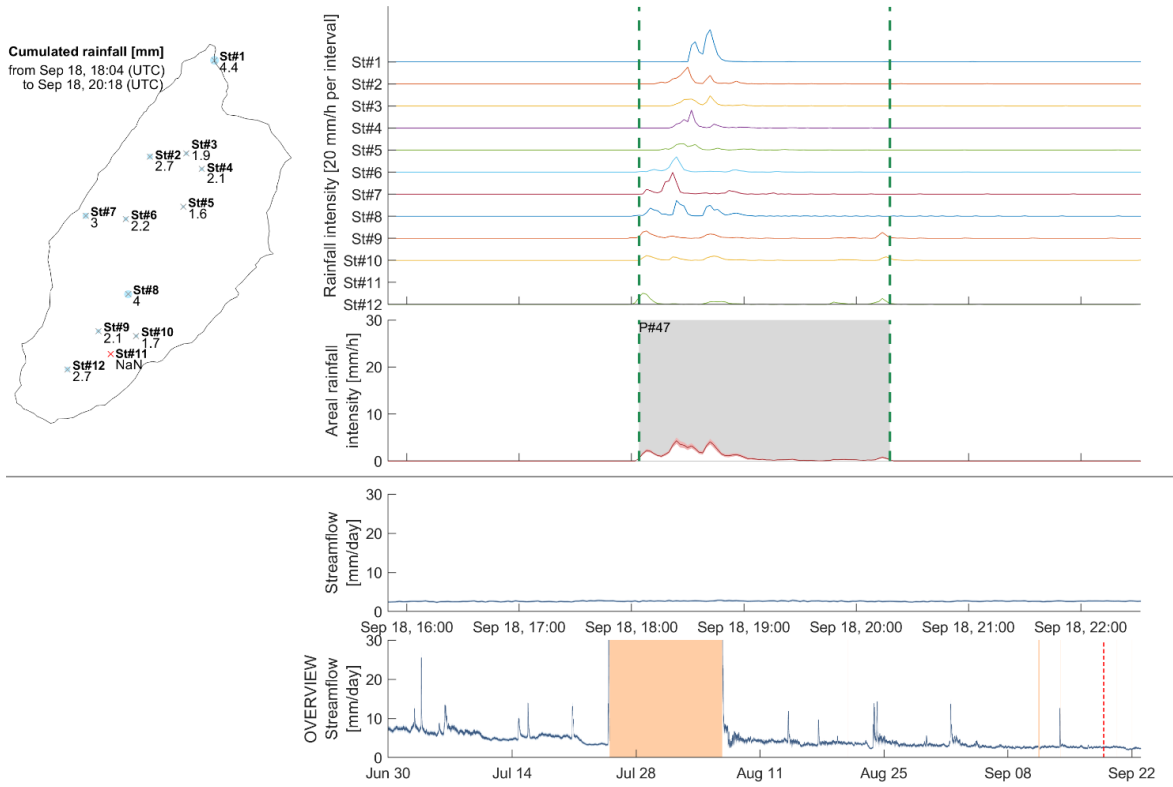


Figure S122. Precipitation event No. 47 from September 18th 06:04 PM to September 18th 08:18 PM

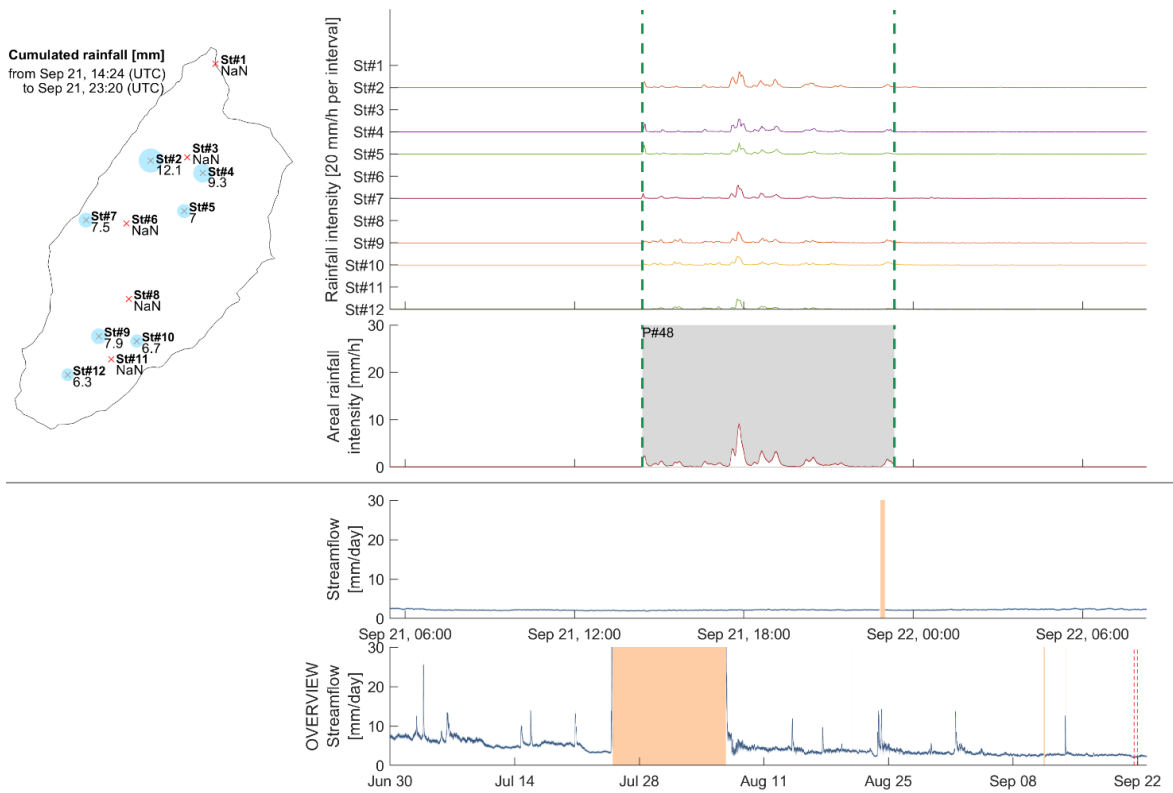


Figure S123. Precipitation event No. 48 from September 21st 02:24 PM to September 21st 11:20 PM

Supplementary material - Chapter 6

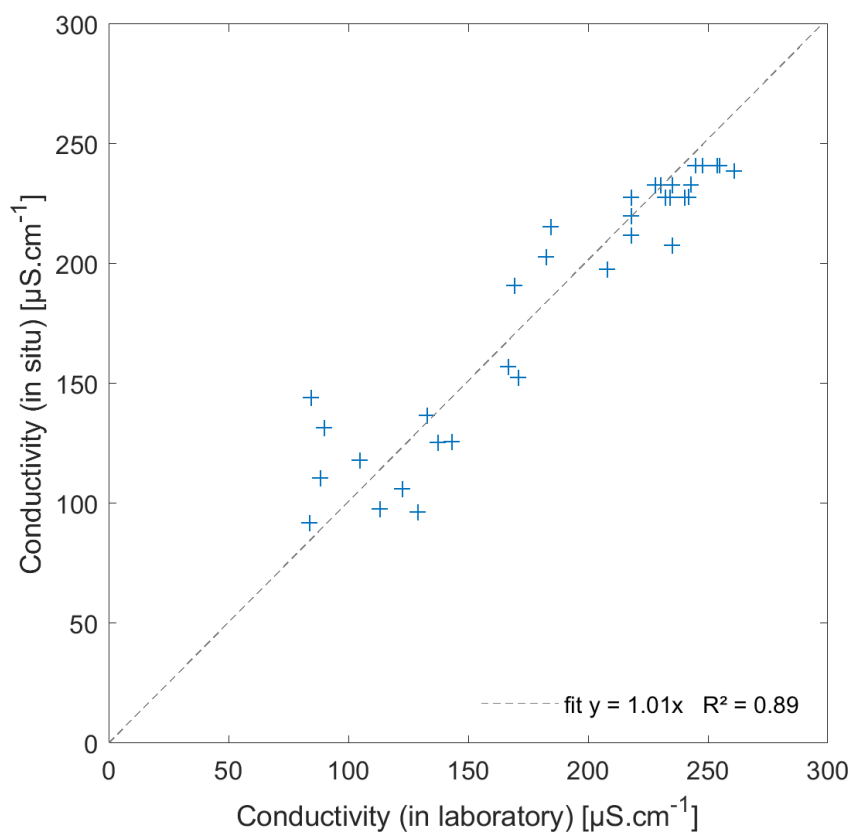


Figure S124. Comparison of 38 samples conductivity measured on the field using a WTW Multi 3510 IDS with a WTW TetraCon 925 probe (Xylem Analytics Germany Sales GmbH & Co, Weilheim, Germany) or later in the laboratory directly within the 12 mL amber silicate vials using a JENWAY 4510 Conductivity Meter with a 6 mm glass probe (Stone, UK).

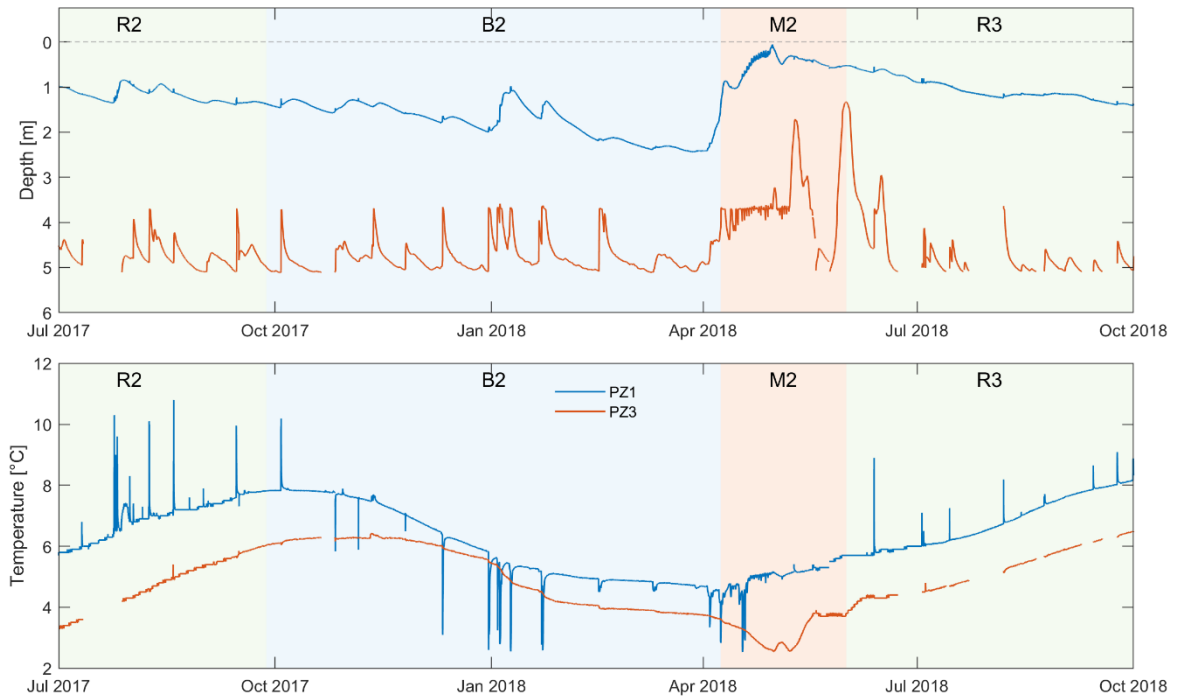


Figure S125. Water table depth (top) and temperature (bottom) at PZ1 and PZ2 from 1 July 2017 to 1 October 2018. Water table depth and temperature data are from Thornton et al. (2021a).

Table S23. Start and end dates of each hydrological period.

Period	Start date	End date
B0	1 January 2016	31 March 2016
E0	31 March 2016	6 May 2016
M0	6 May 2016	24 June 2016
R1	24 June 2016	27 September 2016
B1	27 September 2016	18 March 2017
E1	18 March 2017	6 May 2017
M1	6 May 2017	2 June 2017
R2	2 June 2017	27 September 2017
B2	27 September 2017	8 April 2018
M2	8 April 2018	31 May 2018
R3	31 May 2018	1 January 2019

Table S24. Start and end dates of each snowcover period at the soil temperature points

Soil temperature site	Start date	End date
1240 masl	3/2/2016	16/3/2016
	4/1/2017	13/3/2017
	25/11/2017	7/4/2018
1530 masl	1/1/2016	14/5/2016
	4/1/2017	9/5/2017
	5/11/2017	29/5/2018
2640 masl	1/1/2016	9/7/2016
	4/10/2016	25/11/2016
	4/1/2017	13/6/2017
	22/10/2017	6/6/2018